Perylene based Liquid Crystals as Materials for Organic Electronics

A Thesis Submitted in Partial Fulfillment of the
Requirements for the Degree of
Doctor of Philosophy
at
IIT Guwahati
by

Ravindra Kumar Gupta

Roll No. 136122022

Department of Chemistry
Indian Institute of Technology Guwahati
Guwahati-781039, Assam
India

May 2018

भारतीय प्रौद्योगिकी संस्थान गुवाहाटी
Indian Institute of Technology Guwahati

“Success consists of going from failure to failure without loss of enthusiasm”.

Winston Churchill

“Simplicity of all things is the hardest to be copy”.

Richard Steele

Dedicated to

my beloved parents and family……….

DECLARATION

I do hereby declare that the research work embodied in this thesis entitled “***Perylene based Liquid Crystals as Materials for Organic Electronics***” has been carried out by me under the supervision of **Dr. A. S. Achalkumar** in the Department of Chemistry, Indian Institute of Technology Guwahati, Assam - 781039, India.

In keeping with the general practice of reporting scientific observations, due acknowledgements have been made wherever the work described is based on the findings of other investigators.

IIT Guwahati	Ravindra Kumar Gupta
May, 2018	Roll No. 136122022

Dr. A. S. Achalkumar
Associate Professor
Department of Chemistry
Indian Institute of Technology Guwahati
Guwahati – 781039, Assam, India
Phone: +91-361-258-2329
Fax: +91-361-258-2349
E-mail: achalkumar@iitg.ernet.in
achalkumar78@gmail.com

CERTIFICATE

This is to certify that the research work presented in this thesis entitled "***Perylene based Liquid Crystals as Materials for Organic Electronics***" is an authentic record of the results obtained from the research work carried out by **Mr. Ravindra Kumar Gupta (Roll No. 136122022)** under my supervision in the Department of Chemistry, Indian Institute of Technology Guwahati, India. This work is original and has not been submitted elsewhere for a degree or award.

IIT Guwahati
May, 2018

Dr. A. S. Achalkumar
Thesis Supervisor

ACKNOWLEDGEMENTS

The journey towards the completion of my thesis with the outcome of the years of experience, ideas generated in the form of knowledge, was full of hurdles paved way to the fruitful success. Over five years of my research career I have been supported and assisted by a large number of people, in regards to whom I want to convey my words of heartfelt thanks for their kindness, grace, attention, encouragement, and support.

At the very outset, with the deepest sense of gratitude, I wish to express my sincere thanks to my supervisor, Dr. Ammathnadu S. Achalkumar for his proficient guidance, inspiration, creative and scientific ideas which helped me to explore the domain of my work assembled in this thesis. He has given me an extraordinary amount of freedom to be creative and to work on the problems that have interested me. I have spent countless hours discussing research and ideas in science with him. Without his patience and guidance, I would not have finished this work. Of course, wherever I was standing in the shadow of fear of travel, he helped me to achieve the target by his constant encouragement with his true scientific spirit. It was one of the best choices I have ever made to choose him as my supervisor. Besides my supervisor, I would also like to express my deepest sense of gratitude and heartfelt thanks to my doctoral committee members, Dr. Bhubaneswar Mondal, Dr. Subhas Chandra Pan and Dr. Chandan Kumar Jana for their periodic evaluation of my work, valuable suggestions, constant support, and encouragement. I would like to express my sincere thanks to Mr. Prasenjit Sarkar, Dr. Samir Ghorai and Dr. Chandan Mukherjee for providing me his electrochemical workstation for the analysis. I would like to thank Prof. A. N. Panda for helpful discussion in DFT calculations. I would like to acknowledge Dr. Dipjyoti Das and Prof. P. K. Iyer, IIT Guwahati for OLED device fabrication and characterization in chapter 3a and 5b, and Dr. H. Ulla and Prof. M. N. Satyanarayan, NIT Karnataka for OLED device fabrication and characterisation in chapter 3b. I would like to acknowledge Dr. Monika Gupta and Dr. Santanu Kumar Pal, IISER Mohali, Dr. D. S. Shankar Rao and Dr. S. K. Prasad, CeNS, Bangalore, for helping me with X-ray Diffraction analysis. I would like to acknowledge Mr. B. N. Veerabhadraswamy and Dr. C. V. Yelamaggad, CeNS, Banglore, for helping me in elemental analysis.

Of course, nothing would function properly without our gifted scientific officer, Dr. Babulal Das and other non-teaching staffs, I acknowledge them gratefully. I would like to acknowledge Central Instruments Facility, IIT Guwahati for providing me the analytical facilities required during my research work. I wish to express my sincere gratitude to Indian Institute of Technology Guwahati for nurturing our research career and for all the facilities and financial support that was made available to me.

It would have been impossible for me to continue my five years stay of Ph.D. research without the help and support of my batchmates; I am greatly indebted to them. I express my deep sense of gratitude to all my lab members Dr. Hemant Kumar Singh, Dr. Nirmalangshu Chakraborty, Dr. Suraj Kumar Pathak, Dr. Subrata Nath, Ms. Pratika Basumatary, Mr. Balaram Pradhan, Mr. Vinod Kumar Vishwakarma, Dr. Sachin Kumar Singh, Dr. Srikant Turlapati, Dr. Hidayath Ulla, Mr. Paresh Kumar Behera and Mr. Sibasankar Pradhan for their help, scientific conversations and also maintaining a pleasant working environment throughout my Ph.D. tenure.

Of course, I would like to thank almighty to fulfill my PhD carrier with bunch of beloved senior and batchmates; Dr. Bedika Phukan, Dr. Sujit Mahato, Dr. Ashraful Haque, Avishek, Subhra, Mahmuda, Jyoti, Sumana, Dhriti for being with me all the time starting from the beginning of my research career and for their help and guidance.

Finally, my Ph.D. would not have been completed without the eternal love, care, bless, support, patience, non-refundable sacrifices and encouragement of my parents Mr. Anand Kumar Gupta and Mrs. Kiran Devi, my elder brother Mr. Govind Gupta and his wife Mrs. Seeta Gupta, Dr. Arvind Gupta and my younger sister Ms. Parul Gupta. They encouraged me to pay attention to the world around me and to wonder why and how things work. I am sending thanks to lovely kids Tejasva and Raghav for their innocent love which was always helpful to make me cheerful during my research period.

Of course, everything will go invalid if I forget the blessings of almighty god without whom nothing will function and I pray him for his blessings.

Ravindra Kumar Gupta

Some of the findings of this thesis have been published in international journals as given below:

1. Self-assembly of luminescent *N*-annulated perylene tetraesters into fluid columnar phases, **R. K. Gupta**, S. K. Pathak, B. Pradhan, D. S. Shankar Rao, S. K. Prasad and A. S. Achalkumar, *Soft Matter*, 2015, **11**, 3629-3636.

2. Perylo[1,12- b, c, d] thiophene tetraesters: a new class of luminescent columnar liquid crystals, **R. K. Gupta**, B. Pradhan, S. K. Pathak, M. Gupta, S. K. Pal and A. S. Achalkumar, *Langmuir*, 2015, **31**, 8092-8100.

3. *Bay*-annulated perylene tetraesters: a new class of discotic liquid crystals, **R. K. Gupta**, S. K. Pathak, B. Pradhan, M. Gupta, S. K. Pal and A. S. Achalkumar, *ChemPhysChem*, 2016, **17**, 859-872.

4. Electroluminescent room temperature columnar liquid crystals based on *bay*-annulated perylene tetraesters, **R. K. Gupta**, D. Das, M. Gupta, S. K. Pal, P. K. Iyer and A. S. Achalkumar, *J. Mater. Chem. C*, 2017, **5**, 1767-1781.

5. Columnar self-assembly of electron deficient dendronized *bay*-annulated perylene bisimides, **R. K. Gupta**, D. S. Shankar Rao, S. K. Prasad and A. S. Achalkumar, *Chem. Eur. J.*, 2018, **24**, 3566-3575. (Hot paper)

6. Perylene-triazine based star-shaped green light emitter for organic light emitting diodes, **R. K. Gupta**, H. Ulla and A. S. Achalkumar, *Eur. J. Org. Chem.*, 2018, 1608-1613. (Selected in outstanding organics section)

7. Microwave-assisted method for the synthesis of perylene ester imides as a gateway toward unsymmetrical perylene bisimides, **R. K. Gupta** and A. S. Achalkumar, *J. Org. Chem.*, 2018, **83**, 6290-6300.

8. First example of white organic electroluminescence, utilizing perylene ester imides, **R. K. Gupta**, D. Das, P. K. Iyer and A. S. Achalkumar, *ChemistrySelect*, 2018, **3**, 5123-5129.

9. Perylene-Based LCs as Materials for Organic Electronics Applications, **R. K. Gupta** and A. S. Achalkumar, *Langmuir*, 2018, 10.1021/acs.langmuir.8b01081.

Articles that are not included in this thesis:

1. Columnar self-assembly of star-shaped luminescent oxadiazole and thiadiazole derivatives. S. K. Pathak, **R. K. Gupta**, S. Nath, D. S. Shankar Rao, S. K. Prasad and A. S. Achalkumar, *J. Mater. Chem. C.* 2015, **3**, 2940-2952.

2. Effect of regioisomerism on the self-assembly and photophysical behavior of 1,3,4-thiadiazole based polycatenars, S. K. Pathak, S. Nath, **R. K. Gupta**, D. S. Shankar

Rao, S. K. Prasad and A. S. Achalkumar, *J. Mater. Chem. C.* 2015, **3**, 8166-8182. (Hot article)

3. Aromatic π-π driven supergelation, aggregation induced emission and columnar self-assembly of star-shaped 1,2,4-oxadiazole derivatives, S. K. Pathak, B. Pradhan, **R. K. Gupta**, M. Gupta, S. K. Pal and A. S. Achalkumar, *J. Mater. Chem. C*, 2016, **4**, 6546-6561.

4. Star-shaped fluorescent liquid crystals derived from s-triazine and 1,3,4-oxadiazole moieties, B. Pradhan, S. K. Pathak, **R. K. Gupta**, M. Gupta, S. K. Pal and A. S. Achalkumar, *J. Mater. Chem. C*, 2016, **4**, 6117-6130.

5. Nonsymmetrical cholesterol dimers constituting regioisomeric oxadiazole and thiadiazole cores: an investigation on structure-property correlation B. Pradhan, N. Chakraborty, **R. K. Gupta**, G. Shanker, A. S. Achalkumar, *New J. Chem.*, 2017, **41**, 879-888.

6. Room temperature columnar liquid crystalline self-assembly of acidochromic, luminescent, star-shaped molecules with cyanovinylene chromophores, **R. K. Gupta**, S. K. Pathak, J. De, S. K. Pal and A. S. Achalkumar, *J. Mater. Chem. C*, 2018, **4**, 6117-6130.

7. Columnar self-assembly of luminescent bent-shaped hexacatenars with a central pyridine core connected with substituted 1,3,4-oxadiazole and thiadiazoles, B. Pradhan, **R. K. Gupta**, S. K. Pathak, J. De, S. K. Pal and A. S. Achalkumar, *New J. Chem.*, 2018, **42**, 3781-3798.

8. Tetrazole based supergelator as a sensitive and selective sensor for picric acid, with a fluorescence switching response, S. Nath, S. K. Pathak, B. Pradhan, **R. K. Gupta**, K. Anki Reddy, G. Krishnamoorthy, A. S. Achalkumar, *New J. Chem.*, 2018, **42**, 5382-5394.

9. Room temperature helical fluids in a single-component system, G. Shanker, A. Bindushree, K. Chaithra, P. Pratap, **R. K. Gupta**, A. S. Achalkumar and C. V. Yelamaggad (under revision)

Papers presented in National/International conferences: (Oral/Poster)

1. Discotic liquid crystals based on *N*-annulated perylene tetraesters
   R. K. Gupta, and A. S. Achalkumar.
   Poster presented at Symposium in Advances in Sustainable Polymers (ASP-15) held at IIT Guwahati 2015.

2. Annulated perylenetetraesters: a new class of luminescent discotic liquid crystals
   R. K. Gupta, and A. S. Achalkumar.
   Poster presented at Chemconvene 2015, IIT Guwahati (Awarded with Best Poster prize).

3. Host-guest OLEDs based on perylene based room temperature columnar liquid crystals
   R. K. Gupta, D. Das, P. K. Iyer, A. S. Achalkumar.
   Poster presented at Chemical Research Society of India National Symposium in Chemistry (CRSI-NSC-21) held at Gauhati University, Guwahati 2017.

4. *Bay*-annulated perylene tetraesters-structure property correlation
   R. K. Gupta, and A. S. Achalkumar.
   Oral presentation at National conferences on Liquid Crystals (NCLC-22) held at DIT University, Dehradun 2015.

5. Electroluminescent room temperature columnar liquid crystals based on *bay*-annulated perylene tetraesters
   R. K. Gupta, D. Das, P. K. Iyer, A. S. Achalkumar.
   Poster presented at Frontiers in Chemical Sciences (FICS-2016), IIT Guwahati (8-10 Dec.)

6. Perylene based room temperature columnar liquid crystals for host-guest OLEDs application
   R. K. Gupta, and A. S. Achalkumar.
   Oral presentation at 14th European conference on Liquid Crystal (ECLC-2017) held at Lomonosov Moscow State University, Moscow, Russia. (June 25 - 30, 2017)

7. Luminescent stilbene based star-shaped molecules stabilizing wide range columnar phase
   R. K. Gupta, S. K. Pathak and A. S. Achalkumar.
   Poster presented at National conferences on Liquid Crystals (NCLC-24) held at IISER Mohali, Punjab. (11-13 October, 2017) (Awarded with Best Poster prize)

8. Room temperature columnar liquid crystalline self-assembly of acidochromic, luminescent, star-shaped molecules with cyanovinylene chromophores
   R. K. Gupta, S. K. Pathak and A. S. Achalkumar.
   Poster presented at Fourth International Symposium on Advances in Sustainable Polymers (ASP-17) held at IIT Guwahati. (08-11 January, 2018)

9. Columnar self-assembly of electron deficient dendronized *bay*-annulated perylene bisimides
   R. K. Gupta, and A. S. Achalkumar.
   Poster presented at Research Conclave (RC-18) held at IIT Guwahati. (08-11 March, 2018) (Awarded with 3rd prize in Poster session)

CONTENTS

Chapter 1 **Introduction to perylene based discotic liquid crystals and their applications**

Chapter 2 ***Bay*-annulated perylene tetraesters stabilizing columnar mesophase**

Chapter 3a Electroluminescent room temperature columnar LCs based on *bay*-annulated perylene tetraesters

Chapter 3b Perylene-triazine based star-shaped green light emitter for OLEDs

Chapter 4 Columnar self-assembly of electron deficient dendronized *bay*-annulated perylene bisimides

Chapter 5a Microwave-assisted method for the synthesis of PEIs as a gateway toward unsymmetrical perylene bisimides

Chapter 5b **First example of white organic electroluminescence utilizing perylene ester imides**

List of abbreviations used in the text

anhyd	anhydrous
bs	broad singlet
BPhen	bathophenanthroline
Cr	crystal
Col	columnar
d	doublet
DCM	dichloro methane
dd	doublet of a doublet
DSC	differential scanning calorimetry
equiv	equivalents
Et	ethyl
Et_3N	triethyl amine
EtOAc	ethyl acetate
FRET	förster resonance energy transfer
g	gram
h	hour
Hz	hertz
HRMS	high resolution mass spectrometry
HOMO	highest occupied molecular orbital
I	isotropic
ITO	indium tin oxide
IR	infrared
J	joules
J	coupling constant
K	kelvin
LC	liquid crystal
LiF	lithium fluoride
LUMO	lowest unoccupied molecular orbital
m	multiplet
m	meta

MALDI-TOF-MS	matrix assisted laser desorption/ionisation - time of flight mass spectrometry
MHz	megahertz
min	minutes
mmol	milli mole(s)
n	normal
N	nematic
NMR	nuclear magnetic resonance
NTO	natural transition orbital
OFET	organic field-effect transistor
OLED	organic light emitting device
p	para
PEDOT:PSS	poly(3,4-ethylenedioxythiophene)-poly(styrenesulfonate)
POM	polarising optical microscopy
PVK	poly(9-vinylcarbazole)
q	quartet
R_f	retention factor
RISC	reverse intersystem crossing
rt	room temperature
s	singlet
t	triplet
TGA	thermogravimetric Analysis
TPBi	2,2′,2"-(1,3,5-benzinetriyl)-tris(1-phenyl-1-H-benzimidazole)
THF	tetrahydrofuran
TMS	tetramethyl silane
TLC	thin layer chromatography
UV/vis	ultraviolet-visible
XRD	x-ray diffraction

GENERAL REMARKS

All commercially obtained chemicals were used as received. As required the solvents were dried as per the standard protocols. Silica gel (60-120 mesh) or neutral alumina used as stationary phase for column chromatography. Aluminum sheets coated with silica gel were used for thin layer chromatography (TLC) to monitor the reactions and column purifications. Infrared spectra were measured on a Perkin Elmer IR spectrometer at room temperature by preparing the KBr pellet. ^{1}H and ^{13}C NMR spectra were recorded using Varian Mercury 400 MHz (at 298K) or Bruker 600 MHz NMR spectrometer. Mass spectrometry was carried out using MALDI-TOF mass spectrometer (Bruker Autoflex Speed MALDI TOF/TOF Mass Spectrometer) or High Resolution Mass Spectrometer. Polarizing optical microscope (POM) (Nikon Eclipse LV100POL) in conjunction with a controllable hot stage (Mettler Toledo FP90) was used for the characterization of mesogens. The phase transitions, associated enthalpy changes were obtained by differential scanning calorimeter (DSC) (Mettler Toledo DSC1). X-ray diffraction (XRD) studies were carried out using image plate and a detector. This setup had Cu Kα ($\lambda = 0.15418$ nm) radiation from a source (GeniX3D, Xenocs) operating at 50 kV and 0.6 mA in conjunction with a multilayer mirror was used to irradiate the sample. Glass capillaries containing the sample were used for the measurements. Thermogravimetric analysis (TGA) was accomplished with a thermogravimetric analyzer (Mettler Toledo, model TG/SDTA 851 e). Perkin-Elmer Lambda 750, UV/VIS/NIR spectrometer was used to obtain UV-Vis spectra, while Fluoromax-4 fluorescence spectrophotometer and Perkin Elmer LS 50B spectrometer were used to obtain emission spectra in solution state and solid thin film state respectively. Steady State anisotropy experiment was performed on Horiba Scientific Fluoromax spectrofluorometer 4. Time resolved lifetime measurements were done on time correlated single photon counter from Horiba Jobin Yvon. Cyclic Voltammetry (CV) studies were carried out using a Versa Stat 3 (Princeton Applied Research) instrument. Millimolar solution of all the compounds were spin coated on glass substrate at 2500 rpm for one minutes for thin film photophysical studies. Atomic Force microscopy (AFM) images were obtained for the spin-coated films using Agilent 5500-STM instrument in tapping mode. TD-DFT / DFT calculations were performed by employing the combination of Becke3-Lee-Yang-Parr (B3LYP) hybrid functional and 6-31G(d,p) basis set using the Gaussian 09 package, to obtain the information related to molecular conformation and frontier molecular orbitals (HOMO-LUMO) of compounds.

General OLED device configuration is composed of a pre-cleaned and pre-patterned indium tin oxide (ITO) as the transparent anode. The ITO surface was ultrasonically agitated and cleaned in 2% soap solution, Millipore water, acetone and isopropanol, each for five minutes at room temperature. The ITO substrates were then treated with UV-Ozone for 30 min. PEDOT: PSS film was spin-coated onto the ITO substrates from aqueous dispersion and dried at 120 °C for 30 min. After that, separate solutions of PVK and organic materials were made in chlorobenzene solution and were mixed in 90:10 ratio and the mixture was then stirred for 30 minutes to ensure efficient doping. The solution was then spin-coated at 3000 rpm for 60 seconds and thermally treated to 120 ^{o}C for one hour in inert argon gas environment. BPhen / TPBi / BCP / Alq3, LiF and aluminium was thermally evaporated in base pressure of ~10^{-6} mbar. The active area of the devices was 16 mm^2. The current density-voltage (J/V) spectra were measured using a Keithley 2400 source meter and the brightness of the OLEDs was measured using Konica Minolta CS2000 spectroradiometer. All OLEDs were fabricated and tested under inert atmosphere in a glove box.

PREFACE

Liquid crystals (LCs) are unique functional soft materials combining both order and mobility on molecular, supramolecular and macroscopic levels. The shape anisotropic molecules which exhibit this unique behavior are also known as mesogens. They can be organic (forming thermotropic and lyotropic phases), inorganic (metal oxides forming lyotropic phases) or organometallic (metallomesogens) in nature. Conventionally, the anisometric molecules employed to stabilize thermotropic LC phases are either rod-like (calamitic) or disc-like (discotic). Calamitics form the backbone of the well-established flat panel display industry. Discotic LCs also have made notable progress in recent years, both from scientific and application viewpoints and slowly they are finding a foothold in the main stream of organic electronics. The discotic LCs mainly exhibit either N phase or columnar (Col) phase. The arrangement of disc-like molecules with a long-range orientational order stabilizes the N phase, while the stacking of these disc-like molecules one above the other leads to the stabilization of Col phase.

This thesis entitled *"Perylene based liquid crystals as materials for organic electronics"* has been divided into five chapters. Contents included in this thesis are based on the research output gained from my research programme. Chapter 1 is an introductory chapter to liquid crystals including perylene based discotic liquid crystals and their applications in photovoltaic devices, OLEDs and OFETs. Chapter 2 deals with the synthesis and mesomorphic behavior of *bay*-annulated perylene tetraesters. Chapter 3 is divided into two parts, 3a gives an account of the stabilization of room temperature columnar liquid crystals based on *bay*-annulated perylene tetraesters and their application in organic light emitting diodes. 3b contains the synthesis and electroluminescence studies of the star-shaped perylene-triazine donor-acceptor molecule. Chapter 4 describes the microwave assisted synthesis and columnar self-assembly of electron-deficient dendronized *bay*-annulated perylene bisimides. Chapter 5 is sub-divided into two sections. 5a includes the microwave-assisted synthesis of unsymmetrical perylene ester monoimides and 5b comprises the fabrication of the technologically important white organic light emitting diodes utilising *bay*-annulated perylene ester imides.

Chapter 1 deals with introduction to LC and perylene based LCs. Columnar phases formed by the stacking of disc-like molecules with an intimate π-π overlap forms a one-dimensional (1D) pathway for the anisotropic charge migration along the columns. Columnar (Col) phase have a great potential in organic electronic devices to be utilized as an active semiconducting layer in comparison to the organic single crystals or amorphous polymers. They have advantages in terms of processability, ease of handling and high charge carrier mobility. Intelligent molecular engineering of the perylene and its derivatives provided an access to tune the physical properties and self-assembly behavior. Col liquid crystal (LC) phases formed by perylene derivatives have great potential for the fabrication of organic electronic devices. This chapter attempts to provide an overview of the molecular design developed to tune the applicable properties and self-assembly of perylene derivatives, as well as the recent developments on their utilization in the fabrication of organic solar cells, organic light emitting diodes and organic field effect transistors.

Chapter 2 deals with the synthesis and characterization of several heteroatoms (nitrogen, sulphur and selenium) *bay*-annulated PTEs which exhibited interesting thermal and photophysical behaviors. *Bay*-annulated PTEs stabilized ordered Col$_h$ phases over a wide temperature range. Increase in the length of the flexible chain, reduced the mesophase thermal range owing to a lowering of the clearing point, however this did not influence the photophysical behavior. Notably, the thermal range of the mesophase was enhanced and good hemoetropical alignment of the Col$_h$ phase was observed in comparison to PTEs due to the attractive and favourable –NH-, S···S and Se···Se interaction. We have prepared *N*-, *S*- and *Se*-annulated PTEs. They exhibited a visually perceivable green, sky blue, weakly bluish emission in solution respectively. The hetero atom *bay*-annulation of PTEs thus provides an access to tailor the thermal and optoelectronic properties of perylene derivatives and to the synthesis of several technologically important Col LCs based on perylene.

Chapter 3a deals with the synthesis of room temperature Col LCs with a wide thermal range, based on *bay*-annulated PTEs. Through the incorporation of heteroatoms like N, S and Se in the *bay* position of the PTE the emission behavior in the solution state has been effectively tuned, where the *N*, *S* and *Se*-annulated derivatives showed bright green, blue and weak yellowish green fluorescence respectively. The electroluminescence behavior of these compounds has been explored as emissive layers in organic light emitting diodes. Further, a remarkable improvement in the emission was achieved, when these molecules were doped in a matrix of polyvinyl carbazole (PVK), which is due to a combination of

Förster resonance energy transfer (FRET) from the host to the guest and charge carrier trapping in the emissive layer.

Chapter 3b deals with a star-shaped triazine-perylene (PT-T) conjugate that can be utilized as an emissive layer in OLEDs. This star shaped donor-acceptor (D-A) structure was a low melting solid with a good solubility and film forming nature due to its propeller shape. From the time-dependent density functional theory (TDDFT) calculations, we have visualized the changes in the energy levels of HOMO, LUMO levels and energy separation with respect to the molecular structure. Similarly, the changes in the singlet, triplet energies and the value of ΔE_{ST} with respect to the molecular structure was calculated. Further studies to enhance the steric hindrance between the donor groups and the central acceptor to achieve a large dihedral angle is required to get a lower ΔE_{ST} value. This may lead to the spatial separation of highest occupied and lowest unoccupied natural transition orbitals (NTOs), which in turn lead to a small ΔE_{ST} and improved reverse intersystem crossing (RISC). Additionally, this star-shaped molecule exhibited bright green fluorescence with a high quantum yield. When used as a sole emissive layer in OLEDs, this material exhibited a good performance, while as a guest material in a PVK matrix led to a much improved performance. Thus, the introduction of star-shaped architecture with a push-pull design promotes an improved charge migration along with a better charge recombination, to enhance the device efficiency.

Chapter 4 deals with microwave-assisted synthesis of three new heteroatoms *bay*-annulated perylene bisimides (PBIs), in excellent yield. *N*-annulated and *S*-annulated perylene bisimides exhibited columnar hexagonal phase, while *Se*-annulated perylene bisimide exhibited low temperature columnar oblique phase in addition to the high temperature columnar hexagonal phase. The cup-shaped *bay*-annulated PBIs pack into columns with enhanced intermolecular interactions. In comparison to PBI, these molecules exhibited lower melting and clearing temperature, with good solubility. A small red shift in the absorption was seen in the case of *N*-annulated PBI, while *S*- and *Se*-annulated PBIs exhibited blue-shifted absorption spectra. The band gaps of PBI and PBI-N were almost same, while an increase in the band gaps were observed in the case of *S*- and *Se*-annulated PBIs. The tendency to freeze in the ordered glassy Col phase for PBI-N and PBI-S will help to overcome the charge traps due to crystallization, which are detrimental to 1D charge carrier mobility. These solution processable electron deficient columnar semiconductors with good thermal stability may form an easily accessible promising class of n-type materials.

Chapter 5a deals with a high yielding microwave-assisted synthetic method to obtain unsymmetrical perylene diester monoimide (PEI), by treating the perylene tetrester (PTE) with requisite amine. Perylene based molecules are widely used in the construction of self-assembled supramolecular structures because of their propensity to aggregate under various conditions. In comparison to PBIs, PEIs are less studied in organic electronics/self-assembly due to the synthetic difficulty and encountered low yields in preparation. In comparison to PBIs, PEIs stand as less electron deficient. Further, the PEIs got higher solubility than PBIs, but the synthesis and purification of PEIs, which are inherently unsymmetric is challenging. This method is applicable to aliphatic, aromatic, benzyl amines and *bay*-annulated PTEs. This provides a tuning handle for the optical/electronic properties of perylene derivatives and an easy access to unsymmetrical perylene bisimides (UPBI).

Chapter 5b deals with the fabrication of host-guest OLEDs utilizing a series of *bay*-annulated perylene ester imides (PEIs) doped in polyvinylcarbzole (PVK) as emissive layer, and studied the electroluminescence behaviors of these devices. The devices exhibited emission from both PVK as well as PEI mainly due to the partial Förster resonance energy transfer from PVK to the emissive dopant. In order to achieve better device performance, two different electron transport layers, Bathophenanthroline (Bphen) and 2,2′,2"-(1,3,5-Benzinetriyl)-tris(1-phenyl-1-H-benzimidazole) (TPBi) were used. A remarkable improvement in the emission brightness and lower turn on voltage was observed, when TPBi was used as an electron-transporting layer instead of BPhen. Incorporation of TPBi resulted in a lower electron injection barrier of TPBi-PVK interface, which facilitates more electron injection into the emissive layer thus resulting in an increased recombination at a comparatively lower voltage. Also, the intensity of blue emission from PVK was enhanced in the case of TPBi based devices, resulting in an overall white electroluminescence, which is of high technological importance.

Chapter 1

Introduction

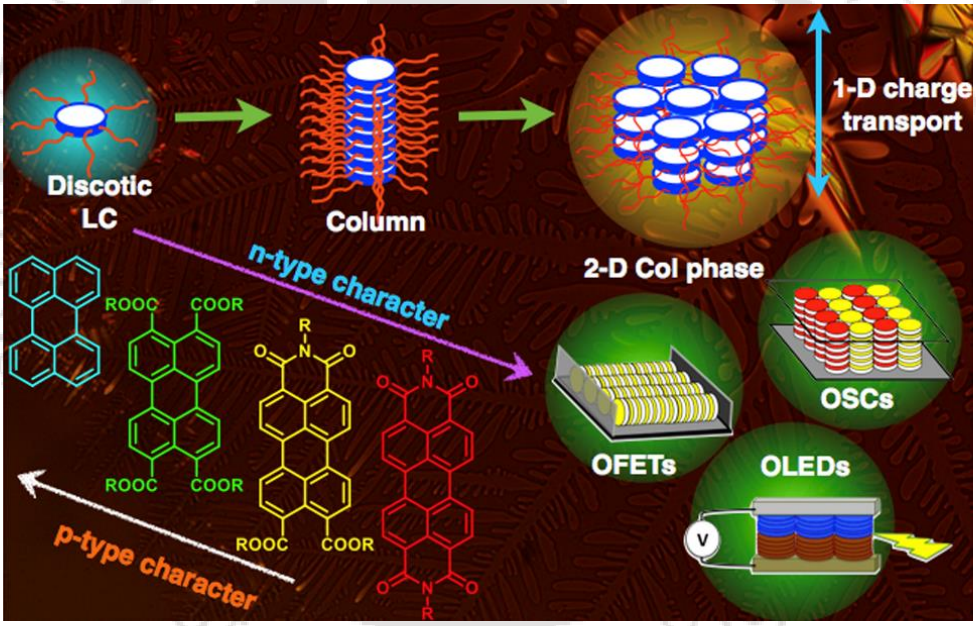

1.1. Introduction

Over the years, research on liquid crystals (LCs) has produced significant advancements in the understanding of supramolecular self-assembly and related technological applications. The discovery of liquid crystal displays and their commercialization made the field more vibrant and multiplied the efforts of the scientific community in quest of new materials with interesting properties.[1] Understanding the structure-property correlations in LCs is a very important area that enables us to translate scientific findings into applications, which require a truly interdisciplinary effort. The special state of matter, which is a unique blend of order and mobility intermediate to solids and liquids is extremely sensitive to external stimuli like temperature, pressure, light, electrical and magnetic origins. Chemically, the LCs can be of organic, organometallic or inorganic in nature. They are broadly classified as thermotropic and lyotropic based on the type of the external stimuli that bring about the phase transitions. Typically, a thermotropic LC is made up of two components, usually a rigid core and flexible chain/s connected to this core by different linking groups. However, the LC self-assembly is sensitive even to the type of linking group between these two units. Based on the shape of the rigid anisotropic shape of the core these LCs are classified into different classes namely, conventional LCs and non-conventional LCs. Conventional LCs mainly include calamitic (rod-like) and discotic (disc-like), LCs, while non-conventional LCs include a wide variety of mesogens like bananas (bent-cores) and phasmidic or polycatenars (dumbbell-shaped or a hybrid of a rod and disc-like structure), star-shaped molecules, dimeric, oligomeric LCs and polymeric LCs. Accordingly, these molecules will self-assemble into different mesophases either by arranging parallel to one another or by the nanoseggregation of their incompatible molecular subunits.[1] The LC self-assembly generally follows the association principle of the condensed soft matter by minimizing the excluded volume and by maximizing the interaction energy. Further secondary interactions like Van der Waals, dipolar, quadrupolar, charge transfer, π-π interactions, metal coordination, ionic interaction and hydrogen bonding also contribute to different extents in promoting the LC self-assembly. Calamitic LCs mainly stabilize nematic (N) phase by orienting parallel to each other; or smectic (Sm) phase by packing into layers with both positional and orientational order. Smectic phases are classified as SmA or SmC with respect to their tilt to the normal layer. Smectic LCs, specially SmA phase also has the potential to be utilized as a charge transport material due to the layered structure and strong aromatic overlap. The discotic LCs mainly exhibit either N phase or columnar (Col) phase.

The arrangement of disc-like molecules with a long-range orientational order stabilizes the N phase, while the stacking of these disc-like molecules one above the other leads to the stabilization of Col phase (Figure 1.1).

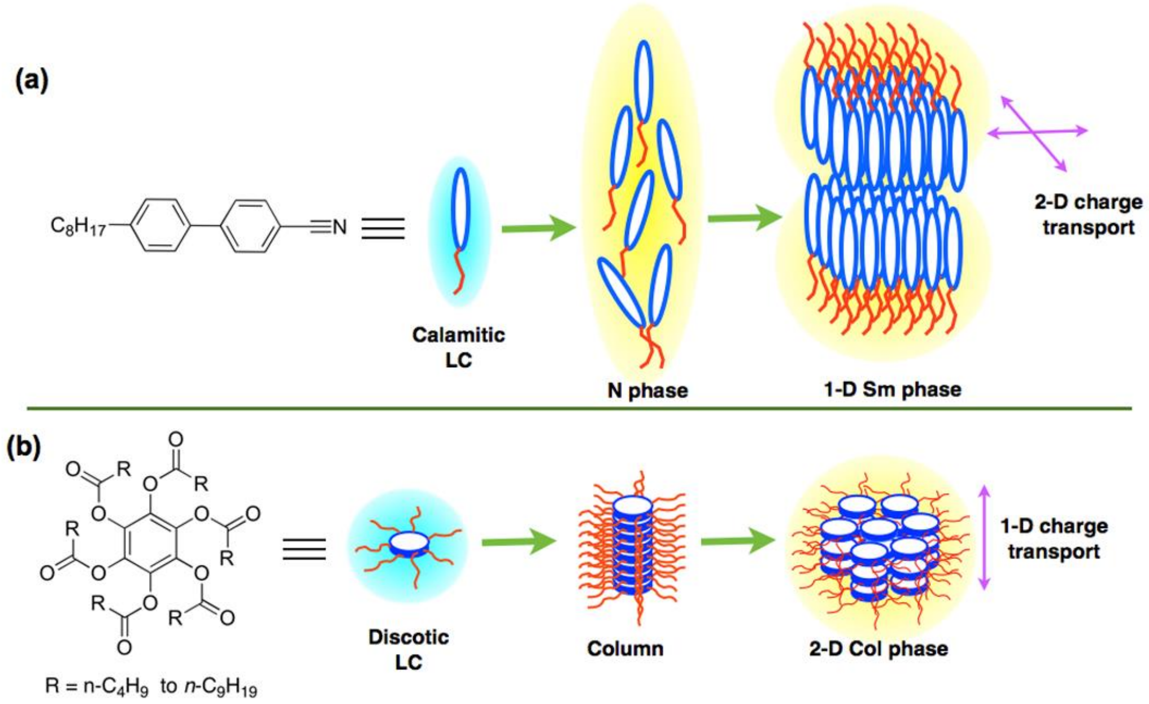

Figure 1.1. (a) Self-assembly of a typical rod-like molecule (8CB) to nematic (N) and smectic (Sm) phases; (b) a series of disc-like molecules (benzenehexa-*n*-alkanoates) to form Col phase.

There is columnar nematic (N_C) phase, where several short columns are arranged without organizing into a 2D lattice; or lateral nematic (N_L) phase, where several discotic aggregates are arranged only with an orientational order. Col phases are formed by the packing of disc-like molecules one above the other in one dimension (1D). These 1D-columns are further organized into different two dimensional (2D) lattices and based on their 2D symmetry, they are classified into different Col phases like hexagonal (Col_h), rectangular (Col_r), square or tetragonal (Col_{sq}) and oblique (Col_{ob}) columnar phases. In the case of columnar lamellar (Col_L) phase, the DLCs are organized in the form of layers. A highly ordered helical (H) columnar phase is reported in the case of hexakis(hexylthio)triphenylenes (HHTT), where the molecules are organized in a helical fashion within the columns, while these columns are further organized in a hexagonal lattice. Columnar plastic (Col_p) phase possess three-dimensional positional order as in a Col_h phase, while the discs within the columns possess rotational freedom about the column axis. Here, the molecules can rotate freely on their sites but lateral and longitudinal displacements are restricted.[2] Columnar, smectic and, more recently, nematic LCs have shown promise as charge-transporting organic semiconductors, due to their spontaneous self-assembling nature to form highly ordered domain free films over large areas.[3,4] Since the present introductory chapter revolves around the application of LC perylene derivatives in organic electronics, the discussion is elaborated on that topic. Several scholarly reviews are written on the self-assemblies of perylene derivatives and their applications.[5]

1.2. Application of Columnar Phases in Organic Electronics

Columnar phases are yet to make a major impact in organic electronics, although they are considered with the potential to behave as ‘molecular wires'. The intimate overlap of the disc-like cores due to the columnar stacking and the peripheral mantle of an insulating sheath of flexible tails help them to act as 1D-charge carriers. Organic electronic devices like organic solar cells (OSCs), organic light emitting diodes (OLEDs), and organic field effect transistors (OFETs) are presently tested with high purity organic single crystals or polymers as active layers (Figure 1.2).

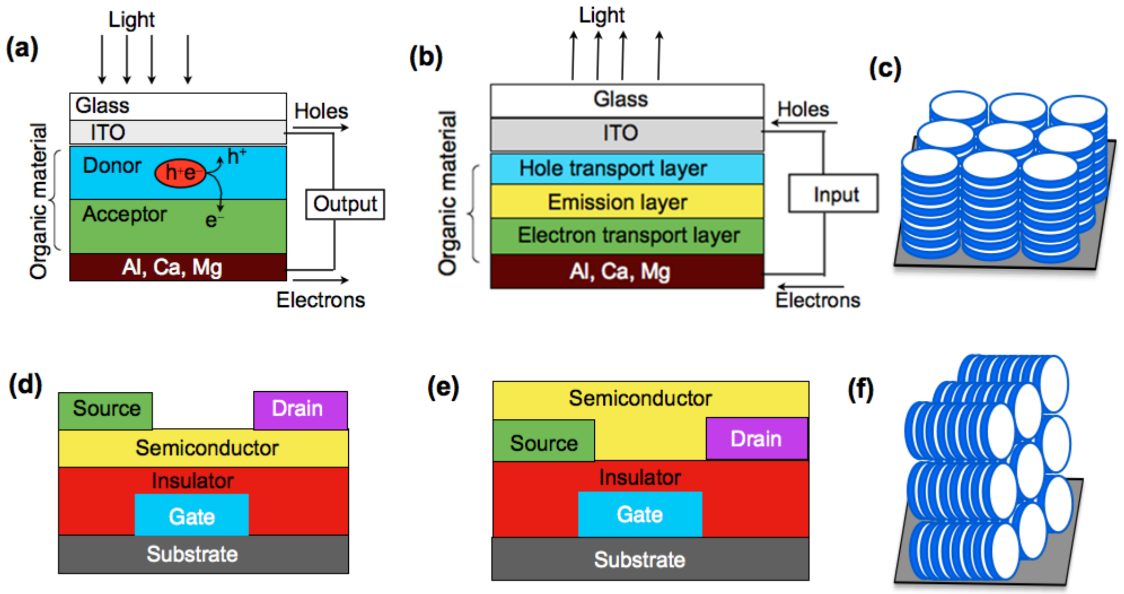

Figure 1.2. (a) Schematic showing the device structure of organic heterojunction solar cell; (b) organic light emitting diode; (c) homeotropic (face-on) alignment of columns; Schematic of the organic field effect transistor with (d) top-contact device, where the source and drain electrodes are deposited on an organic semiconducting layer; (e) bottom-contact device, where the organic semiconductor is deposited on to prefabricated source and drain electrodes; (f) homogeneous (edge-on) alignment of columns.

The difficulty and cost associated with growing high quality organic single crystals often forbid the scalability, processability and flexibility of their widespread use although they show good charge carrier mobility. Polymers can be scalable replacements, but they have a limitation of the batch-to-batch reproducibility and poor solubility. Because of their amorphous nature, they exhibit lower conductivity values than the organic single crystals. Interestingly, Col LCs are scalable, solution processable and reproducible but they suffer from the inferior conductivity in comparison to organic single crystals. This issue can be solved by obtaining a highly aligned Col phase, which then leads to an increased conductivity.[3] The device geometry of OSCs and OLEDs are almost similar, as in both cases the organic semiconductor layers are sandwiched between two electrodes (Figure 1.2a-b). In the case of OSCs, the excitons generated by the light absorption dissociate into electrons and holes and move towards corresponding electrodes under the built-in electric potential. In the case of OLEDs, the voltage applied across the electrodes leads to the movement of electrons and holes, which then recombine at the organic interface to emit light. Thus in the case of OSCs, the molecules should possess a wide absorption spectrum and high exciton diffusion length. Similarly, in the case of OLEDs, molecules should exhibit high charge carrier mobility along with a high luminescence quantum yield. Thus to improve the charge carrier mobility require a perfect 'homeotropic' or 'face on' alignment of the columns (Figure 1.2c). In comparison, the OFETs require the 'homogeneous' or 'planar' alignment of the columns across the source and drain electrodes (Figure 1.2d-f).[6] Thus, the efforts are on to synthesize Col LCs which stabilize either of these alignments. Further, most of the Col LCs are prepared from electron rich cores and they act as 'p-type' semiconductors (for example, triphenylene, pyrene, hexabenzocoronene *etc.*), while the Col LCs derived from electron-deficient cores, *i.e.* 'n-type' semiconductors are less in number (for example, hexaazatriphenylene, naphthalenebisimide, anthraquinone *etc.*). For all the above-said devices to perform better, tunable n-type Col LCs with optimal alignment features are very essential. Here, the Col LCs derived from perylene derivatives can serve as good n-type materials if they are suitably functionalized.

1.3. Perylene as a core for the liquid crystalline organic semiconductor

Highly conjugated organic materials usually exhibit a high degree of crystallinity. As a result, they exhibit a lower solubility in organic solvents. With such materials, it is very hard to obtain high-quality thin films by solution processing. Introduction of several alkyl chains at the periphery as per the general DLC design template promotes the solubility, processability, ease of purification either by recrystallization or by column chromatography.[7] This lowers their melting point and also assist in their columnar self-assembly. However, the introduction of excessive alkyl chains or bulky substituents may turn detrimental to self-assembly and 1D-charge carrier mobility. Over the last two decades, perylene derivatives have fascinated researchers due to their ease of functionalization and potential applications in organic electronics. These dyes combine strong absorption in the visible region with high fluorescence quantum yield and long fluorescence lifetime. Moreover, they exhibit excellent stability for thermal and photochemical degradation.[5] The perylene core has twelve positions that can be functionalized to provide a multitude of possibilities. The first set is the 3,4,9,10 positions which are known *peri*-; the second set is the 1,6,7,12 positions which are known as *bay*-; the third set is the 2,5,8,11 positions that are known as *ortho*-positions (Figure 1.3a). Thus this core has ample handles to tailor the chemical structure and self-assembly and thus to tune the resulting properties.[8]

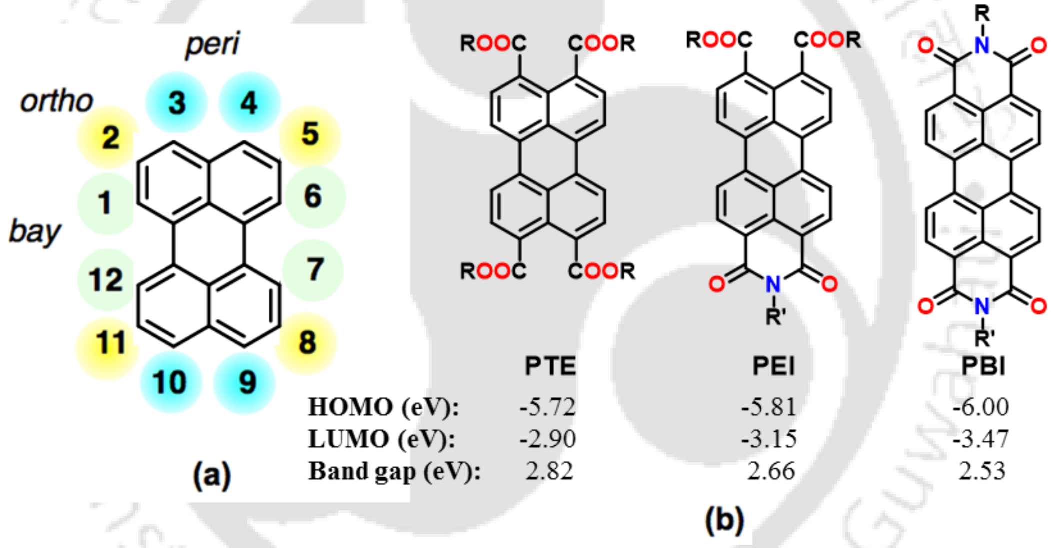

Figure 1.3. (a) Structure of perylene with possible options for substitution; (b) three classes of most commonly studied perylene derivatives for the application in liquid crystals and organic electronics (HOMO and LUMO frontier molecular orbitals and band gaps of **PTE**, **PEI** and **PBI** have been calculated from DFT method employing B3LYP/6-31G(d,p) functional for methyl derivatives).

Perylene based LC materials can be classified mainly into three classes based on the functional group that connects the central disc-like perylene core with the peripheral flexible chains (Figure 1.3b). First one is perylene tetraesters (PTEs); the second one is perylene ester-imides (PEIs) and the third one is perylene bisimides (PBIs). Further modifications in these classes were done, either by extending central core along the long axis or towards the *bay*-region. There are also reports on oligomeric and polymeric LCs based on perylene derivatives. Although huge efforts have been devoted towards the investigation of the charge transport properties,[9] a combined analysis involving the effect of molecular structure and self-assembly of perylene derivatives may shine a new light on their potential applications. Over the years more than 200 LC perylene derivatives were reported and investigations were carried out on their application in organic electronics. Following sections present a brief introduction on the liquid crystalline perylene derivatives and their application in the fabrication of organic electronic devices.

1.3.1. Liquid crystals based on perylene tetraesters and their extended derivatives

PBIs form the majority among the perylene derivatives utilized as organic semiconductors. Their structurally related PTEs are less electron deficient and possess higher LUMO levels than PBIs. However, they are still electron deficient because of the four carboxylate groups and when connected with a suitable donor molecule to form donor-acceptor (D-A) polymers, such solar cells exhibited higher open circuit voltage (V_{OC}) in comparison to the PDI analogue.[10] In addition, they exhibited good solution processability and a good thermal stability. Inspite of that, liquid crystals based PTEs are less in number. Kitzerow *et al.* reported a homologous series of LC 3,4,9,10-tetra-(*n*-alkoxycarbonyl)-perylenes, where the alkyl tails were varied from ethyl to *n*-decyl[11] (Compounds **T1-T10**, Figure 1.4). Except for the lowest and highest homologue, all of these compounds exhibited Col_h phase with a good homeotropic (face-on) alignment (Figure 1.2c). An increase in the chain length noticed the lowering of melting and clearing points, consequently the reduced mesophase width. They show intense green fluorescence in dilute solution, while a red-shifted orange to red emission in the solid state.[12] This red-shifted emission is accounted for the excimer emission.

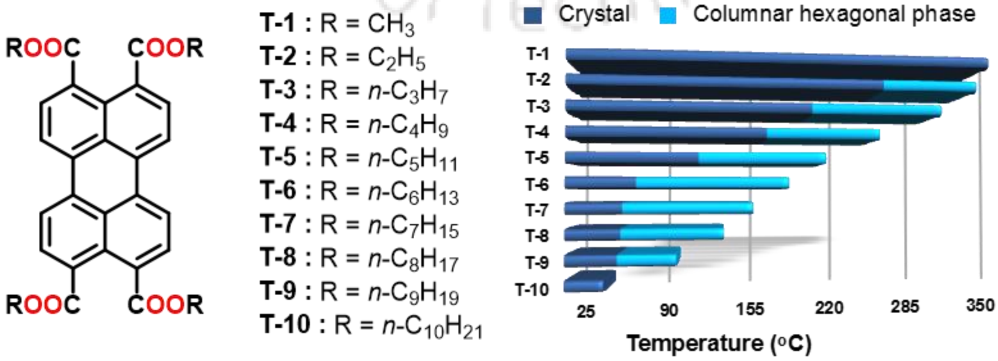

Figure 1.4. Bargraph showing the thermal behavior of PTEs with respect to the chain length.

The incorporation of *rac*-2-ethylhexyl chain lowered the melting point of the PTE, widened the range Col phase starting from the room temperature (RT).[13] Yang *et al.* investigated a series of perylene tetra methyl alkyl esters (*secondary* alkyl esters). They observed that the PTE with four *sec*-octyl (**Ts-8**) chains showed a decrease in the melting point, along with a fall in the clearing point.[14] Substitution with 2-ethylhexyl chains also had a similar effect with lowered clearing point. PTEs with *sec*-butyl (**Ts-4**) and *sec*-hexyl (**Ts-6**) chains also exhibited room temperature Col_h phase, but they decomposed before reaching the clearing point (Figure 1.5).[13] In comparison to **Ts-8,** the PTE with four 3,7-dimethyl octyl tails (**T-3,7**) showed a much-lowered clearing point along with an RT Col_h phase.[15]

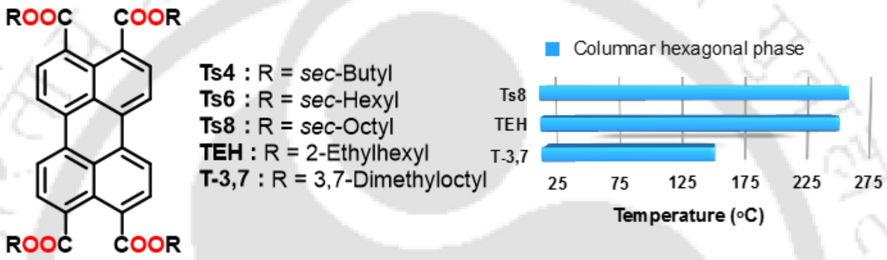

Figure 1.5. Bargraph showing the effect of branching on the thermal behavior of PTEs.

Further investigations on PTEs with expanding the core in the *bay*-region was carried out to alter the thermal and electronic properties. Bock *et al.* reported benzoperylene-hexa- and tetracarboxylic esters, by expanding the PTE core in the *bay* region (Figure 1.6).[16] The hexa and tetraesters showed strikingly different behavior in the mesophase formation. Surprisingly, the compound with four alkyl tails was far more mesogenic than the hexaester. However, the electronic properties have been found to change as expected, with the hexaester being more electron-accepting in nature than the tetraester. For example, compounds **EE-2** to **EE-4** (hexaesters with ethyl to *n*-butyl chains) exhibited monotropic Col_h phase. Substitution with 2-ethylhexyl chains **(EE-EH)** turned the compound to be liquid. However, the tetraester with ethyl chains (**EE-TE**) exhibited a Col_h phase of around 100 °C, while the corresponding ethyl hexyl derivative (**EE-TEH**) exhibited RT Col_h phase over a broad thermal range. Tetraesters bearing slightly lengthier *n*-alkyl chains like propyl and butyl chains too exhibited monotropic Col_h phase with a reduced mesophase range (Figure 1.6). On comparison of the thermal behavior of *bay*-extended hexaesters with *bay*-extended tetraesters Bock *et al.* derived some conclusions.[16] For example, the tetraethyl ester **EE-TE** in comparison with the hexaethylester **EE-2** exhibited a greatly enhanced mesomorphism. Although both show nearly the same melting points the mesophase of **EE-TE** was enantiotropic and with wider thermal range. The effect was even more pronounced on comparing the 2-ethylhexyl derivatives **EE-EH** and **EE-TEH**. Although none of them are crystalline at room temperature (RT), compound **EE-TEH** assumes a Col_h phase over a wide thermal range, which is a clear contrast to the room temperature liquid **EE-EH**. Further, the Col_h phase of **EE-TEH** exhibits highly ordered homeotropic non-birefringent domains on annealing the isotropic melt. The dramatic enhancement in the mesomorphic behavior on going from *bay*-extended hexaesters to corresponding tetraesters specifies that at least with medium sized aromatic cores, it is extremely difficult to accommodate sterically demanding six alkoxycarbonyl side chains without any out-of-plane orientation. This steric bulk is detrimental in achieving the overall disc-like shape that promotes the columnar packing. This is completely contrasting to alkoxy- or alkanoyloxy-substituted mesogens, especially hexaalkoxy- and hexaalkanoyloxy-triphenylenes, for which six is the usual number of flexible chains that are used to imbue mesomorphism.

Bock *et al.* further extended the *bay* region of the tetraethyl PTE with a dimethyl ester of naphthalene dicarboxylic acid to obtain a hexaester (**EE-N2**), which showed an exceptional mesomorphic behavior.[17] From literature it is learnt that, in the case of alkyl-, alkoxy-, alkylthio-, and alkanoyloxy-substituted DLCs, alkyl chains containing a minimum of five carbon atoms connected linear fashion is essential to stabilizing columnar mesomorphism.[2] However in the case of **EE-N2** and in many alkoxycarbonyl-substituted PTEs, the ethyl derivatives also stabilize Col phase, although at higher temperatures. The dimethyltetraethyl derivative **EE-N2** also exhibited a high-temperature mesophase on heating. But in complete contrast to all other known short-chain columnar PTEs, here the Col_h phase was maintained at RT, which was stable even after 2 months as evidenced from XRD. Notably, this molecule showed a good homeotropic alignment. Here, the influence of the distortions in the arene core, which are mainly caused by the three pairs of ester groups that are in close proximity to each other and the axially chiral overcrowded helicene structure formed by the naphthalene extension at bay region stabilizes the mesophase. However, dinaphtho[1,2-*a*:1′,2′-*j*] coronene-8,9,18,19-tetracarboxylic tetraesters (with straight and branched chains), which are bilaterally extended PTEs with naphthalene moieties turned to be crystalline with high melting temperature (**EE-DN1** to **EEDNBO**, Figure 1.6).[18]

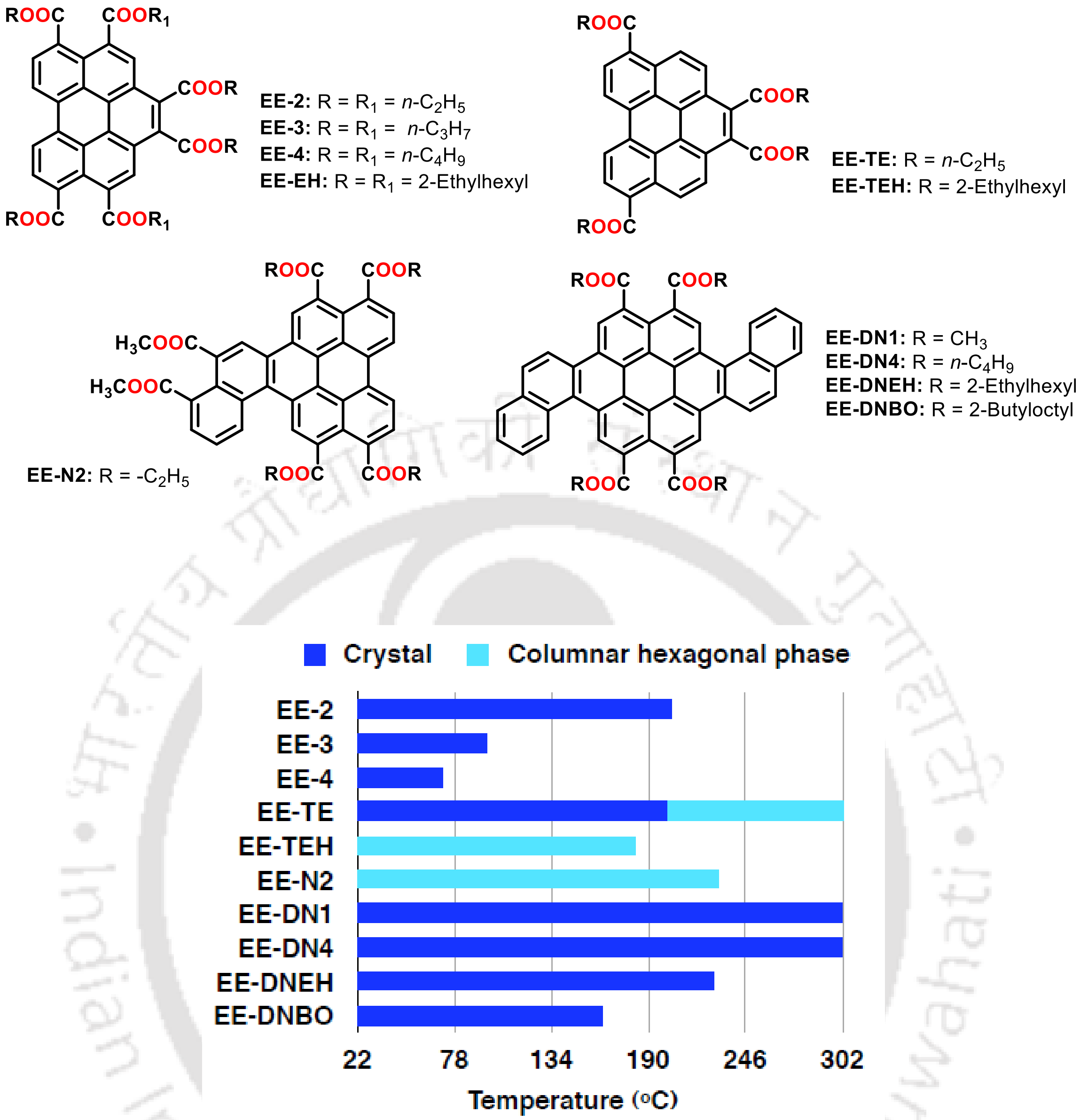

Figure 1.6. Structures and bar graph of other *bay*-extended perylene esters.

In general, Col PTEs exhibit homeotropic alignment on slow cooling from isotropic liquid state.[11] However, Wolarz *et al.* reported planar alignment of **T-6**, on depositing its THF solution on a hydrophilic glass substrate using the zone-casting technique.[19] They observed dendritic or flower-like structures at RT. It was established that such exclusive structures were not formed by the recrystallization of **T-6** from a Col phase. The molecular aggregation in the dendritic structures was confirmed by the absorption and fluorescence studies. WAXS study proved the crystallization of **T-6** in the monoclinic arrangement. The dendritic branches were birefringent and with a characteristic angle of 60° between them. These observations led to an explanation that the dendrites were built with the molecules packed in a columnar fashion. Further, these columns were aligned along the dendrite branches. The perylene units inside the columns were aligned with an edge-on or homogeneous orientation with respect to the substrate and with an inclination angle of about 30° with respect to the column axis. These dendritic structures vanished on annealing at the thermal range of the Col phase and were not rebuilt even after an extended annealing at RT. The homogeneous alignment of these molecules in the dendrites, growing at a temperature below the crystallization point is in contrast to the usual homeotropic alignment of the dendritic structures obtained in the Col_h phase on annealing from the isotropic liquid.

1.3.2. Liquid crystals based on perylene diesters

PTEs usually show a wide range Col_h mesophase, and further lowering of melting point to obtain the RT mesophase can be achieved by the integration of racemically branched alkyl chains. LC PTEs usually exhibit good homeotropic alignment. They contain a reasonable electron density in the aromatic core as evidenced by their E_{LUMO} and E_{HOMO} values of –3.5 and –5.8 eV, *vs* vacuum correspondingly. This feature makes them potential electron-acceptor or electron-donor layer materials depending on the nature of the material they are coupled with at a donor-acceptor interface. Dialkyl diimide analogues (PBIs) of PTEs exhibit a more prominent acceptor-type behavior with an E_{LUMO} value of about –4.2 eV. In contrast to PTEs, PBIs do not possess an adequate number of alkyl chains to support a stable Col_h phase at RT. This also renders them less soluble. However, imido-diesters[20] have an enhanced acceptor-type behavior in comparison to PTEs. They also possess a sufficient number of alkyl chains to obtain a stable RT mesophase, along with accessible clearing points, that allow the controlled growth and alignment of Col LC phases. However, compared to the LCs based on PTEs and PBIs, the LCs based on PEIs are less in number, which is partially due to the synthetic difficulty in obtaining these unsymmetrical structures. Most of the reported PEIs are limited to the aliphatic derivatives.[20-21]

Bock *et al.* reported unsymmetrical PEIs which stabilized wide range Col_h mesophase (Figure 1.7a).[20] Though 2-ethylhexyl derivative (**PEI-EH)** (like the propyl analogue **PEI-3**), was crystalline at RT with a single mesophase at higher temperature, the higher homologues (with 2-butyloctyl and 2-hexyldecyl chains) were found to be LC at RT (Figure 1.7a). The textures of all four PEIs showed homeotropically aligned Col_h phase. Powder XRD studies of **PEI-HD** at RT confirmed the Col_h phase. This property along with their known acceptor-type character and good absorption makes them promising materials for organic electronic devices that are based on the unidirectional charge carrier mobility. These PEIs exhibit high fluorescence quantum yield in a dilute solution that is close to unity.

As mentioned earlier the PBIs are having a problem of solubility and highly soluble PBIs are often obtained by the *bay*-substitution, but often the *bay*-substitution leads to the loss of planarity and loss of strong interactions because this modification often leads to the twisting of the perylene core. This is contradictory to the strong π-π interactions that are required for the intermolecular order and efficient charge carrier mobility. PTEs exhibit good solubility in organic solvents,[18] but they absorb mostly in the blue region. They are comparatively less electron deficient with respect to PBIs.[10a] Materials with strong π-π overlap, absorption over the entire visible-NIR region and electron deficient nature are of fundamental interest in the development of OSCs. Thelakkat *et al.* approached this problem, by introducing a benzimidazole unit fused to the perylene core (Figure 1.7b).[22] All these molecules exhibited an extended absorption up to 680 nm, *i.e.* in the red region. In comparison to PBIs, these materials absorb at a longer wavelength with a 130 nm red-shift, due to the extended π-conjugation through the benzimidazole group. This resulted in lowered optical bandgap energy due to a shift of the HOMO value. All the perylene diester benzimidazoles (PEBIs) self-organize into $\mathrm{Col_h}$ phases at higher temperatures below 250 °C; **PEBI 2** and **3** even stabilized RT $\mathrm{Col_h}$ phases. A lamellar ordering for **PEBI-1** and a columnar hexagonal plastic phase ($\mathrm{Col_{hp}}$) was observed for **PEBI-2** at RT (Figure 1.7b). All these properties make PEBIs a very promising class of *n*-type materials for applications in organic electronics.

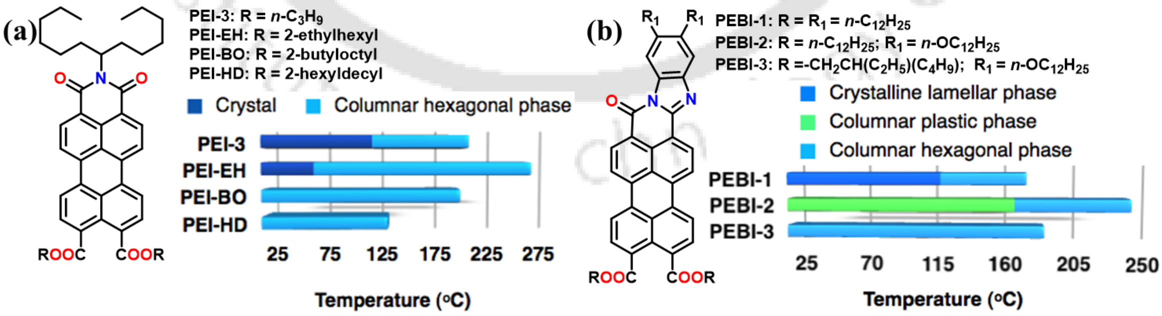

Figure 1.7. Bargraph showing the thermal behavior of **PEIs** and **PEBIs.**

1.3.3. Liquid crystals based on perylene bisimides

1.3.3.1. Symmetrical perylene bisimides with oligoethoxy chains

PBIs form a class of the most studied organic semiconductors. Cormier *et al.* reported the first LC PBIs in 1997.[23] PBIs **1b**-**1c** are based on the well-known perylenebis(phenethylimide) structure (**1a**, where R = H), while PBIs **2a-2h** have purely linear aliphatic side chains (**2a-2c**, **2h**) or branched aliphatic side chains (**2d**, **2e**, **2f-g**). All these compounds exhibited thermotropic LC phases as evidenced from DSC and POM. Compound **1b** and **1c** showed a solid phase (crystalline or highly viscous LC) before transforming to a LC phase. PBI **2d** is a RT LC with a clearing point of ~55 ^{o}C. The spin-coated thin film undergoes a slow (~24 h) crystallization on standing. On rapid cooling, it freezes to form an isotropic glassy state, which undergoes slow crystallization. When it is spin-coated on untreated glass slides, the thin films of **2d** spontaneously organize to form long, ribbon-like crystals. Both absorption and emission studies suggested that this spontaneous transformation is complemented by a reduced energetic disorder in the film, which in turn resulted in a decreased density of the exciton quenching sites. The propensity of self-healing of defects and glass formation is promising from the viewpoint of organic semiconductors. Similarly, several polyoxyethylene derivatives of PBIs have been investigated for their thermal behavior with the help of DSC and POM.[24] Most of these PBIs exhibited a LC phase over a wide thermal range. The thin films of **2e**, a RT LC, self-organizes into a well ordered crystalline phase that possesses superior photophysical properties in comparison to thermally evaporated, solvent vapor annealed films of the prototype PBI, **1a**. Compounds **2f** and **2g** were crystalline in nature (Figure 1.8 and 1.9).

Cyclic voltammograms of thin polycrystalline films of LC PBI, **2b** showed the evidence for strong attractive interactions between the PBI molecules and implied that the film undergoes two structural rearrangements to accommodate reduction to the anionic and dianionic states, which is also supported by spectroelectrochemical measurements. The redox conductivity of the film with respect to electrochemical potential was measured with the use of interdigitated array electrodes. The conductivity reaches the semiconducting level before the appearance of the first noticeable reduction wave. The maximum conductivity of 4.4×10^{-2} S/cm was observed when the film was reduced by 1 equivalent of electrons, in contrast to the anticipation that this state should be a Mott insulator.[25]

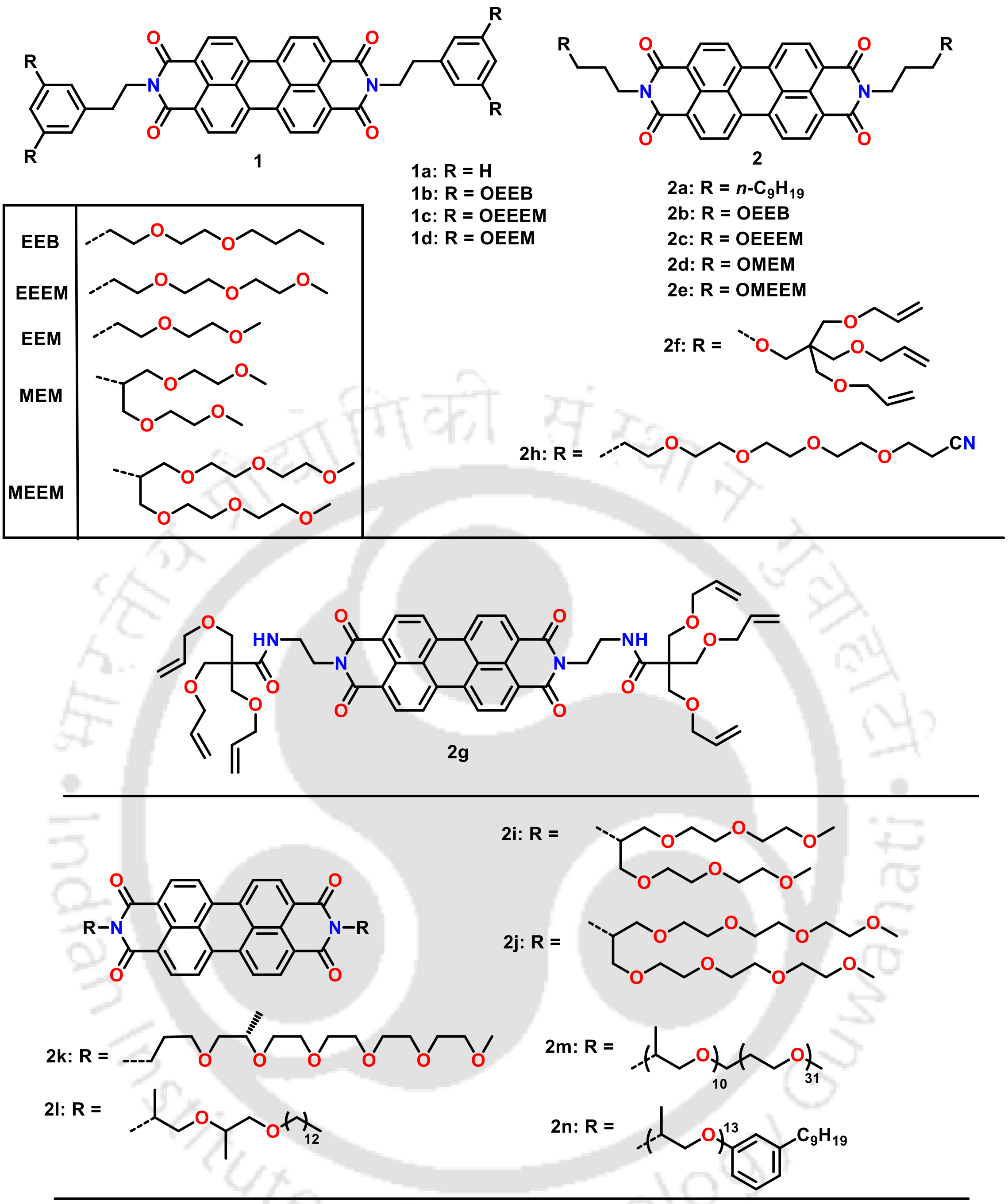

Figure 1.8. Structures of symmetrical PBIs with oligoethoxy chains.

Three different LC PBIs (**2b**,[24] **2e**[23-24] and **2h**) were studied with respect to the optical and physical characteristics in their thin film state.[26] These films were prepared by different techniques like spin-coating, thermal evaporation under vacuum and Langmuir-Blodgett (LB) techniques on wide variety of substrates like glass slides, indium tin oxide (ITO) coated glass slides and highly oriented pyrolytic graphite (HOPG). All the films were characterized by POM, UV-Vis and fluorescence spectroscopy as well as XRD studies. It was noted that the changing of the preparation procedures/conditions, or using different substrates did not significantly alter the properties of the resultant thin films (Figure 1.8 and 1.9). The self-organizing ability of these LC PBIs permits them to quickly reach a stable, low-energy configuration, unlike many other thin film forming materials and discloses that they are compelled to self-assemble and orient in a highly specific fashion. Notably, such ordering is independent of the substrate or deposition method. The molecules incline to form a J-type organization that takes advantage of attractive π-π interactions, where the π-π stacking axis is in parallel orientation to the substrate. The LC PBI **(2b)** perylene cores are oriented to the substrate with a tilt angle of ~47 °C along the stacking axis and ~58 °C perpendicular to this direction. The two other LC PBIs (**2e** and **2h**) also exhibited comparable structures. An investigation of the intermolecular electronic and steric interactions and the interactions between the molecules and the substrates were proposed to explain this strongly preferred orientation. For comparison, thin films of compounds **2b** and **1a** were also prepared by vacuum deposition with similar thickness, and LC PBI **2b** was shown to exhibit highly ordered films due to its liquid crystalline nature.[25]

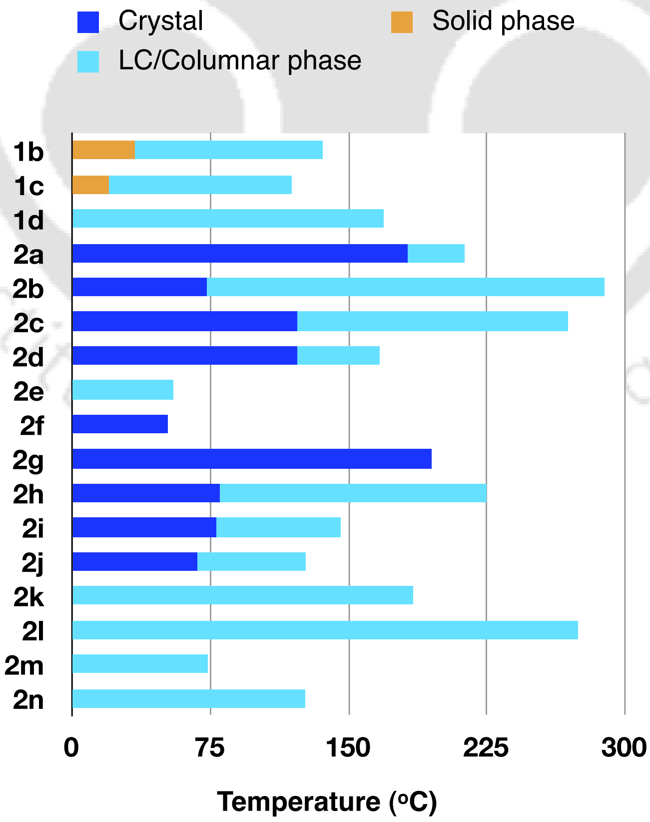

Figure 1.9. Bargraph showing the thermal behavior of symmetrical **PBIs**.

Thelakkat *et al.* reported swallowtail substituted symmetrical PBIs (**2i** and **2j**) based on oligoethoxy chains (with two and three elthyleneoxy units), which stabilized $\mathrm{Col_h}$ phase. In contrast to symmetrical dialkyl swallowtail PBIs (**3g** [27] and **3h**, Figure 1.10), the compounds **2i** and **2j** exhibited a much broader enantiotropic thermal behavior. Moreover, the length of the oligoethyleneglycol swallowtail substituent affects the clearing temperature of PBIs. As expected PBI **2j** with longer oligoethoxy chains (three elthyleneoxy units in each branch) exhibited a lower clearing point, whereas the enthalpy change associated with $\mathrm{Col_h}$-I transition remains nearly the same (Figure 1.8 and 1.9).[28]

Bijak *et al.* reported RT thermotropic PBIs (**2l**, **2m** and **2n**) with wide mesophase range.[29] PBIs **2m** and **2n** had a number of ethyleneoxy repeating units. They exhibited high relative photoluminescence quantum yield. The cyclic voltammogram of these PBIs showed two reversible reductions and one irreversible (except for PBI-**2l**) oxidation signals. These compounds also showed a low electrochemical band gap (1.46–2.11 eV). The combination of the high fluorescence, excellent processability, low band gap, moreover a single RT mesophase structure makes these PBIs promising materials for optoelectronic applications. PBI with chiral oligoethoxy chains (four ethyleneoxy units connected to a chiral ethyleneoxy unit) exhibited a wide range Col phase including RT.[30] Thus, in general the substitution with oligoethoxy chains improved the mesomorphic behavior and often stabilized the RT mesophases. But, the only problem with glycolic ether chains is their chelating nature with various cations, making such PBIs to be contaminated with ionic impurities for subsequent application in electronic devices (Figure 1.8 and 1.9).

1.3.3.2. Symmetrical perylene bisimides with alkyl chains

PBIs constitute a prominent class of strongly luminescent acceptor materials in organic electronics along with strong absorption characteristics and electron affinities comparable to fullerenes. Dialkyl PBIs specifically exhibit a low LUMO energy (-3.85eV), which makes them good acceptors even with respect to other aromatic PBIs of the similar band gap. This opens up the possibility of charge separation at interfaces between electronically complementary aromatic PBIs. PBI **3a** though it is crystalline, provides a useful reference, as it has been utilized as an active *n*-type carrier in many organic electronic devices (Figure 1.10).[31] Kim *et al.*[32] reported the excellent semiconducting behavior of PBI **3b**, after annealing the vapour-deposited polycrystalline film in its LC phase due to its ordered intermolecular structure. The increase in the chain length as in the case of compound **2a** and **3c** reduced the clearing temperatures. The incorporation of (*S*)-3,7-dimethyloctyl chain as in the case of **3d**, surprisingly showed the increase in clearing point than that of the compound **3b** with two *n*-heptyloxy chains. This compound was crystalline suggesting the increased order induced by the two chiral chains. Incorporation of swallowtailed symmetric alkyl chains brought down the clearing temperatures, but the compounds were crystalline (**3e-3h**).[28a-c,33] It is to be noted that only compound **3f** exhibited a monotropic Col$_h$ phase. Introduction of branched chains as the *N*-substituents brought down the clearing temperatures as in the case of PBIs **3i** and **3j**. Here compound **3i** was crystalline, whereas compound **3j** was liquid.[28b] Thus, the dissymetrization of the alkyl chains from swallowtails to 1-hexylnonyl (**3i**) and 1-hexyldecyl (**3j**) suppresses the clearing point and mesomorphic behavior together. Bock *et al.* thus introduced multiple racemic branching in alkyl chains, assuming that this will increase the volume of alkyl tails in the periphery to provide an overall disc-like shape to the PBIs. Compound **3k**, with two different racemic centers per alkyl chain and two alkyl chains per molecule, would be a mixture of four

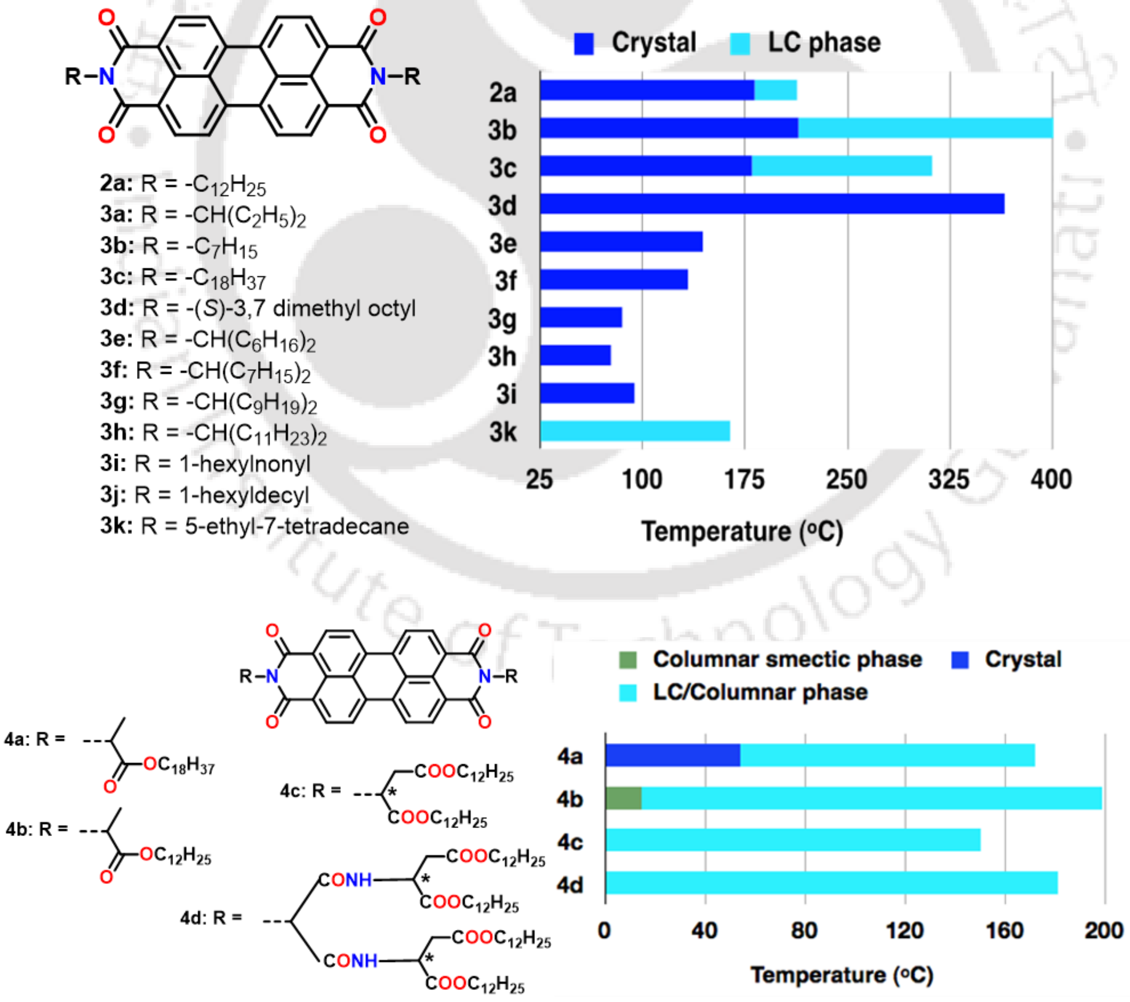

Figure 1.10. Structures and graphical representation of the thermal behavior of symmetrical PBIs **2a, 3b-3k** and **4a-d**.

diastereomeric pairs of enantiomers and two *meso* forms. This does not alter the clearing temperature but would lower the melting point. As expected the PBI **3k** with two doubly racemic triple-tail alkyl chains stabilized enantiotropic Col$_h$ phase over a long range including RT. This compound also exhibited good homeotropic alignment. This may be due to the increased volume of alkyl chains surrounding the hard core leading to efficient space filling and effective nanoseggregation.[28b,34]

Gao *et al.* introduced branched chains with amide units that are based on the chiral amino acid *L*-aspartic acid (Figure 1.10).[35] The swallowtailed amino acid based PBI **4c** as well as its next dendritic analogue PBI **4d**, stabilized room temperature, helically organized Col$_h$ phase over a long range. The increased clearing point in the case of **4d** is due to the increased number of intermolecular hydrogen bonding. The hydrogen bonds also resulted in a lower core-core distance of the individual discs within the column (Figure 1.10).

Zhang *et al.* introduced *L*-alanine based long chain esters as side chains to prepare PBI **4a** (Figure 1.10), which exhibited columnar smectic phase in spite of having two flexible chains. This PBI with P3HT formed a good bulk heterojunction solar cell with an optimized efficiency of 0.94%. This was found to be four-fold higher than the similar device based on a non-LC PBI **3a**.[36] The broad thermal range of the PBI **4a**, provides the option to thermally anneal at higher temperatures. This usually leads to a mild aggregation that improves the order and morphology of the **4a**:P3HT amalgamated films. Such film morphology is favorable for the balanced transport of oppositely charged carriers, leading to higher power conversion efficiency (PCE). However, when using non-LC **3a** as an acceptor, its strong aggregation leads to poor exciton dissociation and charge transport of the blend films. Jin *et al.* reported similar PBI **4b** based on *L*-alanine, but with a dodecyl chain. This compound showed highly ordered mesophase at RT in addition to a high temperature LC phase. The low-temperature phase was assigned as a columnar smectic phase, which is having a distinct long-range lamellar order, with 2D-crystalline in-layer positional order in addition to the π-stacking order (Figure 1.10).[37]

1.3.3.3. Symmetrical perylene bisimides with silyloxy chains

PBIs based on oligosiloxy chains at the terminal have been synthesized in the place of alkyl chains (Figure 1.11 and 1.12). A comparison of the thermal behavior of symmetrical PBIs with silyloxy chains show that PBI **5a** with two terminal chains was crystalline[38] (with a lamellar structure), so as the one with two cyclic silyloxy derivatives (**5f**). This means that the thermal movement created by the two oligosilyloxy chains is not sufficient to induce a mesophase and lower the transition temperatures. Symmetrically branched swallowtail type PBIs (**5b-5e**) with silyloxy chains stabilize LC phases at room temperature,[39] which create more flexibility and nanoseggregation. This should be appreciated in comparison to swallowtailed PBIs **3e-3h** with alkyl chains, which were crystalline in nature. The extremely wide mesophase ranges exhibited by these set of PBIs bearing oligosiloxane chains make it possible to study their electron transport mechanism. Compound **5b**

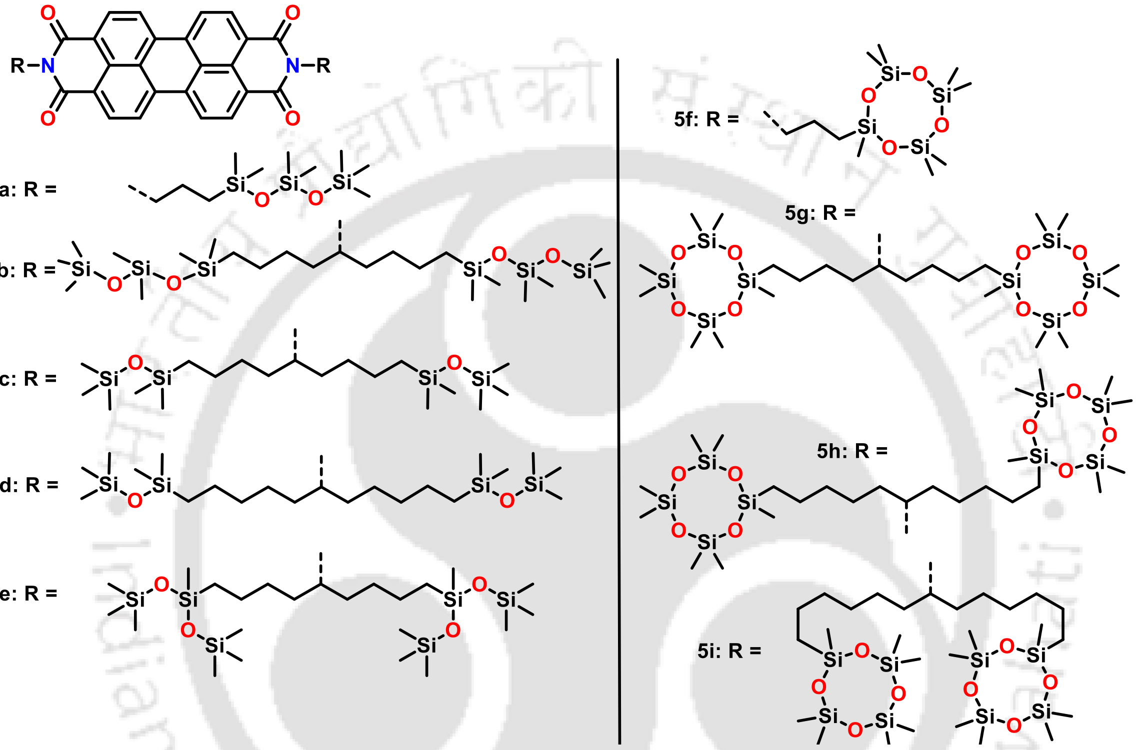

Figure 1.11. Structures of the symmetrical PBIs with silyloxy chains **5a-i**.

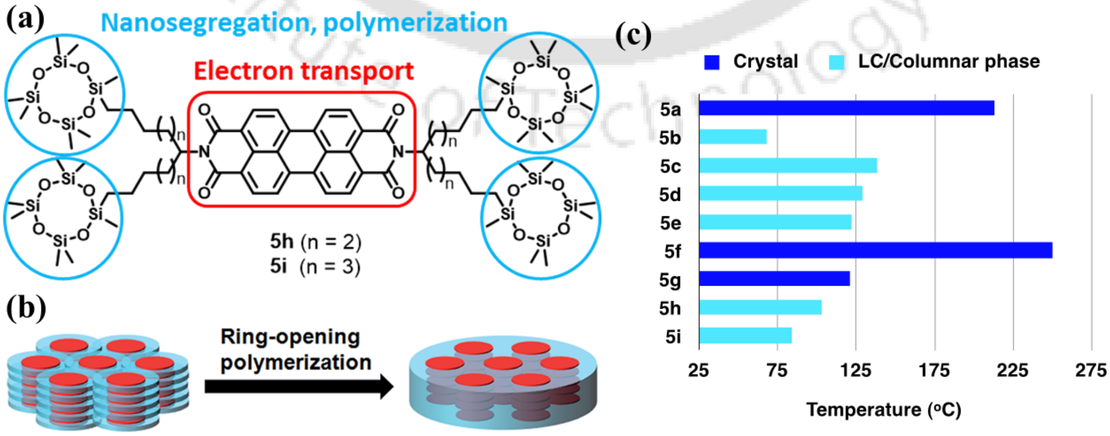

Figure 1.12. (a) Molecular structures of compounds **5h** and **5i** (Reproduced from reference [41b] with the permission of The Royal Society of Chemistry) and (b) schematic illustration of ring-opening polymerization in the columnar phase. (c) Thermal behavior of symmetrical PBIs with silyloxy chains **5a-i**.

exhibited an electron mobility of over 10^{-3} cm^2 V^{-1} s^{-1} in the LC phase. This compound also showed a transition from Col$_r$ phase to Col$_h$ phase.[40] On moving from **5b** to **5c** and **5d** where the length of the chains increased through a hydrocarbon spacer but with a reduction in the trimethylsilyl unit led to an increase in clearing point, while in the case of **5b**, where the length is increased by a trimethylsilyloxy unit led to a drastic lowering of clearing point to around 50 °C. In the case of swallowtail type cyclotetrasiloxane derivatives compound **5f** and **5g** were crystalline, while PBI **5h** and **5i** with increased chain length turned out to be liquid crystalline. This may be due to the reduced restriction for the movement of cyclotetrasiloxane moieties at the chain terminals. Compound **5h** exhibits a Col$_r$ phase and exhibit a high electron mobility of 10^{-2} cm^2 V^{-1} s^{-1} at RT.[41] The main driving forces that stabilize the columnar self-assembly phase is the pronounced nano-segregation that occurs between the rigid aromatic cores and cyclotetrasiloxane rings. Further, the cyclotetrasiloxane moiety can be polymerized, which provides new possibilities in organic electronics (Figure 1.12b).

1.3.3.4. Symmetrical perylene bisimides with aryl groups

Würthner *et al.* reported the PBI **6b**, which is obtained by the condensation of 3,4,5-tridodecyloxy aniline with perylene bisanhydride (Figure 1.13). This stabilized a wide range Col$_h$ phase from RT to 373 °C, with a high thermal stability.[42] Corresponding PBI with trialkyl phenyl groups **(6a)** also exhibited a wide range Col$_h$ phase but with a reduced clearing temperature by ≈70 °C.[43] PBI **6c** with chiral peripheral chains exhibited an ordered Col$_h$ phase where the molecules are packed in a helical fashion. The chiral peripheral chains bring a higher order within the Col phase leading to an increased charge-carrier mobility in the Col phase.[44] Substitution with other aromatic groups with flexible chains as in the case of dialkyl fluorenyl and carbazolyl groups did not induce any mesomorphic behavior because of the lack of space filling in such molecular design.[45] When the 3,4,5-trialkoxy phenyl group is connected through a flexible $-CH_2$-, as in the case of PBI **7a**, brings a lowering in the clearing temperature while keeping the mesomorphic behavior intact. The Col$_h$ phase is disordered as in the case of **6a** and **6b**. The charge carrier mobility measured by steady-state space-charge limited current obtained for **6b** in the LC state was 0.2 cm^2 V^{-1} s^{-1}, while that obtained for compound **7a** was found to be 1.3 cm^2 V^{-1} s^{-1}.[46] This value is higher than that of amorphous silicon. Use of suitable alignment methods may enhance the mobility further in such materials along with a proper choice of electrodes with suitable work functions to improve the charge injections.

Percec *et al.* studied dendronized PBIs, where the PBIs are derived by connecting the 3,4,5-tridodecyloxyphenyl units through spacers of different length (Figure 1.13).[47] The PBIs **7a-d** exhibited Col$_h$ phase but with a reduced clearing point in comparison to compound **6b**. The clearing points have reduced with the increase in the spacer length. Compounds **7a** and **7b** were liquid crystalline at RT, while compounds **7c** and **7d** were crystalline at RT. This shows that the PBI **6a** (without any spacer), **7b-7d** with di, tri and tetramethylene spacers self-assembled into complex helical columns generated from tetramers of PBI. Dendronized PBI **7a** with one methylene spacer, self-assembled into helical columns formed from the PBI dimers. At high temperature, all helical columns self-organize to form thermodynamically stable 2D Col$_h$ lattices with the intracolumnar order, which is due to fast self-assembly process. At low temperatures, dendronized PBIs self-organize in the thermodynamically stable 3D columnar simple orthorhombic (for **6a, 7b-7d**) and in 3D columnar monoclinic (for **6b**) lattices. This is through a very slow self-assembly process, that takes place from the closely related kinetic 2D product. These studies demonstrate the self-assembly of complex helical columns created from dimers and tetramers of dendronized PBIs that are persistent in 2D and 3D lattices formed in the solid state. In the 2D Col$_h$ phase with the intracolumnar order, the dendronized PBI exhibits an extraordinary dynamics able to leave the columns without the disorder. This provides a self-healing mechanism of structural defects. These complex helical columnar 2D and 3D periodic arrays are first reported for self-assembling dendritic structures. The complex helical columns observed here are racemic in nature. The general self-assembly processes reported in this class of molecules may help in explaining the mechanism of charge carriers transport. Further, this may improve the design methodology to obtain supramolecular electronic materials based on PBIs and other electron-deficient structures, which are of primary importance in the fabrication of OSCs and other organic electronic devices.

Usually, reported PBIs are known to stabilize only Col or lamellar assemblies. Percec *et al.* shown that suitably functionalized PBI (**7e**) can be self-assembled into a supramolecular sphere.[48] This PBI functionalized at its imide groups with a second generation dendron, self-assembled into supramolecular spheres. These spheres self-organized into a body-centered cubic (BCC) lattice, which is rarely seen for self-assembling dendrons but often noticed in the case of block copolymers (Figure 1.13b). These supramolecular spheres also assembled into a Col$_h$ array at a lower temperature and thus exhibited a rare transition from Col$_h$ to cubic phase.

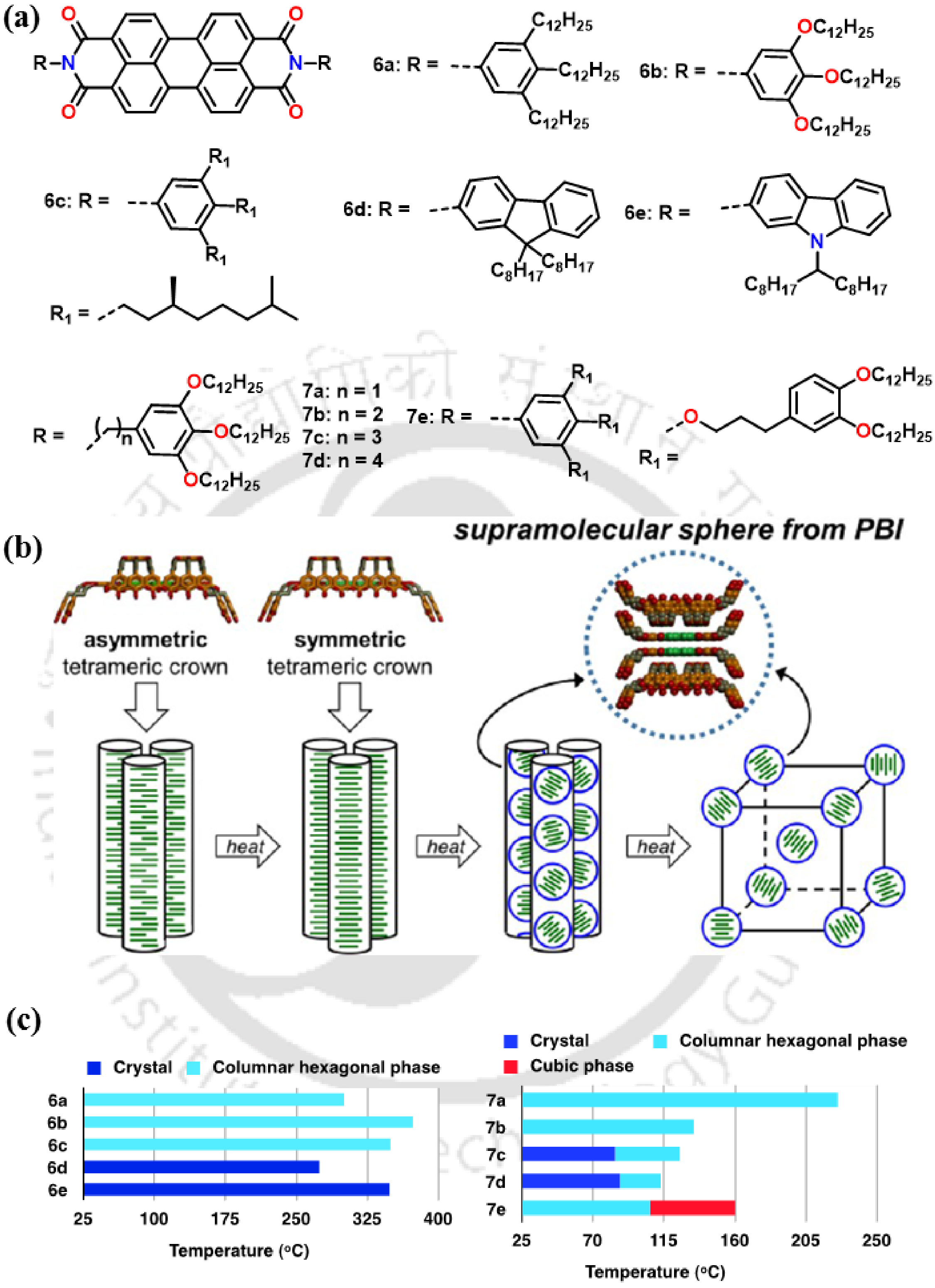

Figure 1.13. (a) Structures of symmetrical **PBIs** with aryl (**6a-6e**) and dendron substitution (**7a-7e**); (b) Schematic showing the self-assembly of dendronized PBI 7e in col$_h$ phase and transformation to BCC phase (Reproduced from reference [48] with the permission of American Chemical Society); (c) Graphical representation of the thermal behavior of **PBIs 6a-6e** and dendron substitution **7a-7e**.

Asha *et al.* reported a series of highly fluorescent LC PBI molecules having amide/ester linkage with an end-cap of phenyl, monododecyloxy phenyl, or tridodecyloxy phenyl moieties (Figure 1.14).[49] The amide-functionalized series self-assembled to form H-type or head-on aggregates irrespective of their end-capping in polar organic solvents (for example, like tetrahydrofuran (THF), toluene, and dichloromethane). On the other hand, only the monododecyloxy phenyl end-capped molecule in the ester series showed a tendency to self-organize with a typical J-type or slip-stacked aggregation in toluene.

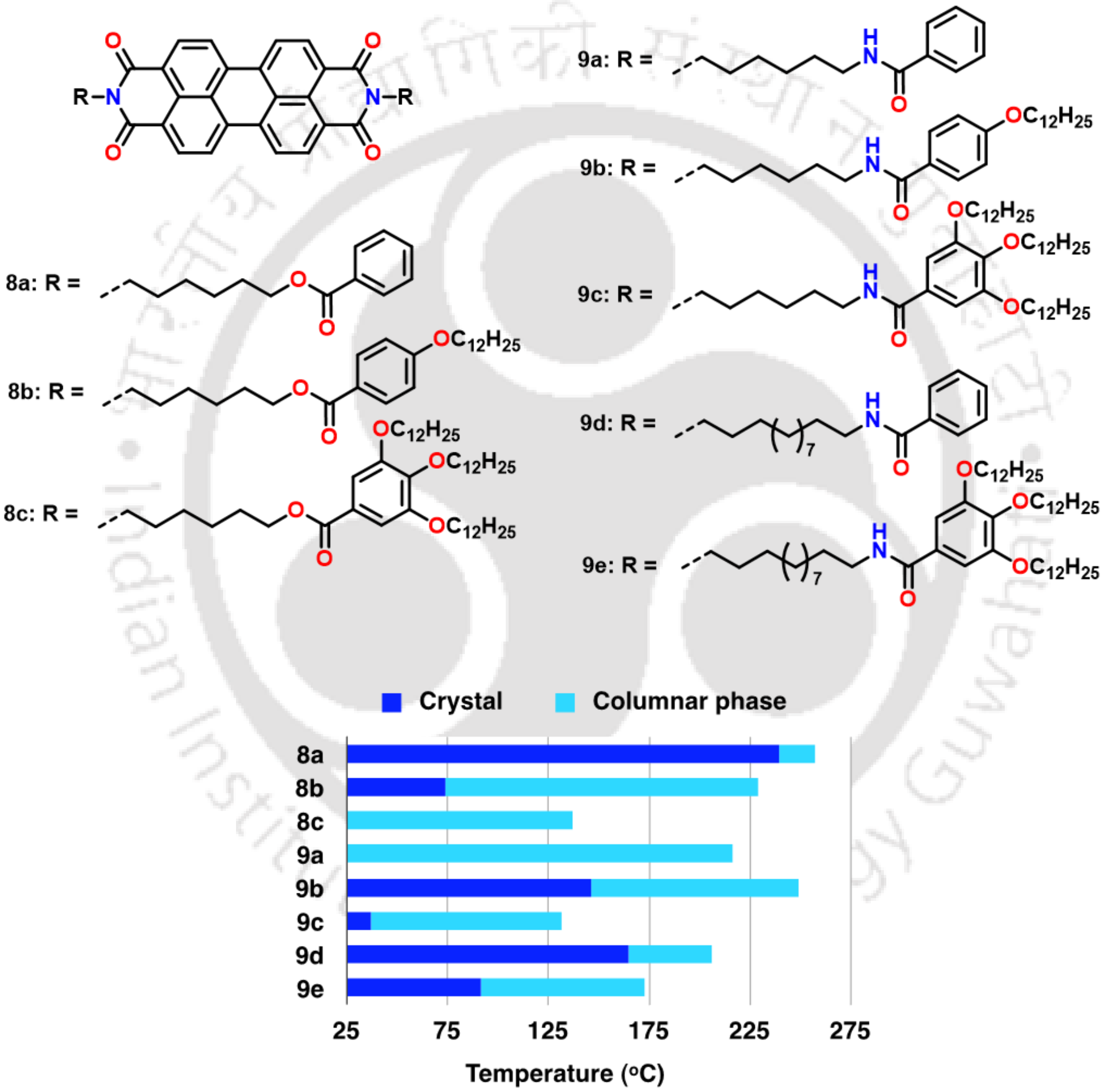

Figure 1.14. Structures and bar graph of symmetrical **PBIs** with aryl groups connected with a long spacer (**8a-8c, 9a-9e**).

Usually connecting the trialkoxyphenyl group directly to the perylene core to form PBIs quench the luminescence and authors suggested that connecting them through the spacers would stabilize liquid crystallinity and also preserve the luminescence in an aggregated state. The ester and amide molecules here can be classified into three groups: (a) molecules without a terminal substitution, (b) molecules with monododecyloxy terminal substitution, and (c) molecules with tridodecyloxy terminal substitution. In the first case, for example, consider ester **8a** and amide **9a**: the melting and clearing points have been reduced in the case of amide **9a**. Increase in the spacer length from 6 to 12 as in the case of amide **9d** reduced the clearing point but increased the melting point in comparison to **9a**. However, in the case of compound **9d**, the mesophase was frozen in a glassy state in cooling cycle. Increase in the number of flexible chains on the periphery of the benzene end cap of the esters (**8b** and **8c**) reduced the melting and clearing points, with the tridodecyloxy derivative **8c** showing RT LC phase. In the case of corresponding amide derivatives, this trend was not there. Compound **9b** exhibited higher melting and clearing point, while the tridodecyloxy derivative **9c** exhibited a lower melting and clearing temperature. Increase in the spacer length to 12 (**9e**), led to an increase in the melting and clearing point in comparison to **9c** but reduced the same in comparison to **9d**.

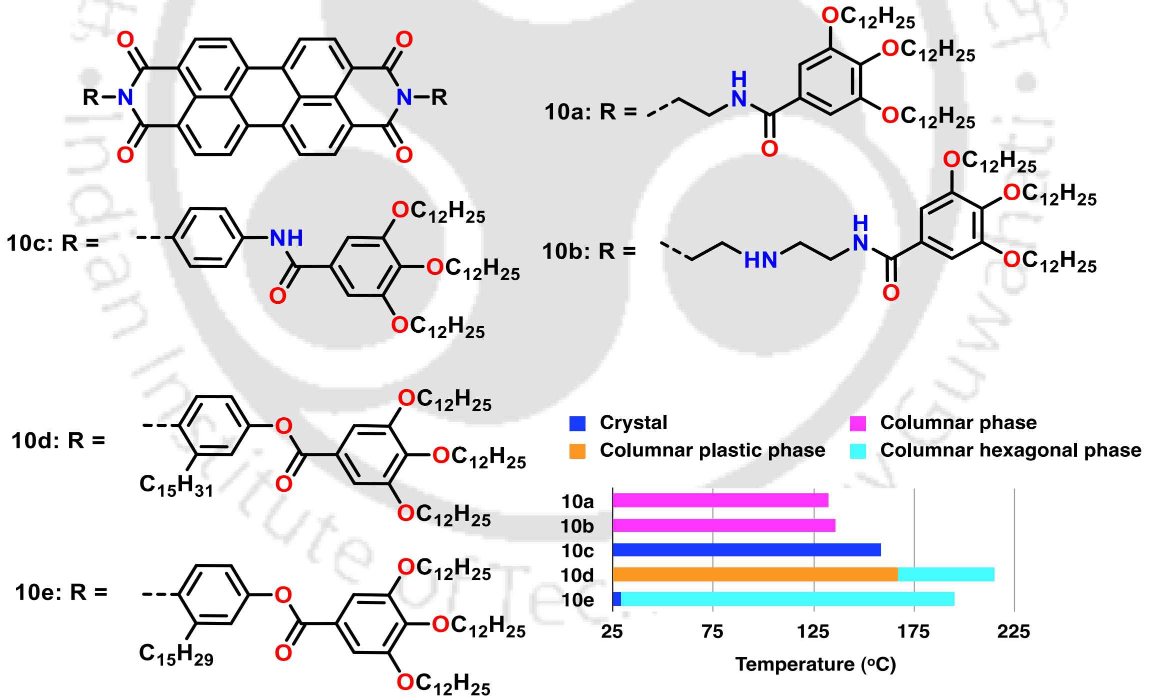

Figure 1.15. Structures and Graphical representation of the thermal behavior of symmetrical **PBIs** with aryl groups connected with different linking groups (**10a-e**).

Yang *et al.* reported symmetrical PBIs, where the 3,4,5-tridodecyloxy benzoyl units are connected through different spacers containing amines at their termini (Figure 1.15). PBIs **10a** and **10b** with soft-alkylene spacers with amine units exhibited RT Col phase, while compound **10c** with rigid aromatic spacer turned to be crystalline in nature.[50] Asha *et al.* reported PBIs **10d** and **10e,** where the 3,4,5-tridodecyloxy benzoyl units are connected through a pentadecyl phenol (PDP) or cardanol.[51] The compound **10d** which had saturated side chain exhibited more crystalline order. This compound displayed a low temperature $\mathrm{Col_h}$ plastic phase and a high temperature $\mathrm{Col_h}$ phase, while the compound **10e** with an unsaturated side chain exhibited $\mathrm{Col_h}$ phase spanning over a broad thermal range. The presence of the long pentadecyl chain in the *ortho*-position to the imide linkage did not harm the ability of these PBIs to arrange in the form of H-type aggregates. Remarkably, a bend in the alkyl chain introduced through the *cis*-double bond did not cause any change in the type of the resulting aggregates but led to a drastic reduction in the aggregate length.

1.3.3.5. Unsymmetrical perylene bisimides with alkyl groups

Thelakat *et al.* reported unsymmetrical PBI **11a** with two unsymmetrical swallowtails, which turned to be crystalline (Figure 1.16).[52] By keeping the 4-heptyl chain in the swallowtail constant, they have also prepared **11b** and **11c** with *n*-dodecyl chain and 10-nonadecyl chains (swallowtail) at the other ends. Compound **11b** with a combination of linear and swallowtails[53] and compound **11c** with different swallowtails turned to be crystalline.[28a] Interestingly, unsymmetrical PBIs with 4-heptyl swallow chains at one end and swallowtail type oligoethoxy chains at the other end stabilized $\mathrm{Col_h}$ phase. Increasing the length of the oligoethoxy chains brought down the melting and clearing points of the PBIs **11d** and **11e**. Unsymmetrical bisimides with a 12-undecyl chain at one end and oligoethoxy chain at the other end (**11f** and **11g**) also showed reduced melting and clearing point in comparison to corresponding PBIs with 4-heptyl chain (**11d** and **11e**). PBI **11h** with *n*-dodecyloxy chain at one end and with swallowtail type oligoethoxy chains at the other end stabilized $\mathrm{Col_h}$ phase over a wide temperature including RT.[53] PBI **11i** with a swallowtail type 12-undecyl chain and linear oligoethoxy chains turned to be crystalline, which means that the reverse combination of **11h** is not supportive of the liquid crystallinity.[28a] However, the unsymmetrical PBIs with a combination of linear oligoethoxy chain with swallowtail type oligoethoxy chains (**11j**)[53] and silyloxy chains (**11k**) proved to be superior by stabilizing the wide range of $\mathrm{Col_h}$ phase including RT.[54]

1.3.3.6. Symmetrical core-substituted perylene bisimides

Würthner *et al.* reported core chlorinated PBI (**12a**) with four chlorine substituents in the *bay*-positions stabilizing $\mathrm{Col_h}$ phase and exhibiting a charge carrier mobility

(6 × 10^{-6} cm^2 V^{-1} s^{-1}) in the Col phase similar to its nonchlorinated compound **6b** (5 × 10^{-6} cm^2 V^{-1} s^{-1}). Remarkably, the charge carrier lifetime was over 100 times greater, than that observed in the non-chlorinated parent compound (Figure 1.17).[31] This dramatic enhancement in the lifetime was explained in terms of the increased order in the case of chlorinated PBI. This enhanced lifetime endures when the material is blended with p-type hexabenzocoronene (HBC) derivatives and hints the chlorinated derivative may find usefulness in device architectures, where an extended carrier lifetime is much desired. However, the width of the Col_h phase was reduced with the decrease in clearing and an increase in the melting points with respect to the parent compound. They have also reported PBIs, which are substituted with different phenoxy derivatives in *a bay* region (**12b-12e**).[42] Compounds **12b-12d** stabilized wide range Col_h phase including room temperature, while compound **12e** turned to be crystalline because of the lack of space filling and nanoseggregation of the aromatic cores and the flexible peripheral alkyl chain. These compounds exhibit high thermal stability and bright fluorescence making them promising materials for optoelectronics applications. The high fluorescence efficiency is attributed to the J-type aggregation of these molecules.[42] They have also reported several PBIs with two

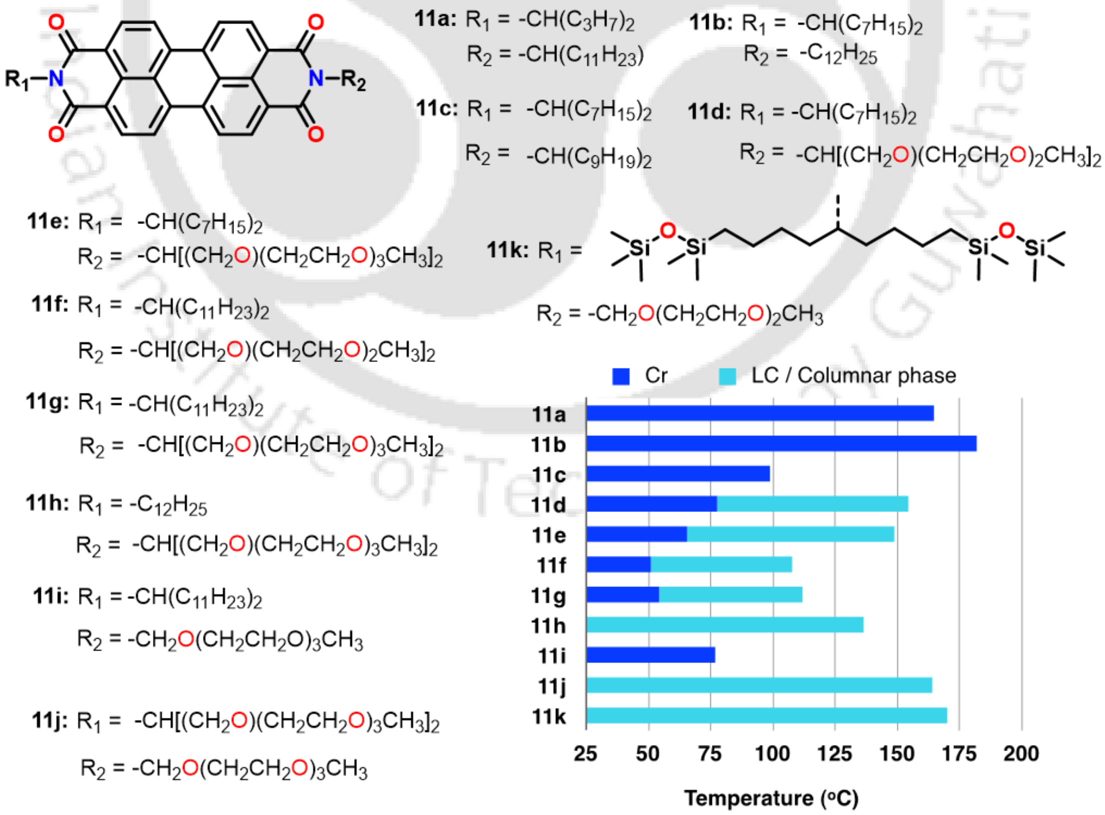

Figure 1.16. Structures and Graphical representation of the thermal behavior of unsymmetrical **PBIs** with aliphatic chains (**11a-k**).

or four substitutions at a *bay* area which bear 3,4,5-tridodecylphenyl groups at imide positions. These compounds exhibited either Col$_r$ (for compound **12f**) or Col$_h$ phases (for compounds **12g-i**) with low clearing point and room temperature liquid crystallinity. Compounds **12j** and **12k** were crystalline. Contrary to the extended oligomeric π-stacks formed for planar unsubstituted PBIs, here the aggregation was limited to π-π stacked dimers in the apolar solvent due to the twisted aromatic structure. The fluorescence observed in solution was due to the dimeric aggregates. Interestingly, these PBIs exhibited fluorescence even in the mesophase. The core twisting brings a substantial effect on the π-π stacking manner of the molecules in solution, as well in the Col phases. In both cases, the more twisted tetrasubstituted PBIs prefer longitudinally slipped stacks with J-type emissive behaviors, whilst for the less twisted disubstituted PBIs, the rotational displacement between the PBIs in cofacial aggregates was confirmed.[43]

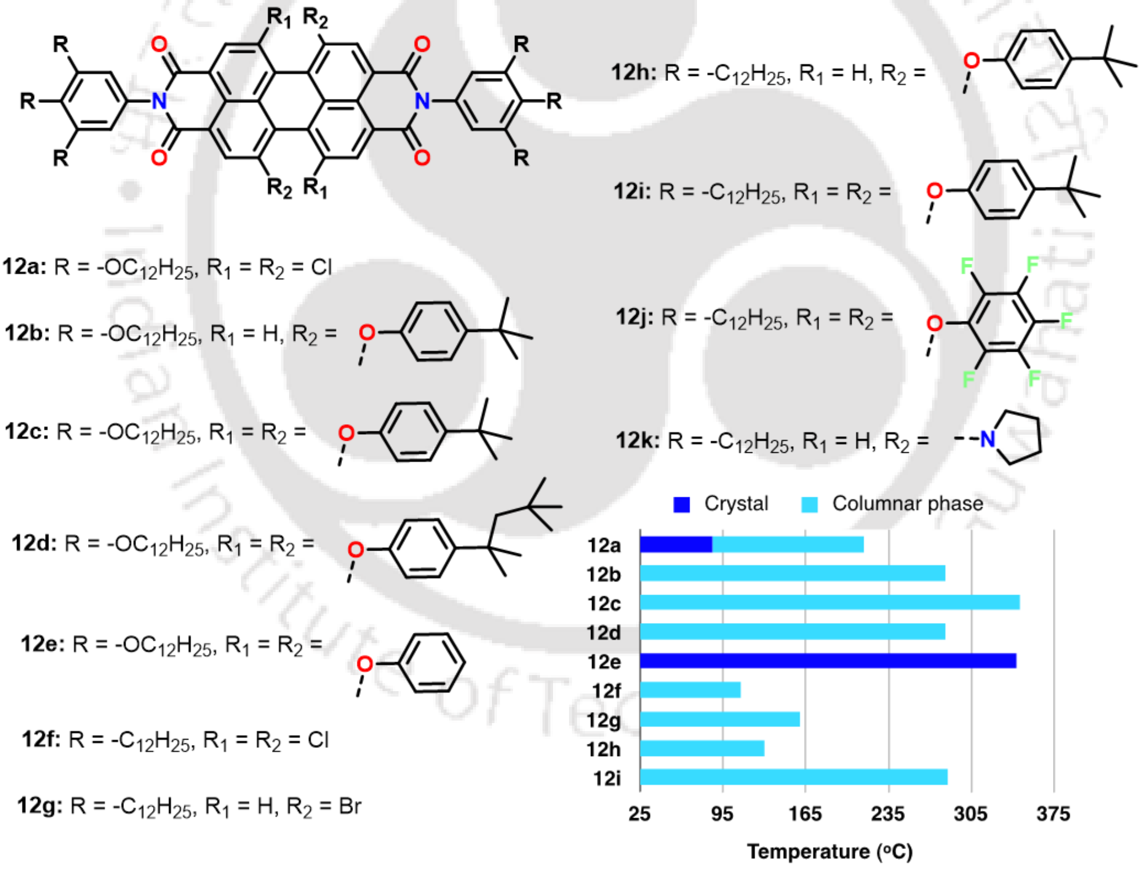

Figure 1.17. Structures and Graphical representation of the thermal behavior of unsymmetrical **PBIs** with aliphatic chains (**12a-k**).

Zhang *et al.* reported a series of symmetrical and unsymmetrical *bay*-chlorinated PBIs with siloxane terminal chains at imide positions.[55] Symmetrical PBI **Si/1OEt** bearing one ethoxy group in the terminal silyl end exhibited an enatiotropic Col$_h$ phase, while all the other symmetrical (with two or three ethoxy groups) and unsymmetrical PBIs (with an *n*-octyl chain at another terminus) exhibited monotropic Col$_h$ phase. They also exhibited a strong aggregation in concentrated THF solution along with a lyotropic LC behavior, which was also confirmed by red shifted absorption spectra. (Figure 1.18).

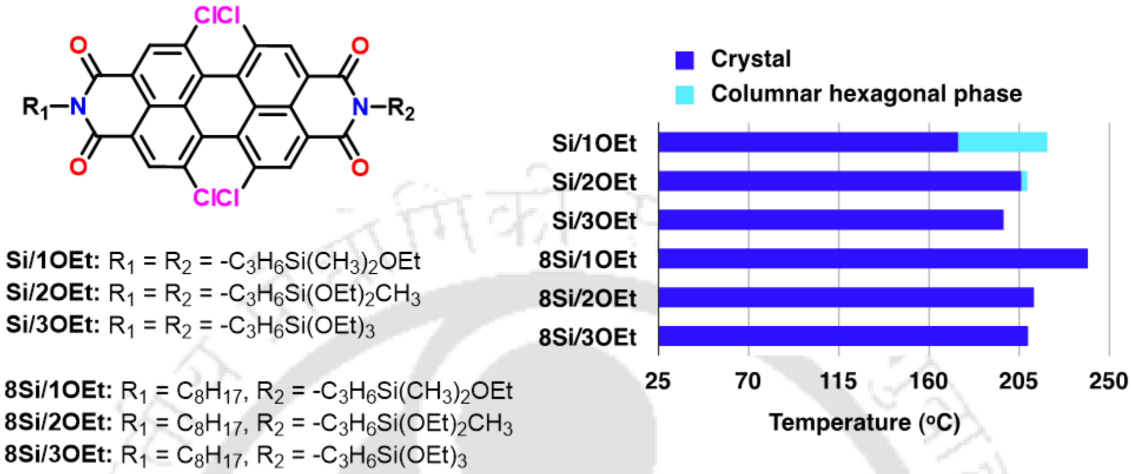

Figure 1.18. Structures and bar graph of symmetrical and unsymmetrical **PBIs** with silyl chains (**Si/1OEt-8Si/3OEt**).

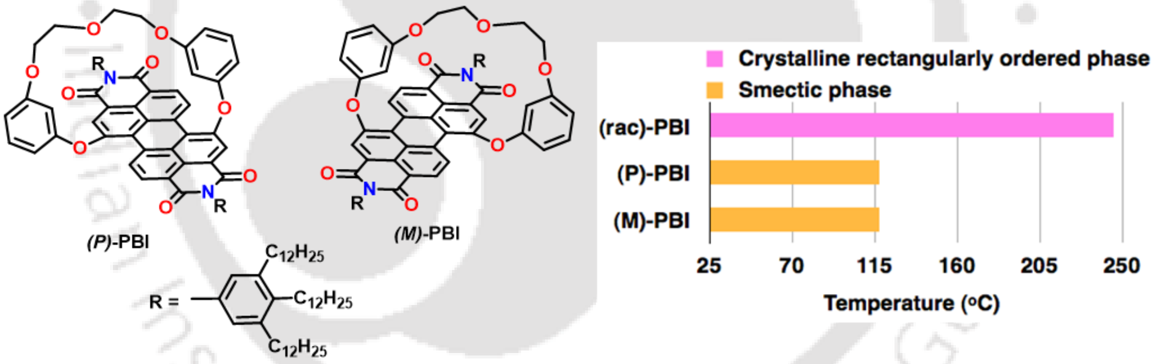

Figure 1.19. Structures and bar graph of core-twisted *bay*-substituted **PBIs.**

Würthner *et al.* reported[56] the three-dimensional (3D) self-assembly of a racemic core-twisted PBI and its pure atropo-enantiomers ((***P*)-PBI** and **(*M*)-PBI**) (Figure 1.19). In the condensed state, they studied the influence of core chirality in such materials. These studies showed characteristic differences in the bulk state properties of the racemic and enantiopure PBIs. The racemic material forms a soft crystalline phase, while the pure enantiomers ((***P*)-PBI** and **(*M*)-PBI** stabilized a smectic phase with far lower viscosity. The presence of equal amounts of each enantiomer at the same time in the case of (*rac*)-**PBI** permits this material to self-assemble in a soft columnar crystalline phase with higher thermodynamic stability in comparison to the enantiopure **(*P*)-PBI** and **(*M*)-PBI**, which organizes in lamellar/smectic LC phase. Here nano-segregation and interaction between the bridging units are the two crucial factors that lead to an observed difference in their bulk state behaviors. Alternation of *MM* and *PP* homochiral dimers in the condensed LC phase of (*rac*)-**PBI** provides an excellent nanosegregation and dense packing of the dimeric PBI building blocks into columns. In contrast, for enantiomerically pure **(*P*)-PBI** and **(*M*)-PBI**, the bridging units sterically prevent their packing into columns, which finally leads to the lamellar organization of the PBIs and a less viscous LC phase.

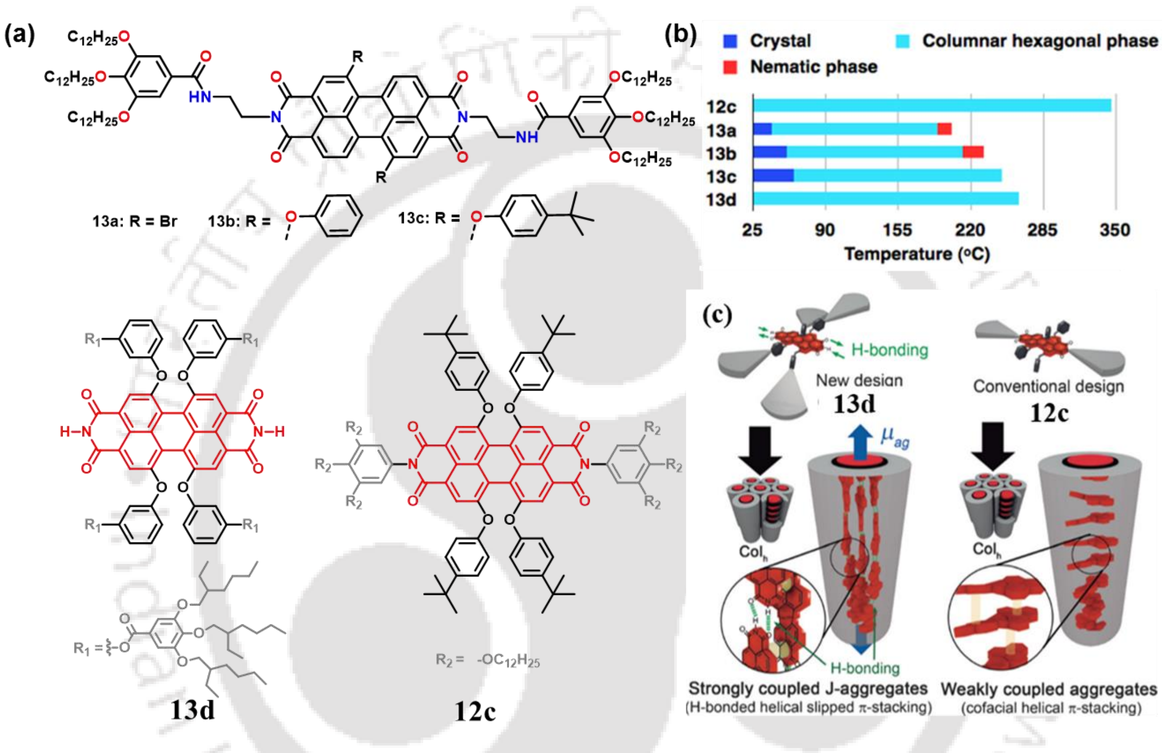

Figure 1.20. (a) Structures of symmetrical **PBIs** with aliphatic chains (**12c**,**13a-d**); (b) Graphical representation of the thermal behavior of *bay*-substituted **PBIs** (**12c**,**13a-d**); (c) Illustration of the molecular self-assembly of **13d** and **12c** into columnar hexagonal LC phases that exhibit orthogonal orientation of the PBIs. Blue arrows indicate the direction of the main transition dipole moments (mag) of the PBI molecules for 13d (Reproduced from reference [57] with the permission of Wiley VCH).

Yang *et al.* further reported several PBIs with H, Br, phenyl and *tert*-butylphenyl substituents on *bay*-positions and studied their mesomorphic and photophysical properties (Figure 1.20).[50b] The PBIs **13a-c** with Br, phenyl and *tert*-butylphenyl at *bay*-positions stabilized Col_h phase in comparison with similar PBI **10a** with no substituents on *bay*-position. Compounds **13a** and **13b** exhibited a short range (12-19 ^oC) nematic phase before reaching the clearing point. The photophysical studies revealed that the compounds **13a-c** possess stronger luminescence intensities, larger Stokes shifts and higher fluorescence quantum yields than that of PBI **10a**. Lehmann and Würthner reported a new PBI derivative **13d** that self-assembles through hydrogen bonds and π-π interactions into

J-aggregates. These J-aggregates in turn self-assemble to form Col_h phase (Figure 20c).[57] The PBI cores self-organized with their transition dipole moments parallel to the columnar axis, which is a unique type of structural organization in the case of Col LCs. XRD studies unravel a helical structure comprising of three self-assembled hydrogen-bonded PBI strands that create a single column of the Col_h phase. Interestingly this Col_h phase spans over a wide thermal range including RT.

1.3.3.7. *Bay*-extended perylene bisimides

Over the years, several research groups explored the properties of PBIs with extended core structure. The core extension was carried out either along the long axis or in the *bay*-region. Extension along the long axis usually leads to a bathochromic shift in the absorption, while the same along the *bay*-region leads to a hypsochromic shift in the absorption spectra. Bock *et al.* reported benzo[*ghi*]perylene 1,2,4,5,10,11-hexacarboxylic trialkylimide (**14a-c**) and dialkylimido-dialkyl ester (**15**) derivatives, exhibiting a enantiotropic Col_h phase at RT. Here, they have utilized previously unknown chiral racemic α-branched alkylimide functions (Figure 1.21). Compounds **14c** and **15** exhibited RT Col_h phase with good homeotropic alignment. They showed that racemic side-chain branching is valuable in the stabilization of Col phases of polycyclic aromatic oligo-dicarboximides with RT stability and accessible clearing points. This makes them suitable materials to study their optoelectronic properties, alone or in combination with complementary materials.[16] In an interesting report Bock *et al.* showed that the incorporation of configurational molecular design features like atropoisomeric moieties possessing low racemization barrier in the aromatic system may provide an option to stabilize Col phases at RT.[17] They have also shown how the collective effects of the variation of carboxylic substitution and of the lateral extension of perylene-type molecules can be adjusted to achieve electronically modified donor–acceptor couples for organic heterojunction devices. Compound **17** and diimidediester **15** showed a room temperature Col_h phase.[16-17] The bilateral extension of PBIs led to compound **16**, which turned out to be crystalline in nature suggesting the impact of very minor changes on columnar self-assembly. The bilateral extension led to a nonplanar structure which made the molecules unable to stack one above the other to form Col phase.[18]

Müllen *et al.* investigated the effect of the core extension of PBIs on the thermotropic self-assembly.[33] They have compared a homologous series of swallowtail

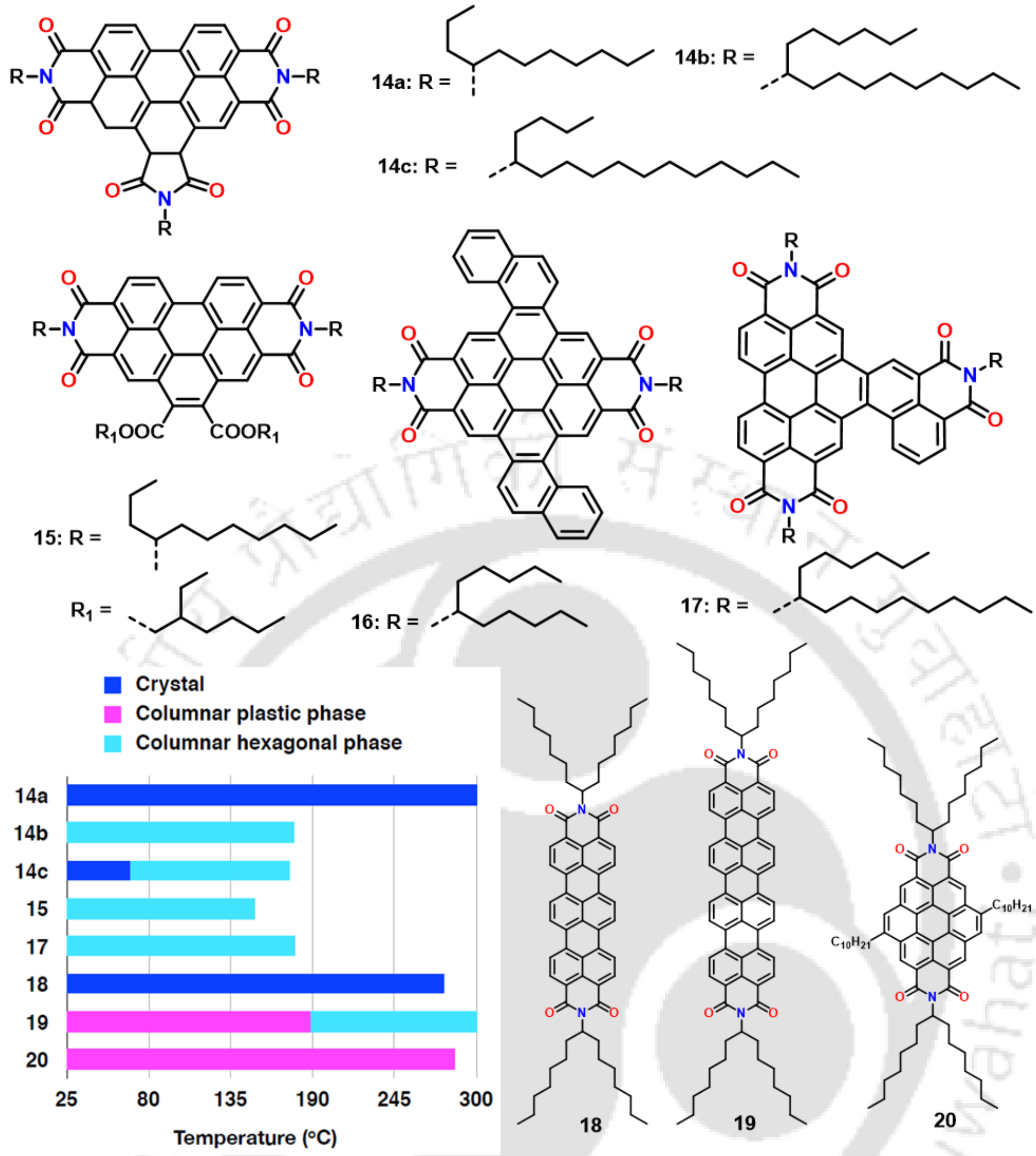

Figure 1.21. Molecular structures and Graphical representation of the thermal behavior of *bay*-extended PBIs (**14-20**).

type alkyl substituted tetracarboxdiimides, namely, PBI (**3f**), terrylene diimide (**18**), quaterrylene diimide (**19**) and coronene diimide (**20**), was synthesized (Figure 1.21). These compounds exhibited absorption maxima in the range of 430-760 nm with high extinction coefficients and showed a high thermal stability. All the compounds exhibited an identical columnar self-assembly, where the individual molecules are rotated with an angle of 45 °C to each other resulting in a helical structure with a pitch comprising four molecules. Molecules with larger aromatic cores exhibited higher clearing points, within this series as expected. However, differences in the self-assembly during crystallization from the isotropic phase was noticed. PBI **3f** and terrylene tetracarboxdiimide (**18**), both were crystalline and formed large as well as highly ordered domains with molecules arranged in an edge-on orientation. Quaterrylene diimide (**19**) was bimesomorphic exhibiting a transition from Col$_p$ to Col$_h$ phase. Circular shaped coronene tetracarboxdiimide (**20**) exhibited a homeotropically aligned columnar plastic phase.

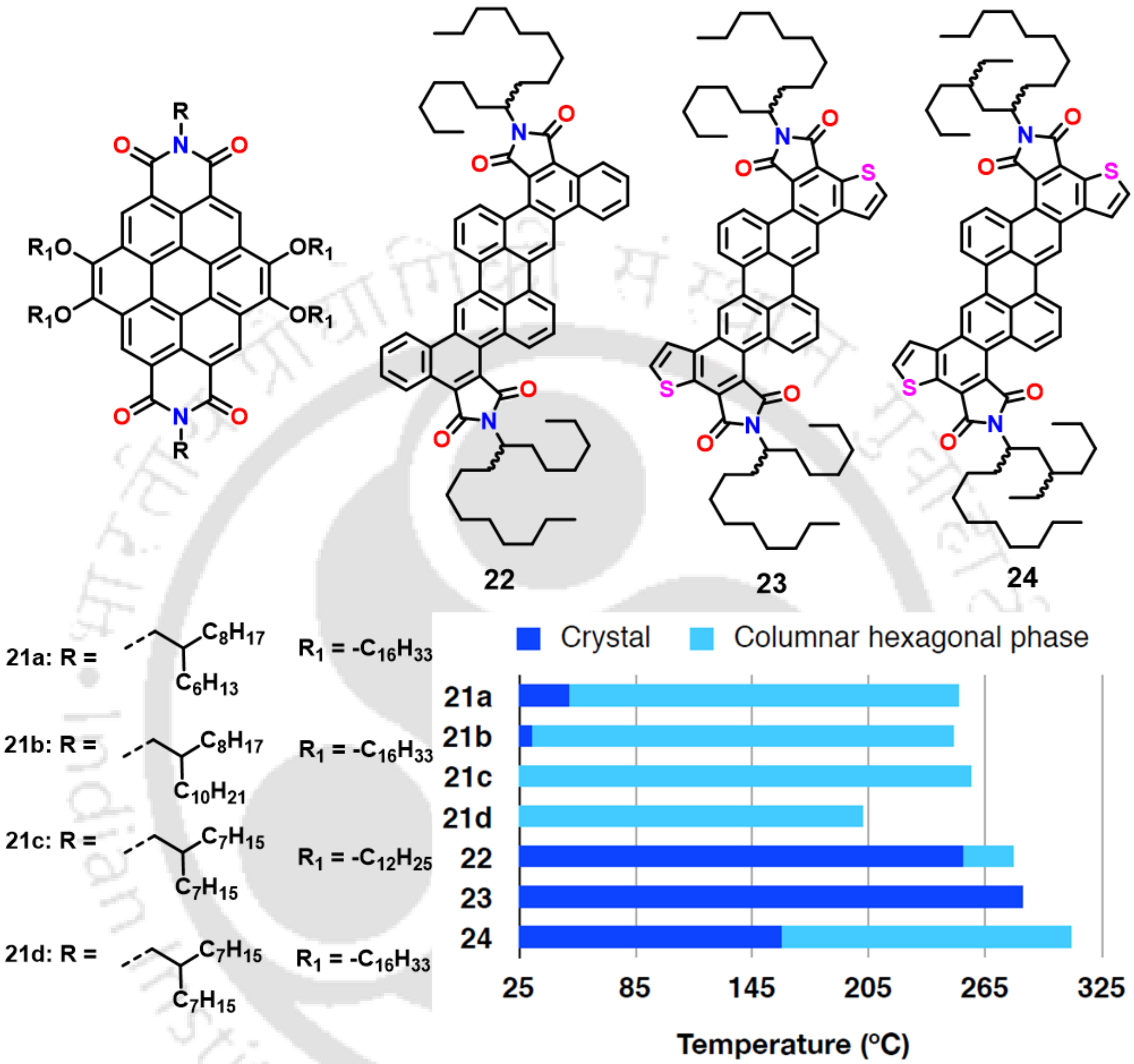

Figure 1.22. Molecular structures and Graphical representation of the thermal behavior of core-extended **PBIs** (**21a-d, 22-24**).

Wang *et al.* synthesized[58] a series of novel dibenzocoronenediimide derivatives with *α*- or *β*-branched alkyl and different alkoxy groups (Figure 1.22). Introduction of swallowtail like alkyl chains and alkoxy substituents lowered the clearing temperatures. Compound **21c** and **21d** stabilized wide range RT Col$_h$ phase. Similar to coronene diimide **20**, these compounds also exhibited a good homeotropic alignment on cooling from the isotropic liquid state.

Bock *et al.* recently reported[34] core-extended perylene derivatives (**22-24**) with two imide units substituted with branched or racemic doubly branched alkyl chains

(Figure 1.22). They incorporated two polarizable thiophenic sulfur atoms in the molecular structure (**23-24**). Incorporation of racemic doubly branched alkyl chains brought down the melting temperature in the case of **24** and increased the mesophase range.

1.3.3.8. Perylene based oligomers

Pal *et al.* reported oligomers based on 3,4,9,10-tetrasubstituted perylene, with four different mesogenic units like cholesterol, 4-cyanobiphenyl, triphenylene and pentalkynylbenzene connected through different flexible spacers to get corresponding tetraesters **25a-f** (Figure 1.23). All the oligomers were mesogenic. PTE **25a** with four cholesteryl groups exhibited monotropic chiral nematic (N*) phase, while PTE **25b** exhibited an enantiotropic nematic phase. PTE **25c** with four triphenylene units exhibited enantiotropic Col_h phase including RT.[15] PTE oligomers **25d-f**, were reported by the same group where the perylene core is connected with pentalkynyl benzene through hexa, octa and decamethylene spacers.[59] Compound **25d** and **25e** exhibited soft crystalline Col_{ob} phase, while **25f** with longer spacer exhibited RT nematic columnar phase. All the molecules showed a green emission in solution and in the solid state.

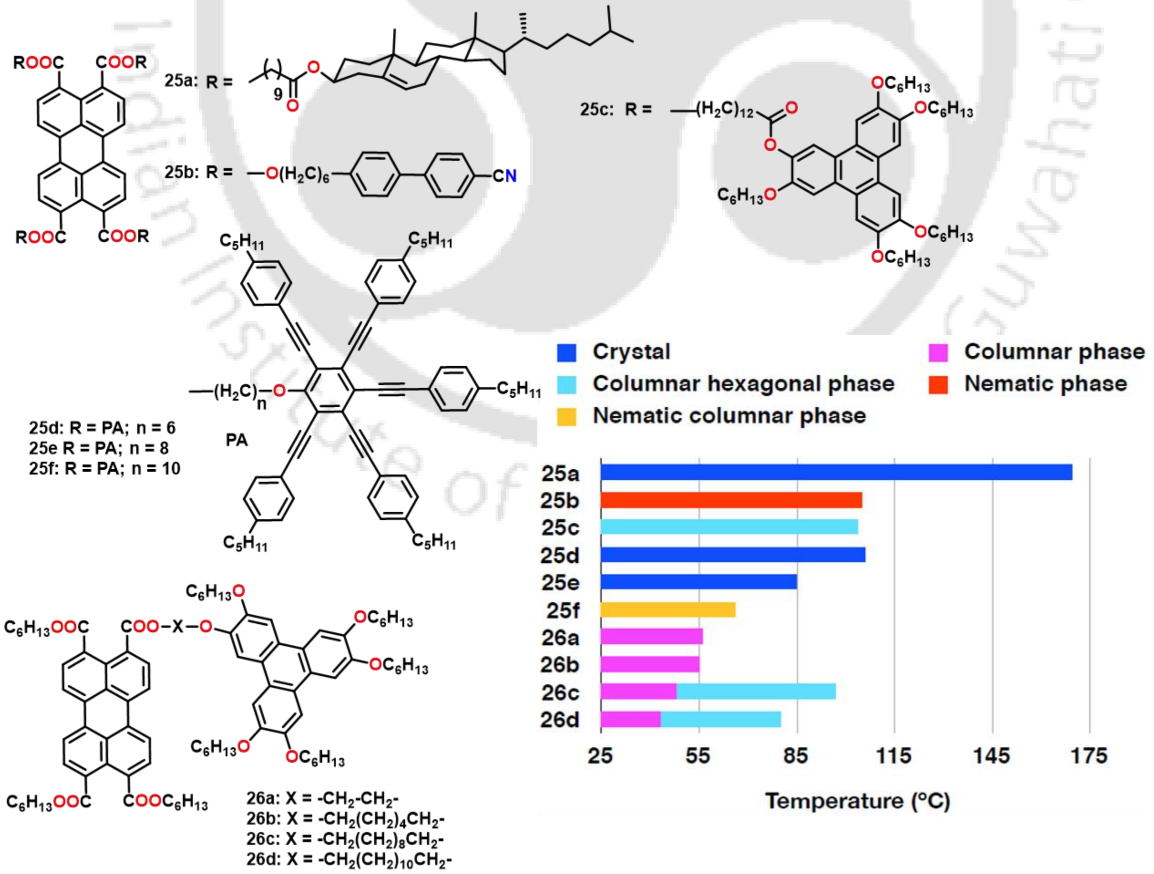

Figure 1.23. Molecular structures of PTE based oligomers (**25a-f** and **26a-d**).

Wang *et al.* reported four perylene ester triphenylene dimers separated by spacers of dimethylene, hexamethylene, decamethylene and dodecamethylene units.[60] These donor-acceptor dyads preserved the genuine electrochemical behaviors of the donor and acceptor units (**26a-d**). The fluorescence quenching of the acceptor unit varies with the spacer length, which is ascribed to the ground state charge transfer from donor to acceptor unit. Dimers **26a** and **b** were monomesomorphic and exhibited unidentified Col phase, while dimers **26c** and **d** were bimesomorphic exhibiting a low temperature Col phase and high temperature Col_h phase. All the dimers exhibited a RT Col phase and the clearing temperatures were increased with the spacer length.

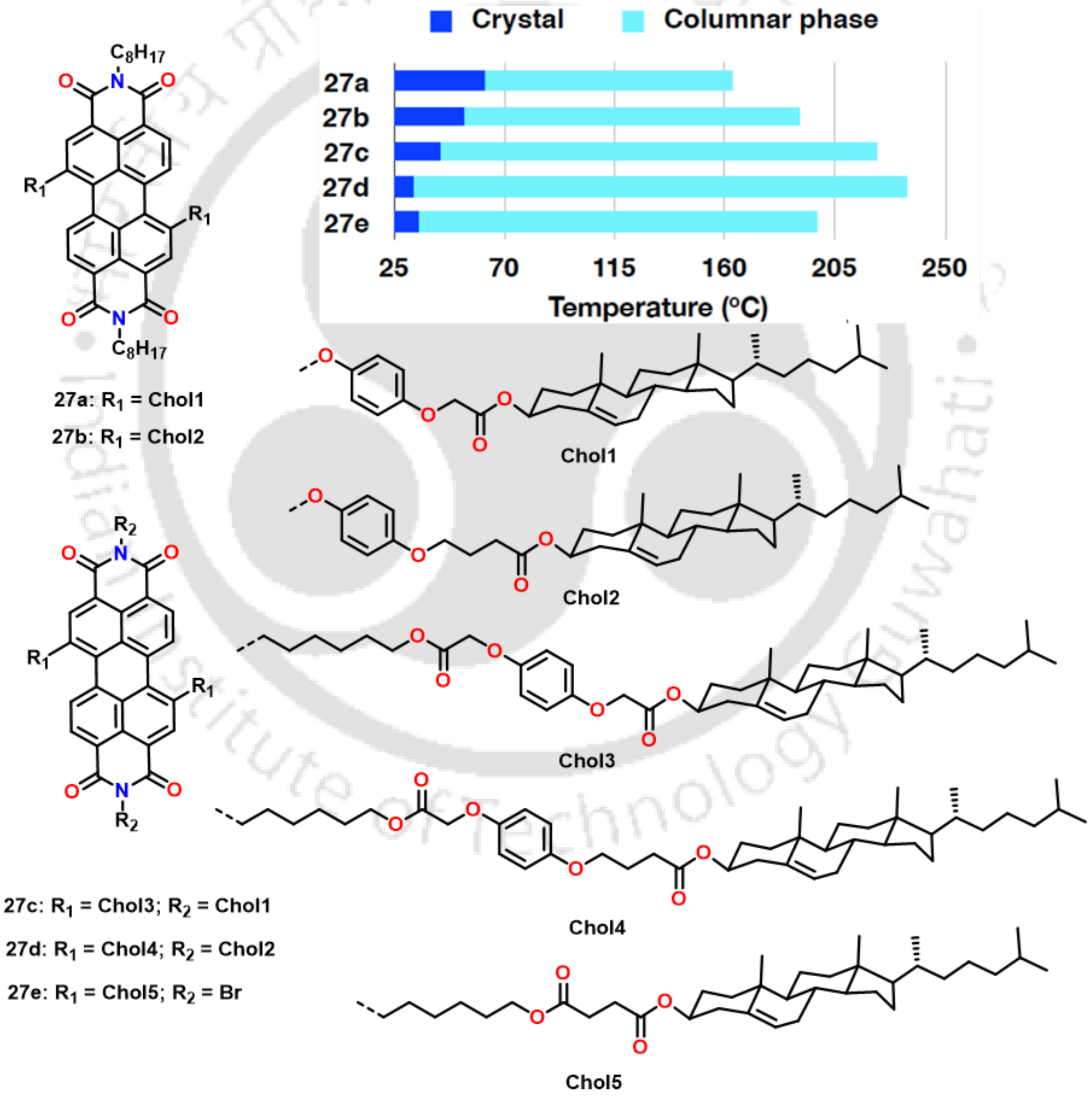

Figure 1.24. Molecular structures and bar graph of PBI based oligomers (**27a-e**).

Yang *et al.* synthesized trimers (**27a-b**) and pentamers (**27c-e**) derived from 1,7-*bay* substituted perylene (Figure 1.24).[61] The trimers were prepared by connecting two cholesterol moieties at the *bay*-position or four cholesterol moieties on both *bay*-position and imides position. All the oligomers exhibited good fluorescence in comparison to similar PBIs with alkyl units on imides position. The presence of more cholesterol units lowered the melting temperature, widened the mesophase range and enhanced the fluorescence. Increase in the spacer length was found to be favorable for improved thermal behavior and luminescence.

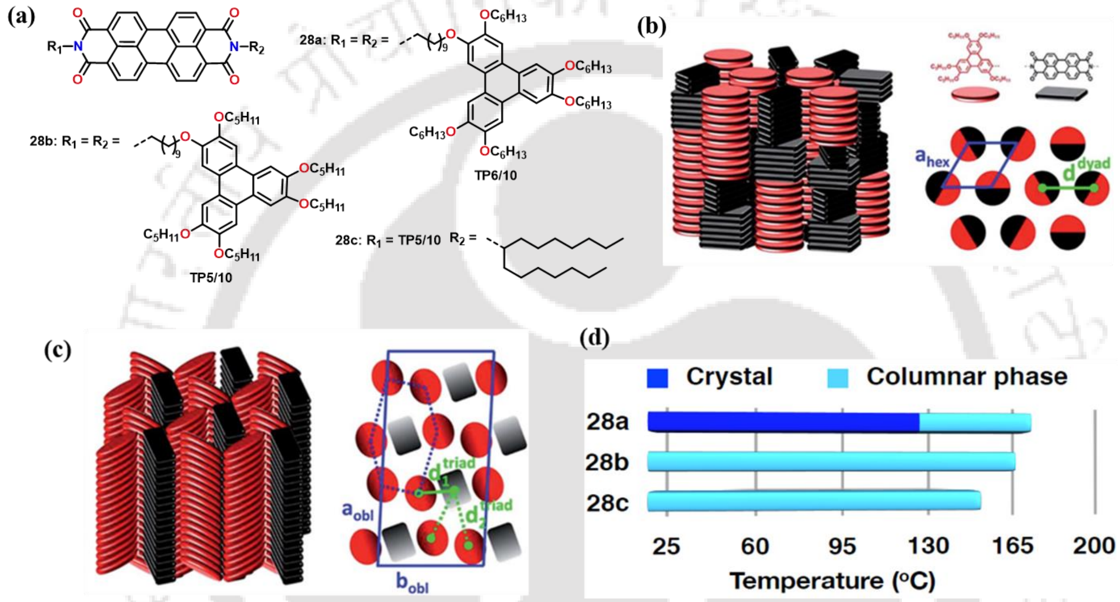

Figure 1.25. (a) Molecular structures of PBI-triphenylene oligomers (**28a-c**); (b) Schematic representation of (left) the self-organization within the Col_h mesophases of the D–A dyad and (right) the hexagonal lattice (blue lozenge) formed by undifferentiated columns (Reproduced from reference [63]); (c) Schematic representation of (left) the self-organization within the Col_{ob} mesophases of the D–A–D triad after annealing and (right) the oblique lattice (blue parallelogram) formed by intermingled distinct columns located at the nodes of distorted hexagonal lattices (blue dashed distorted hexagon) (Reproduced from reference [63]); (d) Graphical representation of the thermal behavior of PBI based oligomers (**28a-c**).

Cammidge *et al.* reported triphenylene-perylene-triphenylene triads separated by the spacers of 2, 4, 6 and 10 methylene units (Figure 1.25).[62] Hexahexyloxy triphenylene connected through 2, 4 and 6 methylene units to central PBI unit turned to be crystalline, while the one with decamethylene spacer **28a** exhibited enantiotropic Col phase. Doping hexahexyloxytriphenylene, which exhibited a Col phase between 70-100 °C with 0.1% of mesogenic triad **28a** gives a Col phase below 76 °C with no separation of the trimer from its host matrix. This suggests that the trimer can act as a vehicle to introduce functional constituents into the columnar matrices of parent hexaalkoxy triphenylenes without any phase separation. No evidence was found for the charge transfer or other ground state interactions. The stability of the Col phase is likely to result from the favorably matched core-core separations. In this trimer, the luminescence of the central perylene core remains preserved, and the excitation spectrum clearly establishes that the excitation of the triphenylene leads to emission from the perylene. Lee *et al.* reported donor (D)- acceptor (A) diads (**28c**) and D-A-D triads (**28b**) where triphenylene and PBI units are connected covalently through flexible decycloxy spacers.[63] The diad **28c** self-assembles to form Col$_h$ phase while the triad **28b** self-assemble to form Col$_{ob}$ phase. Fluorescence and subpicosecond transient absorption measurements in films confirmed a complete quenching of the singlet excitons through a highly effective photo-induced charge transfer process. On photo-excitation, they observed that photo-induced charge transfer states, that are formed in both dimer and trimer in a time of about 0.2–0.3 ps. The charge recombination process was significantly slower with characteristic time constants ranging between 150 and 360 ps. Such features are important for the development of organic photovoltaics.

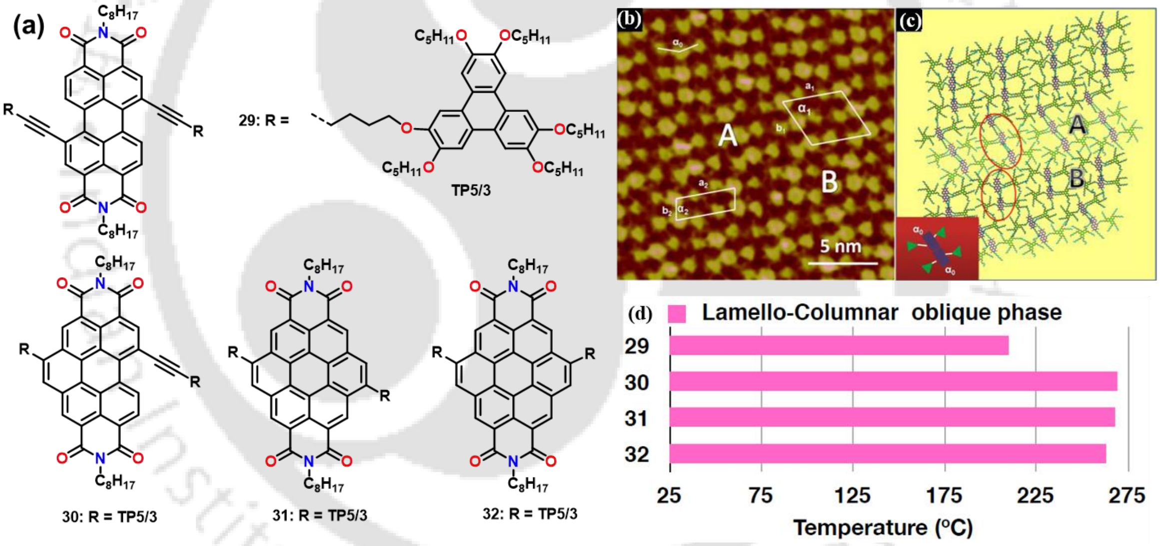

Figure 1.26. (a) Molecular structures of Perylene/core extended PBI-triphenylene oligomers (**29-32**); (b) High-resolution STM image (20 nm×20 nm) of **29**. I_{set}=349.1 pA, V_{bias}=599.1 mV; (c) Illustrated molecular model for (b). In domains A, **29** molecules from three neighbouring rows associate with close contacts between PI segments, while only two rows in domains B. Sub-image in (c) shows a schematic illustration of the molecular packing in domains B; (Reproduced from reference [64] with the permission of Wiley VCH) (d) Graphical representation of the thermal behavior of PBI based oligomers (**29-32**).

Zhao *et al.* reported D-A-D triads, where the donor triphenylene units are connected to central PBI (**29**), benzo[*ghi*]perylenediimide (**30**), or coronene bisimide acceptor units (**31**, **32**) (Figure 1.26).[64] All D–A–D triads self-organize to form a lamello-columnar oblique mesophase. This LC phase shows a well-separated donor-acceptor (D–A) heterojunction organization, resulting from efficient molecular self-sorting. Here, the donor and acceptor molecules form separated conducting pathways for the movement of holes and electrons. The electron mobility was found to be about 15 times higher than the hole mobility due to the co-existence of two different inter-locked and immiscible carrier pathways. Such developments are exciting from the viewpoint of organic solar cells.

Asha *et al.* reported dimeric molecules of PBIs connected through central alkyl spacer where the length was varied from methylene to dodecamethylene spacer.[65] Here, the PBI unit with an ethyl hexyl chain at one end and pentadecyl phenol at the other end. The phenolic -OH was connected through the polymethylene spacer to form the dimers. The differential packing allowed by the spacer parity (odd and even number central methylene segments) led to an odd-even oscillation of the melting points and associated enthalpies. Higher values were observed for the even-spacered dimers. This odd-even effect was prominent for the spacers up to heptamethylene spacer from the lower end after which this effect was reduced. Lower homologues with methylene and trimethylene spacers exhibited inclinations to stabilize smectic phases while most of the dimers with longer spacers exhibited tendencies to show high temperature nematic phases.

1.3.3.9. Perylene based polymeric liquid crystals

Unsymmetrical PBI **11b** was crystalline, while its side chain polymeric analogue, poly (perylene bisimide acrylate) (**33**) exhibited a 2D lamellocolumnar LC phase over a wide temperature including RT (Figure 1.27).[66] The structure of the side-chain polymer in the thin film state in response to different thermal treatments were investigated by GIWAXS. The results connect well with a previously observed difference in electron mobilities. Though the columnar stacking in the polymer is disordered, the LC nature of **33** allowed its magnetic alignment in addition to the alignment by thermal annealing. A high mobility was observed in OFET experiments utilizing annealed films in comparison to spin-coated films. Such a polymeric LC compound brings the benefits of molecular order and easy processability, together with the film forming properties exhibited by polymeric materials. Thelakkat *et al.* reported two highly soluble LC side chain polymers, namely poly (perylene diester imide acrylate) (**34**) and poly (perylene diester benzimidazole acrylate) (**35**). Polymer **34** exhibited short-range mesophase in comparison to polymer **35**. Polymer **35** shown n-type semiconducting properties with an electron mobility of 3.2×10^{-4} cm^2 V^{-1} s^{-1}, whereas polymer **34** exhibited a p-type behavior with a hole mobility of 1.5×10^{-4} cm^2 V^{-1} s^{-1}, as determined from SCLC measurements.[67] Feng *et al.* reported a novel polysiloxane-modified PEI **36** (Figure 1.27).[68] This polymeric LC exhibited a Col$_h$ phase with a thermal range of 27 °C to 61 °C. Further, this polysiloxane modified perylene derivative exhibited good thermal stability, excellent optical and hydrophobic behavior.

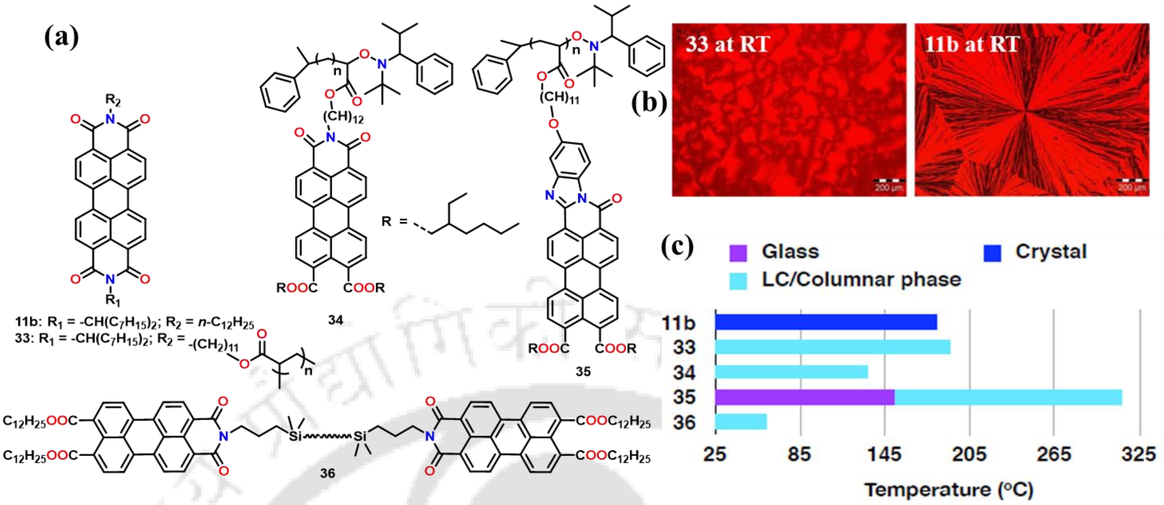

Figure 1.27. (a) Molecular structures of **11b** and perylene based polymers (**33-36**); (b) POM images of **33** and **11b (**Reproduced from reference [66] with the permission of American Chemical Society); (c) Graphical representation of the thermal behavior of PBI based oligomers (**11b** and polymers **33-36**).

1.4. Applications of perylene derivatives in organic electronics

1.4.1. Perylene based LCs for organic solar cells

Schmidt-Mende *et al.* first utilized a perylene dye in conjunction with a Col LC, hexaphenyl-substituted hexabenzocoronene to fabricate an organic photovoltaic device.[69] Thin films formed by a mixture of these two components led to the vertically separated perylene and HBC assemblies, with a large interfacial surface area. When these films are integrated into diode structures, they exhibited an excellent photovoltaic response (external quantum efficiencies > 34 % and power efficiencies of up to ≈2% near 490 nm). This is the result of the efficient photoinduced charge transfer between the HBC and perylene, as well as the effective charge transport through the vertically segregated perylene and HBC π-systems. It is interesting to note that the PBI (**3a**) utilized, was a crystalline material. Kim *et al.* fabricated an OSC, where the LC **3b** acts as an electron acceptor and a zinc phthalocyanine (ZnPc) acts as a donor.[70] The cell performance under illumination was studied with respect to the change in the thickness of organic layers. A cell comprising 25 nm thick organic layers exhibited a short circuit photocurrent (I_{SC}) of 1.6 mA/cm^2, an open circuit photovoltage (V_{OC}) of 0.6 V, and a fill factor (FF) of 0.4 with a white Xe light illumination (wavelength P400 nm, intensity:100 mW/cm^2) (Figure 1.28).

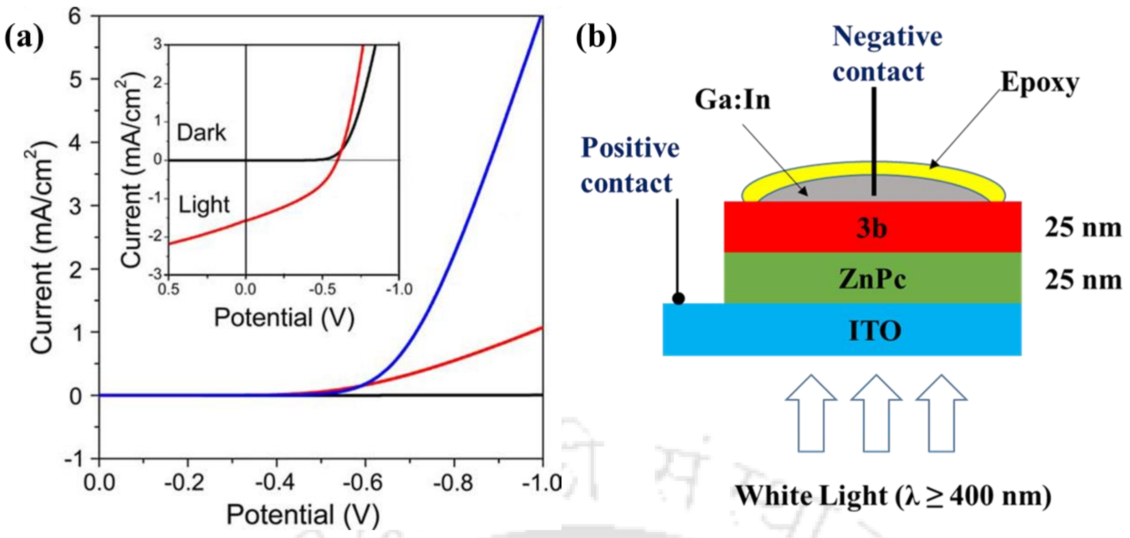

Figure 1.28. (a) Dark current potential characteristics for ZnPc:**3b** films of 100:100 nm (black trace); 50:50 nm (red trace); and 25:25 nm (blue trace); Inset: Current-potential characteristics for the device with configuration as ITO/ZnPc (25 nm)/**3b** (25 nm)/Ga; (b) device configuration (Reproduced from reference [70] with permission of Elsevier.

Bock *et al.* recently reported a homeotropically aligned bilayer heterojunction formed by a pair of DLCs, which were aligned from their isotropic liquid state[71] (Figure 1.29b). These materials exhibited properties like selective solubility, a low degree of miscibility, adjusted transition temperatures and RT Col$_h$ phase. The two materials they used was a PTE (regioisomeric mixture, acceptor**, PT-1**) and a pyrene tetraester (donor, **PY-2**). This represented the first proof of principle of an organic heterojunction that is based on two oriented columnar LC layers.

Kelly *et al.* reported four different PBI based acceptors (**A1-A4**) with similar electron affinities but different LC phases. These compounds were blended with nematic LC electron-donors comprising a fluorene-thiophene structure (**D1** and **D2**) to form single layer OSCs (Figure 1.29a). Superior results were attained when the nematic donor (**D2**) is mixed with an amorphous acceptor (**A1** or **A4**). This gave a supercooled nematic glass at RT. Atomic force microscopy images revealed the phase separation on a nanometer scale of varying domain sizes. The OSC devices with the **A1** exhibited the best performance. A power conversion efficiencies (PCE) of 0.9 % was found for the **D1, A1** combination. The morphologies were correlated with the device performances and PCEs of 0.9% was achieved at 470 nm. **D2** is a polymerizable mesogen that can be polymerized thermally or by UV light irradiation to give a polymer network. The polymerization of an electron–donating reactive mesogen mixed with a non polymerizable PBI acceptor was expected to change the extent of phase separation and also the composition of the phase-separated domains.[45a] They have also demonstrated the solution-processed bilayer OSCs, where the lower electron-donating layer was photopolymerised prior to the deposition of a perylene-based acceptor layer on top. It was interesting to note that the performance of the polymerized and non-polymerized blended devices was similar; dispelling fears that photopolymerization might lead to photodegradation.[45b] They have also utilized a LC composite approach to preparing a nematic LC polymer network from **D2** with a porous surface and electron-donating properties. This is infilled with an electron-acceptor **A1** to form a bilayer device. The diffused interface created allowed the excitons to dissociate and move towards the respective electrodes[72]. The monochromatic power conversion efficiency was seen to vary between 0.8% and 0.3% with input irradiance.

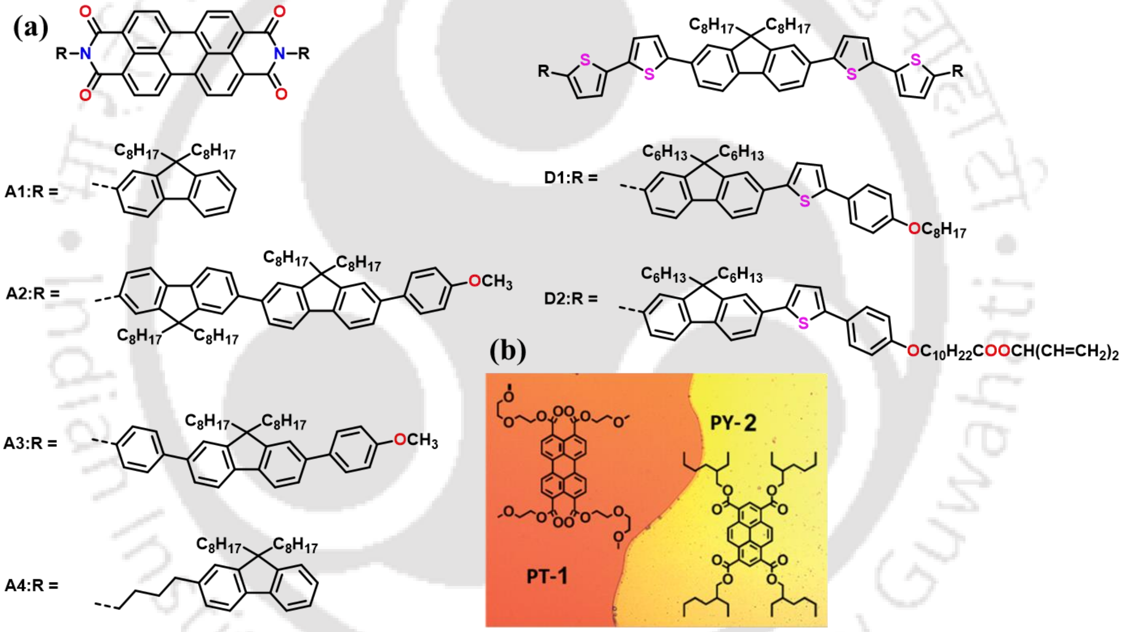

Figure 1.29. (a) Molecular structures of perylene based oligomers (**D1-D2** and **A1-A4**); (b) Schematic structure of the two compounds **PT-1** (where only one of the two regioisomers is sketched) and **PY-2**. Their low degree of miscibility is shown by a contact preparation between coverslip and glass slide in the isotropic liquid phase (Reproduced from reference [71] with permission of American Chemical Society).

1.4.2. Perylene based LCs for organic light emitting diodes

Bock *et al.* reported a red light emitting diode from perylene tetraester **T-2** with a very simple device structure with single emissive layer (Figure 1.30). They prepared LEDs consisting of a ITO coated glass anode layer, one to three organic layers, and an aluminum cathode layer. All the PTEs **T1-T6**, **T-8** and **TEH** exhibited a strong electroluminescence even in a single layer device. A single-layer light-emitting diode of **T-2** with a film thickness of about 50 nm, exhibited an emission above a threshold of 7-8V, and the maximum luminance was 100 cd cm^{-2} at a voltage of 20 V. They have also shown that color-tuning towards white emission, the color stability, and the lifetime of the device may be improved by simultaneous co-deposition of several kinds of emissive materials based on triphenylene or pyrene derivatives of very similar electro- and photochemical stability.[13] They have also reported red light emitting diodes with a device configuration of ITO-coated glass/triphenylene hexaether/PTE/aluminum.[73]

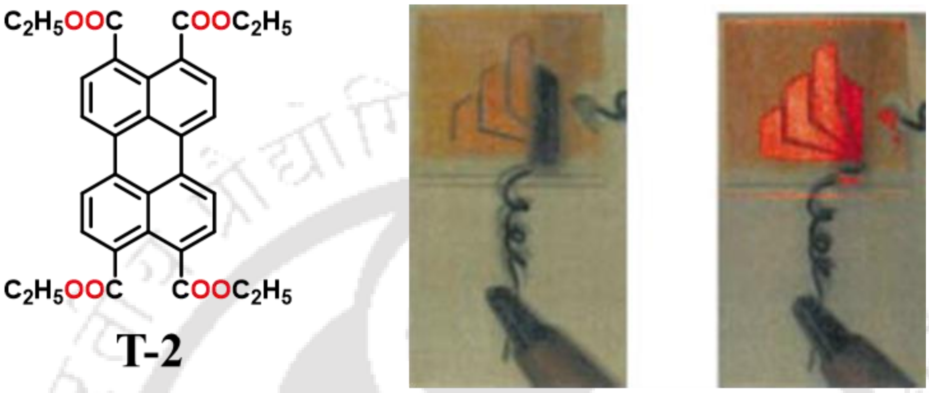

T-2

Figure 1.30. Photograph of a light-emitting diode that contains compound **T-2**, without (left) and with (right) applied voltage (Reproduced from reference [13] with permission of WILEY VCH).

Bechtold *et al.* compared the electrical responses of Col LC **15** in a device that was fabricated either by spin coating or by thermal evaporation.[74] For the spin-coated film, homeotropic alignment was obtained by thermal annealing, which was correlated with the enhanced charge carrier mobility. For the evaporated films, such alignment could not be obtained by thermal annealing. However, a three orders higher degree of rectification and more luminance was accomplished, even without annealing. The electrical response was similar to the response of the aligned spin-coated film. Spin coated thermally aligned film shows a good homeotropic alignment, while the thermally evaporated film exhibited planar alignment suitable for OFETs. However, the superior molecular packing in the evaporated films can be utilized either in OLEDs[75] or OFETs, showing an acceptable electrical response.

1.4.3. Perylene based LCs for organic field effect transistors

Organic field effect transistors form an important component for emerging low-cost, large-area and flexible electronics. There number of organic p-type semiconductors with hole mobilities more than 0.5 cm^2 V^{-1} s^{-1} are available in large numbers and they are utilized in OFETs with outstanding performance under ambient conditions, but n-type counterparts are still scarce. Among the investigated n-type organic semiconductors, the ones based on naphthalene tetracarboxylic bismides (NBIs) and PBIs appear so far as the most encouraging ones. This is because of their performance under ambient conditions is comparable with that of the p-type materials used in OFETs.[76] Figure 2d and 2e depict usually used OFET device configurations. Most of the OFETs are tested with bottom gate top contact device structure and the Col LC should be aligned with an 'edge on' or planar orientation with respect to the substrate to exhibit good charge carrier mobility (Figure 2f). The research on n-type semiconductors is lagging behind due to the more difficult electron injection, because of the large energy barrier between the Fermi level of the source and drain contacts and the LUMO level of the n-type semiconductor. Additionally, a poor stability of radical anions and their vulnerability towards water and oxygen have been deliberated as a great hurdle. PBIs usually exhibit low lying LUMO levels, good stability and reversible oxidation and reduction cycles in cyclic voltammetry. Further, various possibilities of substitution in the core provide opportunities to tailor the HOMO and LUMO energy levels. The advantage of PBIs is that their electronic properties can be tuned by core substitution, while their solubility can be tuned by the variation of alkyl groups at imide position. Usually, these PBI derivatives are fabricated into device either by vacuum deposition or solution processing technique. The best performing devices are achieved by vacuum deposition, but this is very slow and time-consuming method. It requires the optimization of several parameters to control the type of growth and the crystallinity of the organic semiconductor. Several factors like substrate temperature, surface modification by SAM and deposition rate are considered in achieving a superior deposition on the substrate. Solution processing methods like spin coating or ink jet printing are promising from the viewpoint of cost and large scale manufacturing. But in spite of their fast and cheap processing ability they suffer from the formation of less ordered amorphous films in comparison to those obtained by vacuum deposition. They often require additional steps like thermal annealing to obtain stable devices with good performance.

Facchetti and coworkers reported several dialkyl PBIs substituted with two cyano groups in the core. In particular, one cyano-substituted PBI with -$CH_2C_3F_7$ chain at imide position shown a better performance and stability (inert condition: 0.15 $cm^2 V^{-1} s^{-1}$; after 20 days in the air: 0.08 $cm^2 V^{-1} s^{-1}$).[77] Though the present focus is on the area of solution processed devices, it is directed toward the rational synthesis of polymeric materials, which offer improved morphological stability over a long period. Thelakkat *et al.* reported LC diblock copolymers of polystyrene and poly-(perylene acrylate), which were spin coated to prepare the devices. However, the mobilities were found to be low.[78] Marder *et al.* described a solution-processable, narrow band gap, high-mobility, alternating copolymer of PBI and dithienothiophene building blocks. They have shown broad absorption through the visible region of the absorption spectra extending into the near-IR region.[79] Device measurements show that alternating D-A polymers of this type are encouraging electron-transport materials for n-channel OFETs, promising sensitizers and electron-transport materials for all-polymer OSCs. Recently, Troshin *et al.* did a systematic study on a series of dialkyl PBIs by varying the chain length from *n*-butyl to *n*-dodecyl.[80] The deposition of these PBIs was carried out by thermal evaporation in a vacuum. They found that the increase in the chain length improves both the charge carrier mobility and the on-off current ratio of the OFETs.[81] The branched chain derivative with 2-ethylhexyl side chains exhibited inferior performance in comparison to the isomeric PBI with *n*-octyl chains. This may be due to the increased disorder in the case of branched chain derivative. Although some of these compounds are liquid crystalline in nature, nothing has been mentioned on the effect of liquid crystalline organization on the device efficiency in many of the reports. The larger homologues like terrylene and quaterrylene bisimides are yet to find a foothold in OTFTs with comparable performance as their smaller homologues like NBI or PBI. However as mentioned earlier, terrylene tetracarboxdiimide (**18**), is known to form crystalline, large and highly ordered domains, with molecules arranged in an edge-on orientation.[33] For more information on PBI based OFETs, the readers are advised to refer reviews by Würthner[76] and Marder.[81]

1.5. Conclusion and perspective

Recent 10-15 years noticed the huge interest in the study of perylene based materials apart from their usefulness as dyes for a variety of applications. With the several positions to substitute/modify, they provide a synthetically tunable platform to engineer the physical and chemical properties as well as their supramolecular self-assembly, through various noncovalent interactions. Considering their versatility and applications, it is not surprising that many scholarly reviews are written, which concentrated either on the perylene bisimides or on their higher homologues (rylenes). Self-assembly of perylene derivatives into various liquid crystalline phases has to be explored and there is need to understand the structure-property correlation. In addition to more common LC perylene bisimides, other derivatives like perylene tetraesters, perylene diesters with several variations like the type of flexible chains, the change in the central aromatic core *etc*. has to be considered. In the present introductory chapter, we have limited ourselves from the discussion on the lyotropic LCs based on perylene derivatives, because of the space constraint. Thus, the present literarture survey is more focused on the thermotropic LC behavior of these compounds. At the end, a brief account on the application of LC/ non-LC perylene derivatives in organic electronic devices like OSCs, OLEDs and OFETs has been discussed.

From the vast literature survey, what we can understand is that several novel molecular designs have been tried to achieve the liquid crystalline self-assembly and many derivatives have shown liquid crystalline behavior at room temperature. Most of the studies have been done on perylene bismides. Other classes like perylene tetraesters, perylene diester imides, *bay*-extended and core elongated perylene derivatives are not yet explored to their fullest extent. The *ortho*-substituted LC perylene derivatives are not yet realized to the best of our knowledge. Incorporation of the heterocyclic units in the perylene molecular structure and functionalization of the peripheral chains are other options to tune the electronic and self-assembly behavior. All these derivatives should be explored as they provide many options to engineer the optoelectronic properties of the perylene derivatives. Further studies need to be done on the alignment of LC perylene derivatives in the device configuration. The control of the alignment with respect to the electrodes and their interactions with other materials used in the device has to be analyzed to make them applicable in devices. Perylene bisimides are promising n-type semiconductors and possibly the best soluble alternatives to fullerenes that are utilized in organic solar cells. High thermal and photochemical stabilities, better electronic and optical properties, tailorability to achieve the supramolecular self-assembly in bulk and solution processability definitely make these materials more advantageous than fullerenes. Chemists need to be in constant touch with the device scientists to make a material that meets all the requirements in a particular device. Slowly but with firm steps, perylene derivatives are entering into OLEDs and OFETs. Imbuing liquid crystallinity may enhance their applicability due to the improved processability. In the near future, we hope that such interdisciplinary work will result in a highly ordered self-assembled organic semiconductor material, that is solution processable and stable in ambient conditions may replace the present day inorganic semiconductors.

1.6. References

1. C. Tschierske, *Angew. Chem. Int. Ed.*, 2013, **52**, 8828-8878.
2. T. Wöhrle, I. Wurzbach, J. Kirres, A. Kostidou, N. Kapernaum, J. Litterscheidt, J. C. Haenle, P. Staffeld, A. Baro and F. Giesselmann, *Chem. Rev.*, 2015, **116**, 1139-1241.
3. Q. Li, *Self-organized organic semiconductors: from materials to device applications*, John Wiley & Sons, 2011.
4. a) M. Funahashi and J. I. Hanna, *Adv. Mater.*, 2005, **17**, 594-598; b) A. Van de Craats, J. Warman, A. Fechtenkötter, J. D. Brand, M. Harbison and K. Müllen, *Adv. Mater.*, 1999, **11**, 1469-1472; c) K. L. Woon, M. P. Aldred, P. Vlachos, G. H. Mehl, T. Stirner, S. M. Kelly and M. O'Neill, *Chem. Mater.*, 2006, **18**, 2311-2317.
5. a) F. Würthner, *Chem. Commun.*, 2004, 1564-1579; b) F. Würthner, C. R. Saha-Möller, B. Fimmel, S. Ogi, P. Leowanawat and D. Schmidt, *Chem. Rev.*, 2015, **116**, 962-1052.
6. a) J. Wu, W. Pisula and K. Müllen, *Chem. Rev.*, 2007, **107**, 718-747; b) R. J. Bushby and K. Kawata, *Liq. Cryst.*, 2011, **38**, 1415-1426.
7. M. J. Hollamby and T. Nakanishi, *J. Mater. Chem. C*, 2013, **1**, 6178-6183.
8. C. Li and H. Wonneberger, *Adv. Mater.*, 2012, **24**, 613-636.
9. a) V. Marcon, D. W. Breiby, W. Pisula, J. Dahl, J. Kirkpatrick, S. Patwardhan, F. Grozema and D. Andrienko, *J. Am. Chem. Soc.*, 2009, **131**, 11426-11432; b) N. Tasios, C. Grigoriadis, M. R. Hansen, H. Wonneberger, C. Li, H. W. Spiess, K. Müllen and G. Floudas, *J. Am. Chem. Soc.*, 2010, **132**, 7478-7487; c) E. Di Donato, R. P. Fornari, S. Di Motta, Y. Li, Z. Wang and F. Negri, *J. Phys. Chem. B*, 2010, **114**, 5327-5334.
10. a) Y. Jiang, L. Lu, M. Yang, C. Zhan, Z. Xie, F. Verpoort and S. Xiao, *Polymer Chemistry*, 2013, **4**, 5612-5620; b) M. C. Scharber, D. Mühlbacher, M. Koppe, P. Denk, C. Waldauf, A. J. Heeger and C. J. Brabec, *Adv. Mater.*, 2006, **18**, 789-794.
11. S. Benning, H.-S. Kitzerow, H. Bock and M.-F. Achard, *Liq. Cryst.*, 2000, **27**, 901-906.
12. I. Seguy, P. Jolinat, P. Destruel, R. Mamy, H. Allouchi, C. Courseille, M. Cotrait and H. Bock, *ChemPhysChem*, 2001, **2**, 448-452.
13. T. Hassheider, S. A. Benning, H. S. Kitzerow, M. F. Achard and H. Bock, *Angew. Chem. Int. Ed.*, 2001, **40**, 2060-2063.
14. L. Wang, Q. Cui, X.-F. Chen, Y. Li, Z.-Q. Li, D. Wang and H. Yang, *Aust. J. Chem.*, 2013, **66**, 692-700.
15. S. K. Gupta, S. Setia, S. Sidiq, M. Gupta, S. Kumar and S. K. Pal, *RSC Advances*, 2013, **3**, 12060-12065.
16. J. Kelber, M. F. Achard, B. Garreau-de Bonneval and H. Bock, *Chem. Eur. J.*, 2011, **17**, 8145-8155.
17. J. Kelber, M. F. Achard, F. Durola and H. Bock, *Angew. Chem. Int. Ed.*, 2012, **51**, 5200-5203.
18. J. Vollbrecht, H. Bock, C. Wiebeler, S. Schumacher and H. Kitzerow, *Chem. Eur. J.*, 2014, **20**, 12026-12031.
19. A. Adamski, A. Biadasz, K. Domieracki, M. A. Kojdecki, D. Paukszta, D. Uryzaj and E. Wolarz, *Liq. Cryst.*, 2015, **42**, 456-462.
20. J. Kelber, H. Bock, O. Thiebaut, E. Grelet and H. Langhals, *Eur. J. Org. Chem.*, 2011, 707-712.
21. H. Langhals, S. Sprenger and M. T. Brandherm, *Eur. J. Org. Chem.*, 1995, 481-486.

22. A. Wicklein, M.-A. Muth and M. Thelakkat, *J. Mater. Chem.*, 2010, **20**, 8646-8652.
23. R. A. Cormier and B. A. Gregg, *J. Phys. Chem. B*, 1997, **101**, 11004-11006.
24. R. A. Cormier and B. A. Gregg, *Chem. Mater.*, 1998, **10**, 1309-1319.
25. B. A. Gregg and R. A. Cormier, *J. Phys. Chem. B*, 1998, **102**, 9952-9957.
26. S.-G. Liu, G. Sui, R. A. Cormier, R. M. Leblanc and B. A. Gregg, *J. Phys. Chem. B*, 2002, **106**, 1307-1315.
27. K. Balakrishnan, A. Datar, T. Naddo, J. Huang, R. Oitker, M. Yen, J. Zhao and L. Zang, *J. Am. Chem. Soc.*, 2006, **128**, 7390-7398.
28. a) A. Wicklein, A. Lang, M. Muth and M. Thelakkat, *J. Am. Chem. Soc.*, 2009, **131**, 14442-14453; b) D. M. Pereira de Oliveira Santos, M. G. Belarmino Cabral, A. Bentaleb, R. Cristiano, H. Gallardo, F. Durola and H. Bock, *Chem. Eur. J.*, 2016, **22**, 7389-7393; c) J. A. Quintana, J. M. Villalvilla, A. de la Peña, J. L. Segura and M. A. Díaz-García, *J. Phys. Chem. C*, 2014, **118**, 26577-26583; d) N. Mizoshita, T. Tani and S. Inagaki, *Chem. Commun.*, 2012, **48**, 10772-10774.
29. K. Bijak, H. Janeczek, M. Grucela-Zajac and E. Schab-Balcerzak, *Opt. Mater.*, 2013, **35**, 1042-1050.
30. J. van Herrikhuyzen, A. Syamakumari, A. P. Schenning and E. Meijer, *J. Am. Chem. Soc.*, 2004, **126**, 10021-10027.
31. M. G. Debije, Z. Chen, J. Piris, R. B. Neder, M. M. Watson, K. Müllen and F. Würthner, *J. Mater. Chem.*, 2005, **15**, 1270-1276.
32. J. Y. Kim, I. J. Chung, Y. C. Kim and J.-W. Yu, *Chem. Phys. Lett.*, 2004, **398**, 367-371.
33. F. Nolde, W. Pisula, S. Müller, C. Kohl and K. Müllen, *Chem. Mater.*, 2006, **18**, 3715-3725.
34. M. G. B. Cabral, D. M. Pereira de Oliveira Santos, A. Bentaleb, E. A. Hillard, R. Cristiano, H. Gallardo, F. Durola and H. Bock, *Chem. Eur. J.*, 2016, **22**, 8043-8047.
35. B. Gao, D. Xia, L. Zhang, Q. Bai, L. Bai, T. Yang and X. Ba, *J. Mater. Chem.*, 2011, **21**, 15975-15980.
36. Y. Zhang, H. Wang, Y. Xiao, L. Wang, D. Shi and C. Cheng, *ACS Appl. Mater. Interfaces*, 2013, **5**, 11093-11100.
37. Y. Xu, S. Leng, C. Xue, R. Sun, J. Pan, J. Ford and S. Jin, *Angew. Chem. Int. Ed.*, 2007, **46**, 3896-3899.
38. a) M. Funahashi and A. Sonoda, *Org. Electron.*, 2012, **13**, 1633-1640; b) M. Funahashi and A. Sonoda, *J. Mater. Chem.*, 2012, **22**, 25190-25197.
39. M. Funahashi, N. Takeuchi and A. Sonoda, *RSC Advances*, 2016, **6**, 18703-18710.
40. M. Funahashi and A. Sonoda, *Phys. Chem. Chem. Phys.*, 2014, **16**, 7754-7763.
41. a) M. Funahashi, M. Yamaoka, K. Takenami and A. Sonoda, *J. Mater. Chem. C*, 2013, **1**, 7872-7878; b) K. Takenami, S. Uemura and M. Funahashi, *RSC Advances*, 2016, **6**, 5474-5484.
42. F. Würthner, C. Thalacker, S. Diele and C. Tschierske, *Chem. Eur. J.*, 2001, **7**, 2245-2253.
43. Z. Chen, U. Baumeister, C. Tschierske and F. Würthner, *Chem. Eur. J.*, 2007, **13**, 450-465.
44. V. Dehm, Z. Chen, U. Baumeister, P. Prins, L. D. Siebbeles and F. Würthner, *Org. Lett.*, 2007, **9**, 1085-1088.
45. a) C. Lei, M. S. Al Khalifah, M. O'Neill, M. P. Aldred, S. P. Kitney, P. Vlachos and S. M. Kelly, 2008 *International Society for Optics and Photonics*; p 705214.; b) M. S. AlKhalifah, C. Lei, S. A. Myers, M. O’Neill, S. P. Kitney and S. M. Kelly, *Liq. Cryst.*, 2014, **41**, 402-417.

46. Z. An, J. Yu, S. C. Jones, S. Barlow, S. Yoo, B. Domercq, P. Prins, L. D. Siebbeles, B. Kippelen and S. Marder, *Adv. Mater.*, 2005, **17**, 2580-2583.
47. V. Percec, M. Peterca, T. Tadjiev, X. Zeng, G. Ungar, P. Leowanawat, E. Aqad, M. R. Imam, B. M. Rosen and U. Akbey, *J. Am. Chem. Soc.*, 2011, **133**, 12197-12219.
48. D. Sahoo, M. Peterca, E. Aqad, B. E. Partridge, P. A. Heiney, R. Graf, H. W. Spiess, X. Zeng and V. Percec, *J. Am. Chem. Soc.*, 2016, **138**, 14798-14807.
49. B. Jancy and S. Asha, *Chem. Mater.*, 2007, **20**, 169-181.
50. a) L. Meng, Q. Wu, F. Yang and H. Guo, *New J. Chem.*, 2015, **39**, 72-76; b) M. Zhu, H. Guo, F. Yang and Z. Wang, *Dyes Pigm.*, 2016, **133**, 387-394.
51. G. A. Bhavsar and S. Asha, *Chem. Eur. J.*, 2011, **17**, 12646-12658.
52. A. Wicklein, P. Kohn, L. Ghazaryan, T. Thurn-Albrecht and M. Thelakkat, *Chem. Commun.*, 2010, **46**, 2328-2330.
53. M.-A. Muth, G. Gupta, A. Wicklein, M. Carrasco-Orozco, T. Thurn-Albrecht and M. Thelakkat, *J. Phys. Chem. C*, 2013, **118**, 92-102.
54. M. Funahashi and A. Sonoda, *Dalton Trans.*, 2013, **42**, 15987-15994.
55. T. Zhang, D. Sun, X. Ren, L. Liu, G. Wen, Z. Ren, H. Li and S. Yan, *Soft Matter*, 2013, **9**, 10739-10745.
56. M. M. Safont-Sempere, V. Stepanenko, M. Lehmann and F. Würthner, *J. Mater. Chem.*, 2011, **21**, 7201-7209.
57. S. Herbst, B. Soberats, P. Leowanawat, M. Lehmann and F. Würthner, *Angew. Chem. Int. Ed.*, 2017, **56**, 2162-2165.
58. T. Yang, J. Pu, J. Zhang and W. Wang, *J. Org. chem.*, 2013, **78**, 4857-4866.
59. I. Bala, S. P. Gupta, J. De and S. K. Pal, *Chem. Eur. J.*, 2017, **23**, 12767-12778.
60. X. Kong, L. Xia, H. Zhang, S. Dai, C. Yu, Z. Liu, L. Mu, G. Wang and Z. He, *RSC Advances*, 2017, **7**, 17030-17037.
61. M. Zhu, H. Guo, F. Yang and Z. Wang, *RSC Advances*, 2017, **7**, 4320-4328.
62. X. Kong, Z. He, Y. Zhang, L. Mu, C. Liang, B. Chen, X. Jing and A. N. Cammidge, *Org. Lett.*, 2011, **13**, 764-767.
63. K. J. Lee, J. H. Woo, Y. Xiao, E. Kim, L. M. Mazur, D. Kreher, A.-J. Attias, K. Matczyszyn, M. Samoc and B. Heinrich, *RSC Advances*, 2016, **6**, 57811-57819.
64. K. Q. Zhao, L. L. An, X. B. Zhang, W. H. Yu, P. Hu, B. Q. Wang, J. Xu, Q. D. Zeng, H. Monobe and Y. Shimizu, *Chem. Eur. J.*, 2015, **21**, 10379-10390.
65. K. Prajitha and S. Asha, *New J. Chem.*, 2016, **40**, 8471-8478.
66. P. Kohn, L. Ghazaryan, G. Gupta, M. Sommer, A. e. Wicklein, M. Thelakkat and T. Thurn-Albrecht, *Macromolecules*, 2012, **45**, 5676-5683.
67. M. A. Muth, M. Carrasco-Orozco and M. Thelakkat, *Adv. Funct. Mater.*, 2011, **21**, 4510-4518.
68. Y. Liang, H. Wang, D. Wang, H. Liu and S. Feng, *Dyes Pigm.*, 2012, **95**, 260-267.
69. L. Schmidt-Mende, A. Fechtenkötter, K. Müllen, E. Moons, R. H. Friend and J. MacKenzie, *Science*, 2001, **293**, 1119-1122.
70. J. Y. Kim and A. J. Bard, *Chem. Phys. Lett.*, 2004, **383**, 11-15.
71. O. Thiebaut, H. Bock and E. Grelet, *J. Am. Chem. Soc.*, 2010, **132**, 6886-6887.
72. W. C. Tsoi, M. O'Neill, M. P. Aldred, S. P. Kitney, P. Vlachos and S. M. Kelly, *Chem. Mater.*, 2007, **19**, 5475-5484.
73. I. Seguy, P. Jolinat, P. Destruel, J. Farenc, R. Mamy, H. Bock, J. Ip and T. Nguyen, *J. Appl. Phys.*, 2001, **89**, 5442-5448.
74. J. Eccher, W. Zajaczkowski, G. r. C. Faria, H. Bock, H. Von Seggern, W. Pisula and I. H. Bechtold, *ACS Appl. Mater. Interfaces*, 2015, **7**, 16374-16381.
75. J. Eccher, G. r. C. Faria, H. Bock, H. Von Seggern and I. H. Bechtold, *ACS Appl. Mater. Interfaces*, 2013, **5**, 11935-11943.

76. F. Würthner and M. Stolte, *Chem. Commun.*, 2011, **47**, 5109-5115.
77. C. Piliego, D. Jarzab, G. Gigli, Z. Chen, A. Facchetti and M. A. Loi, *Adv. Mater.*, 2009, **21**, 1573-1576.
78. S. Hüttner, M. Sommer and M. Thelakkat, *Appl. Phys. Lett.*, 2008, **92**, 71.
79. X. Zhan, Z. a. Tan, B. Domercq, Z. An, X. Zhang, S. Barlow, Y. Li, D. Zhu, B. Kippelen and S. R. Marder, *J. Am. Chem. Soc.*, 2007, **129**, 7246-7247.
80. A. V. Mumyatov, L. I. Leshanskaya, D. V. Anokhin, N. N. Dremova and P. A. Troshin, *Mendeleev Commun.*, 2014, **5**, 306-307.
81. C. Huang, S. Barlow and S. R. Marder, *J. Org. Chem.*, 2011, **76**, 2386-2407.

Chapter 2

Bay-annulated Perylene tetratesters Stabilizing Columnar Mesophase

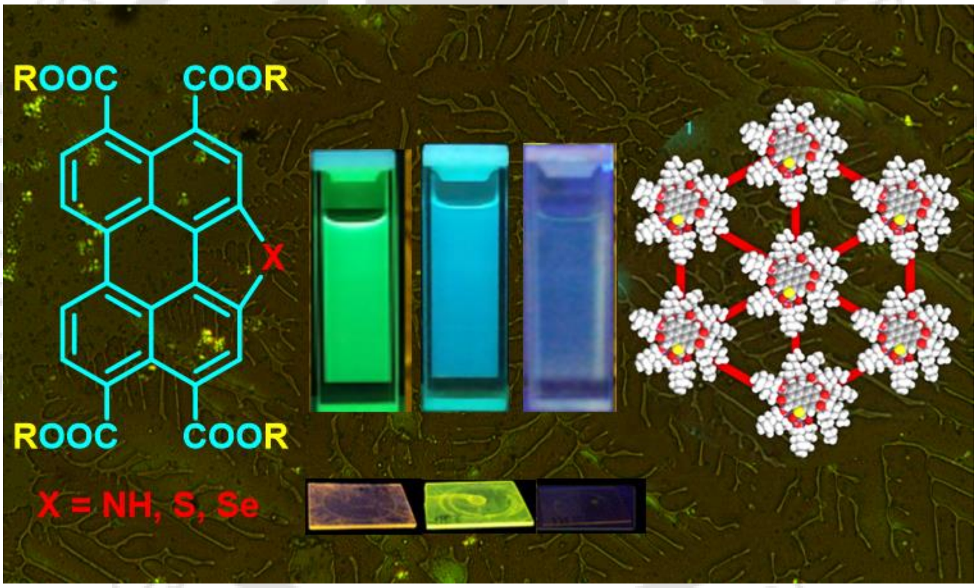

Results have been published in;

- *Soft Matter*, 2015, **11**, 3629-3636
- *Langmuir*, 2015, **31**, 8092-8100
- *ChemPhysChem*, 2016, **17**, 859-872

2.1. Introduction

In recent years, organic semiconductors rose to a prominent interdisciplinary research field and generated a great deal of interest in scientific community. In comparison to inorganic semiconducting materials, this class has the advantage of low cost synthesis and scale up feasibility. In addition, large area thin films required for the organic electronic devices like organic solar cells, organic light emissive displays, organic field effect transistors and sensors can be easily achieved through simple solution processing techniques.[1] Most of the organic semiconductors, whether they are based on small molecules or polymers, possess a common feature of large delocalized conjugated π-electron system. The ordered organization of these conjugated molecules would enhance the anisotropic charge carrier mobility across the molecules. There are different classes of materials explored in this direction *viz.* crystalline, amorphous and liquid crystalline. Crystalline materials exhibit high charge carrier mobility, while that of amorphous materials are low. In spite of the high charge carrier mobility values found in crystalline materials, there are many difficulties like the time and cost involved to obtain good quality crystals, lack of processability in the manufacturing of low cost, flexible large area devices, discourage their applicability. Any industry involved in this area prefers simple and cost effective techniques like spin coating, casting or printing at room temperature. Amorphous materials like polymers satisfy this condition, but because of the high structural disorder, they end up with poor charge carrier mobility values. Liquid crystalline materials exhibit intermediate charge carrier mobility between these two classes with a scope for the improvement by rational molecular design. In addition, they can be handled easily with respect to the issues like purity, reproducibility, and processability to produce homogeneous thin films. The high charge carrier mobility associated with this class is due to the self-healing of defects and self-organizing ability.[1] Smectic (Sm) and columnar (Col) liquid crystalline phases formed from several π-conjugated shape anisotropic molecules exhibited promising charge carrier mobility due to the inherent order provided by the self-organization. These one dimensional (1D) nanostructures provide an anisotropic conduction pathway to the charge carriers along the stacking.[2]

Perylene derivatives are much sought after class of organic semiconductors, as they are inexpensive, stable (thermally and photochemically) and easily functionalizable chromophores with high HOMO-LUMO gap, good absorption and emission characteristics.[3] In addition to the π-π interactions of the large aromatic core of perylene derivatives, there is a option to tailor their self-assembly by proper modification. Since perylene has twelve positions, which can be functionalized (four *peri*-positions, four *bay*-positions and four *ortho*-positions) with various substituents, their self-assembly and photophysical properties can be tuned.[4] Thus, with a proper design one can test them in the field of organic solar cells,[5] organic light emitting diodes,[6] and organic field effect transistors.[7]

Perylene bisimdes are well-known n-type (electron accepting) semiconductors and high performance pigments. Liquid crystalline (LC) perylene bisimides[8] were reported in 1997 and further modifications were reported by varying the amine part (aliphatic[8,9a] or aromatic[9b-g]) to be condensed with perylene bisanhydrides.[9] *Bay* substitution is good option to modify photophysical properties in perylene derivatives, but this severely affect the molecular planarity due to the resulting twist. As a result, there will be weaker interaction between the molecules which in turn disturbs the self-assembly.[10] Thus, alteration of physical properties without sacrificing molecular planarity by extending the aromatic core of perylene derivatives along the long axis or in the *bay* region is explored extensively. These modifications are known to have a bathochromic or a hypsochromic shift on the absorption spectra of the modified compounds.[11] Heteroatom annulation in the aromatic core is another strategy to modify the properties without compromising the molecular planarity. Wang *et al.* reported nitrogen, sulphur and selenium annulated perylene derivatives with interesting properties.[11,12] Introduction of nitrogen by *N*-annulation in the *bay* position can provide a possibility to improve the solubility and lower the transition temperature by means of *N*-alkylation.[13] Introduction of nitrogen in the molecular structure leads to hydrogen bonding with the neighboring molecule which may help in the self-assembly.[14] In recent times incorporation of chalcogen atoms in organic semiconductors is gaining importance.[15] Further, we were also interseted in the introduction of chalcogen atoms like sulphur and selenium in the aromatic system to tailor the electronic and self-assembly behavior. Sulphur and selenium are much widely explored chalcogen atoms in organic semiconductors in comparison to the other member tellurium. It is important to note that intermolecular interactions between chalcogen atoms (S···S and Se···Se interactions) also help in stabilizing the molecular self-assembly and hence improves 1D conductivity.[16] LC alkylperylene tetraesters are relatively less explored when compared to LC perylenebisimides.[17] Weakly electron withdrawing ester groups instead of imide groups at four *ortho*-positions make them somewhat less electron deficient in comparison to perylene bisimides. In addition, they exhibit high luminescence and hence can be ideal hole transporting emissive layers for OLEDs.[17a,b,18] They are also found to be useful in improving the open circuit voltage of solar cells due to higher LUMO and HOMO levels.[19] But the mesophase range of these compounds are not broad; in addition the chain length increment leads to a decrease in the mesophase width. This chapter includes the synthesis of a new class of discotic liquid crystals (DLCs) based on heteroatoms (N, S, Se) *bay*-annulated perylene tetraesters which exhibited an improved mesomorphic behavior. These compounds stabilized homeotropically aligning columnar hexagonal (Col_h) phase over a broad thermal range. Increased molecular planarity as well as the intermolecular hydrogen bonding assists the enhanced thermal range of mesophase in comparison to the parent tetraesters. We are giving an account of a structure-property relationship with parent perylene tetraesters (**5a-d**) and other heteroatom annulated perylene tetraesters (**1a-d**, **2a-d** and **3a-d**).

2.2. Results and Discussion

2.2.1. Synthesis and molecular structural characterization

The synthetic strategy used for the synthesis of the target DLCs is represented in Scheme 2.1. Perylene-3,4,9,10-tetracarboxylic bisanydride under basic condition hydrolyzed to obtain its tetracarboxylate salt. This salt was acidified with hydrochloric acid to make the pH ≈8-9, which, on refluxing in the presence of phase transfer catalyst and *n*-bromoalkanes provided the corresponding tetraesters **5a-d** in good yields.[17c-g] The tetraester were then subjected to controlled nitration mediated by sodium nitrite in presence of nitric acid to obtain the *bay*-substituted mono nitro derivatives **4a-d** in quantitative yields.[20] These *bay*-substituted nitro derivatives are key intermediates required to prepare *N*-, *S*- and *Se*-annulated perylene tetraesters. Refluxing the nitro derivatives **4a-d** in presence of excess triethyl phosphite yields *N*-annulated perylene tetraesters **1a-d** as bright yellow solids. Earlier for perylene bisimides *N*-annulation[12] was reported with Buchwald-Hartwig reaction.[21] However, our attempts to synthesize bis-*N*-annulated perylene tetraesters from dinitro derivatives were unsuccessful, as a result of the strain involved in the accommodating of two pyrrole rings in the *bay* region.

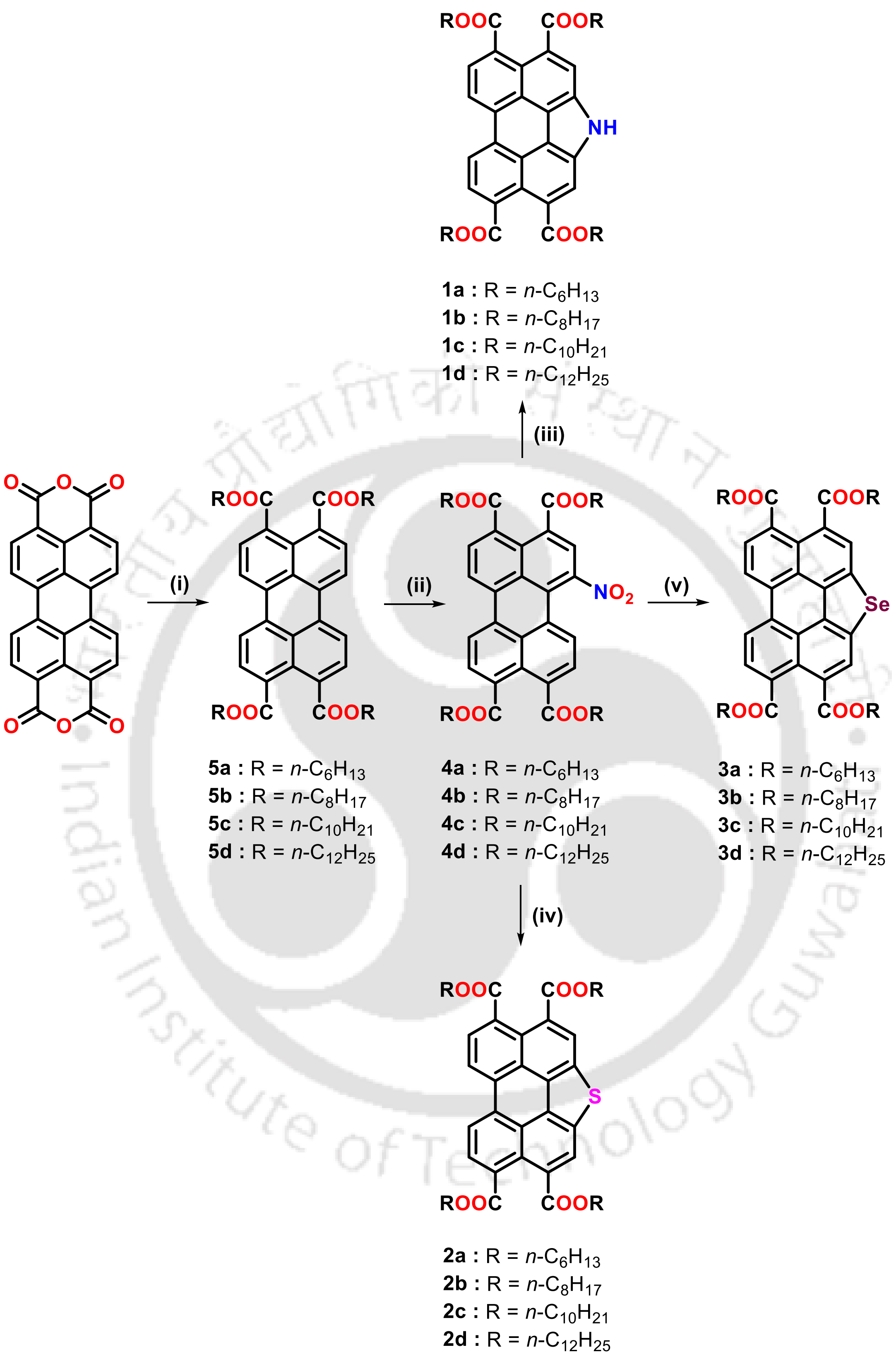

Scheme 2.1. Synthesis of heteroatom-annulated perylene tetraesters; Reagents and conditions: (i) KOH, H_2O,70 °C, 0.5 h, 1M HCl, Aliquat 336, KI, *n*-bromoalkanes, reflux, 12 h (69-75%); (ii) $NaNO_2$, DCM, HNO_3, 0 °C, 1h (80-90%); (iii) triethyl phosphite, 160 °C, reflux, 4 h, N_2 (55-60%); (iv) sulfur powder, anhyd. NMP, N_2, 70 °C, 0.5 h, 180 °C, 17 h (55-60%); (v) selenium powder, anhyd. NMP, N_2, 70 °C, 0.5 h,180 °C, 17 h (55-60%).

Heating of nitro derivatives with sulfur powder in *N*-methylpyrrolidone at 180 °C for 17 h yields *S*- annulated compounds **2a-d** as yellow-orange solid. Similarly, *Se*-annulation was also carried out by heating the nitro compounds with selenium powder in *N*-methylpyrrolidone at 180 °C for 17 h.[22] *Se*-annulated compounds **3a-d** were obtained as bright yellow to orange colored solids. Comparison ^{1}H NMR spectra of parent tetraester **5b** and annulated tetraesters **1b**, **2b** and **3b** (Figure 2.1), revealed that the aromatic region of parent tetraester **5b** showed a simple pattern with two doublets corresponding to the protons of *bay* position (H_b) and *ortho* position (H_c). On *N*-annulation molecular symmetry is broken and the protons near the *ortho* position to –NH- appear as a separate singlet (H_c). As a whole the aromatic signals moved upfield in comparison to parent tetraester. A sharp singlet appeared for –NH- at δ value of 9.5 ppm. Incorporation of S and Se by annulation

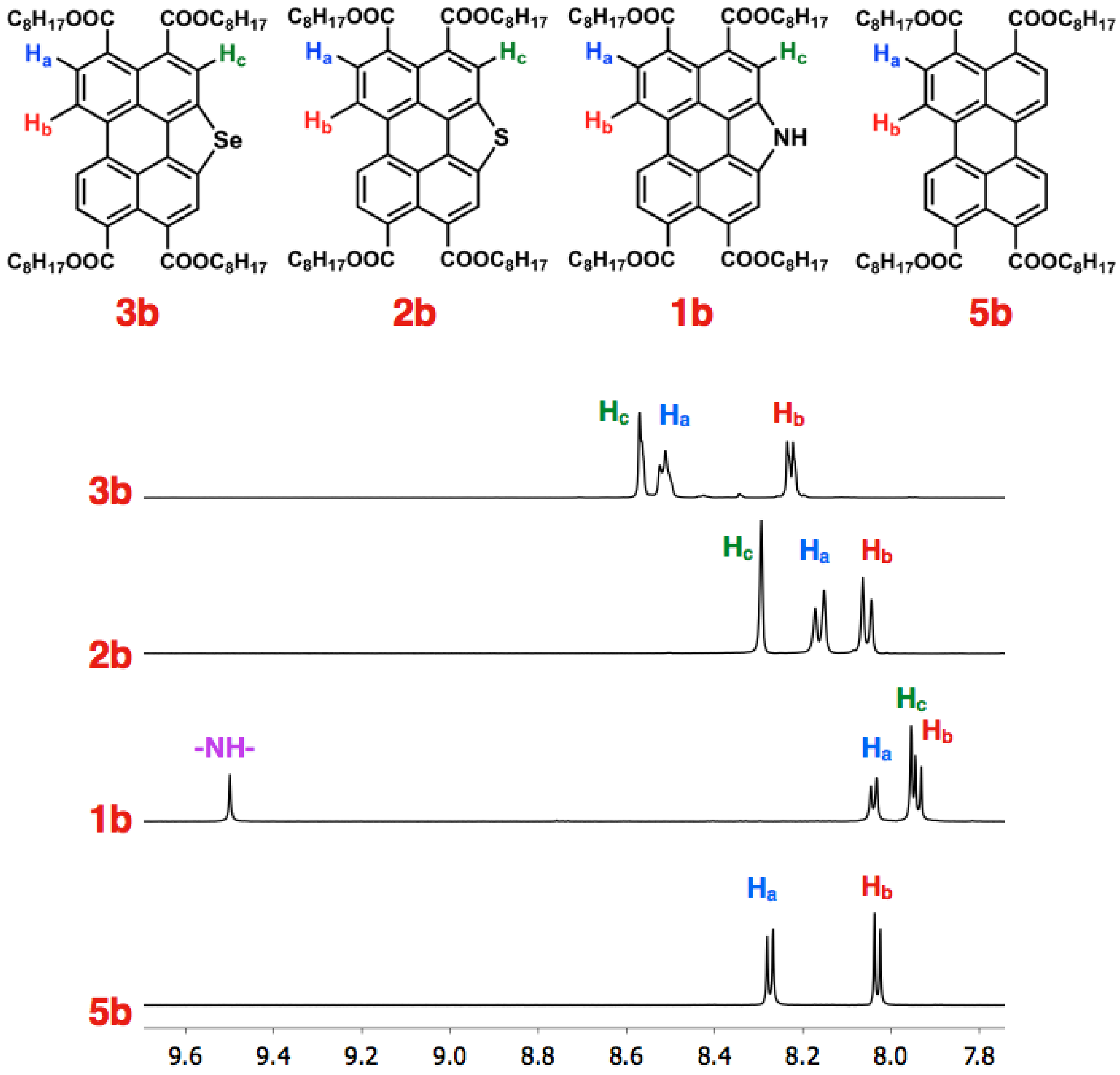

Figure 2.1. Overlay of the expanded portion of the ^{1}H NMR spectra ($CDCl_3$, 600 MHz) for compounds **1b**, **2b**, **3b** and **5b.**

progressively shifted the aromatic protons towards downfield region. In the case of *S*- and *Se*- annulated perylene tetraesters proton H_c appeared at high δ value of 8.30 and 8.54 ppm respectively. Thus the incorporation of nitrogen in the molecular structure make this system electron rich, while the incorporation of chalcogens like sulphur and selenium make the system electron deficient. Hence, in the case of compound **1b**, aromatic protons are shielded, while in the case of compound **2b** and **3b**, protons are deshielded. The molecular structural characterization was carried out with the help of ^{1}H, ^{13}C NMR, IR spectroscopy, HRMS and MALDI-TOF mass spectrometry.

2.2.2. Thermal behavior

The thermal behavior of *bay*-annulated perylene tetraesters (**1a-d**, **2a-d** and **3a-d**) was probed by polarizing optical microscope (POM), differential scanning calorimeter (DSC), thermogravimetric analysis (TGA) and X-ray diffraction (XRD) studies. The transitions from crystal to LC phase were at first investigated with POM observation of strong birefringence in combination with the fluidic nature of the compounds on heating. The phase transition temperatures and related enthalphy changes were determined by DSC. These values were in concurrence with peak temperatures obtained from POM studies. Correlating the optical texture observed in POM and the data obtained from XRD studies revealed the LC phase structure under investigation. The data obtained for the thermal behavior by these complementary studies are provided in Table 2.1 and Figure 2.16.

Representative compounds **1b**, **2b** and **3b** were choosen (each having octyloxy tail) from each series, are described in detail. All *bay*-annulated perylene tetraesters investigated, showed enantiotropic mesomorphic behavior over a broad thermal range except for compound **3d** which turned out to be crystalline.

2.2.2.1. *N*-annulated perylene tetraesters

Compound **1b** with *n*-octyloxy tails, exhibited a crystal to mesophase transition at a temperature of 92 °C with an enthalpy change of 478.6 kJ/mol (Table 2.1). The transition showed an increase in the birefringence with the sample turning to be fluidic and shearable. The mesophase was spanning over a broad thermal range of 200 degrees and converted into an isotropic liquid at 294 °C. This wide thermal range over 200 degrees points to a stronger core-core interactions among the adjacent molecules. On cooling the viscous isotropic liquid, large fern leaf like structures started appearing at 282 °C from the homeotropically aligned area with a dark field of fiew. Further decrease in temperature showed an increase in the birefringence, while the leaf-like structures extended into the existing dark homeotropic domains (Figure 2.2a). The mesophase to crystal transition was observed at 61 °C in DSC thermograms (Figure 2.3b), with a slight decrease in the birefringence and nonshearability as observed under POM.

Table 2.1. Phase transition temperatures[a] (°C) and corresponding enthalpies (kJ/mol) of DLCs.

Compound	**Phase sequence**	
	Heating	**Cooling**
1a	Cr 87.7 (231.8) Col$_h$ 334.7 (26.2) I	I 333.14 (5.8) Col$_h$ 42.12 (56.1) Cr
1b	Cr 91.6 (478.6) Cr 294 (26.6) I	I 281.9 (12.8) Col$_h$ 60.9 (179.9) Cr
1c	Cr 84.51 (565.1) Col$_h$ 273.1 (24.6) I	I 267 (14.6) Col$_h$ 65.3 (213.7) Cr
1d	Cr 103.2 (833) Col$_h$ 201.2 (15.1) I	I 198.8 (11.8) Col$_h$ 76.7 (768.5) Cr
2a	Cr$_1$ 55.1 (114.4) Cr$_2$ 77.4 (117.5) Col$_h$ 235.1 (24.6) I	I 233.1 (23.7) Col$_h$ 62.5 (122.1) Cr
2b	Cr$_1$ 65.1 (143) Cr$_2$ 81.5 (161.8) Col$_h$ 186.4 (23.3) I	I 185.1 (21.7) Col$_h$ 58.6 (164.2) Cr
2c	Cr$_1$ 69.8 (11.5) Cr$_2$ 79.3 (462.8) Col$_h$ 148.1 (19.8) I	I 146.4 (18) Col$_h$ 55.4 (196.4) Cr$_2$ 23.2 (200) Cr$_1$
2d	Cr$_1$ 63.1 (68.4) Cr$_2$ 85.4 (677) Col$_h$ 112.2 (11.9) I	I 109 (9.9) Col$_h$ 60.3 (232.9) Cr$_2$ 43.1 (85.3) Cr$_1$
3a	Cr$_1$ 63.4 (67.2) Cr$_2$ 69.4 (43.4) Col$_h$ 193.1 (2.3) I	I 187.4 (4.73) Col$_h$ 49.3 (104.9) Cr
3b	Cr$_1$ 58.3 (156.6) Cr$_2$ 76 (155.2) Col$_h$ 146.2 (4.1) I	I 140.8 (5.4) Col$_h$ 46.3 (158.4) Cr
3c	Cr$_1$ 77.4 (580.5) Col$_h$ 108.7 (6.6) I	I 103.2 (6.7) Col$_h$ 53.1 (170.5) Cr$_2$ 17.2 (188.7) Cr$_1$
3d	Cr$_1$ 79.8 (41.8) Cr$_2$ 85.1 (441.8) I	I 61 (589.2) Cr

[a]Peak temperatures in the DSC thermograms obtained during the first heating and cooling cycles at 5 °C/min; Col$_h$ = Columnar hexagonal phase, C$_r$ = Cr$_1$ = Cr$_2$ = Crystal, I = Isotropic

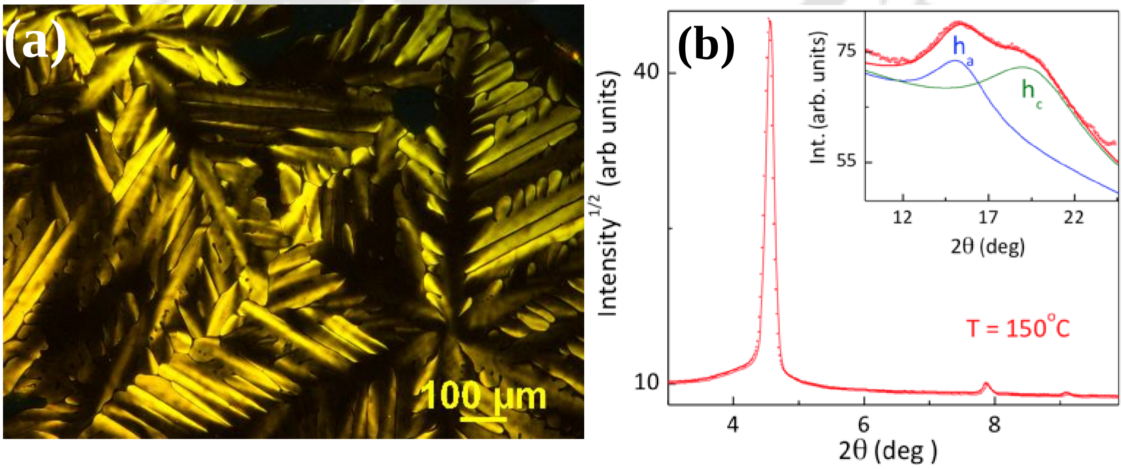

Figure 2.2. (a) Photomicrograph of compound **1b** at 276 °C on cooling from isotropic liquid state (under crossed polarizer); (b) XRD profiles depicting the intensity against 2θ obtained for the Col$_h$ phase of compound **1b**. (h$_a$ and h$_c$ mentioned in the figure corresponds to the stacking of peripheral alkyl chains and central cores respectively).

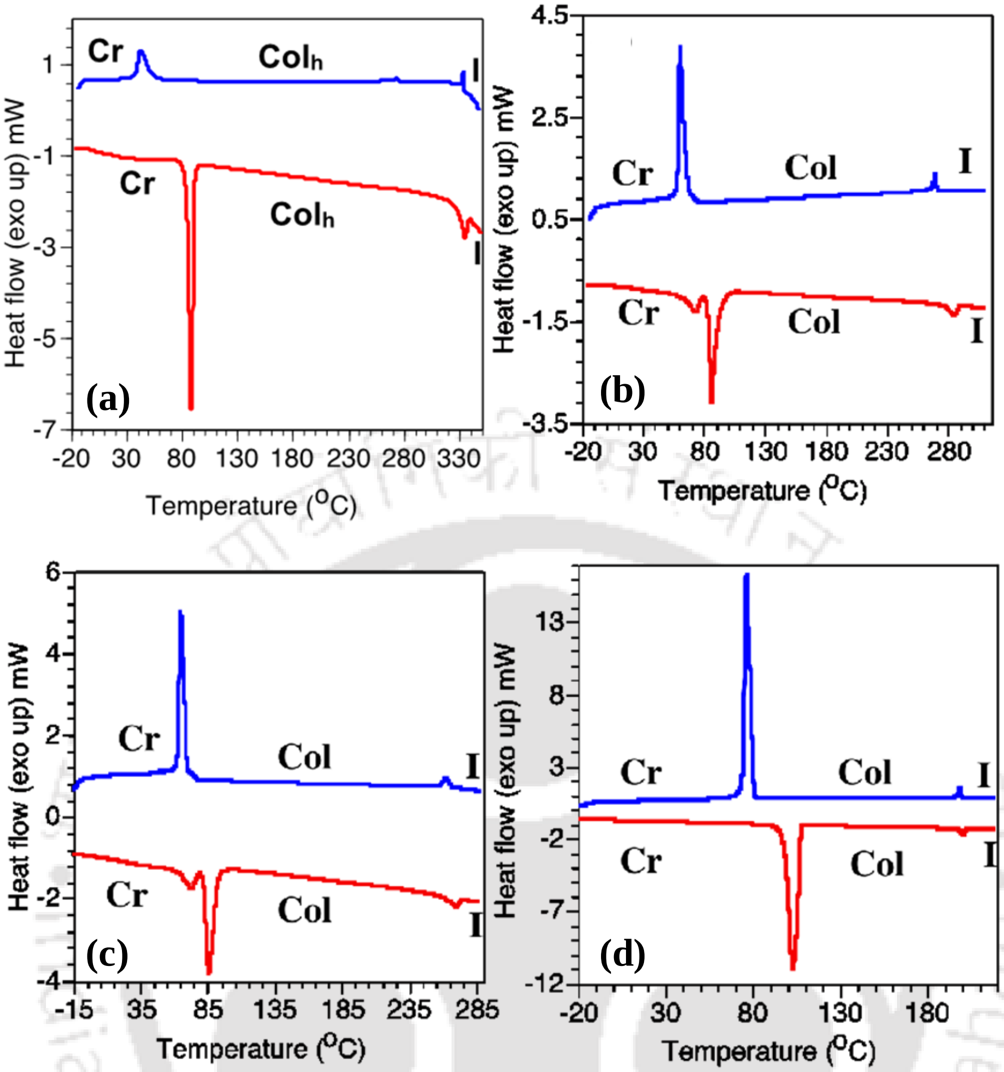

Figure 2.3. (a) DSC thermograms of discotics **1a**; (b) **1b**; (c) **1c** and (d) **1d** showing the second heating (red trace) and the first cooling (blue trace) scans at a scanning rate of 5.0 ˚C min^{-1}.

Powder XRD measurements were conducted to determine the symmetry of the thermodynamically stable Col phase formed by compound **1b** at temperature 150 °C. The results of indexation of the sharp reflections of these XRD profiles to lattices of Col phase are summarized in Table 2.2. The X-ray profile of the Col phase (Figure 2.2b) at 150 °C showed a strong reflection corresponding to a Bragg spacing *d* of 19.37 Å in the low-angle region, followed by reflections with *d* spacings of 11.19 Å, 9.69 Å in the middle-angle region ($7 < 2\theta < 10°$). These reflections are indexed into Miller indices 100, 110, 200 in the ratio $1:1/\sqrt{3}:1/\sqrt{4}$ and therefore these values are fit the lattice of Col$_h$ phase. There are two diffused peaks in the wide-angle region at 5.78 Å and 4.53 Å. The first of these peaks corresponds to the packing of alkyl chains and the second corresponds to core-core stacking. The calculated lattice parameter '*a*' was found to be 22.37 Å. This value is approximately 30% less than the diameter obtained from molecular model in it full trans

Table 2.2. Results of (*hkl*) indexation of XRD profiles of the compounds at a given temperature (T) of mesophases[a]

Compounds (D/Å)	**Phase (T/ºC)**	**d_{obs} (Å)**	**d_{cal} (Å)**	**Miller indices (*hkl*)**	**lattice parameters (Å), lattice area S (Å^2), molecular volume V (Å^3)**
1b (32.81)	150	19.37	19.37	100	a = 22.37
		11.19	11.19	110	c = 4.53
		9.69	9.69	200	S = 433.3
		5.78 (h_a)			V = 1965.3
		4.53 (h_c)		001	Z = 1.33
1c (37.63)	250	20.28	20.28	100	a = 23.42
		11.71	11.71	110	c = 4.73
		10.14	10.14	200	S = 475.0
		5.82 (h_a)			V = 2245.2
		4.73 (h_c)		001	Z =1.35
	227	20.13	20.13	100	a = 23.24
		11.62	11.62	110	c = 4.60
		10.07	10.07	200	S = 468.0
		5.79 (h_a)			V = 2154.8
		4.60 (h_c)		001	Z = 1.29
	100	19.60	19.61	100	a = 22.64
		11.33	11.32	110	c = 4.50
		9.81	9.80	200	S = 444
		5.76 (h_a)			V = 1996.8
		4.50 (h_c)		001	Z = 1.2
1d (42.39)	180	22.49	22.49	100	a = 25.97
		12.98	12.98	110	c = 4.65
		11.25	11.24	200	S = 584.0
		5.56 (h_a)			V = 2716.7
		4.65 (h_c)		001	Z =1.47
	150	22.33	22.34	100	a = 25.79
		12.90	12.90	110	c = 4.61
		11.17	11.17	200	S = 576.0
		5.54 (h_a)			V = 2658.4
		4.61 (h_c)		001	Z = 1.44

[a] The diameter (D) of the disc (estimated from Chem 3D Pro 8.0 molecular model software from Cambridge Soft). d_{obs}: spacing observed; d_{cal}: spacing calculated (deduced from the lattice parameters; a for Col$_h$ phase). The spacings marked h_a and h_c correspond to diffuse reflections in the wide-angle region arising from correlations between the alkyl chains and core regions, respectively. Z indicates the number of molecules per columnar slice of thickness h_c, estimated from the lattice area S and the volume V.

conformation. This can be ascribed to the folding of the flexible chains or possible interdigitation of flexible chains in the neighboring columns.[23] Homeotropically aligned Col phase between cross-polarizers typically do not show birefringence in POM, because in this case, the optical axis is in alignment with the columnar axis.[24] When the polarizers are parallel the texture shows hexagonal dendritic domains. Further cooling results in the developments of fern leaf like structures from homeotropically-aligned domains. The branching of the dendritic growth starts with a 60° angle to the main axis.[24g-i] The homeotropic alignment where the individual column is oriented perpendicular to the substrate is an essential feature, for the construction of organic photovoltaics.[24e] In homeotropic alignment, the first molecule aligns with its face-on to the substrate over which the incoming molecules stack one above the other regularly to give a highly ordered column of indefinite length (Figure 2.4c). Most of the reported DLCs do not attain homeotropic alignment over a large area, instead they align homogeneously (edge-on) or with partial homeotropic alignment. In the case of homogeneous or edge-on alignment the discotic molecules are stacked with their sides on the surface (Figure 2.4d), which is the requirement for the fabrication of field effect transistors. It has been reported that presence of heteroatoms at the periphery of the molecules help them to attain homeotropic alignment on polar surfaces.[24f] Thus, the *N*-annulation at the *bay* position helps in inducing homeotropic alignment. Further, there is a possibility that nitrogen atom of one molecule may form H-bonding with the hydrogen attached to the nitrogen of another molecule. This can happen with another molecule present in the next plane of the same column as shown in Figure 2.4a or it can also happen with another molecule from the other column in the same plane as shown in Figure 2.4b. This also supports the homeotropic alignment of columns over indefinite lengths. Thus, all the molecules investigated exhibited ordered $\mathrm{Col_h}$ phase over a wide range. These compounds have a propensity to align homeotropically on a glass surface on slow cooling. With the increase in the chain length the mesophase range was reduced because of the lowering of clearing temperatures. Similarly, Compound **1a** with *n*-hexyloxy tails, Compound **1c** with *n*-decyloxy tails and compound **1d** with *n*-dodecyloxy tails showed enantiotropic mesomorphic behavior over a broad thermal range (Figure 2.3, 2.5 and 2.6). When compared to the simple perylene tetraesters **5a-d** (**5a** and **5b** was enatiotropic, while **5c** and **5d** were monotropic LCs), the annulated compounds **1a-d** were enantiotropic with broad mesophase range (Figure 2.16). This enhanced mesophase stability is probably attributed to the presence of –NH- at the *bay* position.

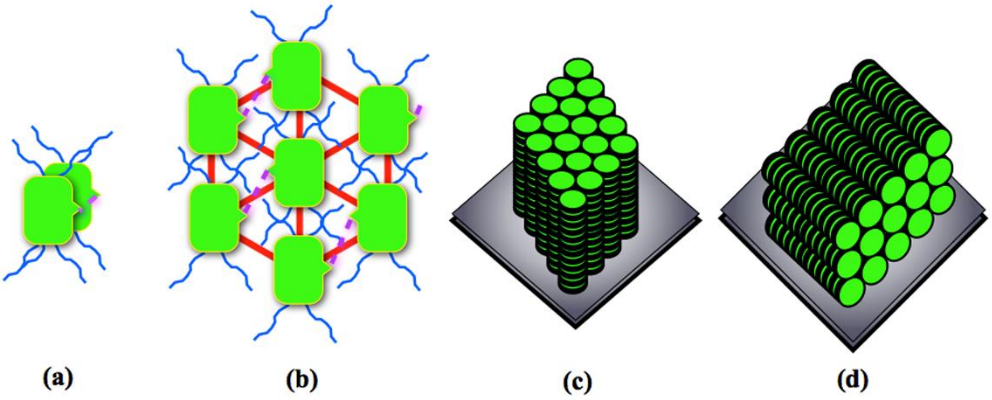

Figure 2.4. (a) Schematics showing the intermolecular H-bonding between the molecules from two different planes and (b) within a plane; Schematic representation of (c) homeotropic (face-on) alignment and (d) homogeneous (edge-on) alignment.

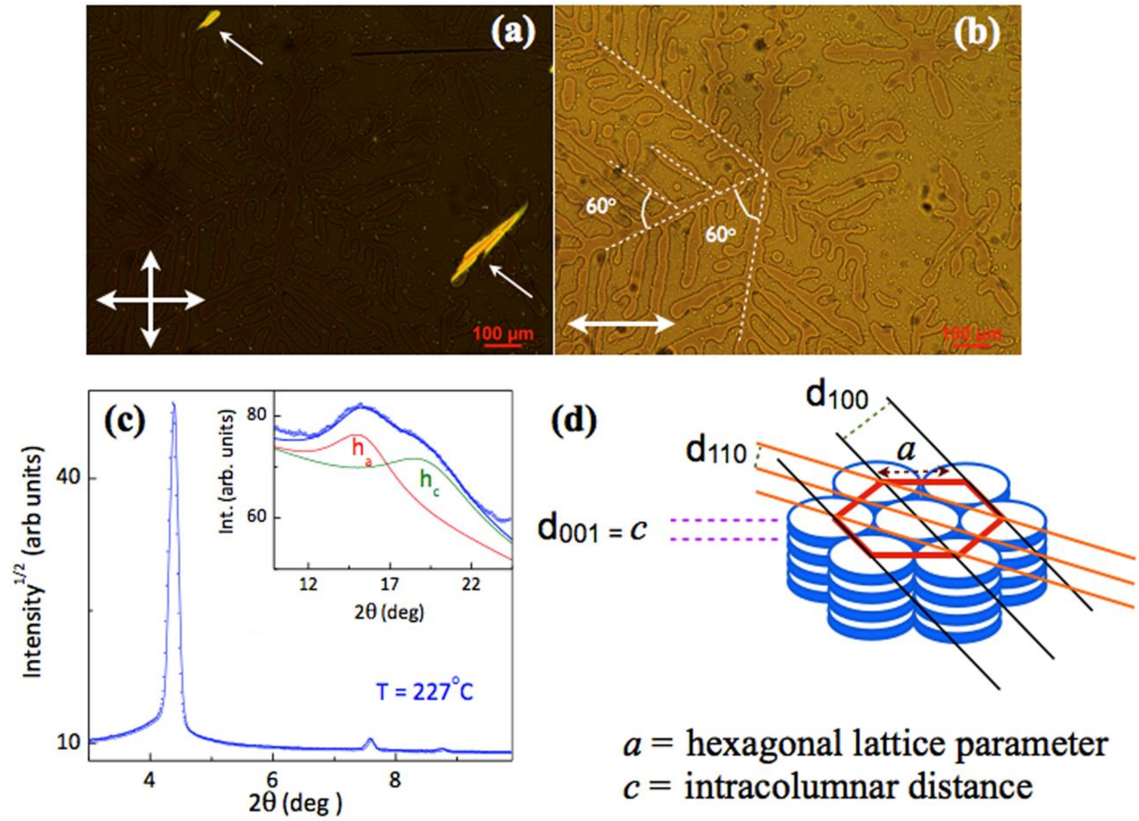

Figure 2.5. Microscopic images of compound **1c** placed between a glass slide and coverslip on slow cooling (1°C/min) from the isotropic phase at 195 °C (a) with crossed polarizers and (b) with parallel polarizers (dashed lines indicate the growth directions of the dendritic structures; the arrows indicate linear defects in the homeotropic alignment); (c) XRD profiles depicting the intensity against 2θ obtained for the Col_h phase of compound **1c** at 227 °C; (d) Schematic of hexagonal columnar (Col_h) phase.

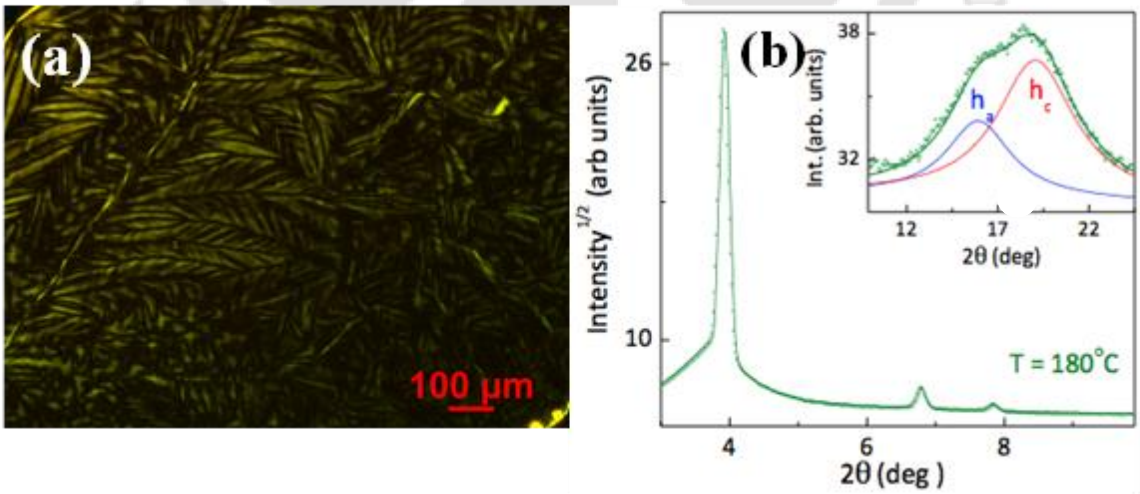

Figure 2.6. (a) Microphotographs of compound **1d** obtained on slow cooling (1°C/min) from the isotropic phase at 102 °C (under crossed polarizer); (b) XRD profiles depicting the intensity against 2θ obtained for the Col_h phase of compound **1d** at 180 °C.

Stability of the compounds has been determined by TGA and it has been shown that these compounds were stable up to at least 280 °C and complete decomposition occurs at ≈550 °C (Figure 2.7).

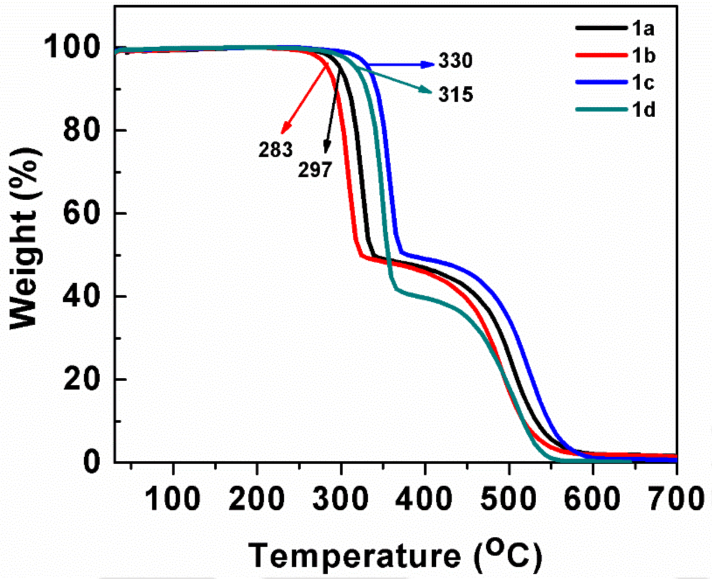

Figure 2.7. TGA plots of compound **1a-d** (heating rate of 10 °C/min, Nitrogen atmosphere).

2.2.2.2. *S*-annulated perylene tetraesters

S-annulated tetraesters also shows enantiotropic mesomorphic behavior over a broad thermal range (Figure 2.8). Compound **2b** with *n*-octyloxy tails, exhibited two crystal-crystal (Cr-Cr) transitions before going to form a mesophase at a temperature of ≈81 °C with an enthalpy change of 161.8 kJ/mol as noticed in DSC scans (Table 2.1). The transition was evidenced with the birefringent sample turning fluidic and shearable. The mesophase was spanning over a broad thermal range of ≈105 degrees with the isotropic temperture of 186 °C. The isotropic liquid on cooling at 5 °C/min rate showed the homeotropically aligned columnar phase with a dark field of view. The dark field of view under cross-polarizers is due the uniaxial alignment of optical and columnar axis (Figure 2.9a).[25] Same field of view through parallel polarizers shows hexagonal dendritic domains. The dendritic branching with a 60° angle to the main axis, which is a characteristic for hexagonal columnar (Col_h) phase. In the homeotropic configuration, the column axes lie perpendicular to the substrate, and thus gives the best geometry to visualize the symmetry of the underlying lattice on the substrate plane. The growth of the dendritic structure itself is due to the diffusion of the latent heat across the isotropic to columnar mesophase. Homeotropically aligned Col_h phase is an ideal feature required in the fabrication of organic solar cells.[26] Incorporation of heteroatoms at the peripheral region of the molecules known to enhance homeotropic (face-on) alignment over homogeneous alignment (edge-on) on polar surfaces (Figure 2.6c and d).[24b] In literature, it is also reported that discotic molecules where the core is connected to several flexible tails through ester groups have shown Col$_h$ phase with good homeotropic alignment.[2b,17b,27] This is probably due to the intercolumnar dipole-dipole interaction exerted by the ester carbonyl group forcing the efficient correlation of columns over a wide thermal range.[27c] Further cooling of the mesophase results in a fibrous texture. This change in the optical texture is only due to the minor change in the alignment of the columns and not due to any mesophase transition as evidenced from the XRD studies. Finally the mesophase was crystallized at 58.6 °C (*ΔH* = 164.2 kJ/mol, Figure 2.8b).

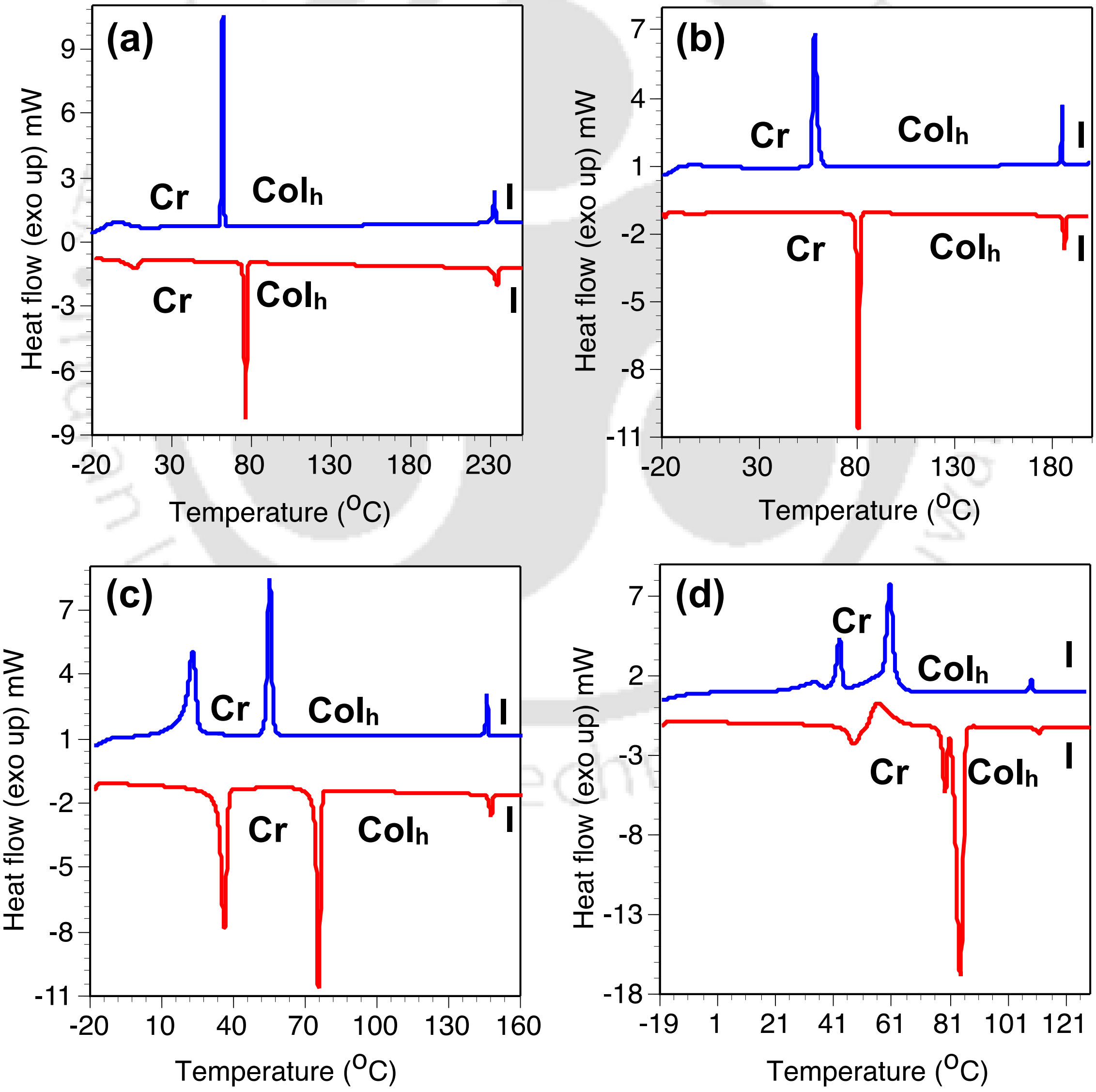

Figure 2.8. (a) DSC thermograms of discotics **2a**; (b) **2b**; (c) **2c** and (d) **2d** showing the second heating (red trace) and the first cooling (blue trace) scans at a scanning rate of 5.0 °C min^{-1}.

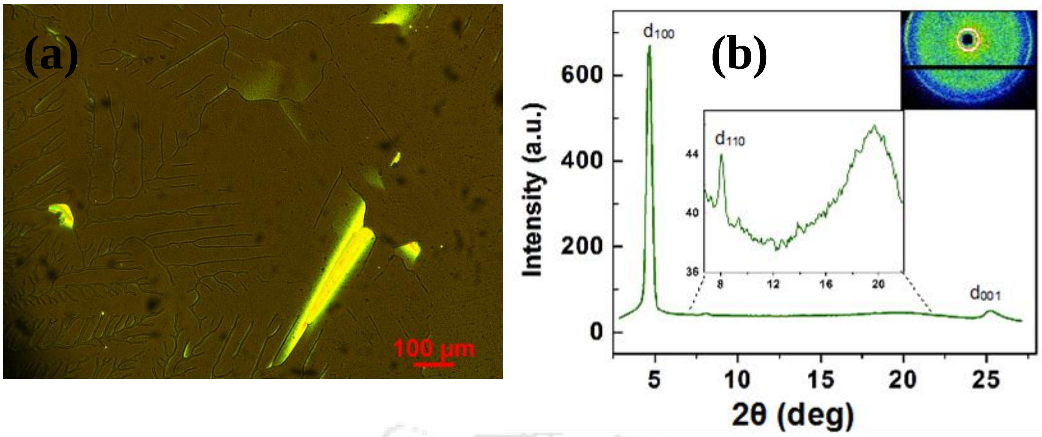

Figure 2.9. (a) Photomicrograph of compound **2b** at 185 °C on cooling from isotropic liquid state (under crossed polarizer); (b) XRD profile depicting the intensity against 2θ obtained for the $\mathrm{Col_h}$ phase of compound **2b** at 100 °C.

Powder XRD measurements were done at temperatures 100 °C to elucidate mesophase exhibited by compound **2b**. The data obtained on indexing the one-dimensional (1D) intensity *vs.* 2θ profile obtained for the Col phases are tabulated in Table 2.3. The XRD profile of the Col phase showed (Figure 2.9b) at 100 °C showed a sharp reflection corresponding to a Bragg spacing d_{100} at 17.33 Å and another corresponding to a Bragg spacing d_{110} at 10.10 Å. The *d* spacings corresponding to first two reflections are in the ratio of 1:0.58. Two diffused reflections were found at wide-angle region, one at 4.48 Å and the other at 3.54 Å. First diffused reflection corresponds to the ordering of alkyl chains, while the second diffused reflection corresponds to the ordered packing of rigid cores. All these features along with the optical textural patterns confirm that the Col phase is having a hexagonal symmetry. From the value of d_{100} one calculate the hexagonal cell parameter '*a*' using the formula $a = d_{100}/\mathrm{Cos}\ 30$ or $2/\sqrt{3} \times d_{100}$; and in this case, the value of '*a*' is found to be 20.01 Å. The value of lattice parameter '*a*' calculated was found to be 27% less, when compared to the diameter obtained from molecular modeling software (32.84 Å). The observed decrease in the value of lattice parameter can be ascribed to the flexible chain folding or their interdigitation in the neighboring columns.[23a,b] The columnar slice thickness is given by core-core stacking distance h_c, which is 3.54 Å. This is also denoted as the lattice parameter '*c*' for the $\mathrm{Col_h}$ phase. The number of molecules '*Z*' filling a unit cell of height $h_c = 3.54$ Å can be calculated from the relation $Z = \delta \times N_A \times V_{\text{unit cell}}/M$. For organic materials density δ is generally assumed as 1 g/cm^3, molecular mass *M* for **2b** is 907.26 g/mol and N_A is Avogadro's number. Volume of the hexagonal unit cell is given by the relation: $V_{\text{unit cell}} = S \times h_c$, where *S* is lattice area, which is calculated using the formula $S = a^2 \times \sin 60$. After substituting all the values thus obtained (Table 2.3), the number of molecules filling the columnar slice *i.e.* Z is found to be 0.96. This means each stratum in the Col phase is made up of a single molecule, and packed in the columns with an intracolumnar distance 3.53 Å.

Table 2.3. Results of (*hkl*) indexation of XRD profiles of the compounds at a given temperature (T) of mesophases[a]

Compounds (*D*/Å)	**Phase (T/°C)**	d_{obs} **(Å)**	d_{cal} **(Å)**	**Miller indices (*hkl*)**	**lattice parameters (Å), lattice area S (Å²), molecular volume V (Å³)**
2a (27.38)	200	17.29 10.02 4.46 (h_a) 3.55 (h_c)	17.29 10.03	100 110 001	a = 19.97 c = 3.55 S = 345.1897 V = 1225.42 Z = 0.93
	100	17.33 10.10 4.48 (h_a) 3.54 (h_c)	17.33 10.05	100 110 001	a = 20.01 c = 3.54 S = 346.7906 V =1227.64 Z = 0.93
2b (32.84)	100	18.81 10.97 4.49 (h_a) 3.53 (h_c)	18.81 10.91	100 110 001	a = 21.72 c = 3.53 S = 408.5513 V = 1442.1861 Z = 0.96
2c (37.38)	95	20.5 11.79 10.17 4.56 (h_a) 3.54 (h_c)	20.50 11.89 10.25	100 110 200 001	a = 23.67 c = 3.54 S = 485.2637 V = 1717.8355 Z = 1.02
2d (41.85)	90	21.52 12.52 10.85 4.56 (h_a) 3.49 (h_c)	21.52 12.48 10.76	100 110 200 001	a = 24.85 c = 3.49 S = 617.4819 V = 1866.2942 Z = 0.99

[a]The diameter (D) of the disc (estimated from Chem 3D Pro 8.0 molecular model software from Cambridge Soft). d_{obs}: spacing observed; d_{cal}: spacing calculated (deduced from the lattice parameters; a for Col$_h$ phase; c is height of the unit cell). The spacings marked h_a and h_c correspond to diffuse reflections in the wide-angle region arising from correlations between the alkyl chains and core regions, respectively. Z indicates the number of molecules per columnar slice of thickness h_c estimated from the lattice area S and the volume V.

Other homologues of this series *i.e.* compounds **2a**, **2c** and **2d** exhibited enantiotropic hexagonal columnar phase with the characteristic optical texture and corresponding XRD profile (Figure 2.10a, 2.11a and c). The mesophase range decreased on going from lower homologue **2a** to higher homologue **2d**. Thus, the increase in the peripheral chain length leads to a lowering of clearing temperatures. TGA analysis showed that these compounds were stable up to ≈300 °C and complete decomposition occured at ≈550 °C (Figure 2.12).

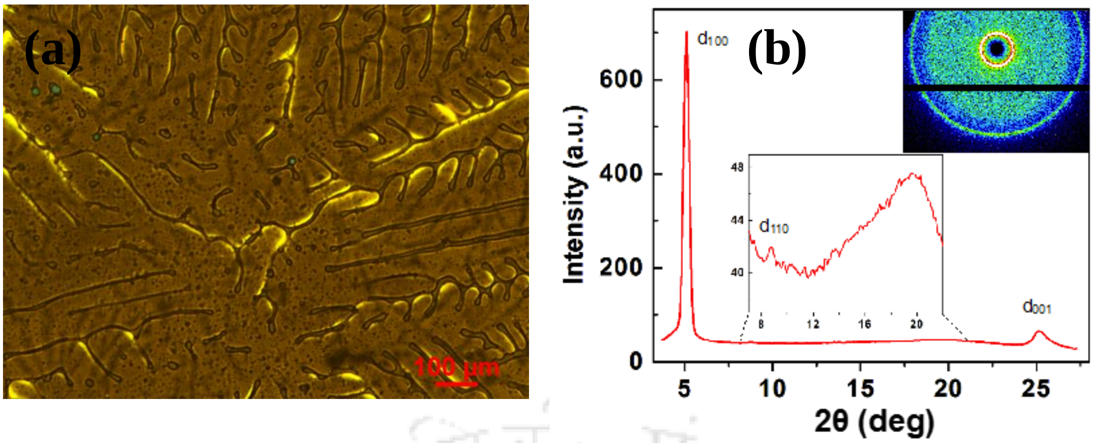

Figure 2.10. (a) Photomicrograph of compound **2a** at 232 °C on cooling from isotropic liquid state (under crossed polarizer); (b) XRD profile depicting the intensity against 2*θ* obtained for the Col$_h$ phase of compound **2a** at 100 °C.

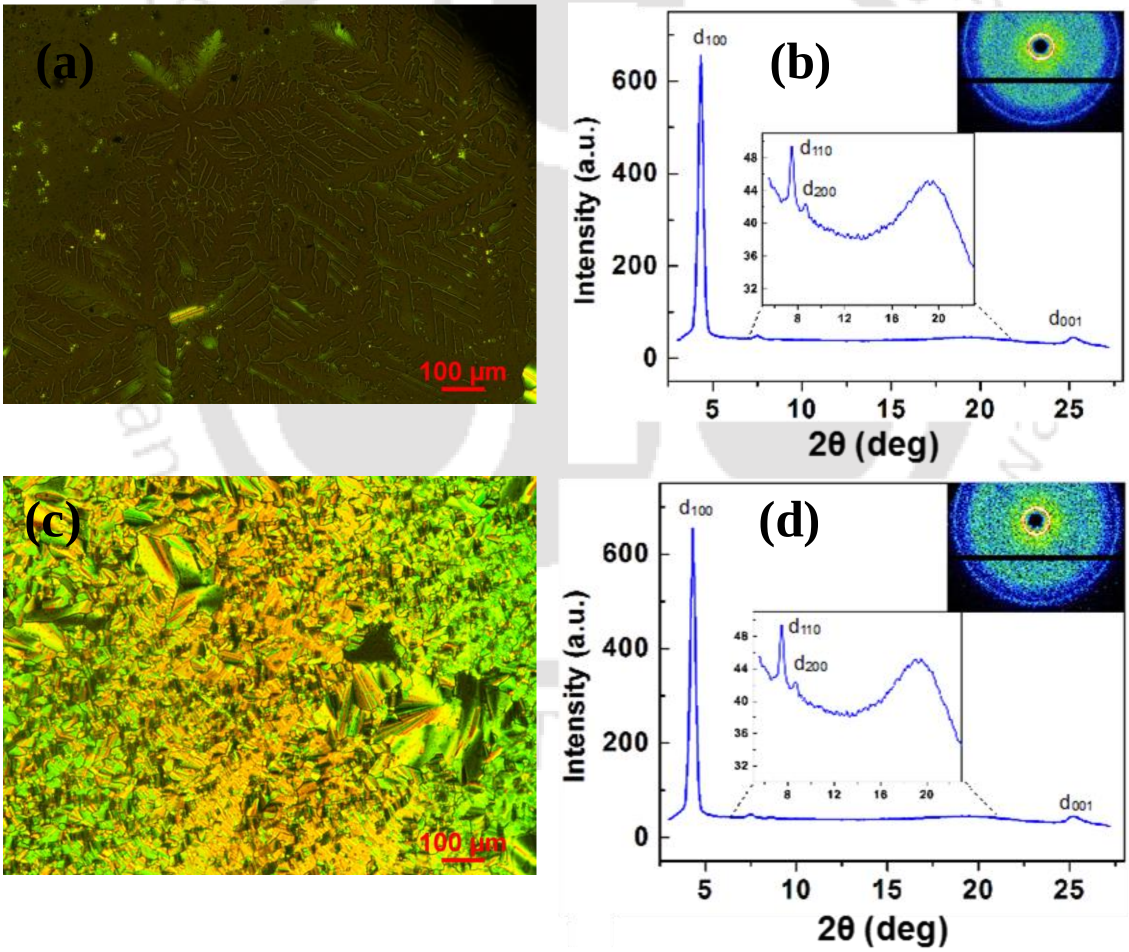

Figure 2.11. (a) Photomicrograph of compound **2c** at 146 °C on cooling from isotropic liquid state (under crossed polarizer); (b) XRD profile depicting the intensity against 2*θ* obtained for the Col$_h$ phase of compound **2c** at 95 °C; (c) Photomicrograph of compound **2d** at 100 °C on cooling from isotropic liquid state (under crossed polarizer); (d) XRD profile depicting the intensity against 2*θ* obtained for the Col$_h$ phase of compound **2d** at 90 °C.

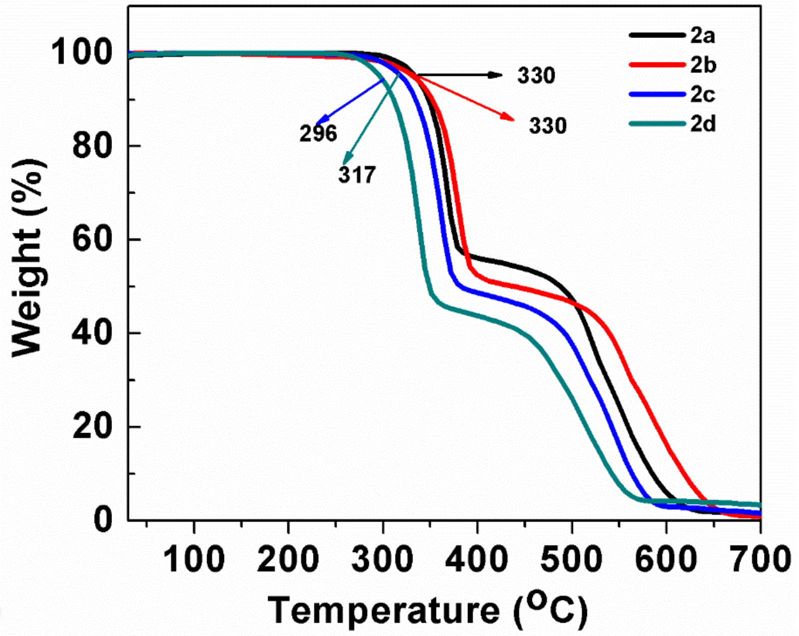

Figure 2.12. TGA plots of compound **2a-d** (heating rate of 10 °C/min, Nitrogen atmosphere).

2.2.2.3. *Se*-annulated perylene tetraesters

All the *Se*-annulated tetraesters investigated, showed enantiotropic mesomorphic behavior except for compound **3d** which turned out to be crystalline (Figure 2.13). Compound **3b** exhibited a crystal to crystal transition at ≈58 °C before transforming to a birefringent fluidic mesophase at a temperature of ≈76 °C (ΔH = 43.4 kJ/mol) (Table 2.1). The mesophase was spanning over a thermal range of 124 degrees and reached the isotropic liquid state at ≈146 °C. The enhanced mesophase width in comparison to parent tetraester **5b** may be due to enhanced Se···Se interactions.[27] On cooling the viscous isotropic liquid, hexagonal germs develop with the branches growing in all directions leading to a fern leaf like structure (Figure 2.14a). This on further cooling coalesces to give a mosaic texture. Finally, the mesophase was crystallized at a temperature of 46 °C as seen in DSC thermograms (Figure 2.13b). This thermodynamically stable mesophase formed by compound **3b** was further studied through powder XRD studies to determine the symmetry at a temperature of 80 °C (Figure 2.14b). The results obtained from the XRD studies are tabulated in Table 2.4. The X-ray profile of the Col phase at 80 °C showed a sharp reflection corresponding to a Bragg spacing d_{100} at 19.15 Å and another corresponding to a Bragg spacing at d_{110} at 11.05 Å. The d spacings corresponding to first two reflections are in the ratio of 1:0.58. Two diffused reflections corresponding to the d spacings of 4.5 Å and 3.54 Å. These parametres are found to be similar to other annulated derivatives, confirms the *Se*-annulated perylene tetraesters also forms Col phase with hexagonal symmetry.

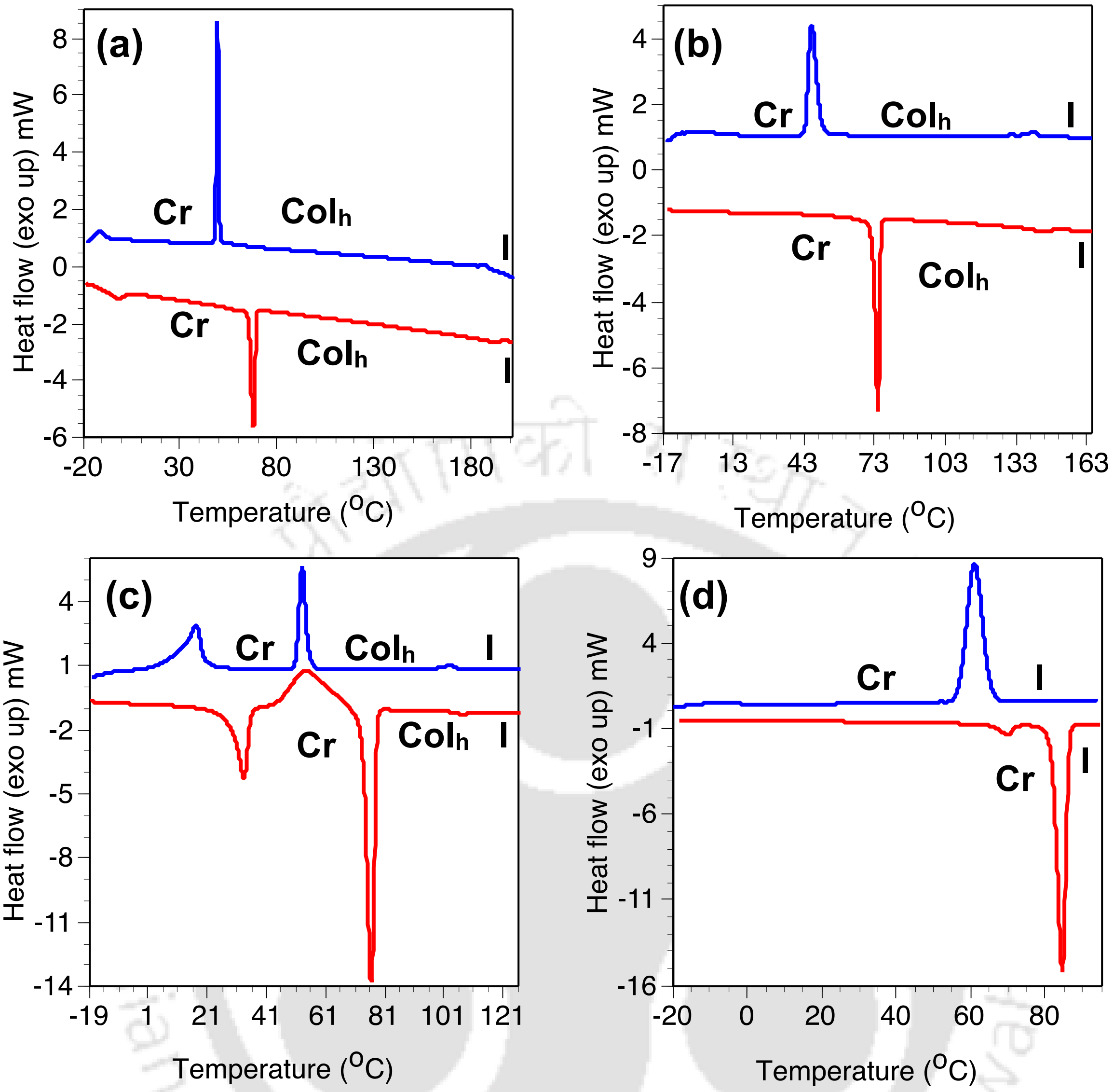

Figure 2.13. DSC thermograms of discotics **3a** (a); **3b** (b); **3c** (c) and **3d** (d) showing the second heating (red trace) and the first cooling (blue trace) scans at a scanning rate of 5.0 ˚C min^{-1}.

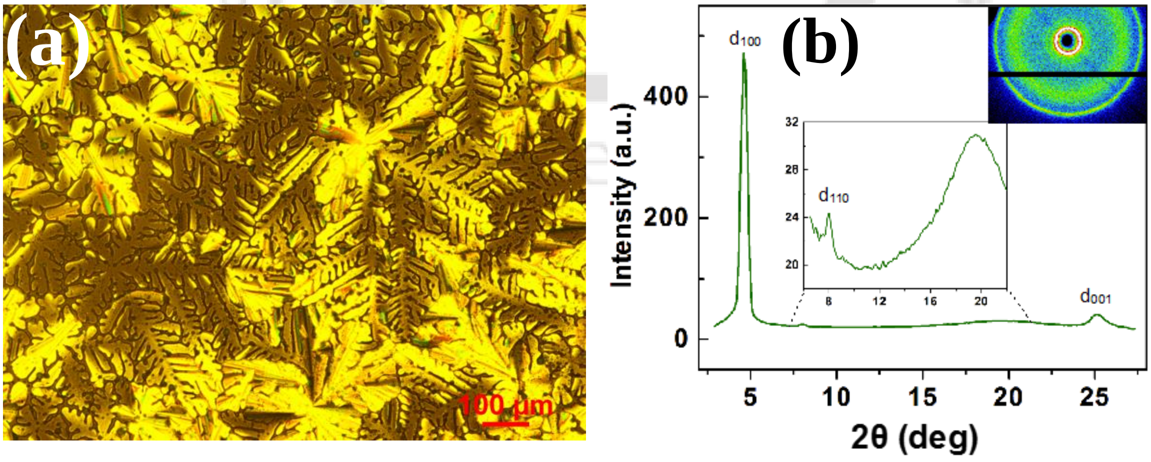

Figure 2.14. (a) Photomicrograph of compound **3b** at 130 ºC on cooling from isotropic liquid state (under crossed polarizer); (b) XRD profile depicting the intensity against 2θ obtained for the Col$_h$ phase of compound **3b** at 80 ºC.

Table 2.4. Results of (*hkl*) indexation of XRD profiles of the compounds at a given temperature (T) of mesophases[a]

Compounds (*D*/Å)	**Phase (T/ºC)**	**d_{obs} (Å)**	**d_{cal} (Å)**	**Miller indices (*hkl*)**	**lattice parameters (Å), lattice area S (Å^2), molecular volume V (Å^3)**
3a (28.05)	85	17.29 4.48 (h_a) 3.51 (h_c)	17.29	100 001	*a* = 19.97 S = 345.2 V = 1211.6 Z = 0.87
3b (32.99)	80	19.15 11.05 4.50 (h_a) 3.54 (h_c)	19.15 11.11	100 110 001	*a* = 22.11 S = 423.5 V = 1499.03 Z = 0.95
3c (37.84)	85	20.5 11.77 10.23 4.53 (h_a) 3.54 (h_c)	20.5 11.89 10.25	100 110 200 001	*a* = 23.67 S = 560.3 V = 1983.6 Z = 1.12

[a] The diameter (D) of the disc (estimated from Chem 3D Pro 8.0 molecular model software from Cambridge Soft). d_{obs}: spacing observed; d_{cal}: spacing calculated (deduced from the lattice parameters; *a* for Col$_h$ phase). The spacings marked h_a and h_c correspond to diffuse reflections in the wide-angle region arising from correlations between the alkyl chains and core regions, respectively. *Z* indicates the number of molecules per columnar slice of thickness h_c, estimated from the lattice area *S* and the volume *V*.

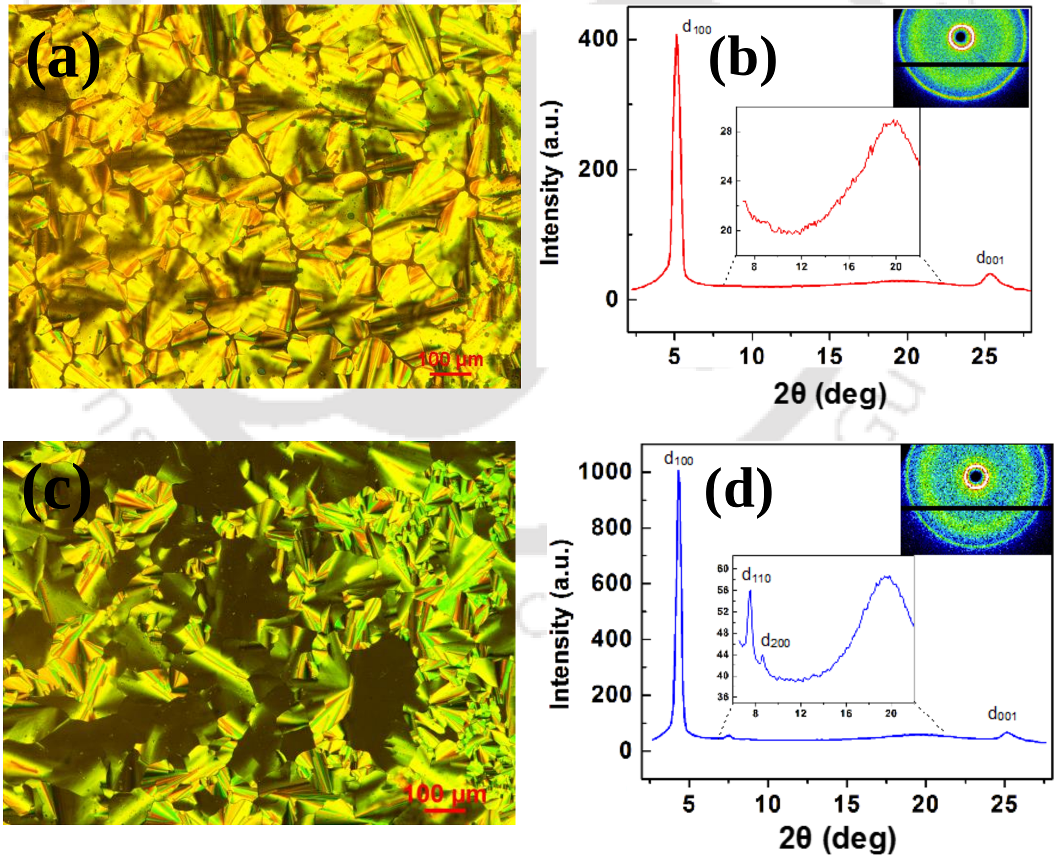

Figure 2.15. (a) Photomicrograph of compound **3a** at 148 ºC on cooling from isotropic liquid state (under crossed polarizer); (b) XRD profile depicting the intensity against 2*θ* obtained for the Col$_h$ phase of compound **3a** at 85 ºC; (c) Photomicrograph of compound **3c** at 60 ºC on cooling from isotropic liquid state (under crossed polarizer); (d) XRD profile depicting the intensity against 2*θ* obtained for the Col$_h$ phase of compound **3c** at 85 ºC.

In the case of compound **3a** and **3c** also such dendritic patterns were exhibited on cooling from isotropic state, but on further cooling these patterns coalesce and lead to the formation of mosaic texture as shown in Figure 2.15a and c. The XRD pattern obtained for these compounds showed similar behavior (Figure 2.15b and d), as shown by compound **3b**. Compound **3d** with *n*-dodecyloxy tails turned out to be crystalline. Thus, from compound **3a-c** there is reduction in the mesophase range while it is completely vanished in the case of **3d**. Thus, increase in the length of the flexible tails lead to a reduction in the isotropic temperature, which reduces the mesophase width as evident in the bargraph shown in Figure 2.16. When compared to parent tetraesters **5a-d**, *Se*-annulated compounds show enhanced mesophase range, probably due to the increased planarity and favourable Se···Se interactions. From figure 2.16, it is visible that, *N*-annulated perylene tetraesters **1a-d**, and *S*-annulated perylene tetraesters **2a-d** show higher mesophase range than parent tetraesters **5a-d** and *Se*-annulated tetraesters **3a-d**.

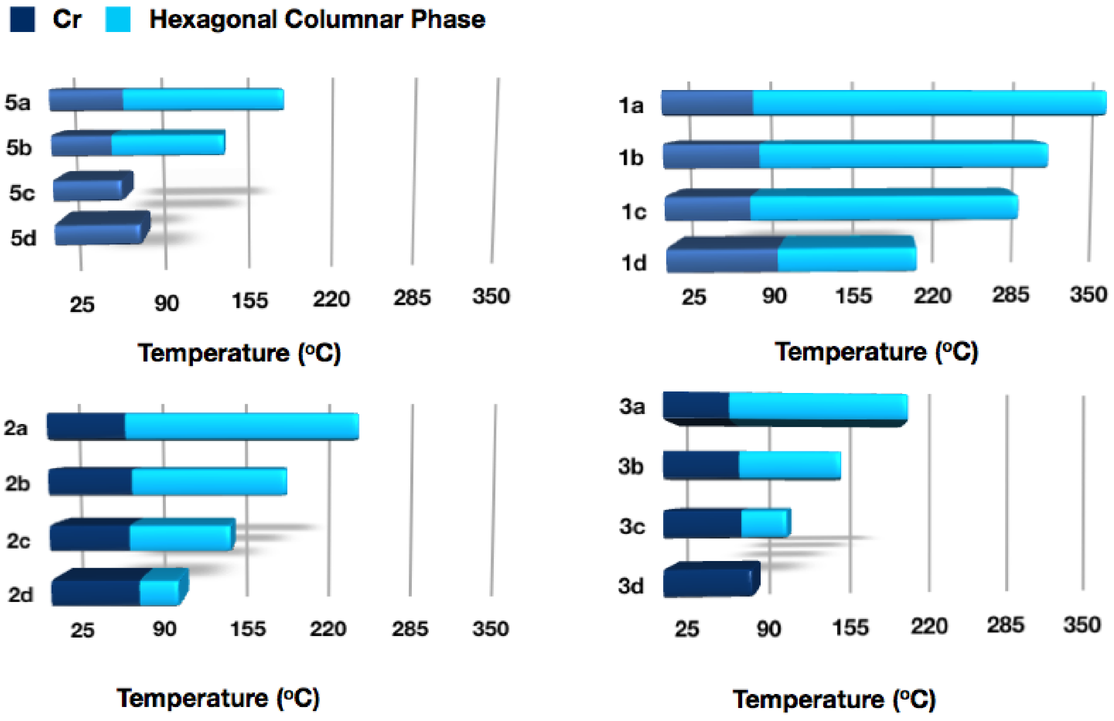

Figure 2.16. Bargraph summarizing the thermal behavior of compounds **5a-d**[17a-d], **1a-d**, **2a-d** and compounds **3a-d** (heating cycle).

TGA studies shown that these compounds were stable up to at least 230 °C and complete decomposition occurs around ≈600 °C (Figure 2.17). These compounds show reduced thermal stability in comparison to compound **1a-d** and **2a-d**.

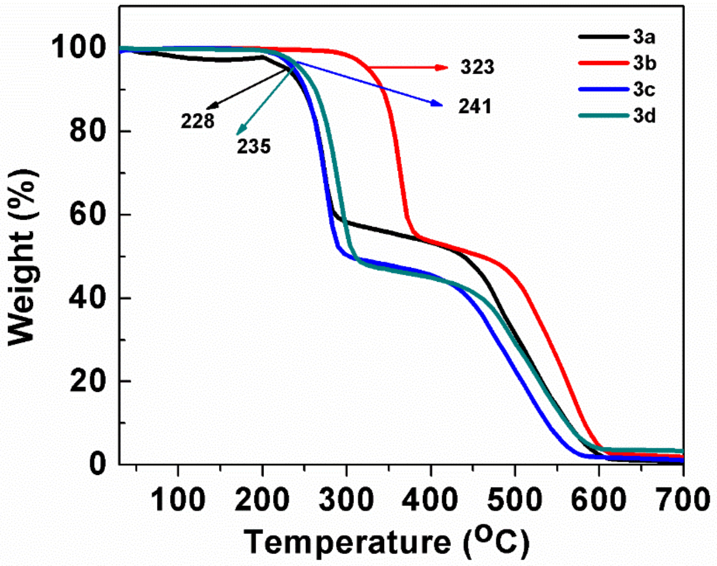

Figure 2.17. TGA plots of compound **3a-d** (heating rate of 10 °C/min, Nitrogen atmosphere).

2.2.3. Photophysical properties

Photophysical properties of these *bay*-annulated perylene tetraesters in solution as well as in thin film are depicted in Table 2.5 and 2.6 respectively. Absorption and fluorescence spectra of the all compounds were taken in micromolar solutions in THF (Table 2.5). Representative spectra for compounds **1b, 2b, 3b** and **5b** are given in Figure 2.18. As can be seen, the absorption spectra obtained for the solutions of **1a-d** showed a single absorption maximum centered at 459 nm, with two shoulder peaks at 434 nm and 410 nm. The absorption spectra for the solutions of **2a-d** showed an absorption maximum centered at 442 nm, with two small shoulders centered at 417 nm and 398 nm. The molar absorption coefficients were calculated and found that the values were comparable to the molar absorption coefficient of perylene tetraester (**1a-d**: ε = >10,500 $M^{-1}cm^{-1}$; **2a-d**: ε = >8930 $M^{-1}cm^{-1}$; **5b**: ε = 14,800 $M^{-1}cm^{-1}$). The absorption spectra obtained for the solutions of **3a-d** showed two absorption maxima, one centered at 449 nm and the other at 422 nm. Compounds **3a-d** showed relatively smaller values of molar absorption coefficients considering the polyaromatic structure of these molecules (**3a-d**: ε = >6,020 $M^{-1}cm^{-1}$). All the *bay*-annulated perylene tetraesters **1b**, **2b** and **3b** exhibited a hypsochromic shift when compared to corresponding parent perylene tetraester **5b** (Figure 2.18a).

Emission spectra of solutions of compounds **1a-d**, excited at their absorption maxima showed emission with their emission maxima centered around 492-495 nm with a Stoke's shift of 33-36 nm while emission spectra of compounds **2a-d** showed the emission maxima centered around 461-464 nm with a shoulder peak at 482 nm with a Stoke's shift of 19-22 nm was observed for these molecules. Compounds **3a-d** showed broad emission band centered around 476 nm with a Stoke's shift of 27-36 nm (Figure 2.18b). Emission spectra of all *bay*-annulated perylene tetraesters are also following same trend as in absorption spectra i.e. shows blue shift in comparison to parent tetraester, while emission spectra of parent tetraester **5b** and *N*-annulated perylene tetraester **1b** showed slight red shift, while *S*-annulated perylene tetraester **2b** showed slight blue shift in comparison to *Se*-annulated tetraester **3b**. Absorption and emission spectra of all these molecules did not vary with the chain length.[17a,15b,28] Solutions of compounds **1a-d** exhibit bright green fluorescence under UV light of long wavelength, solutions of compounds **2a-d** exhibit sky blue fluorescence under UV light of long wavelength while solutions of compounds **3a-d** exhibited weak fluorescence under UV light of long wavelength (Figure 2.19). UV-Vis absorption and emission spectra of *bay*-annulated perylene tetraesters were taken on diluting the micromolar solution. On dilution of the micromolar solutions the pattern of the absorption and emission spectra did not change much except a reduction in the intensity. As a representative case we have measured the quantum yield of compound **1b**, **2b**, **3b** and **5b** with respect to flourescein. The quantum yields for *N*- and *S*-annulated perylene tetraesters **1b** and **2b** was found to almost unity whereas the quantum yield of compound **3b** was very low and found to be 0.07 (Table 2.9).

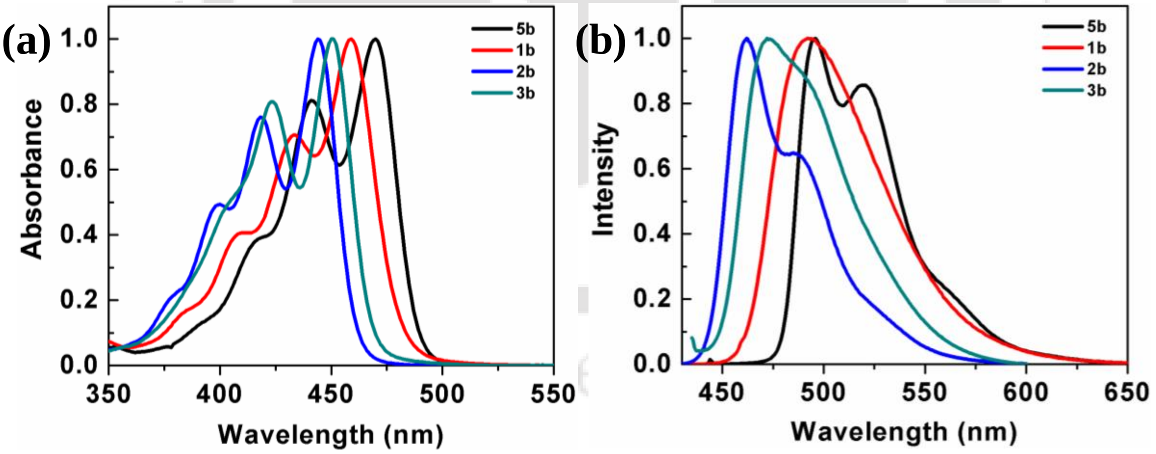

Figure 2.18. Absorption spectra (a) and emission spectra (b) of compounds **5b**, **1b**, **2b** and **3b** in micromolar THF solution.

Fluorescence lifetime and steady state anisotropy measurements were carried out in dilute solutions (3μM solution in dichloromethane). The measured fluorescence lifetime for *bay*-annulated perylene tetraesters were tabulated in Table 2.5 and found to be lower than perylene (5.2 ns in ethanol solution)[29]. The decreased fluorescence lifetime may be

Table 2.5. Photophysical properties of DLCs[a] in solution.

Entry	Absorption (nm)	Emission[b] (nm)	Stokes shift nm (cm^{-1})	λ_{onset} (nm)	$\Delta E_{g,opt}$[c,d]	τ[e,f] (ns)	Steady state anisotropy
1a	459,434,410	493	34 (1502)	501	2.48	3.61	0.182
1b	459, 434, 410	492	33 (1461)	501	2.48	3.60	0.185
1c	459,434,410	495	36 (1584)	501	2.48	3.62	0.179
1d	459,434,410	493	34 (1502)	504	2.47	3.59	0.178
2a	442, 417, 398	461, 481	19 (933)	465	2.67	3.01	0.024
2b	442, 417, 398	464, 482	22 (1073)	463	2.68	3.05	0.029
2c	442, 417, 398	464, 482	22 (1073)	463	2.68	3.02	0.037
2d	442, 417, 398	462, 481	20 (979)	463	2.68	3.01	0.032
3a	449,422	476	36 (1653)	471	2.64	0.27	0.043
3b	449,422	476	33 (1525)	471	2.64	0.11	0.075
3c	449,422	476	27 (1263)	471	2.64	0.15	0.015
3d	449,422	476	27 (1263)	471	2.64	0.13	0.069
5b	470, 441	489, 517	19 (827)	504	2.46	4.04	0.031

[a]in micromolar solutions in THF; [b]the excitation wavelength λ_{ex} = absorption maxima; [c]calculated from the red edge of the absorption band; [d]in eV; [e]Fluorescence life time; [f]3 μM solution in dichloromethane.

Table 2.6. Photophysical properties of DLCs[a] in thin film.

Entry	Absorption (nm)	Emission[b] (nm)	Stokes shift nm (nm^{-1})
1b	416,479	556	140 (6053)
2b	408,471	534	126 (5783)
3b	419,476	552	133 (5750)
5b	497,458	534, 562	37 (1394)

[a]prepared by the spin-coating of millimolar solution in toluene; [b]excited at the absorption maxima.

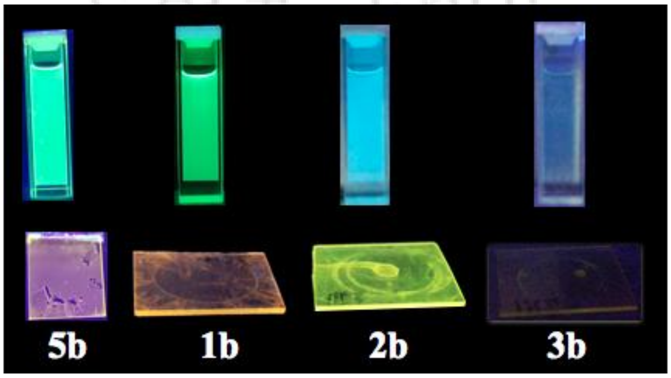

Figure 2.19. Micromolar solutions and spin coated thin-films of perylene tetraester **5b**, *N*-annulated perylene tetraester **1b**, *S*-annulated perylene tetraester **2b** and *Se*-annulated perylene tetraester **3b**.

due to higher non-radiative decay. This may be due to the molecular structure and intermolecular interactions. Heteroatoms incorporation into the molecular structure may be another factor, which led to this observation. The steady state anisotropy values for all *bay*-annulated perylene tetraesters were also found to be comparable to the values reported for perylene tetraester.[17g] The lower anisotropy values observed could be due to higher rotational diffusion which may occur during the life time of the excited state and displaces the emission dipole of the fluorophore.

Millimolar solutions of compound **1b**, **2b** and **3b** in toluene were used to prepare the thin film on glass slide by spin coating (500-2000 rpm). The absorption spectrum of *N*-annulated perylene tetraester **1b** obtained showed two maxima at 416 nm and 479 nm respectively, while the emission spectrum showed a single maximum at 556 nm and Thin film showed orange luminescence under the UV light of 365 nm wavelength (Figure 2.20, inset). The absorption spectrum of of *S*-annulated perylene tetraester **2b** showed two maxima at 408 nm with a shoulder at 471 nm respectively, while the emission spectrum exhibits an emission maximum at 534 nm and Thin film showed yellowish green luminescence under the UV light of 365 nm wavelength (Figure 2.21, inset). The absorption spectrum of *Se*-annulated perylene tetraester **3b** showed a maximum at 419 nm and a shoulder 476 nm, while the emission spectrum exhibited a maximum at 552 nm and thin film showed very weak luminescence under the UV light of 365 nm wavelength (Figure 2.22, inset). The absorption maxima is hypsochromically shifted with respect to that of monomer (solution state) and the emission spectrum in the solid state was bathochromically shifted for all *bay*-annulated perylene tetraesters. The observed red shifted emission in the case of thin film is due to the lowered energy level which is resulted from the close overlap of cores in the thin film state.[30] Kasha *et al.*, described that molecular aggregation in ground state lead to exciton coupling, which in turns splits the excited state aggregates into two energy levels (Davydov splitting).[31] When the molecules are stacked one above the other, which are known as H-aggregates, the transition to the upper level is allowed. A blue shifted absorption band compared to that of the monomer is the characteristic of this phenomenon. Transition to the lower level is allowed when the molecules in aggregates are arranged in a slip stack fashion (J-aggregates). The blue shifted absorption maxima in the case of thin film of compounds points to the formation of H-aggregates, with the molecules being stacked in a co-facial manner within the aggregates.[31,32] Thus the fluorescence gets quenched due to the aggregation.

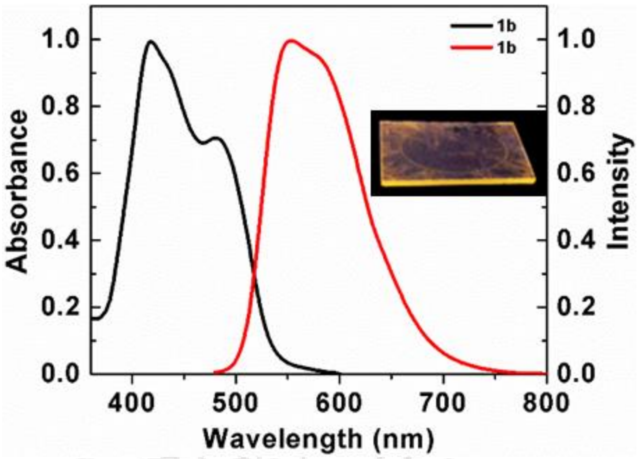

Figure 2.20. Absorption (black trace) and emission (red trace) spectra obtained for the spin coated thin film for compound **1b** (Inset shows the film under UV light of wavelength 365 nm).

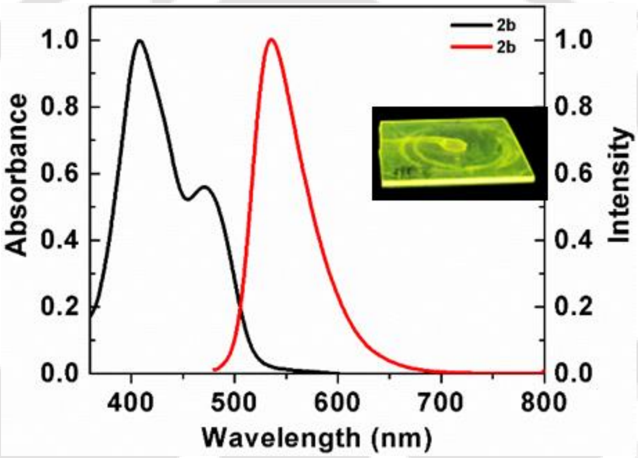

Figure 2.21. Absorption (black trace) and emission (red trace) spectra obtained for the spin coated thin film for compound **2b** (Inset shows the film under UV light of wavelength 365 nm).

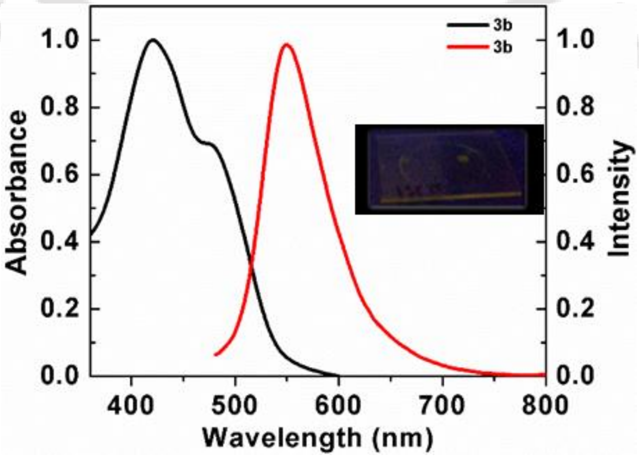

Figure 2.22. Absorption (black trace) and emission (red trace) spectra obtained for the spin coated thin film for compound **3b** (Inset shows the film under UV light of wavelength 365 nm).

2.2.4. Electrochemical behavior

Cyclic voltammetry (CV) gives valuable information and allows the estimation of frontier molecular orbitals (HOMO and LUMO levels) and band gap of the organic materials. *Bay*-annulated perylene tetraesters (**1b**, **2b**, **3b** and **5b**) were investigated by carrying out cyclic voltammetry studies in micromolar THF solution. The energy levels (HOMO and LUMO), band gap value, comparison with molecules **1b**, **2b**, **3b** and **5b** and experimental conditions are tabulated in Table 2.8.

Table 2.8. Electrochemical[a,b] properties of compound **1b**, **2b**, **3b** and **5b**.

Entry	E_{1red}[c]	E_{1oxd}[c]	E_{HOMO}[d,e]	E_{LUMO}[d,f]	$\Delta E_{g,CV}$[d,g]	$\Delta E_{g,opt}$[d,h]
1b	-1.02	0.92	-5.16	-3.22	1.94	2.48
2b	-1.22	-	-5.78[i]	-3.1	-	2.68
3b	-1.18	-	-5.7[i]	-3.06	-	2.64
5b	-1.04	0.89	-5.16	-3.2	1.93	2.46

[a]in micromolar solutions in THF; [b]Experimental conditions: Ag/AgNO$_3$ as reference electrode, Glassy carbon working electrode, Platinum wire counter electrode, TBAP (0.1 M) as a supporting electrolyte, room temperature; [c]in volts (V); [d]in eV; [e]Estimated from the formula $E_{HOMO} = -(4.8 - E_{1/2,\ Fc/Fc^+} + E_{ox,\ onset})$ eV ; [f]Estimated from the formula by using $E_{LUMO} = -(4.8 - E_{1/2,\ Fc/Fc^+} + E_{red,\ onset})$eV; [g]Estimated from the formula $\Delta E_{g,\ CV} = E_{HOMO} - E_{LUMO}$; [h]calculated from the red edge of the absorption band (471 nm); [i]Estimated from formula $E_{HOMO} = E_{LUMO} - \Delta E_{g,opt}$.

The optical band gap $E_{g,opt}$ was estimated from the absorption onset values. (Table 2.8). Compound **1b** exhibited LUMO and HOMO levels of -3.22 and -5.16 eV respectively. The electrochemical band gap was obtained by tabulating the aforementioned values in the formula $\Delta E_{g,CV} = E_{LUMO} - E_{HOMO}$. It is found to be 1.94 eV, which was comparable to parent perylene tetraester **5b.** Compound **2b** exhibited LUMO and HOMO levels of -3.1 and -5.78 eV respectively. Compound **3b** exhibited LUMO and HOMO levels of -3.06 and -5.7 eV respectively. Both (**1b** and **5b**) the electrochemical band gaps are found to be lesser than their respective optical band gap. When compared to the perylene tetraester **5b**, the band gap was found to be higher in the case of **3b**. The HOMO and LUMO levels of **5b** were found to be -5.16 and -3.2 eV respectively with a band gap of 1.93 eV (optical band gap 2.46 eV). Thus in the case of **3b**, HOMO levels are lowered and LUMO levels are slightly higher therefore, bandgap increased as a result of the selenium annulation. This is similar to the behavior of *S*-annulated tetraester **2b**. Since oxidation potential of **2b** and **3b** was not observed so, HOMO was calculated from their optical band gap and LUMO of **2b** and **3b** was found to be similar. Thus, the chalocogen incorporation in the molecular structure lowers the HOMO and LUMO levels in comparison to perylene tetraesters and their *N*-annulated derivatives (Figure 2.23).

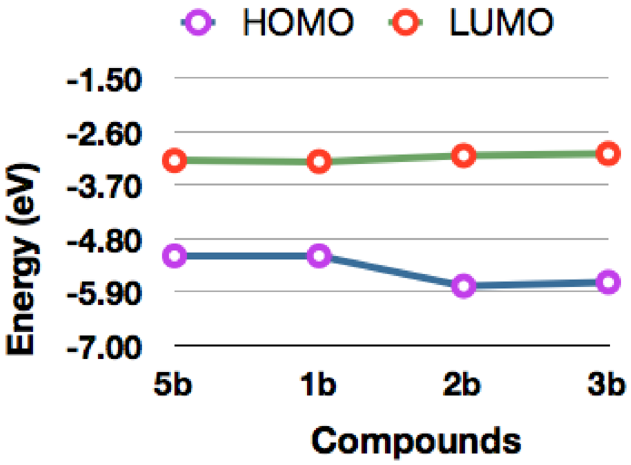

Figure 2.23. Comparison of frontier molecular orbitals for compounds **1b**, **2b, 3b** and **5b**.

2.2.5. Density functional theory (DFT) calculation

Density functional theory (DFT) calculations were used to provide a computational comparison with the experimental data. This also expected to provide information on the geometry and electronic structure of **1b, 2b, 3b** and **5b.** The quantum mechanical calculations of molecular properties were performed using DFT, by employing the combination of Becke3-Lee-Yang-Parr (B3LYP) hybrid functional and 6-31G(d,p) basis set using the Gaussian 09 package,[33] to obtain the information related to molecular conformation and frontier molecular orbitals (HOMO-LUMO) of all the compounds. Full geometry optimizations have been carried out by Hatree Fock method using 321-G basic set followed by DFT calculations using B3LYP hybrid functional and the 6-31G(d,p) standard basis set due to its successful application for larger organic molecules.

The energy minimized structures for **1b, 2b, 3b** and **5b** showed in Figure 2.24. Pictures of frontier molecular orbitals (FMOs) and the differences in their energies provide knowledge about the length of conjugation and band gap level, which helps in comparing the perylene tetraester with their *bay*-annulated derivatives. The contours of the HOMO and LUMO of perylene tetraesters **1b**, **2b**, **3b** and **5b** are shown in Figure 2.25. The HOMO-LUMO energy levels of **1b, 2b, 3b** and **5b** are distributed on the entire aromatic ring. In the case of annulated derivatives, LUMO was found to be spreading over hetero atom. The theoretical band gap for **1b, 2b, 3b** and **5b** is -2.79, -2.95, -2.95 and 2.94 eV respectively. Further, absence of imaginary frequency confirms stable configuration of *bay*-annulated perylene tetraesters.

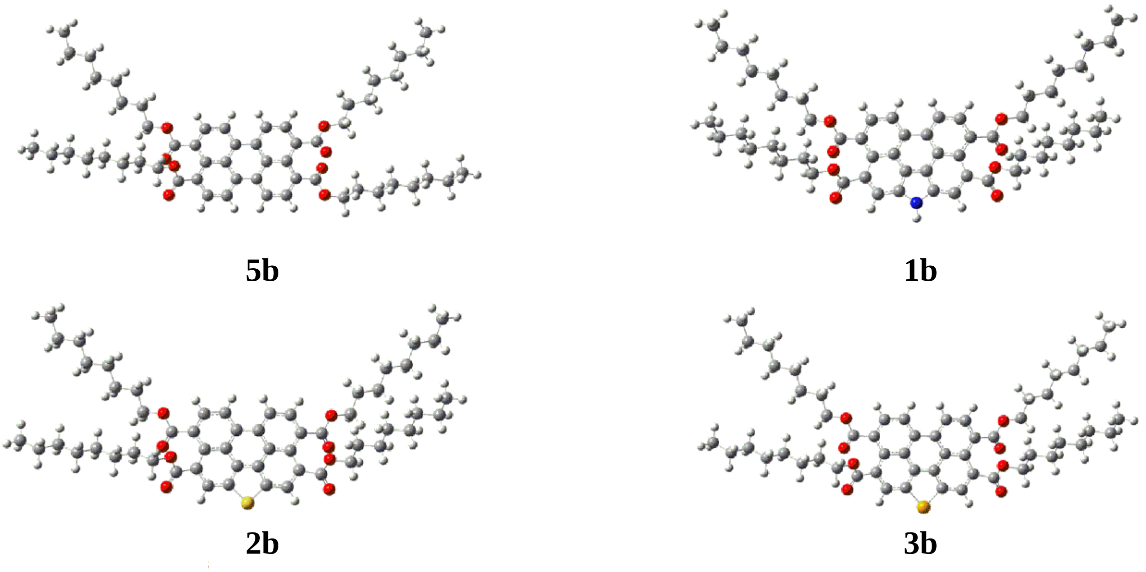

Figure 2.24. Optimized geometry of compounds **5b**, **1b**, **2b** and **3b**.

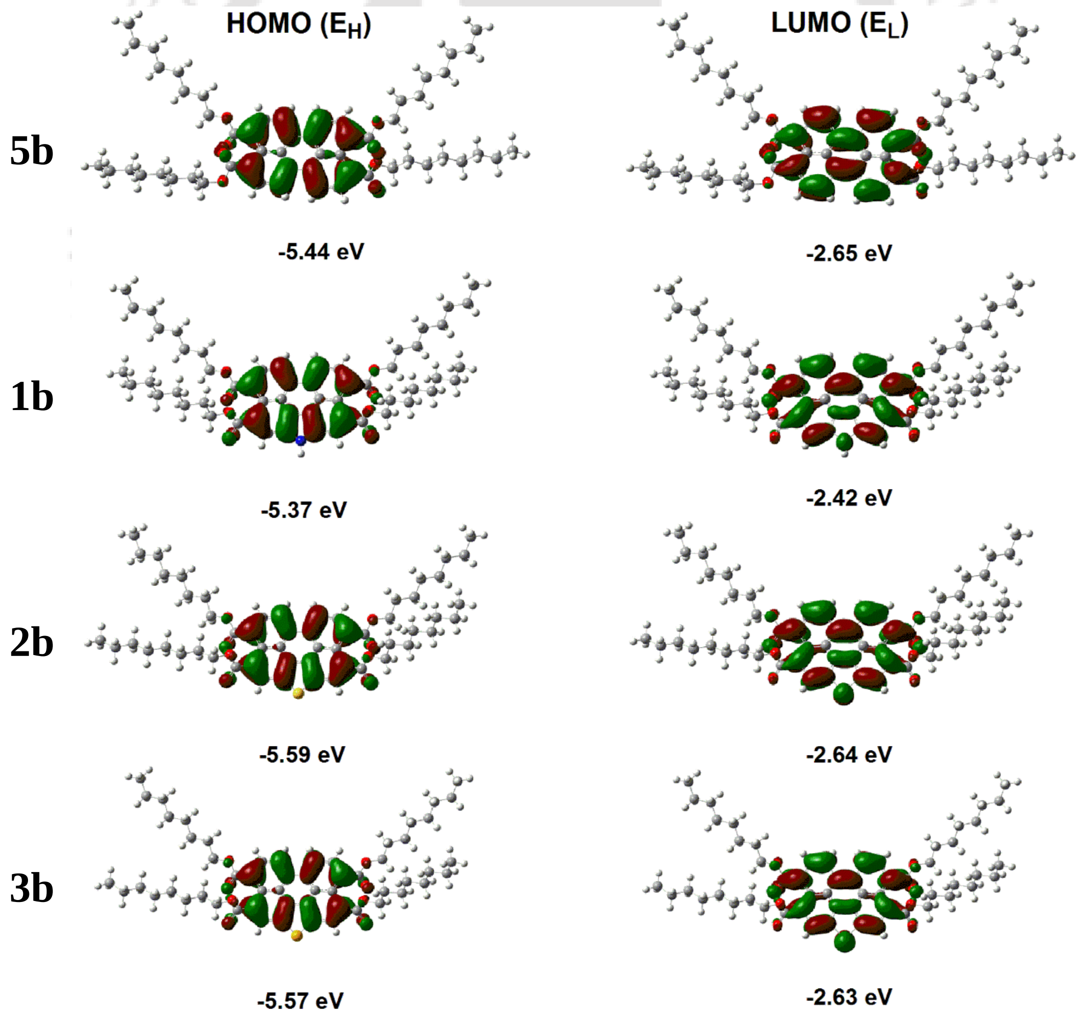

Figure 2.25. HOMO and LUMO frontier molecular orbitals of **5b, 1b, 2b** and **3b** at the B3LYP/6-31G(dp) level. E_H and E_L denote energies of the highest occupied molecular orbital (HOMO) and the lowest unoccupied molecular orbital (LUMO), respectively.

2.2.6. Relative Quantum Yield Calculation

Quantum yield of *N*-annulated perylene tetraesters **1b** and parent tetraester **5b** was measured according to established procedure[34] by using fluorescein in 0.1 M NaOH solution as the standard. Absolute values were calculated according to the following equation:

$Q_S = Q_R \times (m_S / m_R) \times (n_S / n_R)^2$

Where, Q: Quantum yield, m: Slope of the plot of integrated fluorescence intensity *vs* absorbance

n: refractive index (1.407 for THF and 1.33 for distilled water).

The subscript R refers to the reference fluorophore *i.e.* fluorescein solution in 0.1 M NaOH and subscript S refers to the sample under investigation. In order to minimize re-absorption effects, absorbance was kept below 0.15 at the excitation wavelength of 459 and 470 nm. Quantum Yield of fluorescein in 0.1 M NaOH solution is 0.79. Simplified equation for the calculation after substituting the appropriate values is given below:

$Q_S = 0.79 \times (m_S / m_R) \times (1.407/1.33)^2$

$\quad = 0.88401 \times (m_S / m_R)$

Table 2.9. Quantum yield of Compound **1b**, **5b**, **2b** and **3b**.

Entry	**m_S**	**m_R**	**$Q_s^{a,b,c}$**
1b	2.285×10^9	2.001×10^9	1.00
5b	2.278×10^9	1.959×10^9	1.00

[a]Measured in THF; [b]Excited at absorption maxima; [c]Standard fluorescein ($Q_f = 0.79$) in 0.1 M NaOH.

Entry	**m_S**	**m_R**	**$Q_s^{a,b,c}$**
2b	3.203×10^9	3.215×10^9	1.00
3b	2.410×10^8	3.494×10^9	0.068

[a]Measured in THF; [b]Excited at absorption maxima; [c]Standard compound **1b** ($Q_f = 1.0$) in THF solution

Similarly, relative quantum yield of compound **2b** and **3b** was measured with respect to **1b** in THF solution as the standard, which is having the relative quantum yield of 1 with respect to fluorescein ($\mathbf{Q_f} = 0.79$ in 0.1M NaOH). With formula

$Q_S = Q_R \times (m_S / m_R) \times (n_S / n_R)^2$

In this case, n: refractive index (1.407 for THF).

R refers to the reference fluorophore *i.e.* compound **1b** solution in THF and subscript S refers to the sample under investigation. In order to minimize re-absorption effects, absorbance was kept below 0.15 at the excitation wavelength of 442 and 449 nm.

Simplified equation for the calculation:

$$Q_S = 1.0 \times (m_S / m_R) \times (1.407/1.407)^2$$

$$= 1.0 \times (m_S / m_R)$$

2.3. Conclusion

In summary, we have synthesized new class of discotics based on *N*-, *S*- and *Se*-annulated perylene tetraesters. The length of their peripheral alkyl chains was varied to understand their effect on thermal behavior. These compounds were investigated for their thermal and photophysical properties by various techniques. All *bay*-annulated perylene tetraesters stabilized ordered columnar phases with hexagonal symmetry except compound **3d**. The mesophase range of *N*-, *S*- and *Se*-annulated perylene tetraester is enhanced in comparison to parent perylene tetraesters due to the attractive and favourable -NH-, S···S and Se···Se interactions. The mesophase range of *Se*-annulated perylene tetraester is reduced in comparison to *N*-annulated perylene tetraesters and *S*-annulated perylene tetraesters. The homologue with longest alkyl chain turned to be crystalline, while the mesophase range reduced gradually with the increase in alkyl chain length. Columnar hexagonal phase shows good homeotropic alignment on slow cooling. The lower value of hexagonal lattice parameter when compared to the calculated molecular diameter points to the folding or interdigitation of the peripheral alkyl tails. With the increase in the flexible chain length the mesophase range decreases due to the reduction in the clearing temperature. TGA studies have shown that *Se*-annulated perylene tetraesters are stable up to at least 230 °C, which is lesser than *N*- and *S*-annulated perylene tetraesters (stable upto 300 °C for both tetraesters).

N-annulated perylene tetraesters show visually perceivable green light emission in solution and yellowish-orange emission in thin film state . These are low bandgap materials as evidenced from their absorption spectra with a bandgap of 2.48 eV. *S*-annulated perylene tetraesters show visually percievable sky blue light emission in solution and green color in their aggregated state. Both *N*- and *S*-annulated tetraesters exhibiting a high quantum yield in their solution state. These molecules also can be used as standards to measure the quantum yields of unknown compounds owing to their high solubility. Unlike *N*- and

S-annulated tetraesters, *Se*-annulated perylene tetraesters show very weak emission in solution and thin-film state. Length of the peripheral chains does not have much impact on their photophysical properties. Cyclic voltammetry studies have shown that *S*- and *Se*-annulated perylene tetraesters exhibit increased band gaps when compared to perylene tetraesters and their *N*-annulated counterparts. DFT calculations were also carried out to understand the HOMO and LUMO levels and the bandgaps. Finally, this chapter gives an account of structure-property relationships of liquid crystalline annulated perylene derivatives and shows the immense possibility present in tuning the thermal and photophysical behaviors by simple synthetic methods. This also paves the way for the synthesis of other π-extended derivatives of the heteroatom annulated perylene derivatives.

2.4. Experimental section

In this section the detailed synthesis procedure and the molecular structural characterization data have been presented for the intermediates and target compounds mentioned in the scheme.

Synthesis of tetrakis(alkyl)perylene-3,4,9,10-tetracarboxylate **(5a-d)**[17a-d]

Perylene tetracarboxylic dianhydride (2.5 mmol, 1 equiv.) was dissolved in 30 mL aqueous KOH (13.76 mmol, 5.4 equiv.) solution and stirred at 70 °C for 0.5 h. The solution was filtered and pH value of filterate was adjusted to 8-9 using 10% HCl. Then Aliquat 336 (0.9 mmol, 0.4 equiv.) and KI (1.4 mmol, 0.6 equiv.) were charged into the solution and then stirred vigorously for 10 min. *n*-Bromoalkane (15.3 mmol, 6 equiv.) was added to this reaction mixture. After the addition the reaction mixture was refluxed for 12 h until a red oil floats on the top and the rest of the solution becomes clear. Subsequently, chloroform (10 mL) was poured into the mixture and filtered through the celite bed to remove unreacted part and the celite bed was washed with chloroform. This chloroform layer was separated and washed twice with 15% sodium chloride solution, dried over sodium sulfate and concentrated in vacuo to get a viscous concentrate. Methanol was added to precipitate the compound from this concentrate. The solid was precipitated filtered and dried in vacuum.

5a: R_f = 0.56 (10% EtOAc-hexane); Yellow solid, yield: 70%; IR (KBr pellet) ν_{max} in cm^{-1}: 2953, 2926, 2851, 1732, 1712, 1274, 1164; ^{1}H NMR (400 MHz, CDCl$_3$, 298 K): δ 8.21 (d, J = 8 Hz, 4H, H$_{Ar}$), 7.99 (d, J = 7.6 Hz, 4H, H$_{Ar}$), 4.33-4.3 (m, 8H, 4 ×-OCH$_2$), 1.80-1.77 (m, 8H, 4 ×-OCH$_2$-$\underline{CH_2}$), 1.44-1.28 (m, 40H, 20 × CH$_2$), 0.87-0.86 (m, 12H, 4 × CH$_3$); ^{13}C NMR (150 MHz, CDCl$_3$, 298 K): 168.7, 133.3, 130.7, 130.65, 129.3, 129.1, 121.6, 65.9, 32, 29.5, 29.4, 28.8, 26.3, 22.9, 14.3.

5b: R_f = 0.58 (10% EtOAc-hexane); Yellow-orange solid, yield: 69%; IR (KBr pellet) ν_{max} in cm^{-1}: 2956, 2920, 2850, 1731, 1719, 1468, 1281, 1172; ^{1}H NMR (400 MHz, CDCl$_3$, 298 K): δ 8.24 (d, J = 7.6 Hz, 4H, H$_{Ar}$), 8.01 (d, J = 8 Hz, 4H, H$_{Ar}$), 4.32 (t, J = 6.8 Hz, 8H, 4 × -OCH$_2$), 1.83-1.75 (m, 8H, 4 ×-OCH$_2$-$\underline{CH_2}$), 1.44-1.27 (m, 56H, 28 × CH$_2$), 0.87 (t, J = 6.8 Hz, 12H, 4 × CH$_3$); ^{13}C NMR (100 MHz, CDCl$_3$, 298 K): 168.7, 133.3, 130.8, 130.6, 129.3, 129.1, 121.6, 65.9, 32.1, 29.8, 29.6, 29.5, 28.8, 26.3, 22.9, 14.3.

5c: R_f = 0.6 (10% EtOAc-hexane); Yellow solid, yield: 75%; IR (KBr pellet) *v*max in cm^{-1}: 2954, 2919, 2850, 1731, 1720, 1593, 1292, 1173, 1025; ^{1}H NMR (400 MHz, $CDCl_3$, 298 K): δ 8.21 (d, *J* = 8.4 Hz, 4H, H_{Ar}), 7.99 (d, *J* = 7.6 Hz, 4H, H_{Ar}), 4.33-4.3 (m, 8H, -OCH_2), 1.82-1.75 (m, 8H, -OCH_2-$\underline{CH_2}$), 1.46-1.25 (m, 72H, CH_2), 0.88-0.85 (m, 12H, CH_3); ^{13}C NMR (100 MHz, $CDCl_3$, 298 K): 168.74, 132.89, 132.92, 130.46, 128.96, 128.75, 121.43, 65.83, 32.13, 29.89, 29.87, 29.85, 29.80, 29.6, 29.58, 28.86, 26.26, 22.89, 14.31.

5d: R_f = 0.56 (10% EtOAc-hexane); Yellow solid, yield: 70%; IR (KBr pellet) v_{max} in cm^{-1}: 2953, 2929, 2865, 1730, 1273, 1168; ^{1}H NMR (600 MHz, $CDCl_3$, 298 K): δ 8.31 (d, *J* = 12 Hz, 4H, H_{Ar}), 8.05 (d, *J* = 12 Hz, 4H, H_{Ar}), 4.32 (t, *J* = 6 Hz, 8H, 4 ×-OCH_2), 1.81-1.77 (m, 8H, 4 ×-OCH_2-$\underline{CH_2}$), 1.47-1.33 (m, 24H, 12 × CH_2), 0.90 (t, *J* = 6 Hz, 12H, 4 × CH_3); ^{13}C NMR (100 MHz, $CDCl_3$, 298 K): 168.75, 132.84, 130.43, 128.91, 128.71, 121.42, 65.81, 31.76, 28.82, 25.92, 22.79, 14.25.

Synthesis of tetrakis(alkyl)-1-nitroperylene-3,4,9,10-tetracarboxylate (**4a-4d**)

To a solution of perylene tetraester (0.7 mmol, 1 equiv.) in dichloromethane (5 mL), added $NaNO_2$ (0.7 mmol, 1 equiv.) at 0 °C and stirred. To this well stirred suspension, 69% HNO_3 (3.42 mmol, 5 equiv., 10% solution in dichloromethane) was added dropwise. This mixture was stirred at 0 °C for 1 h. The reaction mixture was poured into water and extracted with dichloromethane (25 mL). The extract was washed with water and brine. Finally organic layer was dried over anhyd Na_2SO_4 and concentrated. The crude product was purified by column chromatography on neutral alumina. Elution with 50% dichloromethane-hexane yielded the desired product.

4a: R_f = 0.56 (10% EtOAc-hexane); red viscous liquid, yield: 90%; IR (KBr pellet) *v*max in cm^{-1}: 2956, 2926, 2855, 1721, 1534, 1280, 1169; ^{1}H NMR (400 MHz, $CDCl_3$, 298 K): δ 8.43-8.39 (m, 2H, H_{Ar}), 8.26 (s, 1H, H_{Ar}), 8.21 (d, *J* = 7.6 Hz, 1H, H_{Ar}), 8.14 (d, *J* = 8 Hz, 1H, H_{Ar}), 8.01-7.95 (m, 2H, H_{Ar}), 4.35-4.3 (m, 8H, 4 × -OCH_2), 1.8-1.75 (m, 8H, 4 × -OCH_2-$\underline{CH_2}$), 1.44-1.28 (m, 40H, 20 ×CH_2), 0.88-0.86 (m, 12H, CH_3); ^{13}C NMR (100 MHz, $CDCl_3$, 298 K): 168, 167.8, 167.7, 166.6, 145.9, 133.2, 132.1, 131.9, 131.2, 131, 130.6, 130.1, 129.7, 129.4, 128.8, 128.2, 128.1, 127.3, 126.3, 125.4, 123, 122.4, 66.3, 66, 65.8, 31.83, 31.8, 29.32, 29.3, 29.2, 28.6, 28.5, 26.04, 26, 25.9, 22.6, 14.1; HRMS (-APCI mode) exact mass calculated for $C_{56}H_{75}NO_{10}$ $[M]^-$: 921.5396, Found: 921.5406.

4b: R_f = 0.58 (10% EtOAc-hexane); red viscous liquid, yield: 82%; IR (KBr pellet) *v*max in cm^{-1}: 2956, 2924, 2854, 1722, 1466, 1280, 1168; ^{1}H NMR (400 MHz, $CDCl_3$, 298 K): δ 8.25-8.21 (m, 3H, H_{Ar}), 8.15-8.12 (m, 1H, H_{Ar}), 8.06-8.03 (m, 1H, H_{Ar}), 7.90-7.87 (m, 1H, H_{Ar}), 7.77-7.74 (m, 1H, H_{Ar}), 4.38-4.31 (m, 8H, 4 ×-OCH_2), 1.81-1.69 (m, 8H, 4 ×-OCH_2-$\underline{CH_2}$), 1.46-1.27 (m, 56H, 28 ×CH_2), 0.89-0.86 (m, 12H, 4 × CH_3); ^{13}C NMR (100 MHz, $CDCl_3$, 298 K): 168.2, 168.04, 167.97, 166.8, 146.4, 133.8, 132.5, 132.1, 131.6, 130.9, 130.5, 130.1, 129.8, 129.2, 128.7, 128.5, 127.9, 127.6, 126.7, 125.8, 123.3, 122.7, 66.6, 66.2, 66.15, 66.1, 32.1, 29.6, 29.5, 28.8, 28.7, 26.23, 26.20, 26.17, 22.9, 14.3; HRMS (-APCI mode) exact mass calculated for $C_{64}H_{91}NO_{10}$ $[M]^-$: 1033.6648, Found: 1033.6537.

4c: R_f = 0.6 (10% EtOAc-hexane); red viscous liquid, yield: 80%; IR (KBr pellet) *v*max in cm^{-1}: 2956, 2922, 2852, 1716, 1532, 1281, 1259, 1171, 1108; ^{1}H NMR (400 MHz, $CDCl_3$, 298 K): δ 8.19-8.1 (m, 4H, H_{Ar}), 8.02-7.98 (m, 1H, H_{Ar}), 7.86-7.82 (m, 1H, H_{Ar}), 7.71-7.64 (m, 1H, H_{Ar}), 4.37-4.31 (m, 8H, 4 × -OCH_2), 1.82-1.80 (m, 8H, 4 × -OCH_2-$\underline{CH_2}$), 1.46-1.26

(m, 72H, 36 × CH$_2$), 0.88-0.85 (m, 12H, 4 × CH$_3$); ^{13}C NMR (100 MHz, CDCl$_3$, 298 K): 168.14, 167.95, 167.90, 166.76,146.15, 133.47, 132.32, 132.03, 131.43, 131.23, 130.82, 130.35, 130.31, 129.89, 129.60, 129.03, 128.43, 128.37, 127.51, 127.47, 126.52, 127.64, 123.12, 122.59, 66.51, 66.14, 66, 32.1, 29.8, 29.8, 29.5, 28.8, 28.7, 26.22, 26.2, 26.16, 22.9, 14.3; HRMS (-APCI mode) exact mass calculated for $C_{72}H_{107}NO_{10}$ [M]$^{-}$: 1145.79, Found: 1145.8093.

4d: R_f = 0.56 (10% EtOAc-hexane); red viscous liquid, yield: 90%; IR (KBr pellet) *v*max in cm^{-1}: 2956, 2929, 2858, 1721, 1534, 1280, 1171; ^{1}H NMR (400 MHz, CDCl$_3$, 298 K): δ 8.2-8.17 (m, 3H, H$_{Ar}$), 8.11 (d, *J* = 8 Hz, 1H, H$_{Ar}$) 8.01 (d, *J* = 8.4 Hz, 1H, H$_{Ar}$), 7.85 (d, *J* = 8 Hz, 1H, H$_{Ar}$), 7.7 (d, *J* = 8 Hz, 1H, H$_{Ar}$), 4.38-4.31 (m, 8H, 4 × -OCH$_2$), 1.83-1.78 (m, 8H, 4 × -OCH$_2$-CH$_2$), 1.47-1.35 (m, 24H, 12 ×CH$_2$), 0.93-0.91 (m, 12H, CH$_3$); ^{13}C NMR (100 MHz, CDCl$_3$, 298 K): 168.17, 167.98, 167.92, 166.79, 146.11, 133.47, 132.29, 132.03, 131.39, 131.23, 130.77, 130.30, 129.87, 129.59, 129.01, 128.43, 128.33, 127.49, 126.57, 125.61, 123.15, 122.61, 66.5, 66.15, 66.12, 66.01, 31.69, 31.66, 31.64, 28.77, 28.70, 28.66, 25.87, 25.85, 25.81, 25.79, 22.71, 14.18, 14.16; HRMS (-APCI mode) exact mass calculated for $C_{48}H_{59}NO_{10}$ [M]$^{-}$: 809.4139, Found: 809.4154.

Synthesis of **3a-3d**

A mixture of compound **4a-d** (0.26 mmol, 1 equiv.) and Selenium powder (2.602 mmol, 10 equiv.) was heated to dissolve in *N*-methylpyrrolidone (10 mL) at 70 °C for 30 min. and then refluxed at 180 °C under Ar atmosphere for overnight until the starting material could not be detected by TLC. After cooling to room temperature, 2 M HCl was added, then the precipitate was filtered, washed with water and dried. The crude product was purified by column chromatography on neutral alumina. Elution with 20-30% DCM-hexane system followed by 50% DCM-Hexane system yields the desired product.

3a: R_f = 0.58(20% EtOAc-hexane); Orange solid, yield: 52%; IR (KBr pellet) *v*max in cm^{-1}: 2954, 2928, 2857, 1728, 1581, 1467, 1407, 1341, 1262, 1163, 1157, 1339, 1020; ^{1}H NMR (600 MHz, CDCl$_3$, 298 K): δ 8.54 (s, 2H, H$_{Ar}$), 8.48 (d, *J* = 6 Hz, 2H, H$_{Ar}$), 8.21 (d, *J* = 6Hz, 2H, H$_{Ar}$), 4.42-4.39 (m, 8H, 4 ×-OCH$_2$), 1.88-1.82 (m, 8H, 4 ×-OCH$_2$-CH$_2$), 1.50-1.37 (m, 24H, 12 × CH$_2$), 0.94-0.91 (m, 12H, 4 × CH$_3$); ^{13}C NMR (100 MHz, CDCl$_3$, 298 K): 168.88, 168.69, 137.62, 133.37, 132.26, 130, 129.33, 128.75, 127.02, 125.8, 121.59, 66.07, 65.95, 31.78, 29.91, 28.86, 25.97, 22.81, 14.27. Anal. Calcd for $C_{48}H_{58}O_8Se$: C, 68.48; H, 6.94. Found: C, 68.65; H, 7.14. HRMS (ESI+mode) exact mass calculated for $C_{48}H_{58}O_8SeNa^+$ [MNa]$^+$: 865.3189, Found: 865.3210.

3b: R_f = 0.58(20% EtOAc-hexane); Orange solid, yield: 55%; IR (KBr pellet) *v*max in cm^{-1}: 2955, 2926, 2854, 1722, 1581, 1469, 1407, 1264, 1166, 1027; ^{1}H NMR (600 MHz, CDCl$_3$, 298 K): δ 8.56 (s, 2H, H$_{Ar}$), 8.51 (d, *J* = 12 Hz, 2H, H$_{Ar}$), 8.225 (d, *J* = 6Hz, 2H, H$_{Ar}$), 4.41-4.39 (m, 8H, 4 ×-OCH$_2$), 1.88-1.82 (m, 8H, 4 ×-OCH$_2$-CH$_2$), 1.51-1.29 (m, 40H, 20 × CH$_2$), 0.90-0.87 (m, 12H, 4 × CH$_3$); ^{13}C NMR (100 MHz, CDCl$_3$, 298 K): 168.88, 168.71, 137.69, 133.60, 132.48, 130.17, 129.41, 128.92, 128.87, 127.26, 125.96, 121.65, 66.10, 65.98, 32.05, 29.57, 29.44, 28.9, 26.3, 22.87, 14.32. Anal. Calcd for $C_{56}H_{74}O_8Se$: C, 70.49; H, 7.82. Found: C, 69.74; H, 7.82. HRMS (ESI+mode) exact mass calculated for $C_{56}H_{74}O_8SeNa^+$ [MNa]$^+$: 977.4441, Found: 977.4460.

3c: R_f = 0.60(20% EtOAc-hexane); Orange solid, yield: 56%; IR (KBr pellet) *v*max in cm^{-1}: 2955, 2921, 2851, 1721, 1581, 1469, 1265, 1168; ^{1}H NMR (400 MHz, CDCl$_3$, 298

K): 8.54 (s, 2H, H_{Ar}), 8.48 (d, *J* = 8 Hz, 2H, H_{Ar}), 8.21 (d, *J* = 8 Hz, 2H, H_{Ar}) 4.42-4.39 (m, 8H, 4 × -OCH_2), 1.87-1.83 (m, 8H, 4 × -OCH_2-$\underline{CH_2}$), 1.48-1.27 (m, 56H, 28 × CH_2), 0.88-0.85 (m, 12H, 4 × CH_3); ^{13}C NMR (100 MHz, $CDCl_3$, 298 K): 168.88, 168.7, 137.67, 133.53, 132.41, 130.11, 129.39, 128.87, 127.18, 125.91, 121.62, 66.10, 65.97, 32.12, 29.80, 29.62, 29.55, 28.90, 26.31, 22.89, 14.32. Anal. Calcd for $C_{64}H_{90}O_8Se$: C, 72.09; H, 8.51. Found: C, 72.10; H, 8.55. MALDI TOF MS: *m/z* for $C_{64}H_{90}O_8Se$ $[M]^+$, Calcd: 1066.58. Found: 1066.887.

3d: R_f = 0.58(20% EtOAc-hexane); Orange solid, yield: 58%; IR (KBr pellet) *v*max in cm^{-1}: 2955, 2919, 2850, 1720, 1637, 1470, 1267, 1170, 1025; ^{1}H NMR (400 MHz, $CDCl_3$, 298 K): δ 8.68-8.66 (m, 4H, H_{Ar}), 8.31 (d, *J* = 8.4Hz, 2H, H_{Ar}), 4.40-4.37 (m, 8H, 4 ×-OCH_2), 1.83-1.82 (m, 8H, 4 ×-OCH_2-$\underline{CH_2}$), 1.46-1.25 (m, 72H, 36 × CH_2), 0.88-0.85 (m, 12H, 4 × CH_3); ^{13}C NMR (100 MHz, $CDCl_3$, 298 K): 168.89, 168.72, 137.71, 133.67, 132.54, 130.18, 129.43, 128.94, 128.90, 127.31, 125.99, 121.66, 66.11, 65.99, 32.14, 29.87, 29.79, 29.61, 29.58, 28.88, 26.29, 22.90, 14.33. Anal. Calcd for $C_{72}H_{106}O_8Se$: C, 73.37; H, 9.07. Found: C, 73.32; H, 9.09. MALDI TOF MS: *m/z* for $C_{72}H_{106}O_8Se$ $[M]^+$, Calcd: 1178.71. Found: 1178.514.

Synthesis of **2a-d**

A mixture of compound **4a-d** (0.49 mmol, 1 equiv.) and Sulfur powder (4.95 mmol, 10 equiv.) was heated to dissolve in *N*-methylpyrrolidone (10 mL) at 70 °C for 30 min and then heated at 180 °C under Ar atmosphere for 17 h. After cooling to room temperature, 2 M HCl solution was added, and the resultant precipitate was filtered, washed with water and dried. The crude product was purified by column chromatography on neutral alumina. Elution with 20-30% DCM-Hexane mixture followed by 50% DCM-Hexane mixture yields the desired product.

2a: R_f = 0.6(20% EtOAc-hexane); Yellow solid, yield: 50%; IR (KBr pellet) v_{max} in cm^{-1}: 2954, 2929, 2860, 1730, 1583, 1477, 1415, 1341, 1264, 1167, 1157, 1017; ^{1}H NMR (600 MHz, $CDCl_3$, 298 K): δ 8.65 (d, *J* = 12 Hz, 2H, H_{Ar}), 8.63 (s, 2H, H_{Ar}), 8.31 (d, *J* = 6Hz, 2H, H_{Ar}), 4.42-4.39 (m, 8H, 4 ×-OCH_2), 1.87-1.82 (m, 8H, 4 ×-OCH_2-$\underline{CH_2}$), 1.50-1.34 (m, 24H, 12 × CH_2), 0.93-0.90 (m, 12H, 4 × CH_3); ^{13}C NMR (150 MHz, $CDCl_3$, 298 K): 168.84, 168.75, 135.32, 132.44, 130.99, 130.21, 129.62, 129.52, 126.44, 125.98, 125.69, 122.01, 66.14, 66.02, 31.77, 28.86, 25.96, 22.79, 14.24. HRMS (ESI+mode) exact mass calculated for C48H58O_8SNa$^+$ $[MNa]^+$: 817.3745, Found: 817.3747. Anal. Calcd for $C_{48}H_{58}O_8S$: C, 72.51; H, 7.35; S, 4.03. Found: C, 72.77; H, 7.11; S, 3.92.

2b: R_f = 0.58(20% EtOAc-hexane); Yellow-Orange solid, yield: 55%; IR (KBr pellet) v_{max} in cm^{-1}: 2955, 2925, 2853, 1724, 1468, 1265, 1170, 1159, 1025; ^{1}H NMR (400 MHz, $CDCl_3$, 298 K): δ 8.30 (s, 2H, H_{Ar}), 8.16 (d, *J* = 7.6 Hz, 2H, H_{Ar}), 8.06 (d, *J* = 8Hz, 2H, H_{Ar}), 4.45-4.41 (m, 8H, 4 ×-OCH_2), 1.94-1.84 (m, 8H, 4 ×-OCH_2-$\underline{CH_2}$), 1.55-1.24 (m, 40H, 20 × CH_2), 0.89-0.87 (m, 12H, 4 × CH_3); ^{13}C NMR (100 MHz, $CDCl_3$, 298 K): 168.79, 168.60, 134.88, 131.48, 129.98, 129.62, 129.22, 128.99, 125.99, 125.03, 124.99, 121.66, 66.03, 65.89, 32.04, 32.03, 29.58, 29.46, 28.93, 26.32, 22.85, 14.28. HRMS (ESI+mode) exact mass calculated for $C_{56}H_{74}O_8SNa^+$ $[MNa]^+$: 929.4997, Found: 929.4980. Anal. Calcd for $C_{56}H_{74}O_8S$: C, 74.14; H, 8.22; S, 3.53. Found: C, 74.29; H, 8.13; S, 3.37.

2c: R_f = 0.58(20% EtOAc-hexane); Yellow solid, yield: 58%; IR (KBr pellet) v_{max} in cm^{-1}: 2955, 2921, 2851, 1726, 1469, 1265, 1170, 1159; ^{1}H NMR (400 MHz, $CDCl_3$, 298

K): 8.44 (d, *J* = 2.4 Hz, 2H, H_{Ar}), 8.37 (dd, *J* = 8 Hz, 3.2Hz, 2H, H_{Ar}), 8.16 (dd, *J* = 7.6 Hz, 1.6 Hz, 2H, H_{Ar}) 4.44-4.40 (m, 8H, 4 ×-OCH_2), 1.90-1.83 (m, 8H, 4 ×-OCH_2-$\underline{CH_2}$), 1.51-1.27 (m, 56H, 28 × CH_2), 0.88-0.85 (m, 12H, 4 × CH_3); ^{13}C NMR (150 MHz, $CDCl_3$, 298 K): 168.83, 168.73, 135.25, 132.27, 130.82, 130.12, 129.51, 126.37, 125.80, 125.58, 121.94, 66.13, 66.01, 32.12, 29.80, 29.62, 29.54, 28.91, 26.31, 22.89, 14.31. MALDI TOF MS: *m/z* for $C_{64}H_{90}O_8S$ $[M]^+$, Calcd: 1018.635. Found: 1018.681.

2d: R_f = 0.55(20% EtOAc-hexane); Yellow solid, yield: 60%; IR (KBr pellet) ν_{max} in cm^{-1}: 2955, 2922, 2851, 1727, 1466, 1267, 1171, 1159; ^{1}H NMR (400 MHz, $CDCl_3$, 298 K): δ 8.77 (d, *J* = 8 Hz, 2H, H_{Ar}), 8.72 (s, 2H, H_{Ar}), 8.36 (d, *J* = 7.6 Hz, 2H, H_{Ar}), 4.41-4.37 (m, 8H, 4 ×-OCH_2), 1.85-1.80 (m, 8H, 4 ×-OCH_2-$\underline{CH_2}$), 1.47-1.25 (m, 72H, 36 × CH_2), 0.88-0.85 (m, 12H, 4 × CH_3); ^{13}C NMR (100 MHz, $CDCl_3$, 298 K): 168.84, 168.72, 135.17, 132.11, 130.65, 130.00, 129.44, 129.39, 126.31, 125.63, 125.47, 121.89, 66.12, 66.00, 32.13, 29.88, 29.81, 29.63, 29.58, 28.91, 26.32, 22.90, 14.33. MALDI TOF MS: *m/z* for $C_{72}H_{106}O_8S$ $[M]^+$, Calcd: 1130.760. Found: 1130.730.

Synthesis of **1a-1d**

A mixture of compound **4a-d** (0.6 mmol, 1 equiv.) and triethyl phosphite (7 mL) were refluxed for 4 h under argon atmosphere. Reaction mixture was cooled to room temperature to precipitate the product. This precipitated product was filtered off and washed with water, dried in vacuum. Further purification was done by repeated recrystallization from (10%) dichloromethane-methanol system.

1a: R_f = 0.6 (20% EtOAc-hexane); yellow solid, yield: 55%; IR (KBr pellet) ν_{max} in cm^{-1}: 3353, 2956, 2929, 2857, 1715, 1633, 1593, 1467, 1427, 1274, 1251, 1193, 1155, 1017; ^{1}H NMR (400 MHz, $CDCl_3$, 298 K): δ 9.56 (s, 1H, NH), 8.01 (d, *J* = 8 Hz, 2H, H_{Ar}), 7.93-7.91 (m, 4H, H_{Ar}), 4.50 (q, 8H, 4 × -OCH_2), 1.99-1.90 (m, 8H, 4 × -OCH_2-$\underline{CH_2}$), 1.61-1.54 (m, 8H, 4 ×CH_2), 1.47-1.41 (m, 16H, 8 × CH_2), 0.97-0.93 (m, 12H, 4 × -CH_3); ^{13}C NMR (100 MHz, $CDCl_3$, 298 K): 169.88, 169.87, 131.14, 130.33, 128.53, 127.56, 127.33, 123.23, 122.77, 121.62, 119.38, 117.89, 66.01, 65.92, 31.87, 29.08, 26.08, 22.88, 14.30; HRMS (-APCI mode) exact mass calculated for $C_{48}H_{58}NO_8$ $[M-1]^-$: 776.4162, found: 776.5256.

1b: R_f = 0.6 (20% EtOAc-hexane); yellow solid, yield: 55%; IR (KBr pellet) ν_{max} in cm^{-1}: 3353, 2954, 2922, 2852, 1711, 1593, 1278, 1194, 1156; ^{1}H NMR (600 MHz, $CDCl_3$, 298 K): δ 9.50 (s, 1H, NH), 8.04 (d, *J* = 12 Hz, 2H, H_{Ar}), 7.96-7.93 (m, 4H, H_{Ar}), 4.52-4.47 (m, 8H, 4 × -OCH_2), 1.98-1.92 (m, 8H, 4 × -OCH_2-$\underline{CH_2}$), 1.58-1.31 (m, 40H, 20 ×CH_2), 0.90-0.88 (m, 12H, 4 × CH_3); ^{13}C NMR (150 MHz, $CDCl_3$, 298 K): 169.8, 131.4, 130.5, 128.7, 127.71, 127.6, 123.5, 123, 121.7, 119.4, 118.2, 66, 65.9, 32.1, 29.7, 29.5, 29.12, 29.1, 26.4, 23, 14.32; HRMS (+APCI mode) exact mass calculated for $C_{56}H_{76}NO_8$ $[MH]^+$: 890.5565, Found: 890.6854.

1c: R_f = 0.59 (20% EtOAc-hexane); yellow solid, yield: 60%; IR (KBr pellet) ν_{max} in cm^{-1}: 3353, 2954, 2923, 2852, 1713, 1592, 1467, 1278, 1156, 1019; ^{1}H NMR (400 MHz, $CDCl_3$, 298 K): δ 9.55 (s, 1H, NH), 8.05 (d, *J* = 8 Hz, 2H, H_{Ar}), 7.96-7.94 (m, 4H, H_{Ar}), 4.52-4.46 (m, 8H, 4 × -OCH_2), 1.96-1.91 (m, 8H, 4 × -OCH_2-$\underline{CH_2}$), 1.57-1.25 (m, 56H, 28 × CH_2), 0.88-0.85 (m, 12H, 4 × CH_3); ^{13}C NMR (100 MHz, $CDCl_3$, 298 K): 169.9, 131.4, 130.5, 128.7, 127.7, 127.5, 123.4, 123, 121.7, 119.4, 118.1, 66, 65.95, 32.1, 29.9, 29.7, 29.6, 29.1, 29.09, 26.4, 22.9, 14.3; HRMS (+APCI mode) exact mass calculated for $C_{64}H_{92}NO_8$ $[MH]^+$: 1002.6817, Found: 1002.7582.

1d: R_f = 0.6 (20% EtOAc-hexane); yellow solid, yield: 62%; IR (KBr pellet) *v*max in cm^{-1}: 3353, 2953, 2920, 2850, 1711, 1640, 1279, 1196, 1158, 1047; ^1H NMR (600 MHz, $CDCl_3$, 298 K): δ 9.50 (s, 1H, NH), 8.07 (d, *J* = 6 Hz, 2H, H_{Ar}), 7.97-7.95 (m, 4H, H_{Ar}), 4.50-4.48 (m, 8H, 4 × $-OCH_2$), 1.95-1.94 (m, 8H, 4 × $-OCH_2\text{-}\underline{CH_2}$), 1.57-1.26 (m, 72H, 4 × CH_2), 0.86 (brs, 12H, 4 × CH_3); ^{13}C NMR (150 MHz, $CDCl_3$, 298 K): 169.9, 131.23, 130.4, 128.62, 127.64, 127.4, 123.3, 122.9, 121.7, 119.4, 118, 66.04, 65.9, 32.2, 29.94, 29.9, 29.7, 29.6, 29.13, 29.1, 26.4, 22.9, 14.3; MALDI TOF MS: *m/z* for $C_{72}H_{108}NO_8$ $[MH]^+$, Calcd: 1115.811. Found: 1115.754.

2.5. References

1. a) Q. Li Ed., *Self-Organized Organic Semiconductors: From Materials to Device Applications*, John Wiely & Sons, Inc., New Jersy, 2011; b) H. Klauk, Ed. *Organic Electronics: Materials, Manufacturing and Applications*, Wiley-VCH, Weinheim, 2006; c) J. Roncali, P. Leriche and A. Cravino, *Adv. Mater*., 2007, **19**, 2045-2060; d) S. R. Forrest and M. E. Thompson, *Chem. Rev*., 2007, **107**, 923; e) E. Menard, M. A. Meitl, Y. Sun, J.-U. Park, D. J.-L. Shir, Y.-S. Nam, S. Jeon and J. A. Rogers, *Chem. Rev*., 2007, **107**, 1117.
2. a) L. Li, S.-W. Kang, J. Harden, Q. Sunc, X. Zhou, L. Dai, A. Jakli, S. Kumar and Q. Li, *Liq. Cryst*., 2008, **35**, 3, 233-239; b) X. Zhou, S.-W. Kang, S. Kumar, R. R. Kulkarni, S. Z. D. Cheng and Q. Li, *Chem. Mater*., 2008, **20**, 3551-3553; c) X. Zhou, S.-W. Kang, S. Kumar and Q. Li, *Liq. Cryst*., 2009, **36**, 3, 269-274; d) M. Funahashi, *J. Mater. Chem. C*, 2014, **2**, 7451-7459; e) Y. Yuan, G. Giri, A. L. Ayzner, A. P. Zoombelt, S. C. Mannsfeld, J. Chen, D. Nordlund, M. F. Toney, J. Huang and Z. Bao, *Nat. Commun*., 2014, **5**, 3005; f) C. Xue, K. G.-Cuevas, M. Gao, A. Urbas and Q. Li, *J. Phys. Chem. C*, 2013, **117**, 21603-21608; g) Q. Sun, L. Dai, X. Zhou, L. Li and Q. Li, *Appl. Phys. Lett*., 2007, **91**, 253505-3.
3. a) C. Li, M. Liu, N. G. Pschirer, M. Baumgaten and K. Müllen, *Chem. Rev*., 2010, **110**, 6817-6855; b) F. Würthner, *Chem. Commun*., 2004, 1564-1579.
4. a) X. Zhang, S Rehm, M. M. Safont-Sempere and F. Würthner, *Nature Chemistry*, 2009, **1**, 623-629; b) C. Li and H. Wonneberger, *Adv. Mater*., 2012, **24**, 613-636.
5. a) A. Mishra, M. K. R. Fischer and P. Bäuerle, *Angew. Chem. Int. Ed*., 2009, **48**, 2474-2499; b) C. Li, M. Liu, N. G. Pschirer, M. Baumgaten and K. Müllen, *Chem. Rev*., 2010, **110**, 6817-6855.
6. a) A. C. Grimsdale, K. L. Chan, R. E. Martin, P. G. Jokisz and A. B. Holmes, *Chem. Rev*., 2009, **109**, 897-1091; b) C. Zhong, F. Duan, H. Wu and Y. Cao, *Chem. Mater*., 2011, **23**, 326-340.
7. a) J. Zaumseil and H. Sirringhaus, *Chem. Rev*. 2007, **107**, 1296–1323; b) W. Wu, Y. Liu, D. Zhu, *Chem. Soc. Rev*., 2010, **39**, 1489-1502.
8. a) R. A. Cormier and B. A. Gregg, *J. Phys. Chem. B*, 1997, **101**, 11004-11006; b) R. A. Cormier and B. A. Gregg, *Chem. Mater*., 1998, **10**, 1309-1319.
9. a) C. W. Struijk, A. B. Sieval, J. E. Dakhorst, M. van Dijk, P. Kimkes, R. B. Koehorst, H. Donker, T. J. Schaafsma, S. J. Picken and A. M. van de Craats, *J. Am. Chem. Soc*., 2000, **122**, 11057-11066; b) F. Würthner, C. Thalacker, S. Diele and C. Tschierske, *Chem. Eur. J*. 2001, **7**, 2245-2253; c) S. Alibert-Fouet, S. Dardel, H. Bock, M. Oukachmih, S. Archambeau, I. Seguy, P. Jolinat and P. Destruel, *ChemPhysChem*., 2003, **4**, 983-985; d) B. Jancy and S. K. Asha, *J. Phys. Chem. B*., 2006, **110**, 20937-20947; e) V. Dehm, Z. Chen, U. Baumeister, P. Prins, L. D. A. Siebbeles and F. Würthner, *Org. Lett*., 2007, **9**, 1085-1088; f) B. Jancy and S. K. Asha, *Chem. Mater*., 2008, **20**, 169-181; g) G. A. Bhavsar and S. K. Asha, *Chem. Eur. J*., 2011, **17**, 12646-12658.
10. a) L. Schmidt-Mende, A. Fechtenkotter, K. Müllen, E. Moons, R. H. Friend and J. D. Mackenzie, *Science* 2001, **293**, 1119-1122; b) C. Ego, D. Marsitzky, S. Becker, J. Zhang, A. C. Grimsdale, K. Müllen, J. D. Mackenzie, C. Silva and R. H. Friend, *J. Am. Chem. Soc*. 2003, **125**, 437-443; c) Z. Chen, M. G. Debije, T. Debaerdemaeker, P. Osswald and F. Würthner, *ChemPhysChem*, 2004, **5**, 137-140; d) B. A. Jones, M. J. Ahrens, M. Yoon, A. Facchetti, T. J. Marks and M. R. Wasielewski, *Angew. Chem. Int. Ed*., 2004, **43**, 6363-6366; e) S. Leroy-Lhez, J. Baffreau, L. Perrin, E. Levillain, M. Allain, M. Blesa and P. Hudhomme, *J. Org.*

Chem., 2005, **70**, 6313-6320; f) R. Schmidt, M. M. Ling, J. H. Oh, M. Winkler, M. Konemann, Z. Bao and F. Würthner, *Adv. Mater*., 2007, **19**, 3692-3695.

11. H. Qian, C. Liu, Z. Wang and D. Zhu, *Chem. Commun*., 2006, 4587-4589.
12. H. Qian, W. Yue, Y. Zhen, S. Di Motta, E. Di Donato, F. Negri, J. Qu, W. Xu, D. Zhu and Z. Wang, *J. Org. Chem*., 2009, **74**, 6275-6282.
13. a) Y. Zhen, H. Qian, J. Xiang, J. Qu and Z. Wang, *Org. Lett*., 2009, **11**, 3084-3087; b) Y. Li and Z. Wang, *Org. Lett*., 2009, **11**, 1385-1387; c) H. Chen, C. He, G. Yu, Y. Zhao, J. Huang, M. Zhu, H. Liu, Y. Guo, Y. Li and Y. Liu, *J. Mater. Chem*., 2012, **22**, 3696-3698.
14. W. Jiang, H. Qian, Y. Li and Z. Wang, *J. Org. Chem*., 2008, **73**, 7369-7372.
15. a) A. Patra and M. Bendikov, *J. Mater. Chem*., 2010, **20**, 422-433; b) J. Dhar, K. Swathi, D. P. Karothu, K. S. Narayan and S. Patil, *ACS Appl Mater Interfaces*, 2015, **7**, 670-681.
16. a) Y. Sun, L. Tan, S. Jiang, H. Qian, Z. Wang, D. Yan, C. Di, Y. Wang, W. Wu, G. Yu, S. Yan, C. Wang, W. Hu, Y. Liu and D. Zhu, *J. Am. Chem. Soc*., 2007, **129**, 1882-1883; b) L. Tan, W. Jiang, L. Jiang, S. Jiang, Z. Wang, S. Yan and W. Hu, *Appl. Phys. Lett*., 2009, **94**, 153306-1-3; c) W. Jiang, Y. Zhou, H. Geng, S. Jiang, S. Yan, W. Hu, Z. Wang, Z. Shuai and J. Pei, *J. Am. Chem. Soc*., 2011, **133**, 1-3.
17. a) S. Benning, H.-S. Kitzerow, H. Bock and M.-F. Achard, *Liq. Cryst*., 2000, **27**, 901-906; b) T. Hassheider, S. A. Benning, H.-S. Kitzerow, M.-F. Achard and H. Bock, *Angew. Chem. Int. Ed*., 2001, **40**, 2060-2063; c) X. Mo, H.-Z. Chen, M.-M. Shi and M. Wang, *Chemical Physics Letters*, 2006, **417**, 457-460; d) X. Mo, M. -M. Shi, J. -C. Huang, M. Wang and H. -Z. Chen, *Dyes and Pigments*, 2008, **76**, 236-242; e) C. Xue, R. Sun, R. Annab, D. Jin and S. Abadi, *Tetrahedron Letters*, 2009, **50**, 853-856; f) A. Wicklein, M.-A. Muth and M. Thelakkat, *J. Mater. Chem*., 2010, *20*, 8646-8652; g) S. K. Gupta, S. Setia, S. Sidiq, M. Gupta, S. Kumar and S. K. Pal, *RSC Adv*. 2013, **3**, 12060-12065
18. a) I. Seguy, P. Destruel and H. Bock, *Synth. Met*., 2000, **111**, 15-18; b) I. Seguy, P. Jolinat, P. Destruel, R. Mamy, H. Allouchi, C. Courseille, M. Cotrait and H. Bock, *ChemPhysChem*, 2001, **2**, 448-452.
19. I. Seguy, P. Jolinat, P. Destruel, J. Farenc, R. Mamy, H. Bock, J. Ip and T. Nguyen, *J. Appl. Phys*., 2001, **89**, 5442-5448.
20. Y. Jiang, L. Lu, M. Yang, C. Zhan, Z. Xie, F. Verpoort and S. Xiao, *Polym. Chem.* 2013, **4**, 5612-5620.
21. a) C. V. Yelamaggad, A. S. Achalkumar, D. S. Shankar Rao and S. K. Prasad, *J. Am. Chem. Soc*., 2004, **126**, 6506-6507; b) C. V. Yelamaggad, A. S. Achalkumar, D. S. Shankar Rao and S. K. Prasad, *J. Org. Chem*., 2007, **72**, 8308-8318; c) C. V. Yelamaggad and A. S. Achalkumar, *Tetrahedron Letters*, 2006, **47**, 7071-7075.
22. a) J. F. Hartwig, *In Handbook of Organopalladium Chemistry for Organic Synthesis*; E. I. Negishi, A. de Meijere, Eds.; Wiley-Interscience: Weinheim, Germany, 2002; b) L. Jiang, S. L. Buchwald, In *Metal-Catalyzed Cross-Coupling Reactions*, 2nd ed.; A. de Meijere, F. Diederich, Eds.; John Wiley & Sons: Weinheim, Germany, 2004.
23. a) J. J. Looker, *J. Org. Chem*., 1972, **37**, 3379-3381; b) W. Jiang, H. Qian, Y. Li and Z. Wang, *J. Org. Chem*., 2008, **73**, 7369-7372.
24. a) V. Percec, C.-H. Ahn, T. K. Bera, G. Ungar and D. J. P. Yeardley, *Chem. Eur. J*., 1999, **5**, 1070-1083; b) S. K. Pathak, R. K. Gupta, S. Nath, D. S. Shankar Rao, S. Krishna Prasad and A. S. Achalkumar, *J. Mater. Chem. C*, 2015, **3**, 2940-2952; c) S. Segeyev, W. Pisula and Y. H. Geerts, *Chem. Soc. Rev*., 2007, **36**, 1902-1929; d) J. Eccher, G. C. Faria, H. Bock, H. von Seggern and I. H. Bechtold, *ACS Appl Mater*

Interfaces, 2013, **5**, 11935-11943; e) C. Simpson, J. Wu, M. Watson and K. Müllen, *J. Mat. Chem.*, 2004, **14**, 494-504; f) K. Hatsusaka, K. Ohta, I. Yamamoto and H. Shirai, *J. Mater. Chem.*, 2001, **11**, 423-433; g) W. Pisula, Z. Tomovic, B. El Hamaoui, M. D. Watson, T. Pakula and K. Müllen, *Adv. Funct. Mater.*, 2005, **15**, 893-904; h) T. Yang, J. Pu, J. Zhang, and W. Wang, *J. Org. Chem.*, 2013, **78**, 4857-4866; i) P. Oswald, *J. Phys. France*, 1988, **49**, 1083-1089.

25. a) J. J. Lee, A. Yamaguchi, M. Alam, Y. Yamamoto, T. Fukushima, K. Kato, M. Takata, N. Fujita and T. Aida, *Angew. Chem. Int. Ed.*, 2012, **51**, 8490-8494; b) S. Laschat, A. Baro, N. Steinke, F. Giesselmann, C. Haegele, G. Scalia, R. Judele, E. Kapatsina, S. Sauer and A. Schreivogel, *Angew. Chem. Int. Ed.*, 2007, **46**, 4832-4887.
26. C. D. Simpson, J. Wu, M. D. Watson and K. Müllen, *J. Mater. Chem.*, 2004, **14**, 494-504.
27. a) H. Bock, M. Rajaoarivelo, S. Clavaguera and É. Grelet, *Eur. J. Org. Chem.*, 2006, **13**, 2889-2893; b) E. Grelet, S. Dardel, H. Bock, M. Goldmann, E. Lacaze and F. Nallet, *Eur. Phys. J. E.*, 2010, **31**, 343-349; c) T. Osawa, T. Kajitani, D. Hashizume, H. Ohsumi, S. Sasaki, M. Takata, Y. Koizumi, A. Saeki, S. Seki and T. Fukushima, *Angew. Chem. Int. Ed.*, 2012, **51**, 7990-7993; d) L. Li, S. W. Kang, J. Harden, Q. Sun, X. Zhou, L. Dai, A. Jakli, S. Kumar and Q. Li, *Liq. Cryst.*, 2008, **35**, 233-239.
28. A. Patra and M. Bendikov, *J. Mater. Chem.*, 2010, **20**, 422–433.
29. P. Uznanski, S. Marguet, D. Markovitsi, P. Schuhmacher and H. Ringsdorf, *Mol. Cryst. Liq. Cryst.*, 1997, **293**, 123-133.
30. G.-J. Zhao and K.-L. Han, *J. Phys. Chem. A*, 2009, **113**, 4788-4794.
31. A. S. Achalkumar, U. S. Hiremath, D. S. Rao, S. K. Prasad and C. V. Yelamaggad, *J. Org. Chem.* 2013, **78**, 527-544.
32. a) D. D. Prabhu, A. P. Sivadas and S. Das, *J. Mater. Chem. C*, 2014, **2**, 7039-7046; b) F. C. Spano, *Acc. Chem. Res.*, 2010, **43**, 429-439.
33. a) M. J. Frisch, G. W. Trucks, H. B. Schlegel, G. E. Scuseria, M. A. Robb, J. R. Cheeseman, G. Scalmani, V. Barone, G. A. Petersson, H. Nakatsuji, X. Li, M. Caricato, A. V. Marenich, J. Bloino, B. G. Janesko, R. Gomperts, B. Mennucci, H. P. Hratchian, J. V. Ortiz, A. F. Izmaylov, J. L. Sonnenberg, D. Williams-Young, F. Ding, F. Lipparini, F. Egidi, J. Goings, B. Peng, A. Petrone, T. Henderson, D. Ranasinghe, V. G. Zakrzewski, J. Gao, N. Rega, G. Zheng, W. Liang, M. Hada, M. Ehara, K. Toyota, R. Fukuda, J. Hasegawa, M. Ishida, T. Nakajima, Y. Honda, O. Kitao, H. Nakai, T. Vreven, K. Throssell, J. A. Montgomery, Jr., J. E. Peralta, F. Ogliaro, M. J. Bearpark, J. J. Heyd, E. N. Brothers, K. N. Kudin, V. N. Staroverov, T. A. Keith, R. Kobayashi, J. Normand, K. Raghavachari, A. P. Rendell, J. C. Burant, S. S. Iyengar, J. Tomasi, M. Cossi, J. M. Millam, M. Klene, C. Adamo, R. Cammi, J. W. Ochterski, R. L. Martin, K. Morokuma, O. Farkas, J. B. Foresman, and D. J. Fox, *Gaussian*, Inc., Wallingford CT, 2016; b) C. Lee, W. Yang and R. G. Parr, *Phys. Rev. B*, 1988, **37**, 785-789; c) A. D. Becke, *J. Chem. Phys.*, 1993, **98**, 1372-1377.
34. A. M. Brouwer, *Pure Appl. Chem.*, 2011, **83**(12), 2213-2228.

Chapter 3a

Electroluminescent room temperature columnar liquid crystals based on bay-annulated perylene tetraesters

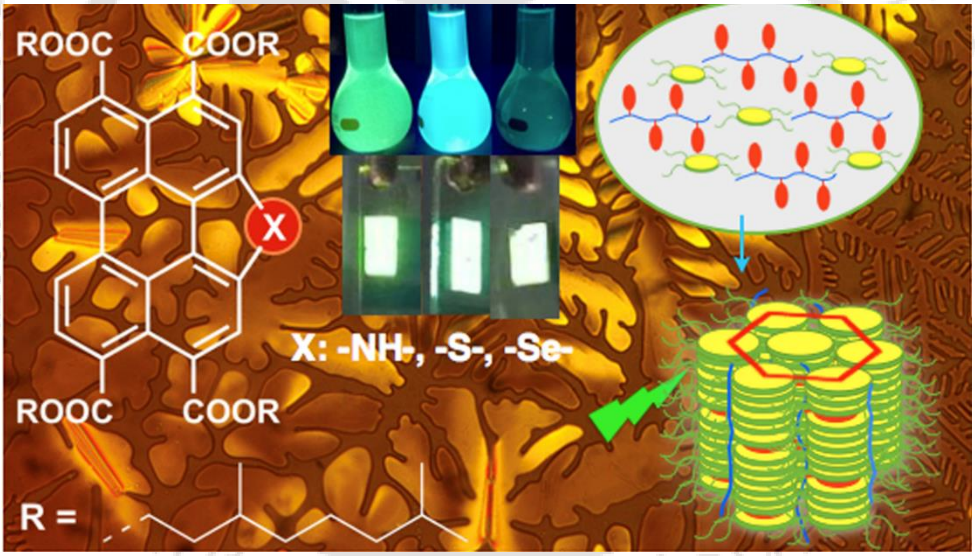

Results have been published in;

- *J. Mater. Chem. C*, 2017, **5**, 1767-1781

3.1. Introduction

Electroluminescence from organic molecules has drawn substantial attention among scientific and technological researchers due to their vast applications in display and illumination technology. Displays based on organic light emitting diodes have many advantages over current mainstay of display systems *viz.* liquid crystal displays (LCD) by producing sharp and high quality images, simpler, lighter, thinner, flexible device structure with higher power efficiency. The expensive organometallic compounds based on rare earth metals are too expensive and unsustainable; while the standard technique of mask based vacuum deposition leads to the wastage of these materials.[1] Reports from Tang[2] and Burroughes[3] have demonstrated that both low molar mass compounds and polymers can be used for the fabrication of OLEDs. In case of low molar mass compounds, liquid crystalline (LC) materials which form columnar phases, where the molecules stack one above the other with a strong π-π overlap, are yet to realize their enormous potential.[4,5] Columnar (Col) phase is usually formed by the one-dimensional (1D) self-assembly of the disc-like molecules decorated with peripheral tails. This self-assembly is driven by shape anisotropy of the molecule, strong π-π interaction and nano segregation of incompatible molecular subunits like central rigid core and peripheral flexible tails. Thus, the Col phase represents a molecular wire formed by the strong π-π overlap of the central core surrounded by the insulating sheath of the alkyl chains.[6] Further, the synthetic flexibility to tailor the structural features to dictate the outcomes of the macroscopic self-assembly hold an edge in comparison to low molar mass materials and polymers.[7] Their thin films can be produced either by spin coating as in the case of polymers or vacuum deposited as in the case of small molecules. Self-healing ability of structural defects by thermal annealing is another property of the Col phase, which overcomes the charge trapping by defects. These unique structural, electronic features in addition to their facile processibility make these class of materials highly promising in organic light emitting diodes (OLEDs),[5,10] organic field effect transistors (OFETs)[8] and organic photovoltaic devices (OPVs).[9] The materials that exhibiting a single Col phase spanning over a wide thermal range including room temperature are desired for potential device applications, as they retain the self-organization and ensure the columnar order over long periods of time after thermal annealing.[11,12]

Perylene derivatives have been extensively studied as semiconductors[13-16] due to their rigid planar conjugation, which exhibit high charge-carrier mobility, intense luminescence, extraordinary thermal and photochemical stability, and unique self-assembly behaviors.[16,17] Liquid crystalline self-assembly of perylene bisimides[18,19] was first reported in 1997 and many derivatives were reported later by varying the amine part (aliphatic[18-20] or aromatic[21,22]). Incorporation of substituents at the *bay* position often changes the photophysical properties of these molecules but also leads to the twisting of the perylene core, thus disturbing the columnar packing. Thus, one has to alter the physical properties of this class of compounds by expansion of the central core, while keeping the planarity intact. Perylenetetracarboxylic tetraesters, show better solubility in common organic solvents than closely related perylene bisimides and also received more attention on account of their high absorption coefficients, fluorescence, mesomorphic and luminescent properties.[23-25] Polarized electroluminescence was observed in a uniaxially aligned perylene tetraester.[23]A maximum luminance of 100 cd/m^2 was observed for the tetra-*n*-ethyl ester of perylene-3,4,9,10-tetracarboxylic acid at a voltage of 20V with orange-red light emission.[24,25] It was also reported that enhanced homeotropic alignment of Col phase exhibited by *bay*-annulated perylene bisimides enhanced the efficiency of the fabricated OLEDs.[26] Further, the superiority of the spin coated annealed film over the thermally evaporated non-annealed films in an OLED was also proved.[27]

These research findings motivated us to explore perylene tetraesters by functionalizing them at the *bay* region by annulation without forfeiting the planarity. In previous chapter, several heteroatoms (Nitrogen, Sulfur and Selenium) *bay*-annulated perylene tetraesters that exhibit wide range Col phases due to the expansion of the core as well as attractive interactions like hydrogen bonding (NH), S···S and Se···Se interactions have been explored. Except the selenium-annulated perylene derivative, *N*- and *S*-annulated perylene tetraesters exhibited a very good fluorescence with high quantum yield. Though the columnar hexagonal (Col$_h$) phase exhibited by these compounds were spanning over a wide thermal range, their melting points were high. Thus, to enhance the processability of the material towards the applications, we envisioned the synthesis of room temperature (RT) LC materials based on *bay*-annulated perylene tetraesters. It is well-known in the liquid crystal field that melting point refers to the melting of flexible chains, while the clearing point refers to the loss of the positional order of the rigid cores in the mesophase. Thus, it is imperative to incorporate branched chains in the periphery of a disc-like molecule that will reduce the melting point, enhance the mesophase thermal range without changing the mesophase.[28-31] This concept was initially demonstrated by Collard *et al.*

when they replaced aliphatic side chains of hexa(*n*-alkanoyloxy)benzenes and hexakis(*n*-alkanoyloxy)cyclohexanes with corresponding branched chains.[28] They observed the widening of columnar mesophase without affecting the type of mesophase formed. A similar design strategy has been applied by Schouten *et al*. to the phthalocyanine derivatives.[29] The mesophase in all branched chain phthalocyanines has broadened significantly and the most dramatic effect was observed in the case of phthalocyanine derivative with the highly branched 3,7,11-trimethyldodecyloxy chain where the clearing temperature is also lowered significantly. The decrease in the transition temperature could be due to the disorder caused by branched chains and stereoheterogeneity. All the target molecules exhibited a wide range of Col_h phase starting from subzero temperatures as anticipated and exhibited good fluorescence. This motivated us to test their applicability as emissive layers in OLEDs.

3.2. Results and discussion

3.2.1. Synthesis and molecular structural characterization

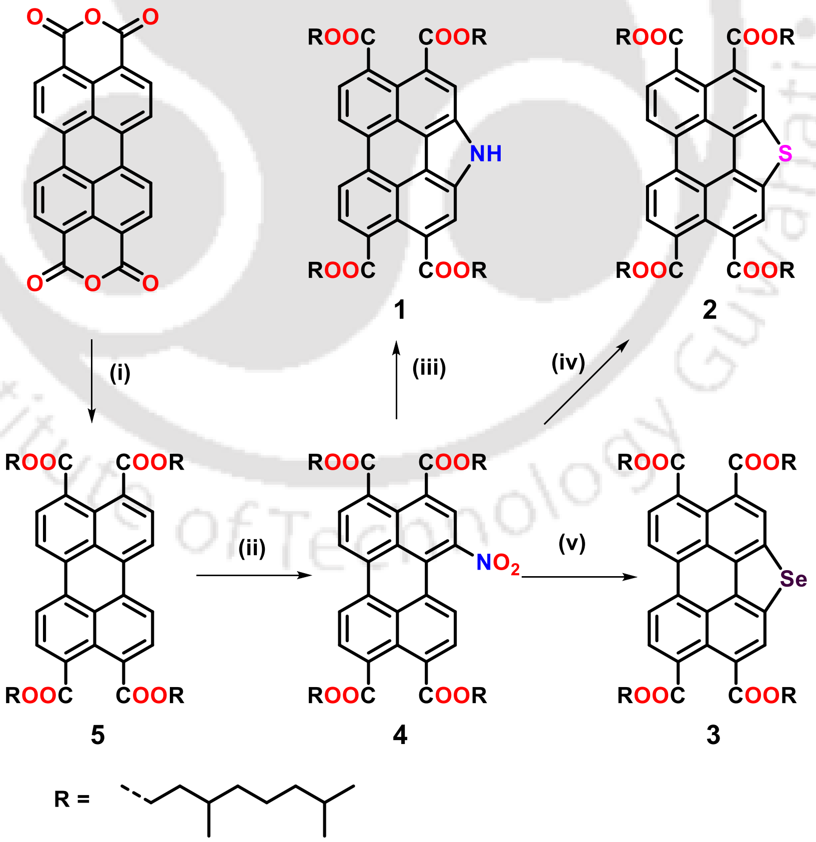

Scheme 3.1. Synthesis of RT LCs; Reagents and conditions: (i) KOH, H_2O,70 °C, 0.5 h, 1M HCl, Aliquat 336, KI, 1-bromo-3,7-dimethyloctane, reflux, 24 h (75%); (ii) $NaNO_2$, HNO_3, 0 °C, 1h (90%); (iii) triethyl phosphite, 160 °C, reflux, 4 h, N_2 (55%); (iv) sulfur powder, anhyd. NMP, N_2, 70 °C, 0.5 h, 180 °C, 17 h (55%); (v) selenium powder, anhyd. NMP, N_2, 70 °C, 0.5 h, 180 °C, 17 h (55%).

The synthetic path followed to obtain the target RT LCs is the same as that in previous chapter with few modifications as shown in Scheme 3.1. All intermediates and final molecules were analyzed by well-established characterization techniques.

3.2.2. Thermal behavior

The occurrence of thermotropic LC phase was confirmed with the characteristic optical texture and shearability of the compounds under polarizing optical microscopy (POM) observation. The transition temperatures and associated enthalphies were obtained by DSC thermograms. Further confirmation of LC phase assignment was made, by correlating the textural pattern observed in POM and the corresponding temperature dependent X-ray diffraction (XRD) pattern. The thermal behavior ascertained from these complementary studies are provided in Table 3.1 and schematically represented in Figure 3.1. The thermal behavior of these compounds were compared with the straight chain analogues (decyloxy chain) from previous chapter, containing the same number of carbons. Thermogravimetric analysis of these compounds showed a good thermal stability at least up to 330 °C (Figure 3.2d).

Table 3.1. Phase transition temperatures[a] (°C) and corresponding enthalpies (kJ/mol) of DLCs.

Compound	**Phase sequence**	
	Heating	**Cooling**
1	Col_h 284.6 (33.5) I	I 279.87 (24.7) Col_h
2	Col_h 199.9 (38.3) I	I 198.41 (33.1) Col_h
3	Col_h 182.2 (29.7) I	I 179.66 (25.9) Col_h
[a]Peak temperatures in the DSC thermograms obtained during the first heating and cooling cycles at 5 °C/min		

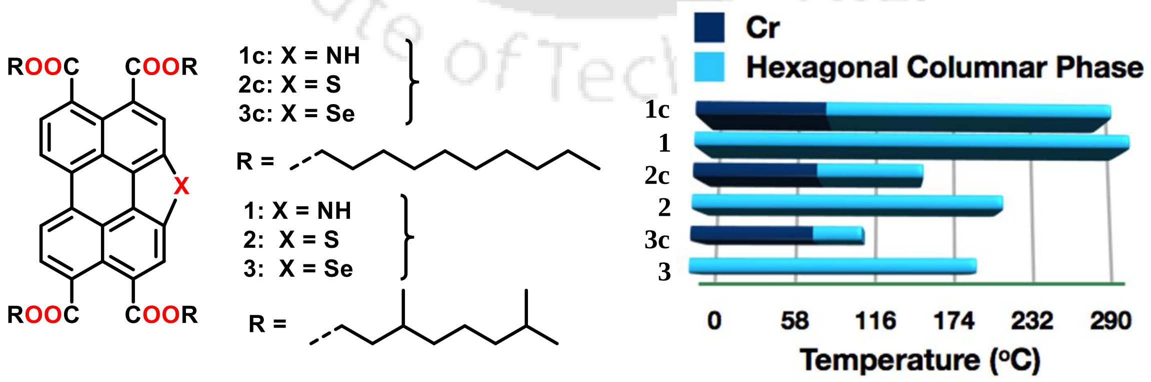

Figure 3.1. Bar graph summarizing the thermal behavior of **1c, 2c, 3c** (with normal decyloxy chain described in previous chapter) and compounds **1**, **2**, **3** (branched chain analogues keeping the total number of carbons constant) (in heating cycle).

All the materials had a waxy sticky appearance. Under POM observation, the molecules appeared bright and were shearable at RT. On heating from room temperature an increase in the birefringence was observed and this remained same till the clearing temperature. On cooling from the isotropic state, the compounds showed a transition to the mesophase, which was stable up to subzero temperature as evidenced from the DSC scans (Figure 3.2). Thus, an enantiotropic mesomorphic behavior over a broad thermal range was observed for all the three compounds. Compound **1** with *N*-annulation exhibited a mesophase to isotropic transition at a temperature of 285 °C with an enthalpy change of 33.5 kJ/mol (Table 3.1, Figure 3.2a). The mesophase spanned over a broad thermal range of more than 300 degrees and retains up to -50 °C as evidenced from DSC scans. Further

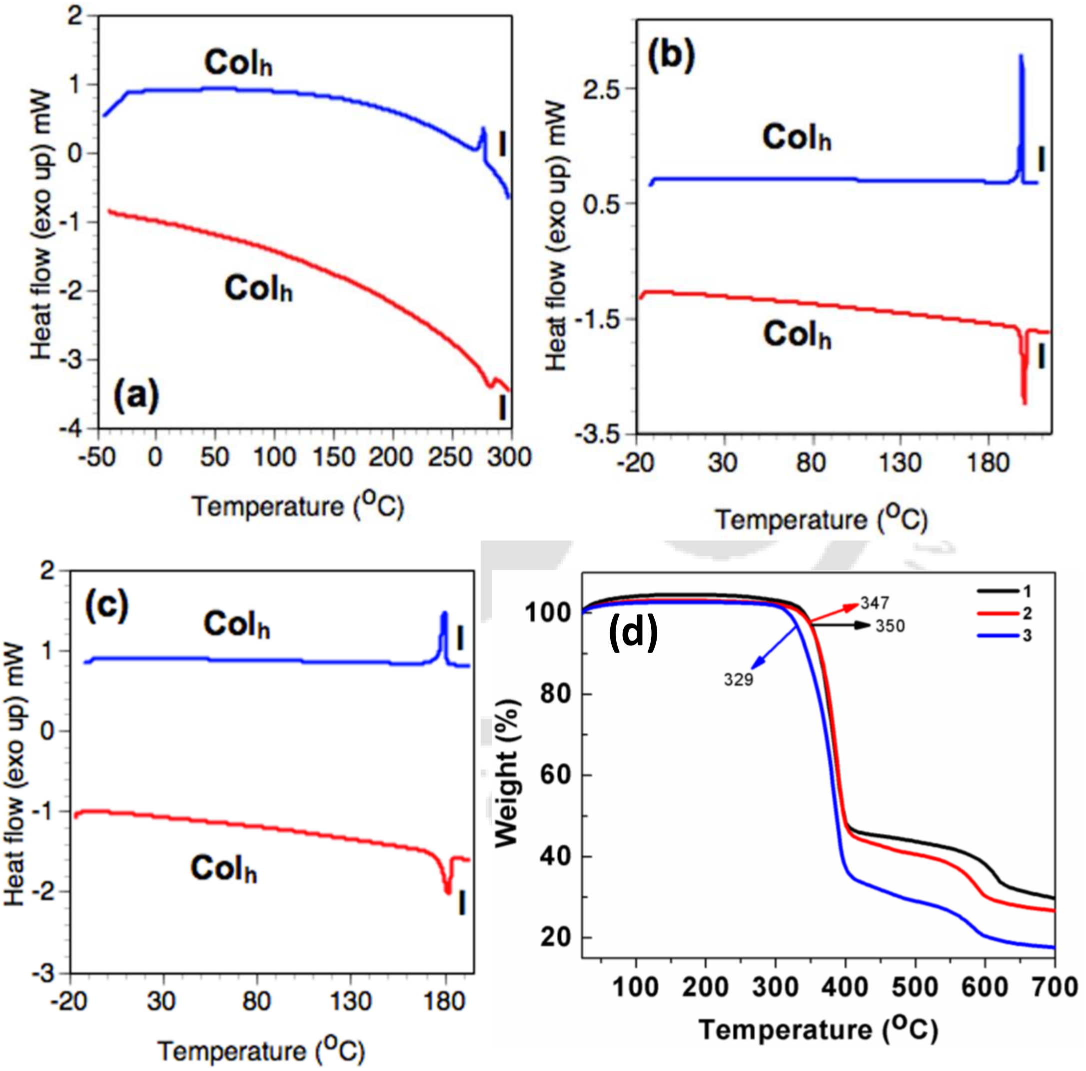

Figure 3.2. (a) DSC traces for first cooling (blue) and second heating (red) obtained at a rate of 5°C/min for compounds **1**, (b) **2** and (c) **3**; (d) TGA plots of compound **1**, **2** and **3** (heating rate of 10 °C/min, Nitrogen atmosphere).

heating did not show any transitions in DSC confirming the compound in a liquid crystalline phase. The wide thermal range (over 300 degrees) indicates an intimate core-core interaction between the molecules in a column. In comparison, the previously described straight chain analogue containing same number of carbon atoms (**1c**) showed higher transition temperatures. The melting point of compound **1c** was 85 °C and the isotropic temperature was 273 °C with a thermal range of around 190 degrees. It is interesting to note the huge increase in the mesophase width and lowered melting point of compound **1** due to the introduction of branched peripheral tails (Figure 3.1). In POM observation, large fern leaf like structures originated on cooling the isotropic liquid were observed along with the hexagonal dendritic patterns (Figure 3.3a). Further cooling led to an increase in the brightness of the leaf-like pattern, which extended and merged together (Figure 3.3b). Usually DLCs prefer to align with homeotropic or face on alignment on slow cooling from their isotropic state, as it is the most thermodynamically favored alignment.[32] Presence of heteroatoms in the molecular structure enhances the interactions with the

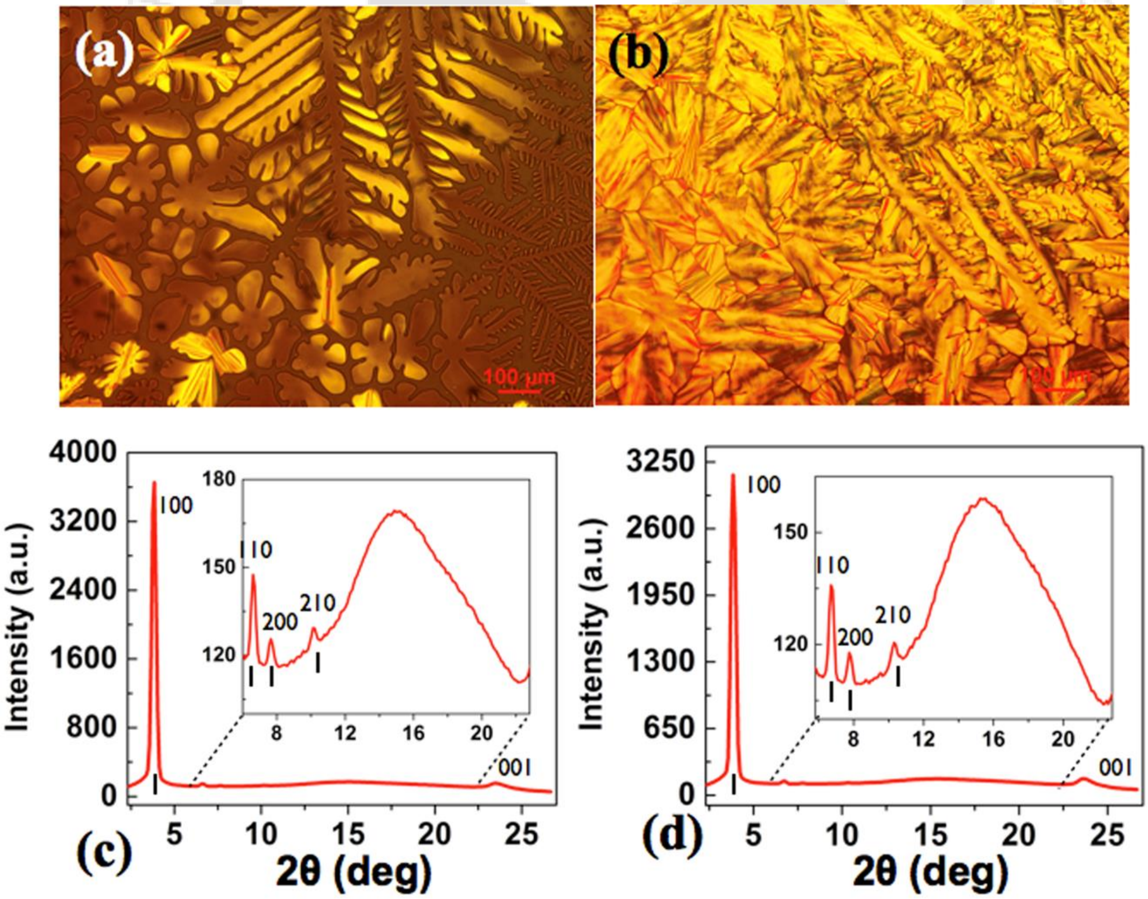

Figure 3.3. (a) Photomicrograph of compound **1** at 255 °C on cooling from isotropic liquid state and (b) at 25 °C (under crossed polarizer); (c) XRD profiles depicting the intensity against 2θ obtained for the Col$_h$ phase of compound **1** at 250 °C and (d) at 25 °C.

substrate surfaces and promote the homeotropic or 'face-on' alignment. This can be visualized by the pseudoisotropic texture in POM. Fast cooling leads to the formation of planar aligned Col phase, where the molecules align with 'edge-on' orientation and the columns oriented parallel to the substrate. As can be seen from the POM images at higher temperatures, we notice the presence of pseudoisotropic domains with a dark field of view or dendritic domains. This corresponds to the upright columns where the columnar axis is aligned with the optical axis. However, at low temperature highly birefringent textures were observed particularly for compounds **1** and **2**, which correspond to the planar alignment of these columns. This may be due to the increased viscosity and reduced rotational freedom of the molecules at low temperature. The results obtained from the indexation of the sharp reflections of the XRD profiles are summarized in Table 3.2. Powder XRD measurements carried out on the enantiotropic Col phase formed by compound **1** at 250 °C showed a sharp reflection in lower angle region which corresponds to Bragg spacing of 21.04 Å (Figure 3.3c). Further, in the middle region ($7 < 2\theta < 10°$), *d*-spacing corresponds to 12.21 Å, 10.58 Å, 7.98 Å. These reflections could be indexed into Miller indices 100, 110, 200, 210 with the ratio $1: 1/\sqrt{3}: 1/\sqrt{4}: 1/\sqrt{7}$ and this value corresponds to the lattice of hexagonal columnar phase. There are two diffused peaks found in the wide-angle region, one at 5.41 Å and the other at 3.51 Å. The broad diffraction peak at 5.41 Å corresponds to the packing of alkyl chains and the relatively sharp peak at 3.51 Å corresponds to core-core stacking. The observation of core-core spacing indicates the intimate overlap of the discotic cores inside the column. The lattice parameter '*a*' was found to be 24.3 Å, which corresponds to the intercolumnar distance. This value is lesser than the molecular diameter (estimated from Chem 3D Pro 8.0 molecular model software from Cambridge Soft) obtained from the molecular model in its all *trans* conformation. This can be attributed to the chain melting or possible interdigitation of the peripheral chains in the adjacent columns.[12] The number of molecules (Z) forming a columnar slice of thickness 3.51 Å (h_c) is 1. X-ray profile obtained at 175 °C showed a similar diffraction pattern corresponding to $\mathrm{Col_h}$ phase with a decrease in the *d*-spacings, intercolumnar distance and core-core separation (Table 3.2). More importantly, the diffraction pattern obtained at room temperature also confirmed that the mesophase remains as such without any signs of crystallization (Figure 3.3d, Table 3.2). XRD studies carried out at regular temperature intervals on cooling from the isotropic state, showed an identical pattern, confirming that there is no phase transition. The wide thermal range of the compound **1** with respect to

Table 3.2. Results of (*hkl*) indexation of XRD profiles of the compounds at a given temperature (T) of mesophases[a]

Compounds (D/Å)	Phase (T/°C)	d_{obs}(Å)	d_{cal}(Å)	Miller indices (*hkl*)	lattice parameters (Å), lattice area S (Å^2), molecular volume V (Å^3)
1 (32.65)	250	21.04	21.04	100	a = 24.29
		12.21	12.15	110	c = 3.51
		10.58	10.52	200	S = 511.2
		7.98	7.95	210	V = 1794.2
		5.41 (h_a)			Z = 1.1
		3.51 (h_c)		001	
	175	20.54	20.54	100	a = 23.72
		11.88	11.86	110	c = 3.45
		10.33	10.27	200	S = 487.2
		7.77	7.76	210	V = 1681
		5.21 (h_a)			Z = 1
		3.45 (h_c)		001	
	25	20.07	20.07	100	a = 23.17
		11.57	11.59	110	c = 3.41
		10.08	10.04	200	S = 465.1
		7.57	7.59	210	V =1586
		4.96(h_a)			Z = 1
		3.41 (h_c)		001	
2 (32.85)	190	21.02	21.02	100	a = 24.27
		11.88	12.14	110	c = 3.58
		10.22	10.51	200	S = 510.2
		7.77	7.94	210	V = 1826.6
		5.11(h_a)			Z = 1.1
		3.58 (h_c)		001	
	25	20.05	20.05	100	a = 23.15
		11.41	11.58	110	c = 3.51
		9.87	10.03	200	S = 464.1
		7.43	7.58	210	V = 1629
		4.76 (h_a)			Z = 1
		3.51 (h_c)		001	
3 (32.95)	145	20.53	20.53	100	a = 23.71
		11.73	11.85	110	c = 3.58
		10.33	10.27	200	S = 486.8
		7.72	7.76	210	V = 1742.9
		4.91 (h_a)			Z = 1
		3.58 (h_c)		001	
	25	20.05	20.05	100	a = 23.15
		11.41	11.58	110	c = 3.52
		9.93	10.03	200	S = 464.2
		4.71 (h_a)			V = 1634
		3.52 (h_c)		001	Z = 1

[a]The diameter (D) of the disc (estimated from Chem 3D Pro 8.0 molecular model software from Cambridge Soft). d_{obs}: spacing observed; d_{cal}: spacing calculated (deduced from the lattice parameters; a for Col$_h$ phase). The spacings marked h_a and h_c correspond to diffuse reflections in the wide-angle region arising from correlations between the alkyl chains and core regions, respectively. Z indicates the number of molecules per columnar slice of thickness h_c, estimated from the lattice area S and the volume V.)

other compounds (**2** and **3**) may be due to the favorable interactions provided by the –NH– moiety, that are likely to help in H-bonding with the molecule in the same or next plane. Similarly, introduction of the branched peripheral tail lowered the melting point significantly in comparison to its straight chain analogue (**1c**) containing the same number of carbon atoms (Figure 3.1).

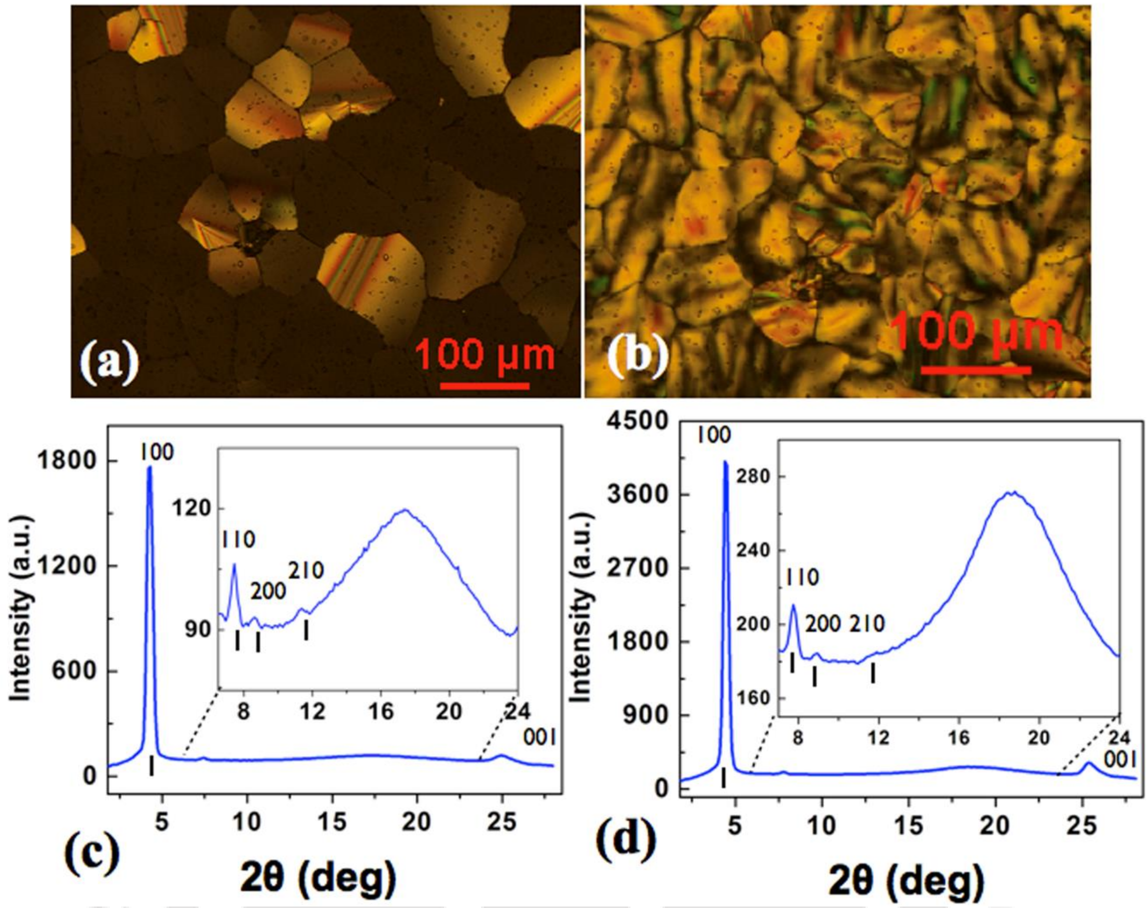

Figure 3.4. (a) Photomicrograph of compound **2** at 195 °C on cooling from isotropic liquid state and (b) at 24 °C (under crossed polarizer); (c) XRD profiles depicting the intensity against 2θ obtained for the $\mathrm{Col_h}$ phase of compound **2** at 190 °C and (d) at 25 °C.

Compound **2** with *S*-annulation and compound **3** with *Se*-annulation showed a reduced mesophase range in comparison to compound **1** (Figure 3.1). Yet it is noteworthy that they have also stabilized a room temperature $\mathrm{Col_h}$ phase along with an increase in the clearing temperature, which resulted in the overall increase of the mesophase width with respect to the straight chain analogues **2c** and **3c**. Compound **2c**, the straight chain analogue of compound **2**, exhibited a melting point of 80 °C and a clearing point of 148 °C, with an overall mesophase range of 68 degrees. In comparison, branched chain analogue **2** exhibited a thermal range of 175 degrees starting from room temperature. Similarly, the thermal range of compound **3c** was only 30 degrees, while that of the branched chain analogue **3** was found to be 155 degrees starting from room temperature. The mesophase exhibited by both these compounds (**2** and **3**) was Col$_h$ as evidenced by the POM textures (Figure 3.4a, b and 3.5a, b) and XRD profiles (Figure 3.4c, d, Figure 3.5c, d and Table 3.2).

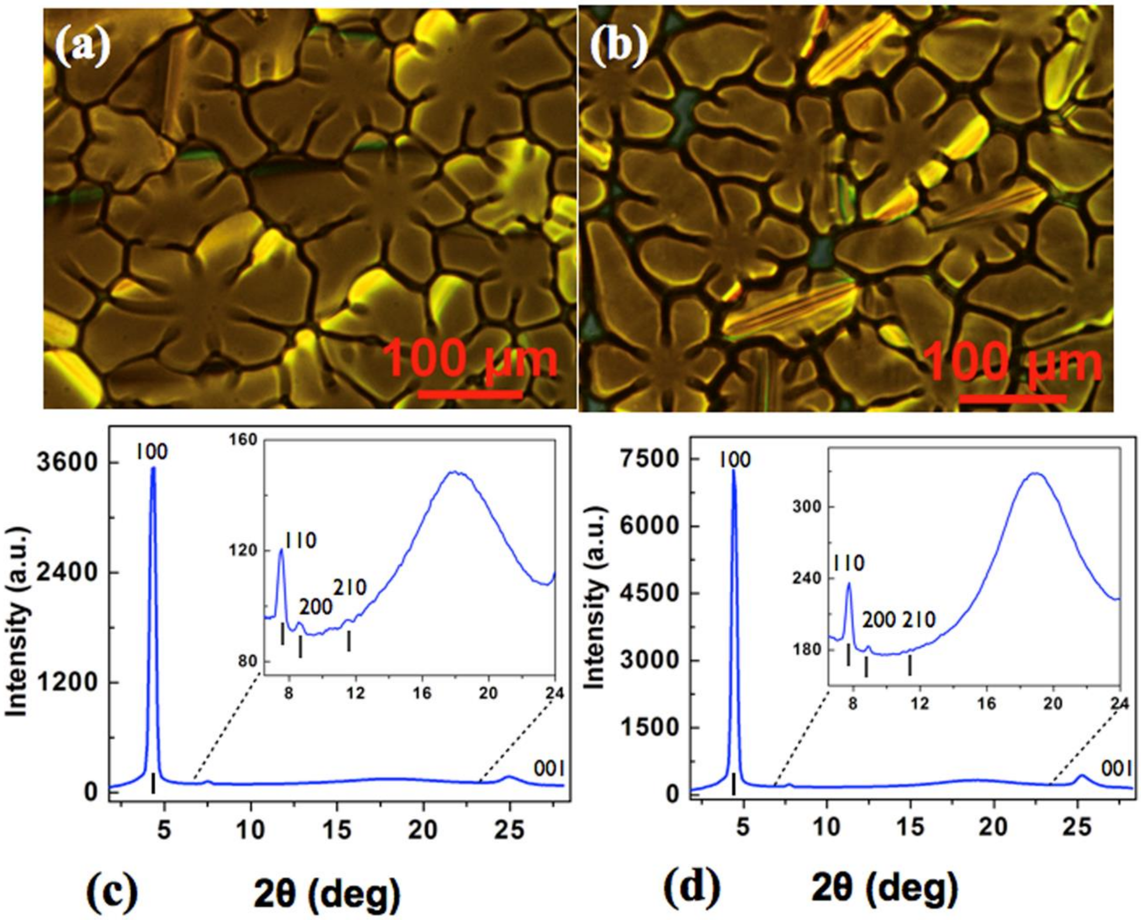

Figure 3.5. (a) Photomicrographs of compound **3** obtained on cooling from the isotropic phase at 145 °C; (b) at 28 ºC (under crossed polarizer); (c) XRD profiles depicting the intensity against 2θ obtained for the Col$_h$ phase of compound **3** at 145 ºC and (d) at 25 ºC.

3.2.3. Photophysical and electrochemical studies

Photophysical properties of the RT LCs **1-3** in solution are illustrated in Table 3.3. Absorption and emission spectra of the compounds **1, 2** and **3** were taken in micromolar THF solutions (Figure 3.6). As can be seen, the absorption spectra obtained for the solution of **1** showed a single absorption maximum positioned at 460 nm, with two shoulder bands at 433 nm and 412 nm. Compound **2** with sulfur annulation showed single absorption maximum at 443 nm with two shoulder peaks at 417 nm and 398 nm. Compound **3** with *Se*-annulation also exhibited blue-shifted absorption spectra with a maximum at 449 nm along with a shoulder band at 422 nm. All the molecules showed large values of molar extinction coefficients which is characteristic of highly conjugated polyaromatic molecules (10800-18480 M^{-1}cm^{-1}).

Table 3.3: Photophysical properties[a] of RT LCs in solution and thin film state.

	Solution state						**Thin film state[f]**		
	Absorption (nm)	**Emission[b] (nm)**	**Stokes shift (nm)**	**$\Delta E_{g, opt}$[c] (eV)**	**Steady state anisotropy[d]**	**Φ[e]**	**Absorption (nm)**	**Emission[g] (nm)**	**Stokes shift (nm)**
1	460, 433, 412	495	35	2.55	0.019	1.00	421, 483	559	138
2	443, 417, 398	462, 482	19	2.68	0.027	0.72	410, 466	549	139
3	449, 422	482	33	2.64	0.068	0.05	421, 472	551	130

[a]micromolar solutions in THF; [b]the excitation wavelength λ_{ex} = 460, 443 and 449 nm respectively for compound **1**, **2** and **3**; [c]calculated from the red edge of the absorption band; [d]3 μM solution in dichloromethane; [e]relative quantum yields are calculated with respect to compound **1b** in THF solution as the standard [f]prepared by spin coating of millimolar solution in toluene; [g]excited at the absorption maxima.

Compound **1** showed an emission maximum positioned around 495 nm with a Stoke's shift of 35 nm. Compound **2** and **3** exhibited slightly blue shifted emission spectra in comparison to compound **1** with their emission maxima centered at 462 nm (shoulder peak at 482 nm) and 482 nm respectively. Solutions of all room temperature *bay*-annulated liquid crystalline derivatives **1**, **2** and **3** exhibit bright green, sky blue and weak greenish yellow fluorescence under the UV light of long wavelength (Figure 3.6e). Absorption and emission spectra of these compounds showed concentration dependence with a regular decrease in the intensity on decreasing the concentration. Compounds **1** and **2** exhibited high fluorescence quantum yields (Table 3.3, Table 3.9 and Figure 3.17). Considering their high solubility, they can be used as standards for quantum yield measurement (at wavelengths 443-460 nm).[33] Compound **3** exhibited a very low quantum yield. The low luminescence quantum yield of compound **3** may be due to heavy atom quenching effect. Heavy atoms in the fluorophore or in close contact to it increase the rate of intersystem crossing (ISC) by strengthening spin–orbit coupling,[34-35] like in the electronic transitions in heavy atoms like mercury. Thus, the decrease of fluorescence (which is due to radiative transition S_1-S_0) yield is in most cases explained by an increase in the probability of the competing S_1-T_n radiationless transition of the fluorophore.[36] In the present study, compounds **1** and **2** containing nitrogen (atomic number: 7) and sulphur (atomic number: 16) as heteroatoms show good fluorescence yield, while compound **3** with selenium (atomic number: 32) exhibit lower quantum yield.

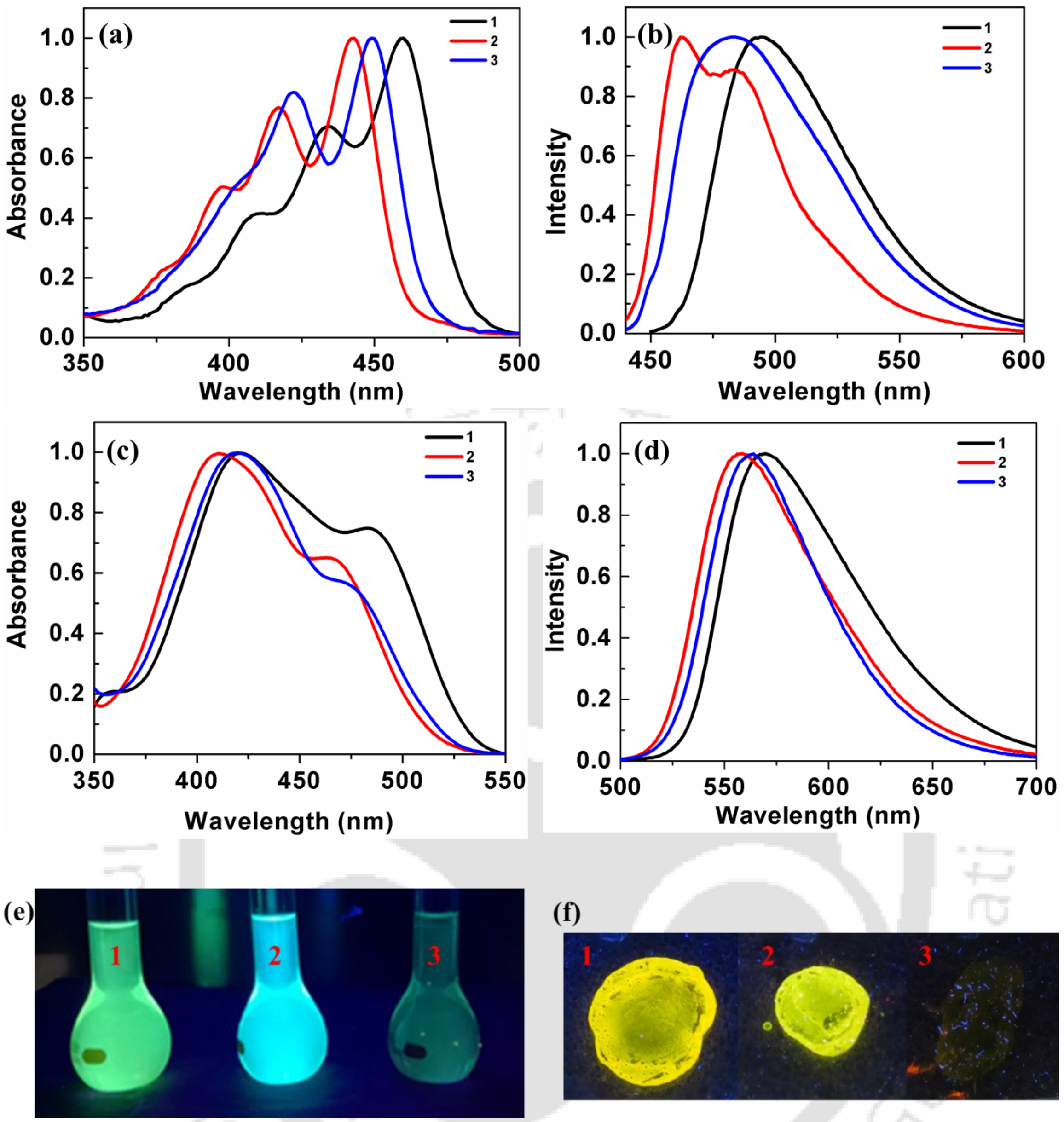

Figure 3.6. (a) Absorption and (b) emission spectra obtained for compounds **1-3** in micromolar THF solutions; (c) Absorption and (d) emission spectra obtained for compounds **1**, **2**, and **3** in spin coated thin films; (e) photographs of the same solutions as seen under the UV illumination (λ = 365 nm); (f) photographs of the thin films as seen under the UV illumination (λ = 365 nm).

The absorption spectrum of the spin coated thin films of these compounds varies from 410-421 nm (maximum) and a shoulder peak (466-483 nm), while the emission spectrum varies from 549-559 nm. The absorption spectrum of the thin film shows a blue shift in comparison to solution state, while the emission spectrum in the thin film state showed a red shift in comparison to solution (Figure 3.6b, d). The blue shifted absorption maxima indicates the formation of H-aggregates, where the molecules are arranged in co-facial manner.[37-39] Although H-aggregates are reported to be non-emissive or weakly emissive, it is not always true. Excitonic coupling in H-aggregates leads primarily to a low oscillator strength of the emitting state and thus to a low rate constant of emission. A small rate constant of emission however does not mean low fluorescence quantum yields because the fluorescence quantum yield is not solely depending on the rate constant of emission but also on all competing nonradiative processes. The total rate for nonradiative processes may include again a rate of internal conversion and rate of intersystem crossing in analogy to the situation in solution. These rates are expected to be as low as those in solution. In addition, the non-radiative processes also include loss of emission processes by trapping. In case of crystalline materials, defects or grain boundaries act as charge traps.[40] But in the case of LC materials these defects, which act as charge traps are reduced, due to the self-healing ability. This could be a reason for these compounds to be emissive even in the LC state, inspite of showing the characteristics of H-aggregates. There are few reports of H-aggregates exhibiting good emission behavior which attributed to the excimer formation or due to the small alternation of the two exciton coupled molecules.[38,39] Thin films of compounds **1** and **2** exhibited yellow and greenish yellow emission, while compound **3** did not show any luminescence under the UV light of long wavelength (Figure 3.6f). The measured fluorescence lifetime in solution was found to be around 4.57 ns (Figure 3.7, Table 3.4) for compound **1**, 3.25 ns for compound **2** and 3.81 ns for compound **3**. The steady state anisotropy values for compounds **1**, **2** and **3** were found to be 0.019, 0.027 and 0.068 respectively.

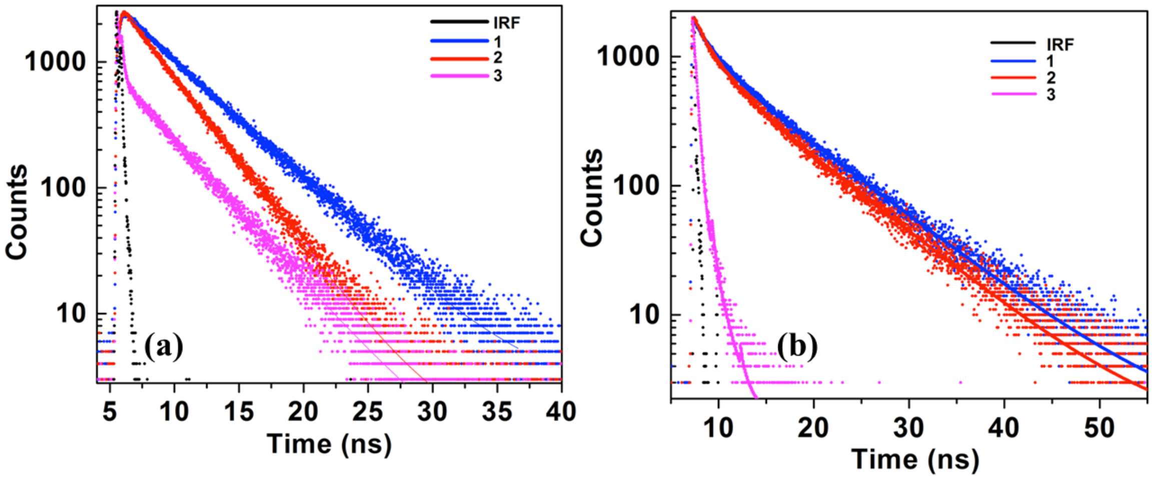

Figure 3.7. (a) TRPL plots of compounds **1**, **2** and **3** in micromolar solution of DCM (black traces shows IRF) and (b) as thin films.

Table 3.4. Data obtained from the time resolved photoluminescence experiments.

Solution[a]		Thin film[b]
Entry	**Fraction (Life time)**	**Fraction (lifetime)**
1	100 % (4.57ns)	22.31 % (1.99 ns); 77.69 % (7.79 ns)
2	100 % (3.25ns)	27.81 % (1.87 ns); 72.19 % (7.39 ns)
3	100 % (3.81ns)	80.13 % (0.34 ns); 19.87 % (1.27 ns)

[a]Concentration: 3 μM solution in dichloromethane; [b]Concentration of solution used for spin coating: 3 mM in toluene

Table 3.5. Electrochemical [a,b]properties of compound **1**, **2** and **3**.

Entry	E_{1red}[c]	E_{1oxd}[c]	E_{HOMO}[d,e]	E_{LUMO}[d,f]	$\Delta E_{g,CV}$[d,g]	$\Delta E_{g,opt}$[d,h]
1	-1.05	1.39	-5.72	-3.28	2.44	2.57
2	-1.26	1.75	-6.08	-3.07	3.01	2.69
3	-1.23	1.71	-6.04	-3.10	2.94	2.65

[a]in Dichloromethane solutions; [b]Experimental conditions: Ag/AgNO$_3$ as reference electrode, Glassy carbon working electrode, Platinum wire counter electrode, TBAP (0.1 M) as a supporting electrolyte, room temperature, scanning rate of 0.1 mVs^{-1}; [c]in volts (V); [d]in eV; [e]Estimated from the formula $E_{HOMO} = -(4.8 - E_{1/2}$, Fc/Fc$^+$ + E_{ox}, onset) eV; [f] Estimated from the formula by using $E_{LUMO} = -(4.8 - E_{1/2}$, Fc$^+$/Fc + E_{red}, onset)eV; [g]Estimated from the formula ΔE_g, CV = $E_{LUMO} - E_{HOMO}$; [h]calculated from the red edge of the absorption band (483, 462, 468 nm respectively). $E_{1/2}$, Fc/Fc$^+$ = 0.465

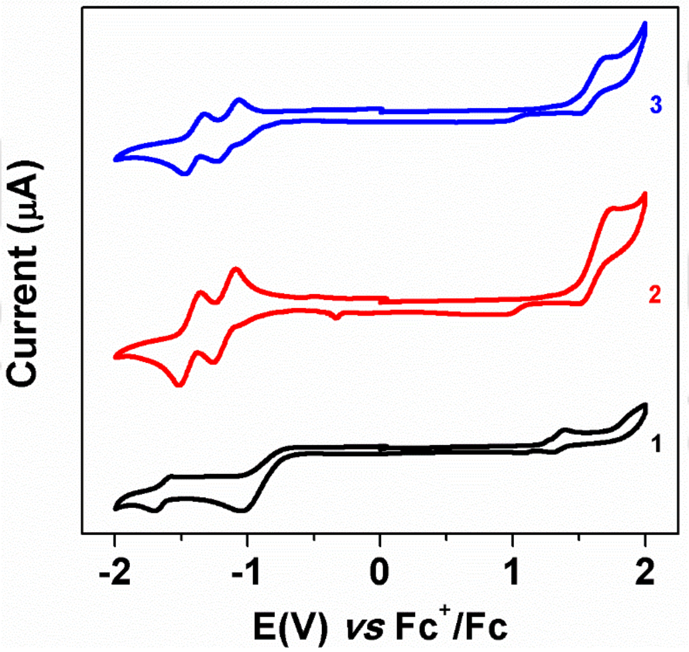

Figure 3.8. Comparison of cyclic voltammogram of compounds **1**, **2** and **3**.

We have carried out the cyclic voltammetry of the *N*-annulated (**1**), *S*-annulated (**2**) and *Se*-annulated (**3**) perylene tetraesters in dichloromethane solution to approximate the relative energy levels of highest occupied molecular orbital (HOMO) and lowest unoccupied molecular orbital (LUMO) and their difference. The energy levels and band gaps calculated from these studies are tabulated in Table 3.5. Figure 3.8 revealed that cyclic voltammogram of compound **1** shows one quasi-reversible oxidation with an onset potential of 1.39 V and one irreversible reduction with an onset potential of -1.05 V. Compound **2** and **3** showed one quasi-reversible oxidation with an onset potential of 1.75 and 1.71 V respectively and two reversible reductions with an onset potential of -1.26, -1.51 and -1.23, -1.48 V respectively. The HOMO energy levels of target compounds **1**, **2** and **3** were found at -5.72, -6.08 and -6.04 eV respectively, while the LUMO energy levels of compounds **1**, **2** and **3** were found at -3.28, -3.07 and -3.10 eV respectively.

3.3. Electroluminescence properties

These molecules with excellent luminescence and solution processability (due to the presence of peripheral alkyl chains) are ideal candidates to obtain solution processable OLEDs. We were interested in fabricating emissive layers with a 'host-guest' configuration, where the host is polyvinyl carbazole (PVK). PVK is a widely used host material due to its excellent film forming property and good miscibility with different emissive materials.[41] To get higher brightness and better efficiency in OLEDs, one of the key factor is to balance the flow of electron and hole in the emissive layer so that we can get maximum recombination. If the material used as emissive layer has imbalanced charge transport property, the performance of such devices will be limited. One of the simple ways of overcoming this is to use a host material which has a comparatively better charge balance than that of the emissive material. In such cases, the emissive material is used as a dopant and a small quantity of that material is doped in the host material. However, the emission in such a host guest system is generally controlled by the energy transfer from host to guest material and therefore needs perfect overlapping of the PL spectra of the host material with the absorption spectra of the emissive dopant material.[42] Figure 3.9a shows that the emission spectrum of PVK and the UV spectra of the LCs in thin film mode. The complete overlap of the PL and UV spectra of PVK and LCs suggest efficient/complete energy transfer from PVK to the LCs.

It is also reported that high molecular weight PVK samples show liquid crystalline behavior. The molecular weight of those samples were in the range of 30,000-40,000 with a degree of polymerization of 150-200.[43] It is clear that sufficiently high molecular weight is necessary to promote the LC phase, otherwise the linear conformation required for the stabilization of LC phase may not be attained. The PVK samples, which were used in these studies, were in the molecular weight range of 25,000-50,000. We expected that, the host

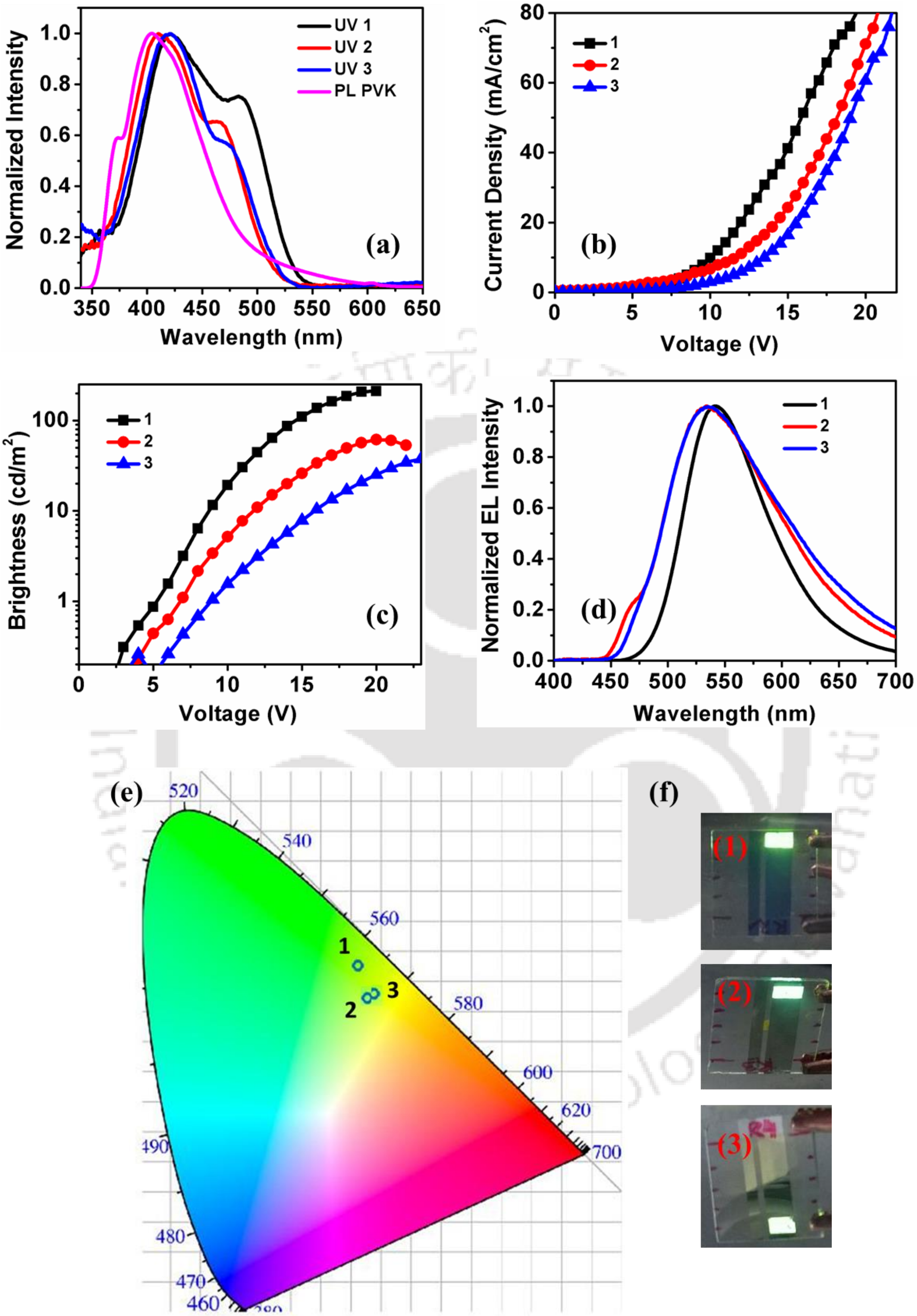

Figure 3.9. (a) Overlay UV spectra of compounds **1**, **2** and **3** over the fluorescence spectrum of PVK in the thin film state; (b) The current density *vs* voltage curves (J−V) curves; (c) the brightness *vs* voltage curves (B-V) curves of fabricated OLEDs with the emissive layers of **1**-**3** (10 wt%) in PVK; (d) EL spectra of the devices; (e) CIE coordinate diagram of fabricated OLEDs with the emissive layers of **1**-**3** (10 wt%) in PVK; (f) Photographs of the OLEDs with the emissive layers of **1**-**3** (10 wt%) in PVK.

and guest might show good compatibility due to their similarity of structure and promesogenic behavior.

To investigate the electroluminescence (EL) performance of the as synthesized room temperature LCs, we fabricated OLEDs with structures of ITO/PVK:10wt% LCs (**1-3**) (80 nm)/BPhen (40 nm)/LiF (1 nm)/Al (100 nm), using PVK and Bphen (benzophenonthroline) as host and electron transporting materials respectively (Figure 3.11a, b). Figure 3.9b shows the current density *vs* voltage curves (J−V curves) in linear scale and Figure 3.9c shows the brightness *vs* voltage curves (B-V) in log-linear scale. As can be seen, the turn-on voltages (at a luminance of 1 cd/m^2) for the three devices are 4.8, 5.9 and 6.7 V and the maximum brightness values obtained are 211 cd/m^2, 61 cd/m^2 and 38 cd/m^2 for the host-guest OLEDs of compounds **1, 2** and **3** respectively (Table 3.6). The EL spectra of the devices are shown in Figure 3.9d and the corresponding CIE coordinate diagram is shown in Figure 3.9e. This shows that all these compounds exhibit bright green to greenish yellow EL. The key device properties are summarized in Table 3.6 and efficiency *vs* brightness plots are given in Figure 3.10a-c.

Further we have tested the performance of these RT LCs as sole emissive layers (Figure 3.11c, d) with a configuration of ITO/PEDOT:PSS (40 nm)/ LCs (80 nm)/BPhen (40 nm)/LiF (1 nm)/Al (100 nm). From the Figure 3.10d it is seen that the turn-on voltages (at a luminance of 1 cd/m^2) for all three devices decreased in comparison to the devices with PVK:LC emissive layer. However, this also witnessed a decrease in the maximum brightness to almost 20% as in the case of compound **1** and **2**. The EL spectra obtained did not show much difference as compared to the devices with PVK:LC emissive layer. The EL spectra (Table 3.6 and 3.7) almost matched the PL spectra (Table 3.3) obtained for the thin films indicating that both are originating from the same excited state.

Table 3.6. Device properties of OLEDs fabricated with PVK

Device with PVK	**Turn on voltage (V)**	**Maximum brightness (cd/m^2)**	**Peak wavelength (nm)**	**CIE coordinate (x,y)**	**Brightness^a (cd m^{-2})**	**Efficiency (cd A^{-1})**
PVK:10 wt % 1	4.8	211.41	545	0.38, 0.58	208.01	0.27
PVK:10 wt % 2	5.9	61.37	533	0.36, 0.53	33.8	0.11
PVK:10 wt % 3	6.7	37.61	535	0.37, 0.54	2.23	0.05
^{a}maximum efficiency at brightness.						

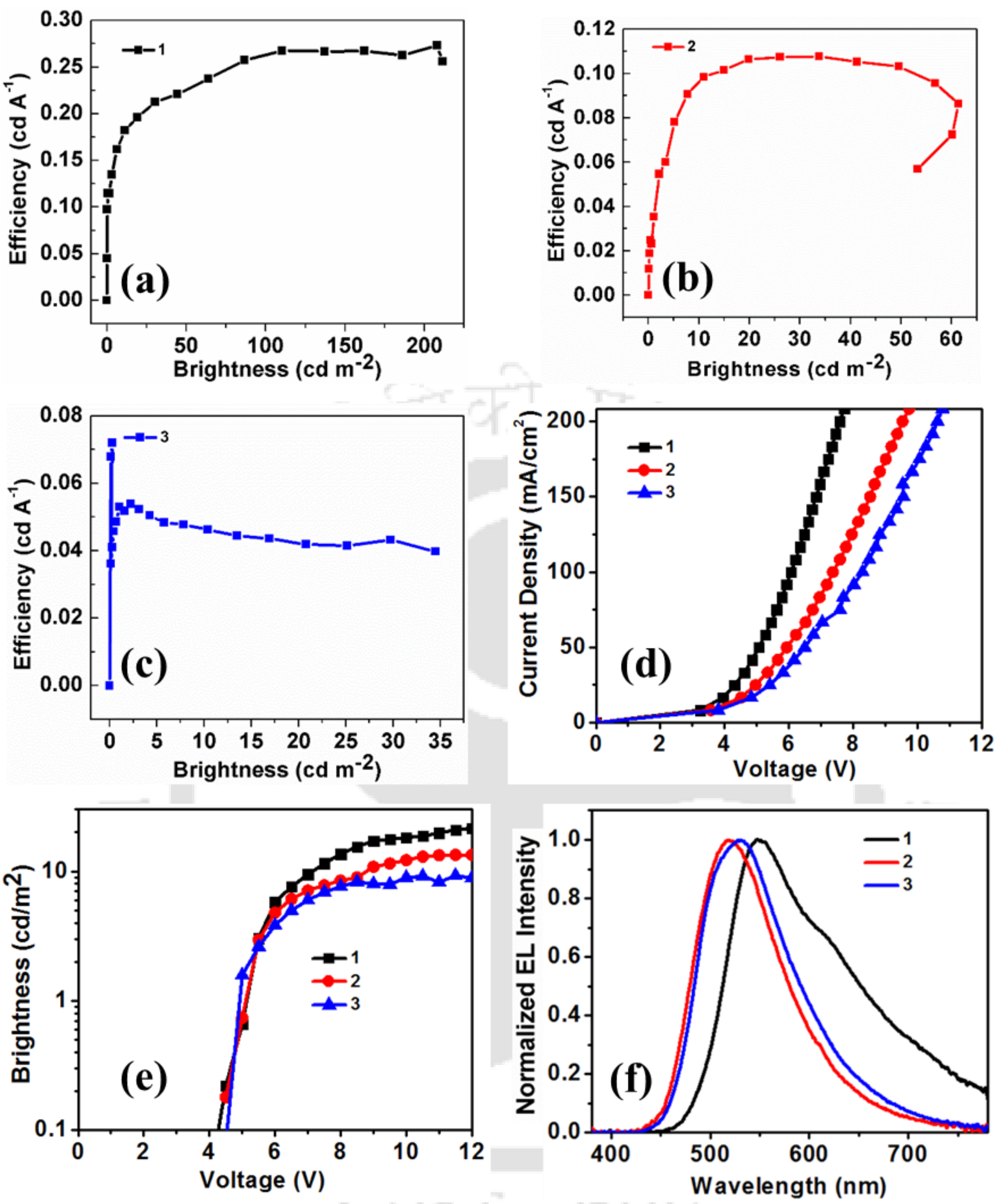

Figure 3.10. Plots of efficiency *vs* brightness obtained for the OLEDs: (a) PVK:10 wt% **1**; (b) PVK:10 wt% **2** and (c) PVK:10 wt% **3**; (d) The current density *vs* voltage curves (J−V) curves; (e) the brightness *vs* voltage curves (B-V); and (f) EL spectra obtained for OLEDs **1**, **2** and **3**, without PVK.

The surface morphologies obtained for the films prepared for the devices further supported the good film forming ability of PVK and liquid crystal mixture, in comparison to thin film formed by the liquid crystal alone. The surface morphology of LC thin films and PVK:10 wt% LCs (**1**/**2**/**3**) were explored using atomic force microscopy (AFM). Figures 3.12a, b and c show the AFM images obtained for liquid crystal films of **1**, **2** and **3** alone respectively. Similarly, Figure 3.12d, e and f show the AFM images obtained for the films prepared from the mixture of PVK and 10 wt% compounds **1, 2** and **3** respectively. All the films were heated to 140 °C to get good alignment. The thin films obtained in the first case (Figure 3.12a-c) were found to have smooth and amorphous surfaces, with a root mean square (RMS) roughness of 1.72 nm, 2.19 nm and 2.81 nm for the compounds **1**, **2** and **3** thin films respectively. The thin films obtained in the second case, *i.e.* prepared from PVK: 10 wt% liquid crystal mixture were found to be much smoother with a root mean square (RMS) roughness of 0.403 nm, 0.645 nm and 0.520 nm for the the thin films prepared from PVK: 10 wt% **1**, PVK: 10 wt% **2** and PVK: 10 wt% **3** mixtures respectively. This can be explained with the excellent film forming property of PVK. Thus the presence of PVK improves the device efficiency in two ways, first by the Förster energy transfer to

Table 3.7. Device properties of fabricated OLEDs without PVK.

Device	Turn on voltage (V)	Maximum brightness (cd/m^2)	Peak wavelength (nm)	CIE coordinate (x,y)
1	3.52	44.36	550	0.43, 0.53
2	3.96	13.73	533	0.33, 0.54
3	4.03	12.16	546	0.40, 0.53

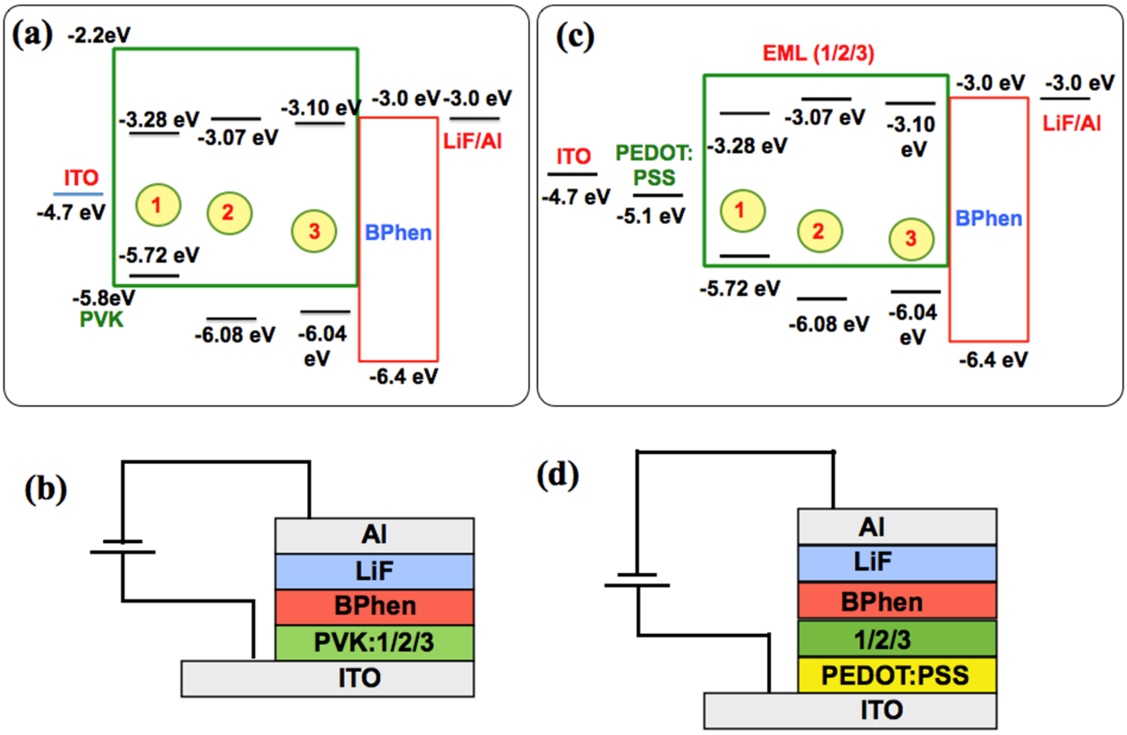

Figure 3.11. (a) Energy level diagram and (b) cartoon showing the device structure, where PVK and a liquid crystal mixture was used as an emissive layer; (c) Energy level diagram and (d) cartoon showing the device structure, where liquid crystal alone was used as an emissive layer.

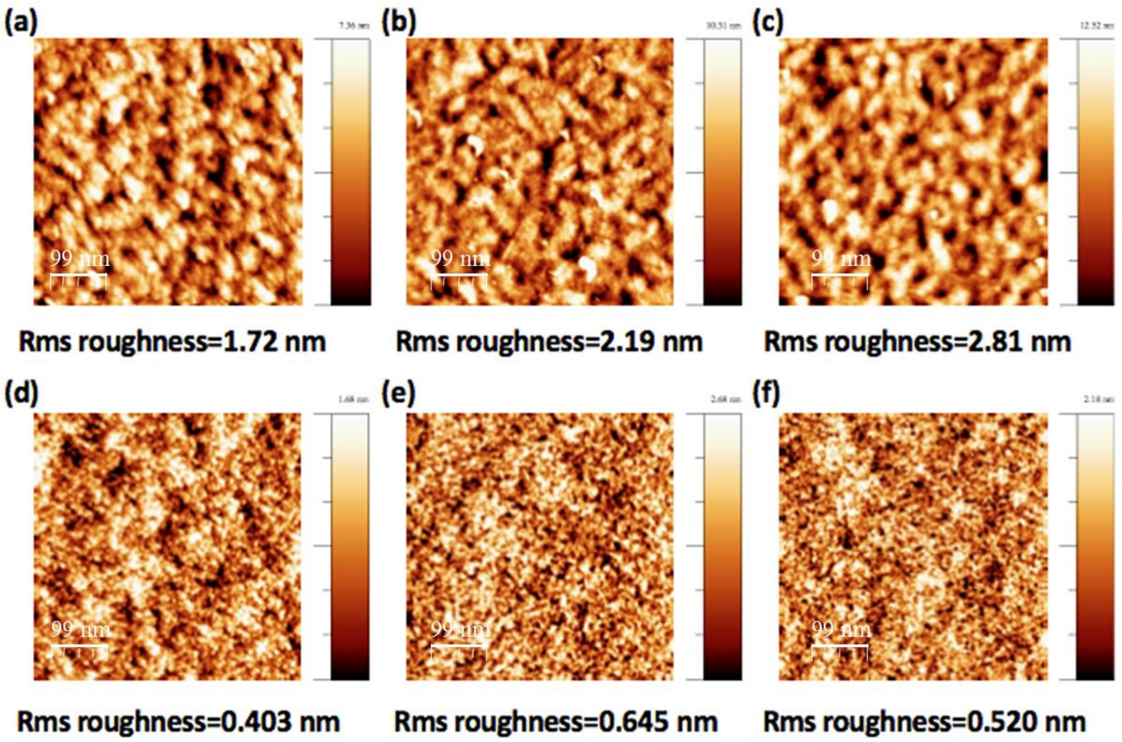

Rms roughness=1.72 nm   Rms roughness=2.19 nm   Rms roughness=2.81 nm

Rms roughness=0.403 nm   Rms roughness=0.645 nm   Rms roughness=0.520 nm

Figure 3.12. (a) AFM images of the spin coated films of compound **1**; (b) compound **2**; (c) compound **3**; (d) PVK:10 wt% **1**; (e) PVK:10 wt% **2**; (f) PVK:10 wt% **3**.

the liquid crystal and second by forming a smooth film devoid of defects, which enhances the charge recombination in the emissive layer.

Fluorescence lifetime measurements carried out for the thin film of compound **1** and for the thin film of PVK:10 wt% **1** showed huge difference suggesting Förster resonance energy transfer (FRET) from PVK to the LCs.[44-45] Fluorescence lifetimes of the excited species formed in the thin film of compound **1** and for the thin film of PVK:10 wt% **1** were measured by monitoring their emission maxima (556 nm for the thin film of **1** and 559 nm for the thin film of PVK:10 wt% **1**). The thin film of compound **1** showed a biexponential decay with two excited species [τ_1 = 2 ns (22 %), τ_2 = 7.8 ns (78 %)] (Table 3.4). For the thin film of PVK:10 wt% **1**, again a biexponential decay was observed with two excited species [τ_1 = 6.6 ns (14 %), τ_2 = 22 ns (86 %)] (Figure 3.13). Thus an almost three times increase in the lifetime of the excited species was observed, which is due to the Förster energy transfer. Thus the functioning of this host guest OLED can be explained as follows. Firstly, the excitons (singlet) are formed in the host matrix (PVK) by the injection of holes and electrons from the corresponding electrodes. Secondly, these excitons are transferred to the guest molecules (LCs) by Förster energy transfer, where they will recombine to emit the light. Alternatively, another mechanism that can likely occur, involves charge carrier trapping in emissive layers. This is possible if the LUMO level of the guest molecule is lower than the host and HOMO level of the guest is higher than that of the host. In such cases the guest molecules constitute traps for both types of charge carriers (electrons and holes) injected into the matrix from the electrodes. Then the excitons are formed directly on the guest molecule without the need of Förster energy transfer from host to guest molecule.[46] In Figure 3.11a, we can clearly distinguish between the energy levels of LC **1**, **2** and **3** with respect to the energy levels of PVK. It is only in the case of LC **1**, the LUMO and HOMO levels are situated between that of PVK, while in the case of LC **2** and **3**, the HOMO levels are lower than that of PVK. This explains the higher electroluminescence efficiency of PVK:10 wt% LC**1** in comparison to other two composites. It should be noted that all the above LCs have good absorption spectral overlap with the emission spectrum of PVK, but except compound **1**, others do not show good electroluminescence. Thus the second mechanism plays a major role in determining the electroluminescence of this class of host-guest OLEDs.

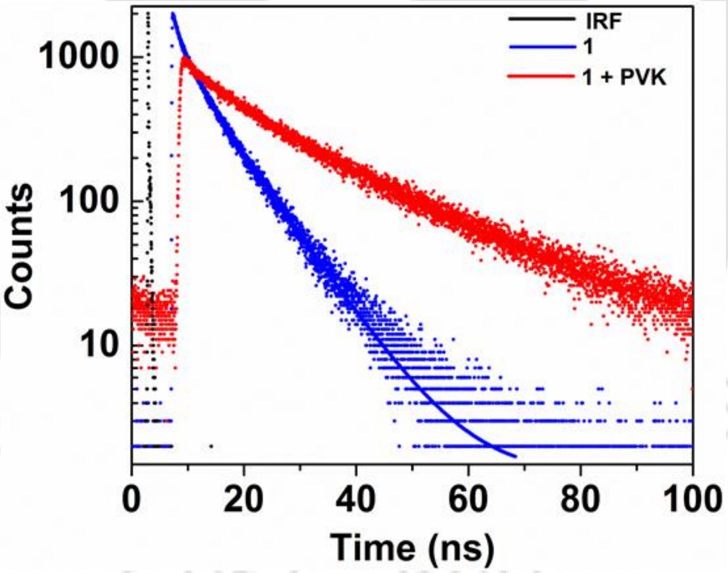

Figure 3.13. The fluorescence decay of compound **1** (blue trace, λ_{exc} = 405 nm, monitored at λ_{max} = 556 nm) and for the thin film of PVK:10 wt% **1** (red trace, λ_{exc} = 336 nm, monitored at λ_{max} = 559 nm); (black trace shows IRF).

3.4. X-ray diffraction studies on the thin film of PVK:10 wt% LC1

We were curious to know the supramolecular assembly of polymer PVK and LC **1** in the thin film obtained by the spin coating of PVK:10 wt% LC **1** mixture. POM image of the film showed a birefringent pattern. POM image of the above sample was taken without any coverslip. Notably, there was no phase separation observed in the thin film of the

PVK:10% LC**1** mixture (Figure 3.14a). Optically, the film formed by the above mixture was more birefringent in comparison to spin coated PVK film under same conditions. Further, the film was annealed at 140 °C for 10 minutes to match the experimental condition. There was an increase in the birefringence of the thin film after annealing. The optical texture did not exhibit the characteristic pseudoisotropic pattern corresponding to homeotropic (face-on) orientation, instead a birefringent pattern was observed that corresponds to the planar orientation of Col LC phase. Usually, Col LCs when they are on single substrates exhibit a planar texture due to the forces acting at the LC–air interface, that favors planar alignment.[47] Usually thermal annealing is done to provide good alignment and miscibility. The POM image of the film formed by the spin coating of LC**1** on a single substrate showed a grainy texture as seen in Figure 3.14b. This texture remained same even after annealing at 140 °C for 10 min. This points to the superior homogeneous nature of the film formed by the PVK:10 wt% LC**1** mixture.

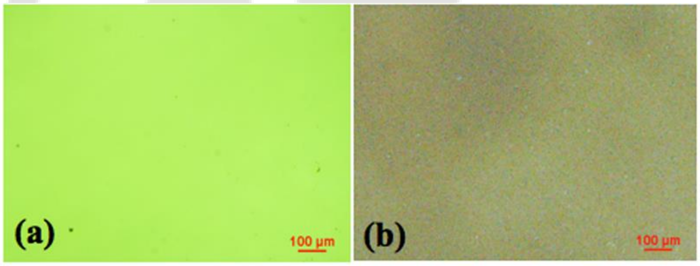

Figure 3.14. (a) POM image of the annealed spin coated film of PVK:10 wt% LC**1** at RT; (b) POM image of the spin coated annealed film of LC**1** at RT.

In order to understand the microstructure of the thin film formed by the spin-coated film of PVK:10 wt% LC**1**, we have carried out the powder XRD studies. This revealed the presence of a single peak at low angle along with several peaks in the mid angle region, which points to the crystalline nature of the sample. The peak at low angle ($2\theta = 8.25^{o}$) corresponds to a *d*-spacing of 10.7 Å (Figure 3.15a). According to literature report, PVK (Molecular weight ≈ 40,000) has been reported to show a nematic LC phase. The XRD pattern for the reported sample showed a single peak at low angle, along with a diffused hallow at wide angle. Thermal annealing of this polymer resulted in stronger single peak at low angle ($2\theta = 8^{o}$) along with a diffused peak at wide angle. The authors interpreted the peak at low angle to a *d*-spacing of 11Å, that is corresponding to a long range order.[48] In the present case, the PVK used was of molecular weight ranging from 25,000-50,000. Thus, it showed completely a different behavior from the reported sample even in the blended state.

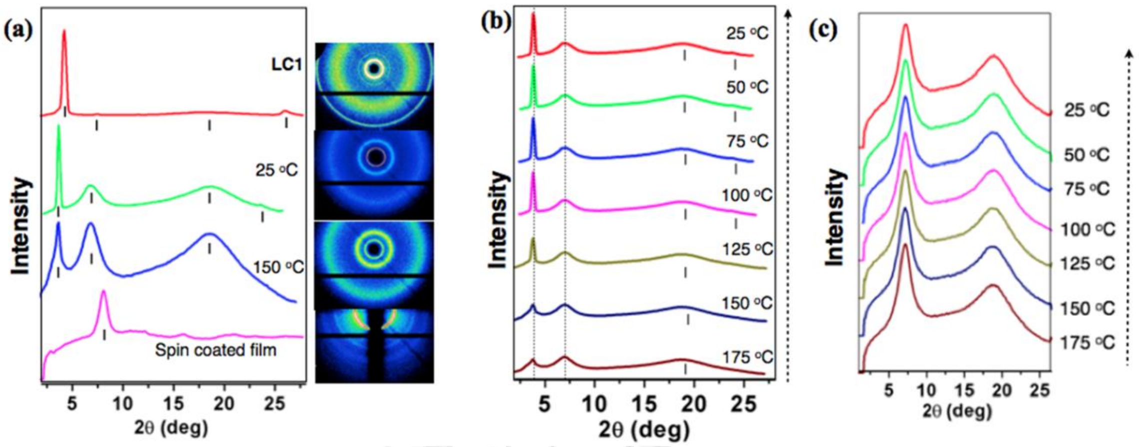

Figure 3.15. (a) XRD profiles depicting the intensity against 2*θ* obtained for the spin coated film of PVK:10 wt% LC**1** at RT (pink trace); For the same sample in capillary at 150 °C (blue trace); at RT (green trace) and for compound **1** at RT(red trace) (corresponding XRD image patterns are given on the right side); (b) XRD profiles depicting the intensity *vs* 2*θ* obtained for the sample PVK:10 wt% LC**1** on annealing from 175 °C to RT in capillary tube; (c) XRD profiles depicting the intensity *vs* 2*θ* obtained for the sample PVK alone on annealing from 175 °C to RT in capillary tube.

Further we were curious to know about the changes occurred during annealing. Since the sample in the thin film could not be heated, we have carried out the XRD of this composite material in capillary. The sample filled in the capillary was heated up to 175 °C and then cooled slowly. Measurements were carried out at regular temperature intervals (Table 3.8, Figure 3.15b). The XRD pattern obtained after annealing at 175 °C showed an additional, relatively sharp peak at low angle and a diffused peak at wide angle. The two peaks obtained at the low angle correspond to the *d*-spacings of 23.4 Å and 12.8 Å, respectively. The diffused halo with a *d*-spacing of 4.74 Å is due to the packing of carbazole units. To understand this a control experiment was carried out by measuring the XRD of PVK sample alone as a function of temperature (Figure 3.15c, Table 3.8). These diffraction patterns were almost similar irrespective of the temperature with a single peak at low angle with a *d*-spacing of 12.4 Å and a diffused peak at wide angle with a *d*-spacing of 4.71 Å. This also confirms that the PVK sample is also liquid crystalline in nature. We also should note the XRD pattern of LC**1** at different temperature intervals showed several peaks at small angles (d_{10} = 20-21Å) with a *d*-spacing ratio fitting into a hexagonal lattice, along with diffused peaks at 5 Å and 3.4 Å. (Figure.3.3d, Table 3.2, Figure.3.15a). The first diffused peak corresponds to the packing of flexible tails and the second one corresponds to the packing of the cores. Thus the *d*-spacing values observed for the composite material were different than the one obtained for LC**1** as well as PVK sample alone, though they showed the signatures of both the materials. This shows the well-dispersed nature of the composite material.

Table 3.8. Results of (*hkl*) indexation of XRD profiles of the PVK:10 wt% LC**1** and PVK alone at different temperature intervals on cooling^{a}

PVK:10 wt% LC1					**PVK**
(T/^{o}C)	**d_{obs}(Å)**	**d_{cal}(Å)**	**Miller indices (*hkl*)**	**Lattice parameters (Å)**	**d_{obs}(Å)**
175	23.42 12.75 4.74 (h_a)	23.42 13.52	100 110	a = 27.04 c = 4.74	12.44, 4.72
150	23.12 12.66 4.72 (h_a)	23.12 13.35	100 110	a = 26.7 c = 4.45	12.46, 4.73
125	23.12 12.64 4.72 (h_a)	23.12 13.35	100 110	a = 26.7 c = 4.72	12.44, 4.71
100	23.11 12.65 4.72 (h_a) 3.76 (h_c)	23.11 13.34	100 110 001	a = 26.69 c = 3.76	12.44, 4.71
75	23.11 12.65 4.71 (h_a) 3.76 (h_c)	23.11 13.34	100 110 001	a = 26.69 c = 3.76	12.45, 4.71
50	23.11 12.59 4.71 (h_a) 3.76 (h_c)	23.11 13.34	100 110 001	a = 26.69 c = 3.76	12.44, 4.71
25	23.11 12.63 4.71 (h_a) 3.74 (h_c)	23.11 13.34	100 110 001	a = 26.69 c = 3.74	12.44, 4.71

$^{a}d_{obs}$: spacing observed; d_{cal}: spacing calculated (deduced from the lattice parameters; a for Col$_h$ phase). The spacings marked h_a and h_c correspond to diffuse reflections in the wide-angle region arising from correlations between the alkyl chains and core regions, respectively.

The first two peaks obtained at the low angle for PVK:10% LC**1** mixture (at 175 ^{o}C) could be indexed into Miller indices (10) and (11) of a Col phase with hexagonal lattice, with a lattice constant a = 27 Å (Table 3.8). This corresponds to the intercolumnar distance, *i.e.* the distance between two neighboring columns. Further cooling of the material to room temperature showed an increase in the intensity of the peaks at low angle, while maintaining the same *d*-spacing ratio. From 100 ^{o}C onwards we observed a second diffused peak at wide angle, which corresponds to the average intracolumnar distance, which is arising from packing of DLC cores or carbazole units within a column. Observation of this peak with a *d*-spacing of 3.74 Å is significant and supports the intimate packing of carbazole units in the polymer backbone and LC**1** (Table 3.8). This distance is higher than the intracolumnar distance observed for LC**1** alone, which is 3.45 Å. This may be due to the insertion of pendant carbazole moieties inside the columns. It should be noted that intercolumnar distance (*a*) observed in the case of LC**1** alone is 23-24 Å (Table 3.2), while for the composite material, the observed intercolumnar distance is *a* = 26-27 Å. Since there is no much change in the intercolumnar distance, we can conclude that polymer chains are arranged along the columnar axis, with the pendant carbazole moieties arranging in a hexagonal columnar lattice. Thus the thermal annealing as a driving force, helps in the reorganization of the polymer chains and DLCs. In total, the thermal annealing enhances the alignment and intermixing of these two different components as shown in Figure.3.16.

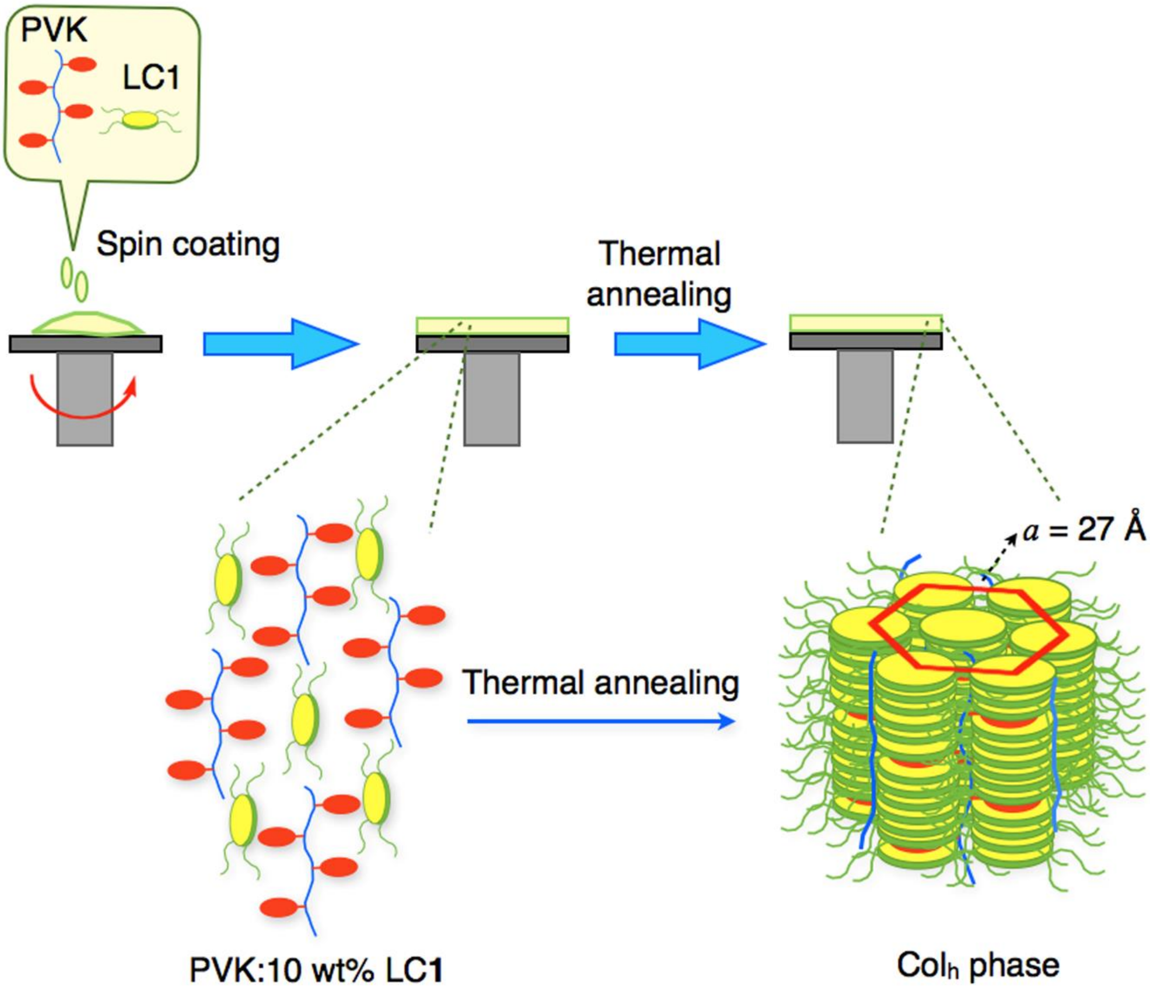

Figure 3.16. Schematic showing the thin film processing of the mixture of PVK:10 wt% LC**1**. Expanded region shows the organization of PVK polymer chain and DLCs in Col$_h$ phase.

3.5. Relative Quantum Yield Calculation

Relative quantum yields of compounds **1**, **2** and **3** were measured with respect to tetrakis(octyl)-1H-phenanthro [1,10,9,8] carbazole-3,4,9,10-tetracarboxylate **1b** (in previous chapter) in THF solution as the standard, which is having the relative quantum yield of **1** with respect to fluorescein (**Q_f** = 0.79 in 0.1M NaOH). Absolute values were calculated according to the following equation: $Q_S = Q_R \times (m_S / m_R) \times (n_S / n_R)^2$

Where, Q: Quantum yield; m: Slope of the plot of integrated fluorescence intensity *vs* absorbance; n: refractive index (1.407 for THF).

The subscript R refers to the reference fluorophore *i.e.* compound **1b** solution in THF and subscript S refers to the sample under investigation. In order to minimize re-absorption effects, absorbance was kept below 0.15 at the excitation wavelength of 449 nm.

Quantum Yield of compound **1b** is 1.0. Simplified equation for the calculation after substituting the appropriate values is given below and values obtained are given in table below.

$Q_S = 1.0 \times (m_S / m_R) \times (1.407/1.407)^2$

$= 1.0 \times (m_S / m_R)$

Table 3.9. Quantum yield of RT LCs.

Entry	**m_S**	**m_R**	**$Q_s^{a,b,c}$**
1	2.3856×10^9	2.001×10^9	1.0
2	2.3214×10^9	3.215×10^9	0.72
3	1.6620×10^8	3.493×10^9	0.05

[a]Measured in THF, [b]Excited at absorption maxima, [c]Standard **1b** (**Q_f** = 1.0) in THF.

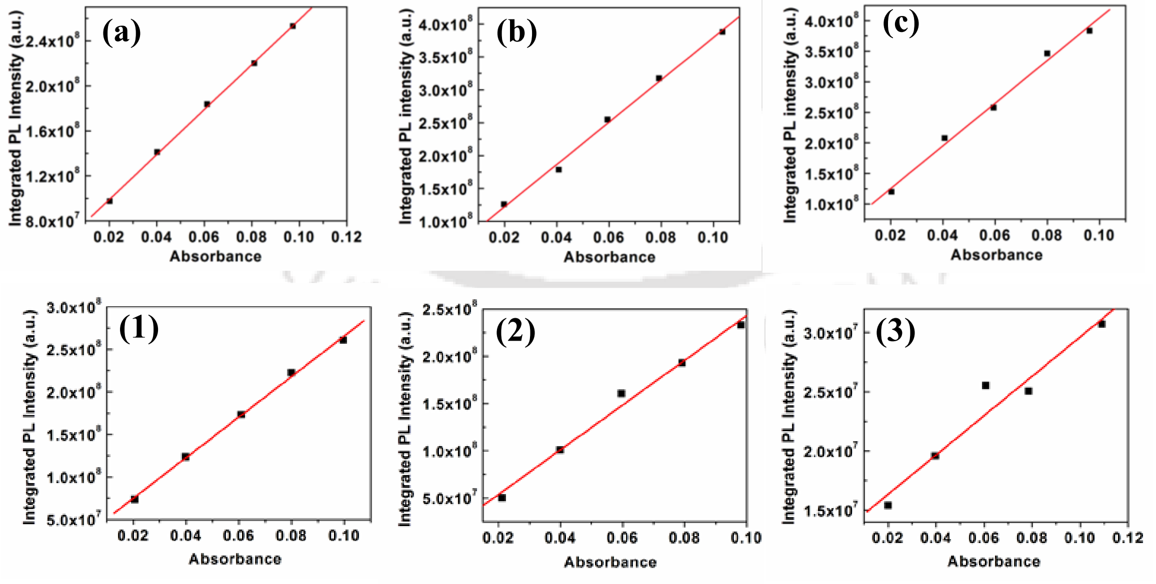

Figure 3.17. (a) Plots of integrated photoluminescence intensity *vs* absorbance of Fluorescein (0.1M NaOH solution) excited at 460 nm; (b) integrated photoluminescence intensity *vs* absorbance of compound **1b** (in THF solution) excited at 443 nm; (c) at 450 nm and for compound **1**, **2** and **3**.

3.6. Conclusion

In conclusion, we have synthesized and comparatively studied room temperature liquid crystals based on heteroatom *bay*-annulated perylenetetraesters. All the *bay* annulated perylenetetraesters exhibited $\mathrm{Col_h}$ phase over a wide thermal range of 200-300 degrees including room temperature, which is important for their applicability in organic electronic devices. TGA studies have proven that these molecules have got high thermal stability. *N*-annulated perylene tetraester and *S*-annulated perylene tetraester exhibited bright green and sky blue emission in solution state, while they exhibited yellow and greenish yellow fluorescence in thin film ($\mathrm{Col_h}$ phase) states. *Se*-annulated perylene tetraester exhibited a weak green emission in solution and thin film states due to the heavy atom quenching effect. Prototype OLEDs were fabricated with the compounds as single emissive layer or by doping them in a host matrix of polyvinyl carbazole. OLEDs formed by the LCs alone as emissive layers exhibited lower efficiency and brightness. Especially, the emissive layer formed by the doping of *N*-annulated perylene tetraester (10 wt%) in polyvinyl carbazole exhibited bright green emission with a brightness of 211 cd/m^2 and an efficiency of 0.27 cd/A. Similar systems with *S*-annulated and *Se*-annulated perylene tetraesters exhibited greenish yellow emissions. But the brightness and efficiencies of these systems were much lower than *N*-annulated perylene tetraester in PVK matrix. Thus the presence of PVK improves the device efficiency in two ways, first by the Förster energy transfer to the liquid crystal and second by forming smooth film devoid of defects, which enhances the charge recombination in the emissive layer. It also increases the lifetime of the excited states to increase the efficiency. The higher efficiency of host-guest OLEDs with *N*-annulated perylene tetraester in comparison to other two compounds, can be explained by its advantageous HOMO-LUMO levels with respect to that of PVK. This helps in the charge trapping within the emissive layer leading to the formation of excitons, in the emissive layer, without the need of Förster energy transfer from host to guest molecule. XRD of the composite material provides a good insight about the self-organization of the polymer and DLCs into a columnar hexagonal phase promoted by thermal annealing. Presently, we have tested the efficiency of these materials by fabricating host-guest OLEDs and also as single emitting layer in OLEDs. Our ultimate aim is to fabricate OLEDs from Col LCs as sole emissive layers, which will simplify the device architecture. For that we have to enhance the luminescence efficiency of these molecules through proper molecular design. In addition, we need to tune the energy levels of the molecules with respect to the electrodes, which will help in the efficient charge injection into the emissive layer. Another major problem with the present materials is that, they are not showing homeotropic alignment, when they are very thin and specially on a single substrate. Thus we have to tailor the molecule in such a way that facile homeotropic alignment will be obtained. In parallel, research is underway to test different combinations of host polymers and LCs in different proportions to obtain good electroluminescent material. Thus the material design to device fabrication is a delicate interplay of several factors, where every minute detail has to be dealt with utmost care.

3.7. Experimental section

In this section the detailed synthesis procedure and the molecular structural characterization data have been presented for the intermediates and target compounds mentioned in the scheme.

Synthesis of tetrakis(3,7-dimethyloctyl) perylene-3,4,9,10-tetracarboxylate **(5)**

Perylenetetracarboxylic dianhydride (2.5 mmol, 1 equiv.) was dissolved in 30 mL aqueous KOH (13.76 mmol, 5.4 equiv.) solution and stirred at 70 °C for 0.5 h. The solution was filtered and pH value of filterate was adjusted to 8-9 using 10% HCl. Then Aliquat 336 (0.9 mmol, 0.4 equiv.) and KI (1.4 mmol, 0.6 equiv.) were charged into the solution and then stirred vigorously for 10 min. 1-bromo-3,7-dimethyloctane (15.3 mmol, 6 equiv.) was added to this reaction mixture. After the addition the reaction mixture was refluxed for 12 h until a red oil floats on the top and the rest of the solution becomes clear. Subsequently, chloroform (10 mL) was poured into the mixture and filtered through the celite bed to remove unreacted part and the celite bed was washed with chloroform. This chloroform layer was separated and washed twice with 15% sodium chloride solution, dried over sodium sulfate and concentrated in vacuo to get a viscous concentrate. This concentrate was poured in cold Methanol to precipitate the product. Waxy solid was filtered and dried in vacuum.

R_f = 0.6 (20% EtOAc-hexane); orange waxy solid, yield: 75%; IR (KBr pellet) ν_{max} in cm^{-1}: 2960, 2926, 2862, 1720, 1703, 1663, 1584, 1455, 1384, 1273, 1170, 1019; ^{1}H NMR (600 MHz, $CDCl_3$, 298 K): 8.25 (d, J = 6 Hz, 4H, H_{Ar}), 8.02 (d, J = 6 Hz, 4H, H_{Ar}), 4.41-4.33 (m, 8H, 4 × $-OCH_2$), 1.85-1.81 (m, 4H, 4 × CH), 1.64-1.54 (m, 12H, 4 ×CH_3), 1.53-1.49 (m, 4H, 4 × CH), 1.35-1.25 (m, 4H, 4 × -CH), 1.20-1.13 (m, 16H, 8 × $-CH_2$), 0.98-0.97 (m, 12H, 4 × $-CH_3$), 0.87-0.85 (m, 24H, 8 × $-CH_3$); ^{13}C NMR (150 MHz, $CDCl_3$, 298 K): 168.76, 133.05, 130.57, 130.5, 129.05, 128.86, 121.5, 64.36, 39.45, 37.47, 35.73, 30.27, 28.16, 24.87, 22.91, 22.81, 19.85; HRMS (-APCI mode) exact mass calculated for $C_{64}H_{92}O_8$ $[M-1]^-$: 989.4105, found: 989.4201.

Synthesis of tetrakis(3,7-dimethyloctyl) 1-nitroperylene-3,4,9,10-tetracarboxylate (**4**)

To a solution of perylene tetraester **5** (0.7 mmol, 1 equiv.) in dichloromethane (5 mL), added $NaNO_2$ (0.7 mmol, 1 equiv.) at 0 °C and stirred. To this well stirred suspension, 69% HNO_3 (3.42 mmol, 5 equiv., 10% solution in dichloromethane) was added dropwise. This mixture was stirred at 0 °C for 1 h. The reaction mixture was poured into water and extracted with dichloromethane (25 mL). Finally, organic layer was dried over anhyd. Na_2SO_4 and concentrated. The crude product was purified by column chromatography on neutral alumina. Elution with 50% dichloromethane-hexane yielded the desired product.

R_f = 0.6 (20% EtOAc-hexane); red solid, yield: 90%; IR (KBr pellet) ν_{max} in cm^{-1}: 3436, 2960, 2926, 2862, 1720, 1703, 1663, 1584, 1455, 1384, 1270, 1170, 1019, 805; ^{1}H NMR (600 MHz, $CDCl_3$, 298 K): 8.35-8.32 (m, 2H, H_{Ar}), 8.21 (s, 1H, H_{Ar}), 8.18 (d, J = 6 Hz, 1H, H_{Ar}), 8.11-8.01 (m, 1H, H_{Ar}), 7.95 (d, J = 6 Hz, 1H, H_{Ar}), 7.89-7.87 (m, 1H, H_{Ar}), 4.42-4.36 (m, 8H, 4 × $-OCH_2$), 1.86-1.83 (m, 4H, 4 × -CH), 1.63-1.50 (m, 8H, 4 × $-CH_2$), 1.36-1.34 (m, 4H, 4 × -CH), 1.29-1.21 (m, 8H, 4 × $-CH_2$), 1.17-1.15 (m, 16H, 8 × $-CH_2$), 0.98-0.97 (m, 12H, 4 × $-CH_3$), 0.87-0.86 (m, 24H, 8 × $-CH_3$); ^{13}C NMR (150 MHz, $CDCl_3$, 298 K): 168.24, 168.05, 167.98, 166.82, 146.32, 133.77, 132.51, 132.08, 131.55, 130.91, 130.51, 130.42, 130.01, 129.76, 129.17, 128.67, 128.50, 127.80, 127.56, 126.69, 125.72, 123.24, 123.71, 65.05, 64.71, 64.65, 64.59, 39.41, 37.44, 37.41, 35.65, 35.62, 30.20, 28.24, 28.14, 24.83, 24.71, 22.89, 22.79, 19.79; HRMS (-APCI mode) exact mass calculated for $C_{64}H_{91}O_{10}$ $[M]^-$: 1033.6643, found: 1033.7297.

Synthesis of **1**

A mixture of compound **4** (0.6 mmol, 1 equiv.) and triethyl phosphite (7 mL) were refluxed for 4 h under argon atmosphere. Reaction mixture was cooled to room temperature and triethylphosphite was removed under vaccum, residue was diluted with DCM and washed with water, brine and dried over sodium sulfate. The crude product was purified by neutral alumina using 50% DCM-Hexane system. Product was dissolved in DCM and added this concentrate solution in cold methanol yields the desired product as a waxy solid.

R_f = 0.6 (20% EtOAc-hexane); orange waxy solid, yield: 55%; IR (KBr pellet) ν_{max} in cm^{-1}: 3432, 2955, 2927, 2869, 1718, 1593, 1496, 1465, 1427, 1384, 1365, 1256, 1207, 1186, 1152, 1049, 1109, 995; ^{1}H NMR (600 MHz, $CDCl_3$, 298 K): 9.48 (s, 1H, NH), 7.96 (d, J = 7.8 Hz, 2H, H_{Ar}), 7.90-7.89 (m, 4H, H_{Ar}), 4.58-4.55 (m, 8H, 4 × $-OCH_2$), 2.03-2.01 (m, 4H, 4 × $-OCH_2-CH_2$), 1.81-1.09 (m, 40H, 20 × $-CH_2$), 0.88-0.86 (m, 24H, 8 × $-CH_3$); ^{13}C NMR (150 MHz, $CDCl_3$, 298 K): 169.94, 169.91, 131.06, 130.31, 128.49, 127.50, 127.26, 123.15, 122.73, 121.63, 119.34, 117.85, 64.57, 64.47, 39.51, 39.42, 37.61, 36.07, 36.00, 30.49, 28.18, 24.96, 22.92, 22.82, 19.94; HRMS (-APCI mode) exact mass calculated for $C_{64}H_{90}NO_8$ $[M-1]^-$: 1000.6666, found: 1000.7407.

Synthesis of **2**

A mixture of compound **4** (0.26 mmol, 1 equiv.) and Sulfur powder (2.602 mmol, 10 equiv.) was heated to dissolve in *N*-methylpyrrolidone (10 mL) at 70 °C for 30 min. and then refluxed at 180 °C under Ar atmosphere for overnight until the starting material could not be detected by TLC. After cooling to room temperature, 2 M HCl was added, then the precipitate was filtered, washed with water and dried. The crude product was purified by column chromatography on neutral alumina. Elution with 20-30% DCM-hexane system followed by 50% DCM-Hexane system yields the desired product. Further purification was done by addition of concentrate solution of compound in cold methanol gives the waxy product.

R_f = 0.6 (20% EtOAc-hexane); orange waxy solid, yield: 55%; IR (KBr pellet) ν_{max} in cm^{-1}: 2955, 2927, 2869, 1720, 1583, 1467, 1414, 1384, 1366, 1259, 1187, 1170, 1155, 1120, 1041, 749; ^{1}H NMR (400 MHz, $CDCl_3$, 298 K): 8.51 (s, 2H, H_{Ar}), 8.48 (d, *J* = 6 Hz, 2H, H_{Ar}), 8.22 (d, *J* = 6 Hz, 2H, H_{Ar}), 4.51-4.43 (m, 8H, 4 × $-OCH_2$), 1.94-1.89 (m, 4H, 4 × $HCCH_3$), 1.69-1.16 (m, 40H, 20 × $-CH_2$), 1.03-1.01 (m, 12H, 4 × CH_3), 0.87-0.85 (m, 24H, 8 × $-CH_3$); ^{13}C NMR (100 MHz, $CDCl_3$, 298 K): 168.83, 168.73, 135.19, 132.15, 130.69, 130.04, 129.44, 129.40, 126.27, 125.68, 125.48, 121.91, 64.62, 64.50, 39.46, 37.49, 35.80, 30.32, 28.17, 24.88, 22.91, 22.81, 19.88; HRMS (-APCI mode) exact mass calculated for $C_{64}H_{89}O_8S$ $[M-1]^-$: 1017.6278, found: 1017.2036.

Synthesis of **3**

A mixture of compound **4** (0.26 mmol, 1 equiv.) and Selenium powder (2.602 mmol, 10 equiv.) was heated to dissolve in *N*-methylpyrrolidone (10 mL) at 70 °C for 30 min. and then refluxed at 180 °C under Ar atmosphere for overnight until the starting material could not be detected by TLC. After cooling to room temperature, 2 M HCl was added, then the precipitate was filtered, washed with water and dried. The crude product was purified by column chromatography on neutral alumina. Elution with 20-30% DCM-hexane system followed by 50% DCM-hexane system yields the desired product. Further purification was done by addition of concentrate solution of compound in cold methanol gives the waxy product.

R_f = 0.6 (20% EtOAc-hexane); orange waxy solid, yield: 55%; IR (KBr pellet) ν_{max} in cm^{-1}: 2955, 2927, 2869, 1719, 1582, 1467, 1406, 1384, 1259, 1189, 1155, 1107, 1041, 800, 748; ^{1}H NMR (400 MHz, $CDCl_3$, 298 K): 8.60 (s, 2H, H_{Ar}), 8.57 (d, *J* = 8 Hz, 2H, H_{Ar}), 8.25 (d, *J* = 8 Hz, 2H, H_{Ar}), 4.47-4.42 (m, 8H, 4 × $-OCH_2$), 1.91-1.87 (m, 4H, 4 × $HCCH_3$), 1.67-1.15 (m, 40H, 20 × $-CH_2$), 1.01-0.99 (m, 12H, 4 × $-CH_3$), 0.86 (dd, *J* = 4 Hz, 24H, 8 × $-CH_3$); ^{13}C NMR (100 MHz, $CDCl_3$, 298 K): 168.89, 168.74, 137.71, 133.70, 132.57, 130.19, 129.40, 128.97, 128.87, 127.35, 125.99, 121.67, 64.60, 64.48, 39.46, 37.47, 35.75, 30.27, 28.16, 24.86, 22.91, 22.80, 19.86; MALDI-TOF: exact mass calculated for $C_{64}H_{90}O_8Se$ $[M]^-$:1066.5801, found: 1066.387.

3.8. References

1. Jean-Francois Tremblay, *Chemical and Engineering news*, 2016, **94**(28), 30-34.
2. C. W.Tang and S. A. VanSlyke, *Appl. Phys. Lett.*, 1987, **51**, 913-915.
3. J. H. Burroughes, D. D. C. Bradley, A. R. Brown, Marks, R. N. K. Mackay, R. H. Friend, P. L. Burns and A. B. Holmes, *Nature*, 1990, **347**, 539-541.
4. J. P. F. Lagerwall and G. Scalia, *Curr. Appl. Phys.*, 2012, **12**, 1387-1412.
5. G. Lussem and J. H. Wendorff, *Polym. Adv. Technol.*, 1998, **9**, 443-460.
6. W. Pisula, M. Zorn, J. Y. Chang, K. Müllen and R. Zentel, *Rapid Commun.*, 2009, **30**, 1179-1202.
7. B. R. Kaafarani, *Chem. Mater.*, 2011, **23**, 378-396.
8. A. M. Van de Craats, N. Stutzmann, O. Bunk, M. M. Nielsen, M. Watson, K. Müllen, H. D. Chanzy, H. Sirringhaus and R. H. Friend, *Adv. Mater.*, 2003, **15**, 495-499.
9. L. S. Mende, A. Fechtenkotter, K. Müllen, E. Moons, R. H. Friend and J. D. MacKenzie, *Science*, 2001, **293**, 1119-1122.
10. A. Bacher, I. Bleyl, C. H. Erdelen, D. Haarer, W. Paulus and H. W. Schmidt, *Adv. Mater.*, 1997, **9**, 1031-1035.
11. A. Wicklein, M.-A. Muth and M. Thelakkat, *J. Mater. Chem.*, 2010, **20**, 8646-8652.
12. *Nanoscience with Liquid Crystals: From Self-Organized Nanostructures to Applications*; Q. Li., Ed.; Springer: Berlin, 2014.
13. F. Würthner, *Chem. Commun.*, 2004, 1564-1579.
14. B. A. Jones, A. Facchetti, M. R. Wasielewski and T. J. Marks, *J. Am. Chem. Soc.*, 2007, **129**, 15259-15278.
15. Z.-J. Chen, L.-M. Wang, G. Zou, L. Zhang, G. J. Zhang, X. F. Cai and M. S. Teng, *Dyes and Pigments*, 2012, **94**, 410-415.
16. G. Li, Y. Zhao, J. Li, J. Cao, J. Zhu, X. W. Sun and Q. Zhang, *J. Org. Chem.*, 2015, **80**, 196-203.
17. J. H. Oh, H. W. Lee, S. Mannsfeld, R. M. Stoltenberg, E. Jung, Y. W. Jin, J. M. Kim, J- B.Yoo and Z. Bao, *Proc. Natl. Acad. Sci. U.S.A.*, 2009, **106**, 6065-6070.
18. R. A. Cormier and B. A. Gregg, *J. Phys. Chem. B*, 1997, **101**, 11004-11006.
19. R. A. Cormier and B. A. Gregg, *Chem. Mater.*, 1998, **10**, 1309-1319.
20. C. W. Struijk, A. B. Sieval, J. E. J. Dakhorst, M. Van Dijk, P. Kimkes, R. B. M. Koehorst, H. Donker, T. J. Schaafsma, S. J. Picken, A. M. van de Craats, J. M. Warman, H. Zuilhof and E. J. R. Sudhölter, *J. Am. Chem. Soc.*, 2000, **122**, 11057-11066.
21. X. Zhang, S. Rehm, M. M. Safont-Sempere and F. Würthner, *Nat. Chem.*, 2009, **1**, 623-629.
22. C. Li and H. Wonneberger, *Adv. Mater.*, 2012, **24**, 613-636.
23. S. A. Benning, R. Oesterhaus and H.-S. Kitzerow, *Liq. Cryst.*, 2004, **31**, 201-205.
24. T. Hassheider, S. A. Benning, H.-S. Kitzerow, M.-F. Achard and H. Bock, *Angew. Chem. Int. Ed.*, 2001, **40**, 2060-2063.
25. S. A. Benning, T. Hassheider, S. Keuker-Baumann, H. Bock, F. D. Sala, T. Frauenheim and H.-S. Kitzerow, *Liq. Cryst.*, 2001, **28**, 1105-1113.
26. J. Eccher, G. C. Faria, H. Bock, H.Von Seggern and I. H. Bechtold, *ACS Appl. Mater. Interfaces*, 2013, **5**, 11935-11943.
27. J. Eccher, W. Zajaczkowski, G. C. Faria, H. Bock, Von Seggern, W. Pisula and I. H. Bechtold, *ACS Appl. Mater. Interfaces*, 2015, **7**, 16374-16381.
28. D. M. Collard and C. P. Lillya, *J. Am. Chem. Soc.*, 1991, **113**, 8577.

29. P. G. Schouten, J. H. Warman, M. P. de Haas, C. F. van Nostrum, G. H. Gelinck, R. J. M. Nolte, M. J. Copyn, J. W. Zwikker, M. K. Engel, M. Hanack, Y. H. Chang and W. T. Ford, *J. Am. Chem. Soc*., 1994, **116**, 6880-6894.
30. S. Kumar, D. S. S. Rao and S. K. Prasad, *J. Mater. Chem*., 1999, **9**, 2751-2754.
31. C. V. Yelamaggad and A. S. Achalkumar, *Tetrahedron Letters*, 2006, **47**, 7071-7075.
32. J. K. Vij, A. Kocot and T. S. Perova, *Mol. Cryst. Liq. Cryst*. 2003, **397**, 231-244.
33. A. M. Brouwer, *Pure Appl. Chem*., 2011, **83**(12), 2213-2228.
34. D. S. McClure, *J. Chem. Phys*., 1949, **17**, 905-913.
35. M. Kasha, *J. Chem. Phys*., 1952, **20**, 71-74.
36. M. N. B. Santos, *PhysChemComm*, 2000, **3**, 18-23.
37. F. Würthner, C. Thalacker, S. Diele and C. Tschierske, *Chem. Eur. J*., 2001, **7**, 2245-2253.
38. D. D. Prabhu, N. S. S. Kumar, A. P. Sivadas, S. Varghese and S. Das, *J. Phys. Chem. B*, 2012, **116**, 13071-13080.
39. S. Basak, S. Bhattacharya, A. Datta and A. Banerjee, *Chem. Eur. J*., 2014, **20**, 1-7.
40. J. Gierschner, L. Lüer, B. Milan-Medina, D. Oelkrug, and H.-J. Egelhaaf, *J. Phys. Chem. Lett*., 2013, **4**, 2686-2697.
41. M. Cai, T. Xiao, E. Hellerich, Y. Chen, R. Shinar and J. Shinar, *Adv. Mater*., 2011, **23**, 3590-3596.
42. E. Kozma, W. Mro´z, F. Villafiorita-Monteleone, F. Galeotti, A. Andicsova´-Eckstein, M. Catellani and C. Botta, *RSC Adv*., 2016, **6**, 61175-61179.
43. Y. Bai, X. Chen, X. Wan and Q. Zhou, Chin. *J. Polym. Sci*., 2002, **20**(2), 155-159.
44. Hu, S.-H -Q.T. Z. Zhou, M. Yang, M.-H.Quan, Q.-B. Mei, B.-C.Zhai, Z.-H. Jia, Z.-H. Lai, W. Y. Lai and W. Huang Ye, *Phys. Chem. Chem. Phys*., 2015, **17**, 8860-8869.
45. K. Kotwica, A. S. Kostyuchenko, P. Data, T. Marszalek, L. Skorka, T. Jaroch, S. Kacka, M. Zagorska, R. Nowakowski, A. P. Monkman, A. S. Fisyuk, W. Pisula and A. Pron, *Chem. Eur. J*., 2016, **22**, 11795-11806.
46. Q. Peng, N. Gao, W. Li, P. Chen, F. Li and Y. Ma, *Appl. Phys. Lett*., 2013, **102**, 193304-1-193304-4.
47. V. D. Cupere, J. Tant, P. Viville, R. Lazzaroni, W. Osikowicz, W. R. Salaneck and Y. H. Geerts, *Langmuir*, 2006, **22**, 7798-7806.
48. a) Y. Bai, X. Chen, X. Wan and Q. Zhou, *Chin. J. Polym. Sci*., 2002, **20**(2), 155-159; b) A. Kimura, S. Yoshimoto, Y. Akana, H. Hirata, S. Kusabayashi, H. Mikawa and N. Kasai, *J. Polym. Sci*., 1970, **8**, 643-648.

Chapter 3b

Perylene-triazine based star-shaped green light emitter for organic light emitting diodes

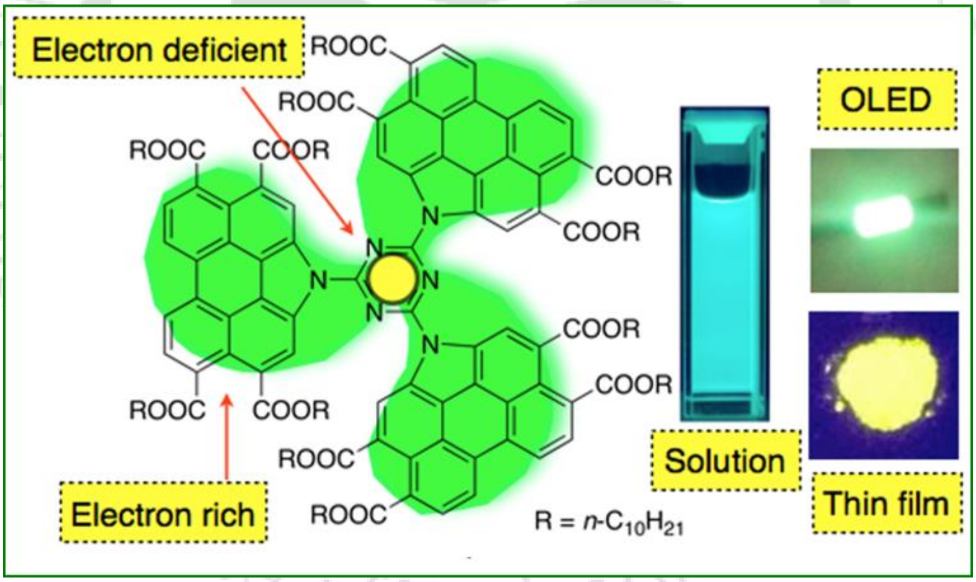

Results have been published in;

- *Eur. J. Org. Chem.*, 2018, 1608-1613.

3.9. Introduction

Star-shaped molecules are distinct from their linear counterparts. They possess improved solution processability, self-assembly behavior, glass forming nature, interesting electrochemical and charge transport behaviors.[1] Donor-acceptor (D-A) molecules were exploited in the construction of organic field effect transistors (OFETs) and bulk hetero junction solar cells. However, application of such molecules in organic light emitting diodes (OLEDs) is comparatively less. Due to the radially branched structures, star-shaped D-A molecules reduce the intermolecular interactions in the solid state, thus leading to enhanced solid-state emission with good film forming property. In addition, this design can be an alternative to polymers, which suffer from batch to batch variation in the molecular weight, purity and polydispersity issues, which affect the reproducibility of the device performance. There is a report, where the star shaped truxene derivative with fluorene arms exhibited higher electroluminescence (EL) and external quantum efficiency (EQE) values in comparison to its linear counterpart.[2] There are several reports with fluorene containing star shaped molecules exhibiting improved device characteristics in comparison to the linear polymers.[3] The better-balanced charge injection and transportation are important factors, which affect the OLED performance. Thus the introduction of D-A architecture with a push-pull design supports the improved charge migration, lowers the bandgap and provides a red-shifted emission spectrum. Such structures also provide the hole and electron traps on a same molecule, thus enhancing the carrier recombination efficiency.[4,7] Star-shaped molecules with central triazine-trioxadiazole (acceptor) with the peripheral carbazole (donor) moieties have been reported to show a blue emission with high efficiency with a resistance to oxidative degradation.[5,8] Several such molecules exhibited phosphorescence and thermally activated delayed fluorescence (TADF) phenomena, which are very hot topics in present day OLED research.[6] Considering all these factors, we designed a novel star-shaped molecule with a central triazine acceptor connected to three *N*-annulated perylene tetraester moieties which are relatively electron rich (Figure 3.19a**,** b). The presence of *n*-decyloxy groups was to enhance the solubility. Incorporation of the *N*-annulated perylene tetraesters to form a star-shaped architecture was motivated by their columnar self-assembly and high luminescence quantum yield. The presence of three *N*-annulated perylene tetraesters is supposed to increase the steric hindrance of the arms leading to a propeller shaped molecule (Figure 3.19). This would suppress the aggregation; reduce the emission quenching to enhance the EQE.

3.10. Results and Discussion

The synthetic route for the star-shaped molecule is presented in Scheme 3.2. The *N*-annulated perylene tetraester (**1c**) prepared in previous chapter, was treated with cyanuric chloride in presence of *n*-BuLi as a base to obtain the product **PT-T** in 55 % yield (Scheme 3.2). Compound **PT-T** was found to be a waxy substance and was characterized with the ^{1}H NMR, ^{13}C NMR, IR spectroscopy and MALDI-TOF analysis.

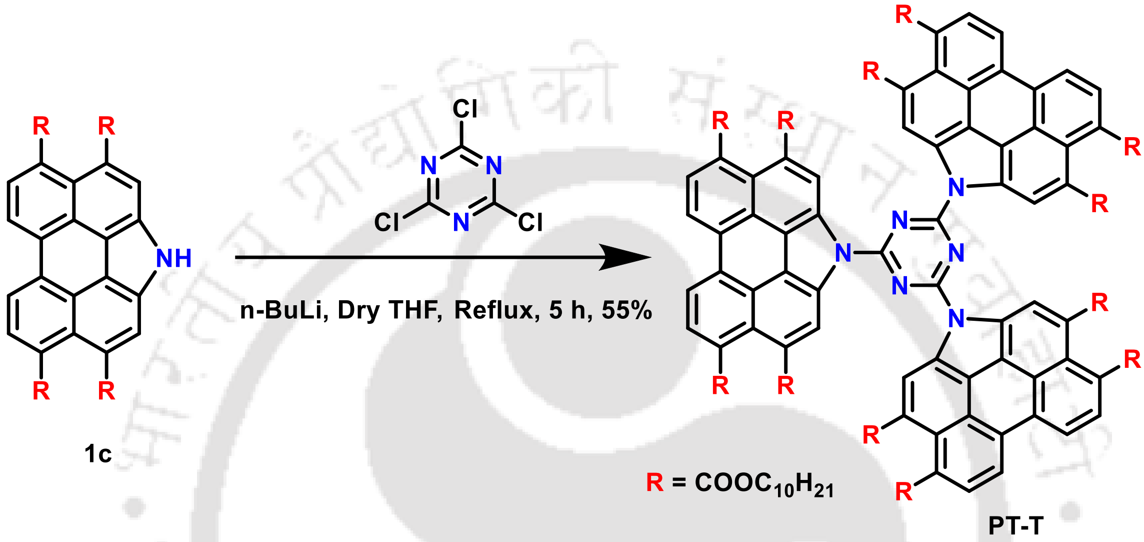

Scheme 3.2. Synthesis of compound **PT-T**.

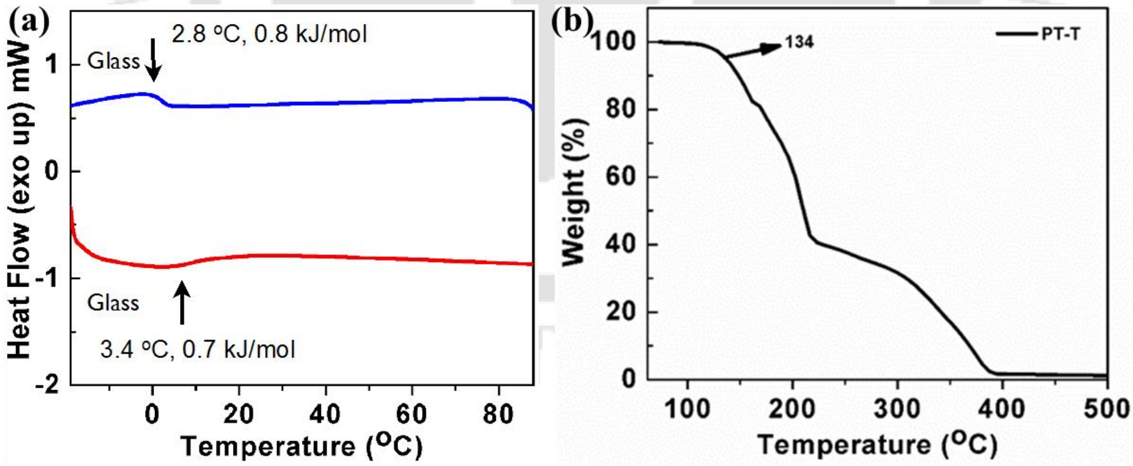

Figure 3.18. (a) DSC traces obtained for compound **PT-T** at a rate of 5 °C/min (red trace: 2nd heating scan; blue trace: 1st cooling scan); (b) TGA curve obtained for compound **PT-T** at a rate of 10 °C/min under N_2 atmosphere.

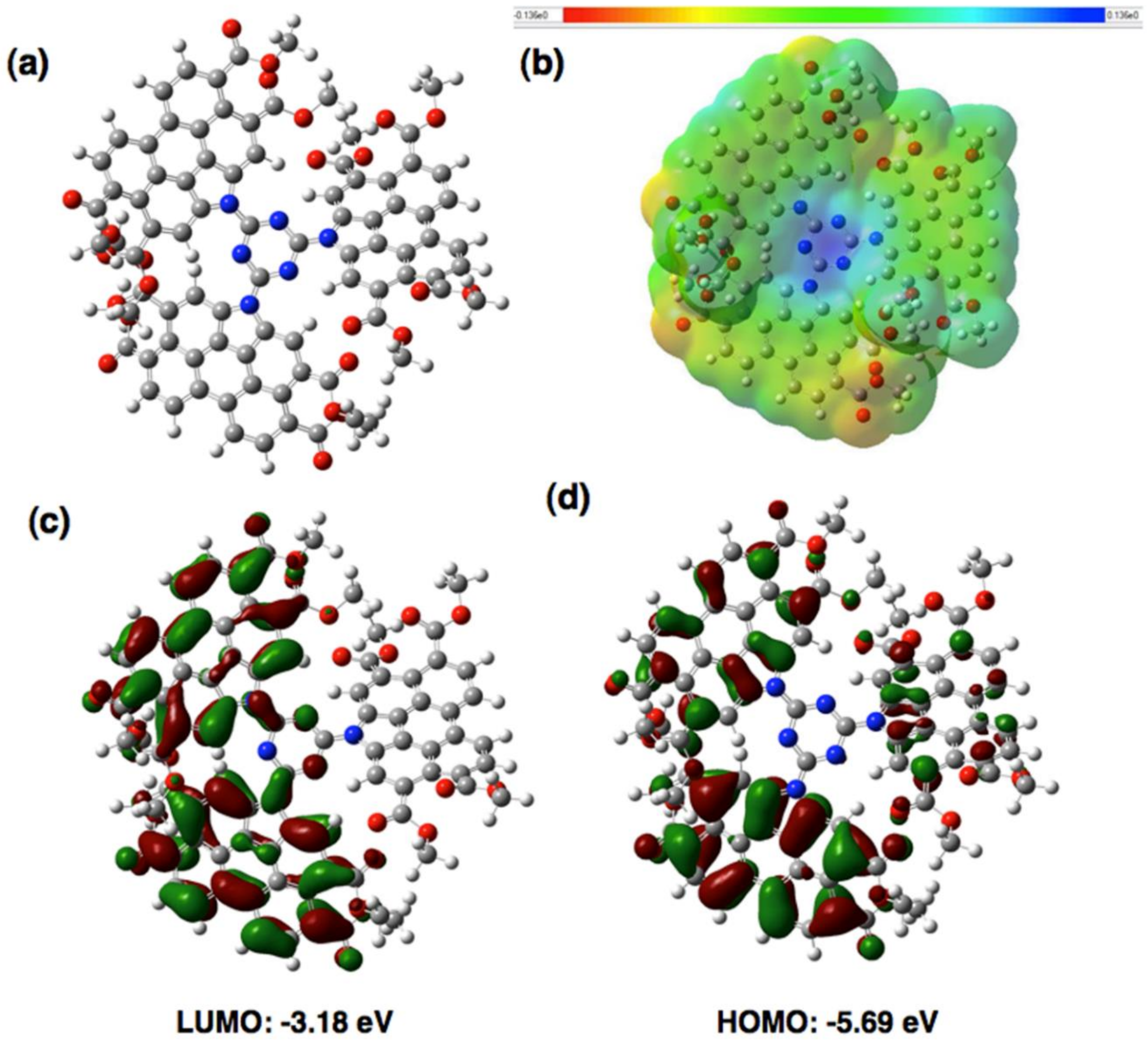

Figure 3.19. (a) Optimized geometry of compound **PT-T**; (b) 3D molecular electrostatic potential contour map of optimized structure of **PT-T** (In the mapped electrostatic potential surface, red and blue colours refer to the electron-rich and electron-poor regions respectively whereas the green colour signifies the zero electrostatic potential); (c) LUMO and (d) HOMO frontier molecular orbitals of compound **PT-T** (Obtained by TDDFT method employing B3LYP/6-31G(d,p) functional. For the purpose of clarity, the chain length is confined to -CH_3).

The melting of compound **PT-T** was not detected in polarizing optical microscopy (POM). However, in differential scanning calorimetry (DSC), we noticed a reproducible glass transition peak at 2.8 ^{o}C (ΔH = 0.81 kJ/mol) in cooling cycle (Figure 3.18a). The propeller structure of the molecule exhibited a twist of the perylene moieties with respect to the central triazine unit as noted from the TDDFT calculations (Figure 3.19a). The low melting behavior of this molecule may be resulting from the inability of the molecule to stack and also due to the presence of twelve *n*-decyloxy chains. Thermogravimetric analysis (TGA) showed that compound is stable up to 134 ^{o}C and complete decomposition was noticed at around 400 ^{o}C (Figure 3.18b).

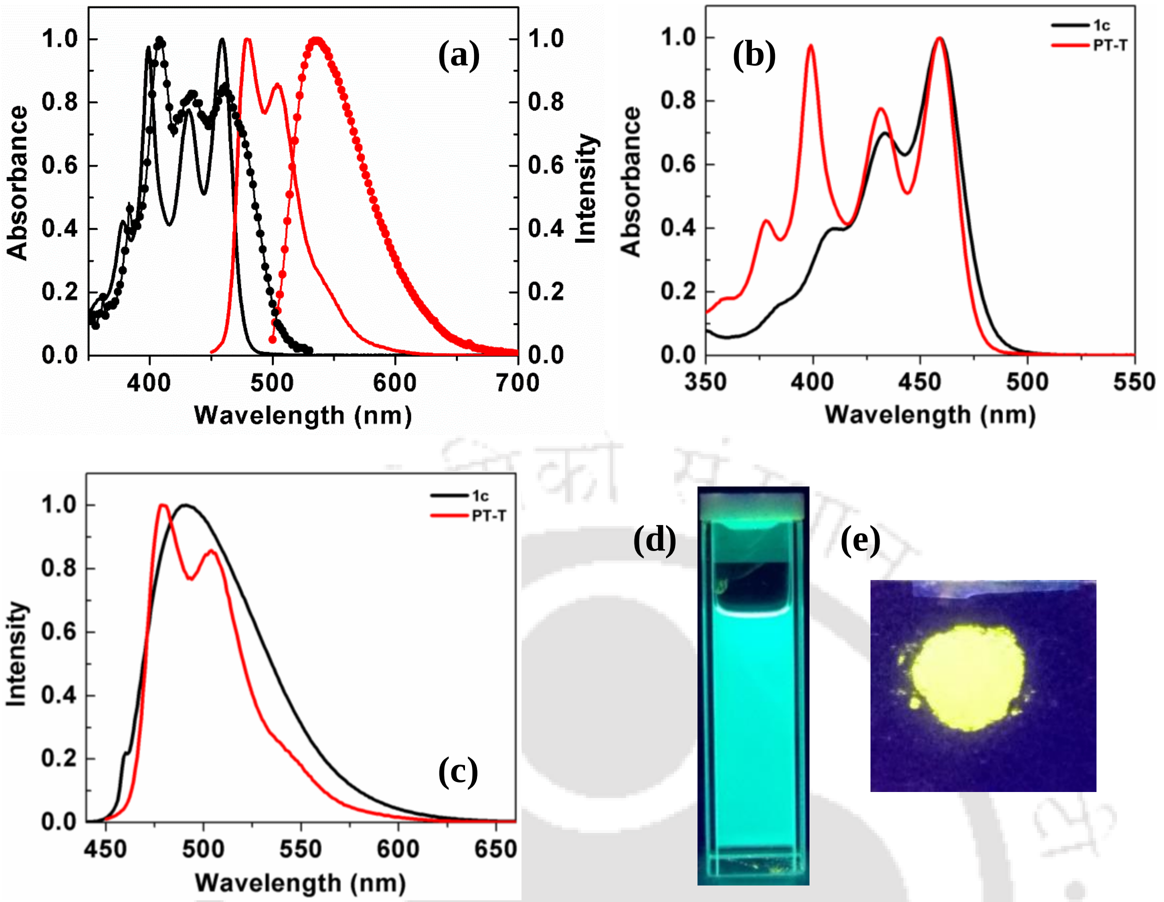

Figure 3.20. (a) Absorption (black trace) and emission (red trace) spectra in micromolar THF solution (solid lines) and in the thin film state (dotted lines) of compound **PT-T**; (b) overlay of the absorption spectra and (c) emission spectra in micromolar THF solution of compound **PT-T** (red trace) and **1c** (black trace); (d) shows the pictures of the solution and (e) thin film as seen under UV illumination of wavelength 365 nm.

Photophysical properties of the compound **PT-T** in solution as well as thin film are presented in Table 3.10. Absorption and fluorescence spectra of the compound **PT-T** were taken in micromolar THF solutions. As can be seen, the solution of **PT-T** showed a structured absorption spectrum (Figure 3.20a). The bands at 457 nm and 430 nm are originating from the perylene tetraester while the bands at lower wavelength are arising from the central triazine moiety (Figure 3.20b). The molar absorption coefficient at 457 nm was found to be very high ($\varepsilon > 23{,}710\ M^{-1}cm^{-1}$) as expected due to the conjugated structure. This value more than double to that of compound **1c**. The emission spectra obtained showed an emission maximum at 484 nm along with a shoulder band at 508 nm. The Stoke's shift was found to be ≈1125 cm^{-1} which is lesser than that obtained for compound **1c** (1584 cm^{-1}). The solution showed a visually perceivable bright green fluorescence under the UV light of long wavelength (λ = 365 nm) (Figure 3.20d). The emission bands are structured with a blue shifted emission maximum in comparison to the corresponding *N*-annulated perylene tetraester **1c** (Figure 3.20c). The relative quantum yield calculated was found to be unity with respect to fluorescein (0.1M NaOH solution; $Q_S = 0.79$), which is comparable to compound **1c**. The thin film of the sample was prepared by annealing of compound **PT-T** (Figure 3.20e) exhibited a red shifted absorption and emission bands in the thin film state, suggesting the formation of aggregates. The red shifted absorption is usually attributed to the development of J-type aggregates, where the molecules are arranged with a 'head to tail' or in a 'slipped stack' manner.[9,10] Compound **PT-T** exhibited a higher optical band gap in comparison to compound **1c** (Table 3.10).

Table 3.10 Photophysical and electrochemical properties of compounds **PT-T** and **1c**.

	Solution[a]			**Thin film**[d]		**Cyclic voltametry**[e, f, g]				
	Absorption (nm)	**Emission**[b] **(nm)**	**ΔE_g, opt**[c]	**Absorption (nm)**	**Emission (nm)**	**E_{1red} (V)**	**E_{1ox} (V)**	**E_{HOMO}**[g] **(eV)**	**E_{LUMO}**[h] **(eV)**	**ΔE_g, CV**[i] **(eV)**
PT-T	457, 430, 399, 378, 360	484, 508	2.59	409, 435, 461	536	-1.04	1.30	-5.59	-3.25	2.34
1c	459, 434, 410	493	2.48	416, 479[j]	556[j]	-0.97	1.38	-5.66	-3.31	2.35

[a]micromolar solution in THF, [b]excited at the absorption maximum, [c]calculated from the red edge of the longest wavelength in the absorption spectrum [d]prepared from the millimolar solution in chloroform, [e]micromolar solution in dichloromethane, [f]Experimental conditions: Ag/$AgNO_3$ as reference electrode, Glassy carbon working electrode, Platinum wire counter electrode, TBAP (0.1 M) as a supporting electrolyte, room temperature, [g]Estimated from the formula $E_{HOMO} = -(4.8 - E_{1/2,Fc/Fc^+} + E_{ox,\ onset})$ eV; [h]Estimated from the formula by using $E_{LUMO} = -(4.8 - E_{1/2,\ Fc/Fc^+} + E_{red,\ onset})$eV; [i]Estimated from the formula $\Delta E_{g,CV} = E_{LUMO} - E_{HOMO}$. $E_{1/2,Fc/Fc+} = 0.517$. [j]Emission in the thin film is provided for the tetraoctyloxy homlogue of compound **1c**, as they have identical optical properties.

Time resolved fluorescence provides valuable information about the interaction of the molecule in the excited state with its environment. The micromolar solution of compound **PT-T** in chloroform showed monoexponential decay with the excited species [τ_1 = 5.12 ns (100%)]. Fluorescence lifetimes of the excited species formed in the thin film of compound **PT-T** was measured by monitoring its emission maxima. The thin film of the compound **PT-T** prepared by spin coating the 3 mM solution in chloroform exhibited a biexponential decay but with an increase in the life time [τ_1 = 4.1 ns (8.1 %), τ_2 = 19 ns (92 %)]. This could be due to the restricted intramolecular rotations of the propeller molecular segments in solid state, which reduce the nonradiative pathways. In addition, such twisted molecular conformation supports loose packing in the solid state, preventing the strong intermolecular π-π interactions and thus helps the luminescent molecules decay to the ground state through radiative decay pathways.[11,12]

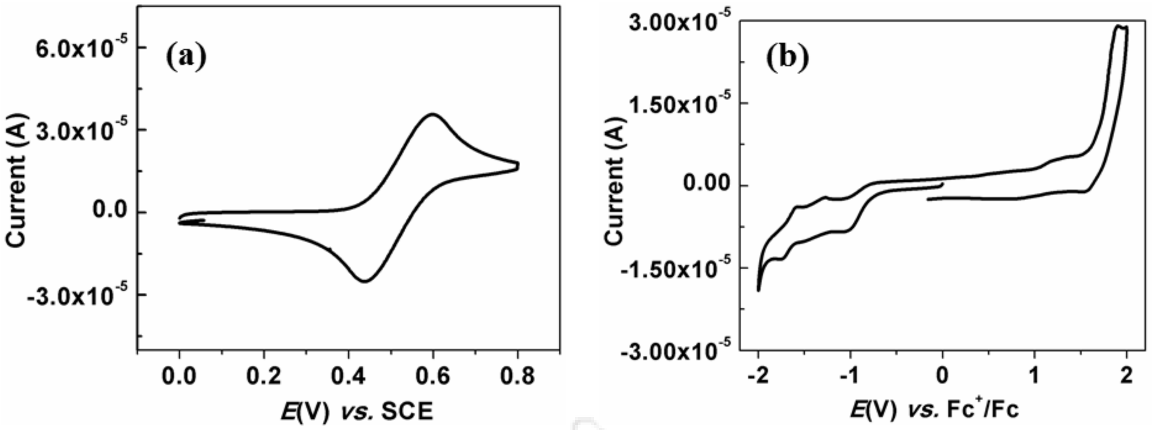

Figure 3.21. (a) Cyclic voltamograms of ferrocene and (b) compound **PT-T** in DCM solution of tetra-*n*-butylammonium perchlorate (TBAP) (0.1 M) at a scanning rate 0.1 mV s^{-1}; the half wave potential of Fc/Fc^{+} was found to be 0.517 V relative to Ag/Ag^{+} reference electrode.

Cyclic voltammetry studies carried out in solution showed the first reduction and oxidation potentials at -1.04 eV and 1.3 eV from which the energy levels and the band gap was calculated. The compound **PT-T** exhibited a HOMO level of -5.59 eV and a LUMO level of -3.25 eV with a band gap of 2.34 eV (Figure 3.21,Table 3.10). This band gap obtained was almost comparable to the optical band gap derived from the long edge of the absorption spectrum (2.59 eV, Table 3.10). Time Dependent Density functional theory (TDDFT) calculations[13] were performed to obtain information on the geometry and electronic structure of compound **PT-T**. The optimized structure resembles a propeller shape (Figure 3.19a), with the contours of the HOMO level are distributed mostly perylene moieties, while the LUMO level was found to be distributed on the central triazine unit and two perylene moieties (Figure 3.19c, d). This hints a partial intramolecular charge transfer although the absorption spectra do not support this (Figure 3.20b). To probe further about the nature of electronic transitions, we considered analyzing the natural transition orbitals (NTOs). The hole and electron densities for compound **PT-T** are depicted in Figure 3.22. It is clear that, we see a dominant S_0-S_1 transition (λ = 0.99). The electron-hole densities are localized either on one of the perylene moieties or covering the central triazine and other two perylene moieties. The overall result is that most of holes and electrons are predominantly localized, hinting the absence of intramolecular charge transfer. The energy levels of HOMO and LUMO orbitals obtained from TDDFT calculations were -5.69 eV and -3.18 eV respectively, with a 2.5 eV separation between them (Figure 3.19c, d). These values are comparable to the data obtained from the photophysical studies and cyclic voltammetry. In comparison to *N*-annulated perylene tetraester **1c**, both HOMO and LUMO levels were lowered, while the band gap was increased which may be due to the inclusion of triazine in the molecular structure.

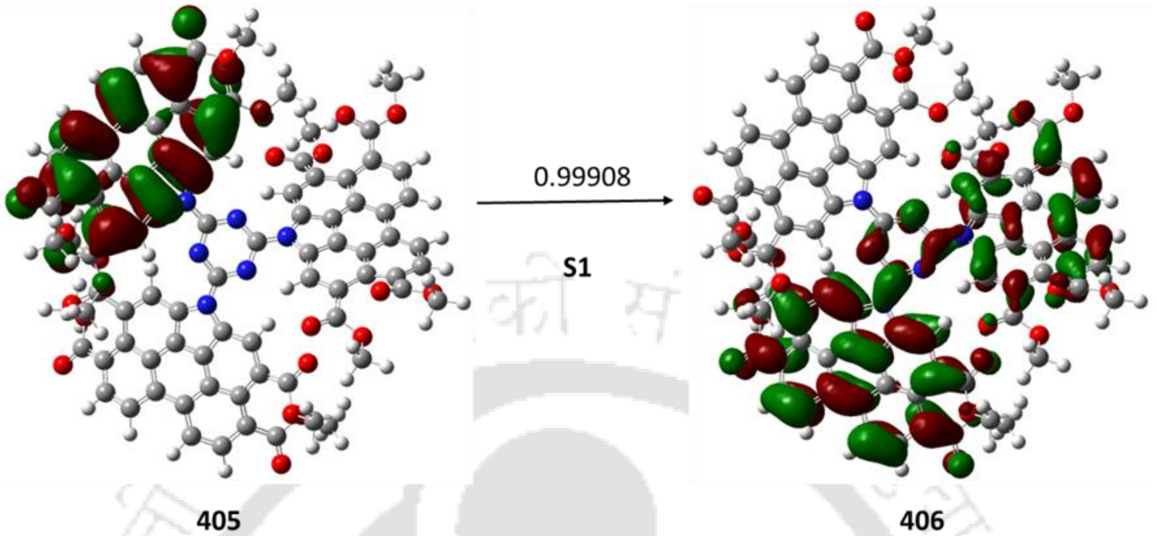

Figure 3.22. Dominant hole-electron pair natural transition orbitals (NTOs) for the electronic transition (S_0 to S_1) of **1-CH$_3$** at an isosurface value of 0.02. The eigen value λ = 0.99908 is the contribution of the pair to the excitation.

To visualize the change in the HOMO and LUMO levels of compounds and the effect of ester groups we have compared the HOMO and LUMO levels of tetramethyl perylene tetracarboxylate (**PTE**), corresponding *N*-annulated derivative (**N-PTE**), analogue of compound **PT-T** without any ester groups (**NP-T**) and methyl analogue of compound **PT-T (1-CH$_3$)** (Figure 3.23). Perylene molecule is known to have a HOMO and LUMO levels of -5.18 eV and -2.16 eV respectively. *N*-annulation of perylene leads to a slight increase in the HOMO and LUMO levels.[14] The addition of four ester groups as in the case of **PTE** leads to the lowering of HOMO and LUMO levels. The *bay*-annulation of **PTE** to get compound **N-PTE** increase the HOMO and LUMO levels along with an increase in the energy gap (Figure 3.24). *N*-annulated perylene is known to have a HOMO and LUMO levels of -5.07 eV and -1.81 eV respectively, which is an increment in comparison to the frontier molecular orbitals (FMO) of perylene.[14] Here, the addition of four ester groups to form **N-PTE** leads to the lowering in the HOMO level (-5.65 eV) and LUMO level (- 2.78 eV). From both examples, it is seen that the addition of ester groups lower the energy levels of frontier molecular orbitals. Compound **NP-T**, where three *N*-annulated perylene moieties are coupled to triazine showed an increase in HOMO level (-4.85 eV) and a reduction in the LUMO level (-1.86 eV) in comparison to *N*-annulated perylene. The methyl analogue of compound **PT-T** showed the lowering of both HOMO and LUMO levels, in comparison to **NP-T**. The lowering of HOMO was by 0.84 eV and the lowering of LUMO was by 1.32 eV. Thus the presence of ester groups had a major impact on the FMOs of compound **PT-T**.

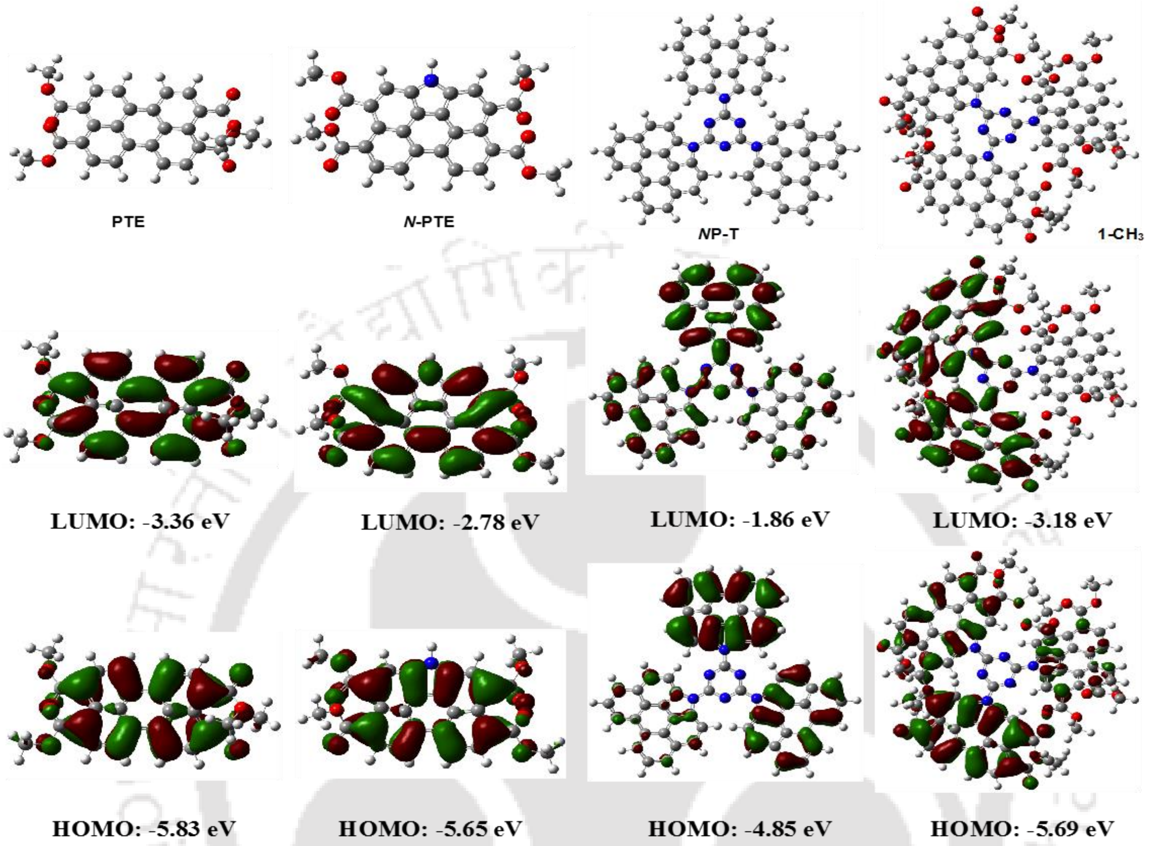

Figure 3.23. A comparison of energy levels of frontier molecular orbitals of **PTE, N-PTE, NP-T** and **1-CH$_3$**.

The energy diagram of a conventional organic molecule, portraying singlet (S_1) and triplet (T_1) excited states and a ground state (S_0) is given below (Figure 3.25a). Usually the S_1 level will be higher in energy than the T_1 level, by 0.5–1.0 eV, because of the electron exchange energy between these levels. However, a careful design of organic molecules can lead to a small energy gap (ΔE_{ST}) between S_1 and T_1 levels.[6e] Such molecules are suitable candidates for TADF emitters. Correspondingly, a molecule with efficient TADF requires a very small ΔE_{ST} between its S_1 and T_1 excited states, which enhances T_1 to S_1 reverse intersystem crossing (ISC). Such excited states are attainable by intramolecular charge transfer within systems containing spatially separated donor and acceptor moieties.[6f] Thus the molecular design must include a small ΔE_{ST} (≈ 100 meV) along with a reasonable radiative decay rate. These two properties require the careful balanced overlap of the highest occupied molecular orbital and the lowest unoccupied molecular orbital. Thus a control on the change in geometries of molecular conformations between the S_0 and S_1 states should be maintained to suppress the nonradiative decay.

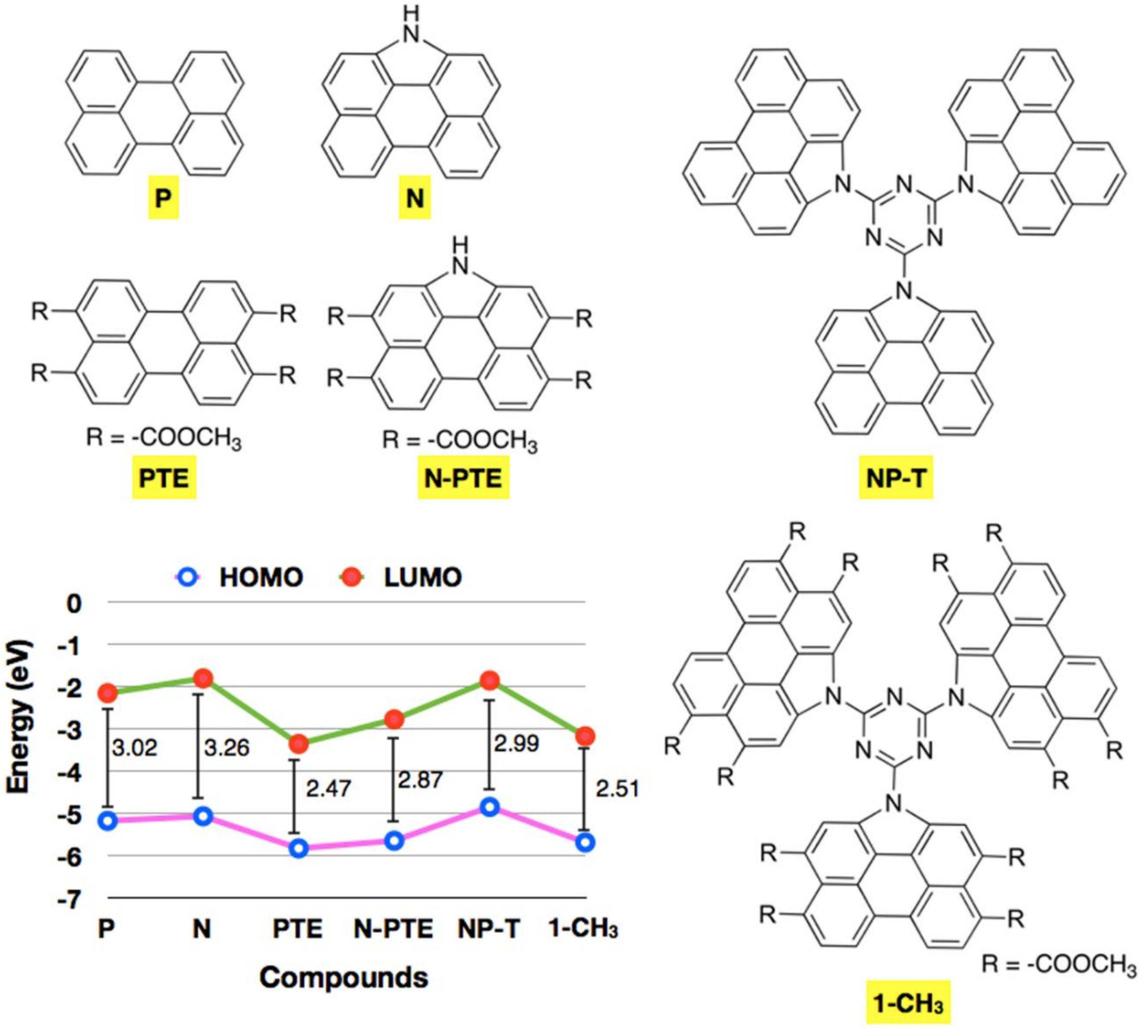

Figure 3.24. Comparison of HOMO and LUMO levels of compounds **P, N, PTE, N-PTE, NP-T** and **1-CH₃** by TD-DFT calculations.

We were curious to investigate the ΔE_{ST} values of the series of molecules given in Figure 3.24. From the calculations we see a gradual decrease in the values of singlet energies, while a gradual increase in the values of triplet energies. There is also a decrease in the ΔE_{ST} (Figure 3.25b). The addition of ester groups helped in the decrease of ΔE_{ST} as we move from **NP-T** to **1-CH₃**. However, the decrease (ΔE_{ST} = 0.76 eV) is not enough to exhibit the TADF phenomenon, which has to be less than 100 meV.[6] From the seminal work of Adachi *et al.*,[6b-g] it is shown that the molecular design should be in such a way to introduce a steric hindrance between the donor groups and the central acceptor to achieve a large dihedral angle. This would lead to the spatial separation of highest occupied and lowest unoccupied NTOs, which will lead to a small ΔE_{ST} and improved T_1 to S_1 reverse intersystem crossing (RISC). Even the presence of twelve *n*-decyloxy chains in compound **PT-T** may not lead to such steric hindrance as the three perylene moieties are not adjacent to each other to create sufficient steric strain.

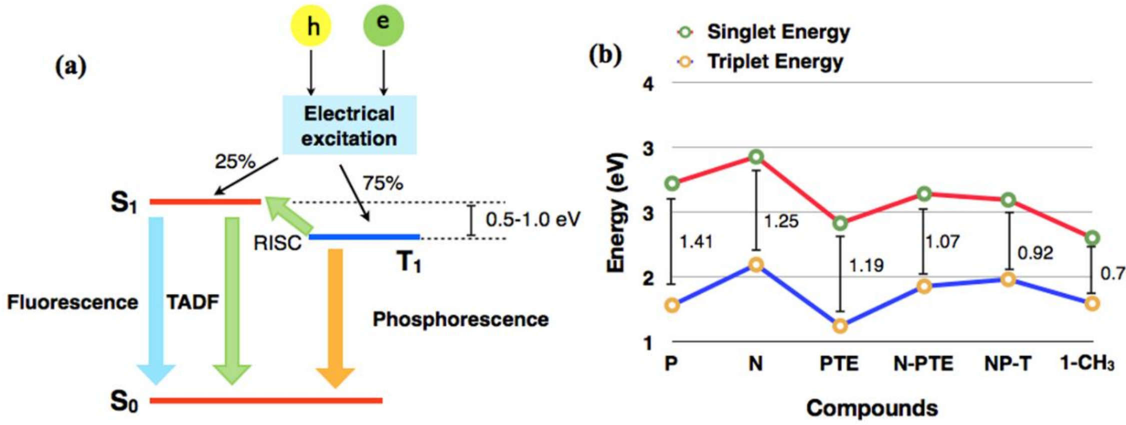

Figure 3.25. (a) Energy diagram of conventional organic molecule; (b) Variation of singlet energy (E_S), triplet energy (E_T) and ΔE_{ST} as a function of molecular structures given in Figure 3.24.

To evaluate the suitability of compound **PT-T** as an emissive material in OLED applications, we fabricated multilayer OLEDs with **PT-T** as a sole emissive material as well as an emissive dopant with the following device architecture (device **A**/**B**): Indium tin oxide (ITO, 120 nm)/Poly(3,4-ethylenedioxythiophene)/poly(styrene sulfonate)(PEDOT:PSS, 50 nm)/ emissive layer (80 nm)/ Bathocuproine (BCP, 6 nm)/ Tris-(8-hydroxyquinoline)aluminium (Alq3, 35 nm)/ Lithium fluoride (LiF, 1 nm)/ Aluminium (Al, 120 nm). Compound **PT-T** acted as a sole emissive material in device **A**, whereas in the case of device **B**, the emissive material was composed of 10 wt% of compound **PT-T** in the host material, polyvinyl carbazole (PVK) which has a good miscibility with different emissive materials.[15] In the devices, ITO was used as a transparent anode, PEDOT:PSS served as a hole injection material, BCP was used as hole-blocking material to restrict the holes to the emitting layer,[16] Alq3 was used to assist the electron injection into the emitting layer and a bilayer cathode comprising of LiF and Al was used. The schematic of the device architecture and the energy levels of the materials are depicted in Figure 3.26 and Table 3.11 summarizes the performance data of the devices. The current density-voltage-luminance (J-V-L) characteristics of the fabricated OLEDs are shown in Figure 3.26c. The device **B** with compound **PT- T** doped in PVK as emissive material

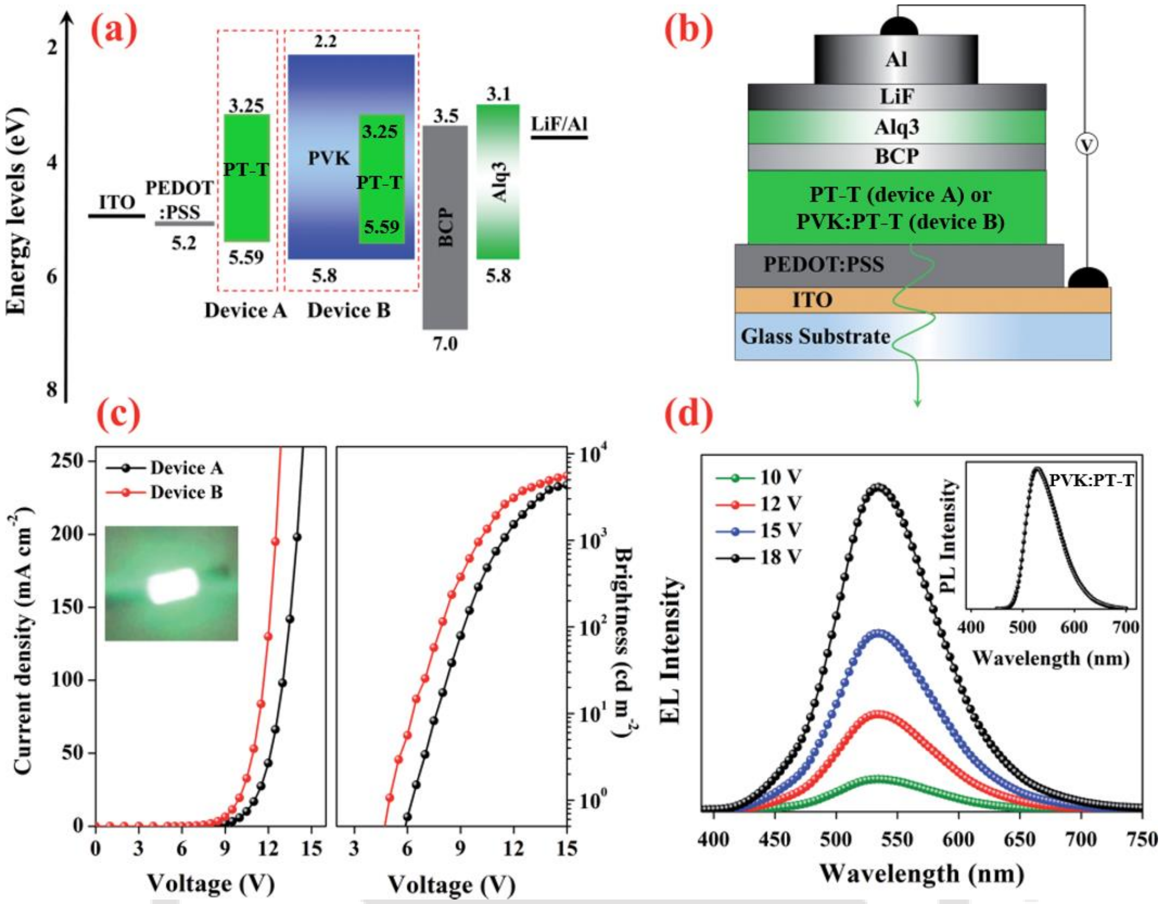

Figure 3.26. (a) Energy-level diagram of the materials used in the OLEDs; (b) schematic of the device architecture; (c) J-V-L characteristics (inset: operating device); (d) EL spectra of device **B** at different bias voltages (inset shows PL spectra of PVK: **PT-T** thin film).

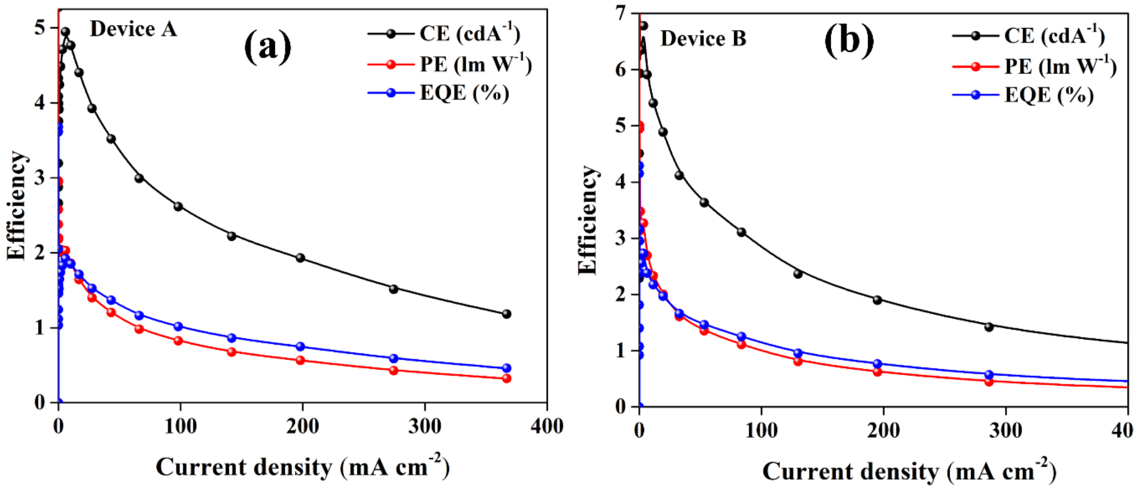

Figure 3.27. (a, b) Plots showing device efficiency (current efficiency, power efficiency and external quantum efficiency) as a function of brightness for devices **A** and **B** respectively.

Table 3.11. Electroluminance performance data of OLEDs.

Device	V_{on} **(V)**[c]	L_{max} **(cd m^{-2})**[d]	η_c **(cd A^{-1})**[e]	η_p **(lm W^{-1})**[e]	η_{EQE} **(%)**[e]	**λ_{em} FWHM (nm)**[f]	**CIE** $_{(x,y)}$ [g]
A[a]	6.16	4334	4.54	2.04	1.76	535 (58)	(0.324, 0.554)
B[b]	4.97	5561	6.37	3.34	2.57	534 (66)	(0.332, 0.535)

[a]Device **A**: ITO (120 nm)/ PEDOT:PSS (50 nm)/ **PT-T** (80 nm)/ BCP (6 nm)/ Alq3 (35 nm)/ LiF (1 nm)/ Al (150 nm); [b]Device **B**: ITO (120 nm)/ PEDOT:PSS (50 nm)/ PVK: **PT-T** (80 nm)/ BCP (6 nm)/ Alq3 (35 nm)/ LiF (1 nm)/ Al (120 nm); [c]V_{on}: turn-on voltage at luminance of 1 cd m^{-2}; [d]L_{max}: Luminance at 15 V; [e]current efficiency (η_c), power efficiency (η_p) and external quantum efficiency (η_{EQE}); [f]λ_{em}: Emission wavelength maximum and FWHM at 15 V; [g]CIE color coordinate.

showed lower turn-on voltage (V_{on}) than device **A** in which **PT-T** acted as the sole emissive material. Also, a significant enhancement in the device performance was observed in device **B** with high luminance (L_{max}) of 5561 cdm^{-2} efficiencies of 6.37 cdA^{-1} (current efficiency, η_c), 3.34 lmW^{-1} (power efficiency, η_p) and 2.57% (external quantum efficiency, η_{EQE}) compared to device **A** (4334 cdm^{-2}, 4.54 cdA^{-1}, 2.04 lmW^{-1} and 1.76 %) (Figure 3.27a, b). The increase in the performance of device **B** can be credited to the effective transfer of exciton energy from PVK (host material) to compound **PT-T** (emissive dopant). Both the devices (**A** and **B**) emitted in the green region. The steady-state electroluminescence (EL) spectra for device **B** are shown in Figure 3.26d. The EL spectra of both the devices were almost same with emission peak (λ_{em}) at 535 nm (device **A**) and 534 nm (device **B**) with full width half maxima (FWHM) of 58 nm and 66 nm, respectively. Also, the EL spectra of the devices were similar to the solid thin film photoluminescence (PL) spectra of PVK: **PT-T** (Figure 3.26d, inset), which infers that the origin of both the spectra are from the same excited state. Furthermore, it can be seen from Figure 3.26d that the device exhibited excellent spectral stability as shown by the EL spectra of the device over a wide range of operating voltages (10-18V). This reveals that the material has good thermal stability during device operation. The CIE chromaticity coordinates tabulated in Table 3.11 corresponds to a bright green emission (Figure 3.28). It is to be noted that the devices are unoptimized and further optimizations of the devices may lead to better device performance. These observations offer the potential use of compound **PT-T** in OLED applications with a further possibility to improve, by minor alterations in the molecular design and device architecture.

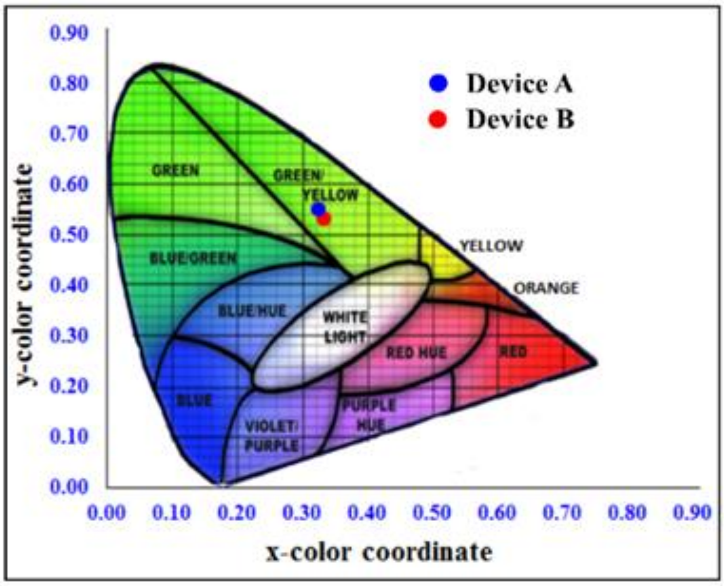

Figure 3.28. Chromaticity diagram of the OLEDs.

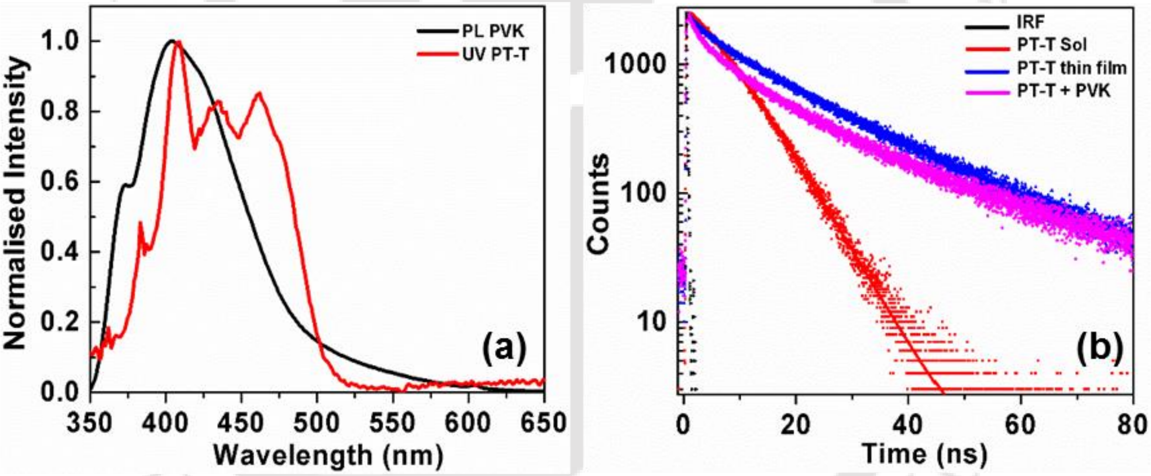

Figure 3.29. (a) Overlay of UV spectrum of **PT-T** over the fluorescence spectrum of PVK in the thin film state; (b) The fluorescence decay of compound **PT-T** in micromolar chloroform solution (red trace, λ_{exc} = 405 nm, monitored at λ_{max} = 484 nm), for the thin film of compound **PT-T** (blue trace, obtained by spin coating 3 mM chloroform solution) PVK:10 wt% **PT-T** (pink trace, λ_{exc} = 405 nm, monitored at λ_{max} = 535 nm, obtained by spin coating the chloroform solution) (black trace: IRF).

Doping the emissive material whose absorption spectra has a near perfect overlap on the emission spectra of the host will help in the energy transfer from host to guest material. This is by Förster energy transfer.[17] Figure 3.29a shows that the overlap of the emission spectrum of PVK and the absorption spectrum of the compound **PT-T** in thin film mode. This also partially contributes to the enhanced brightness in the case of device **B**. The thin film of PVK:10 wt% **PT-T** prepared by similar method exhibited three excited species [τ_1 = 5.4 ns (18.5 %), τ_2 = 19.7 ns (78 %), τ_3 = 0.9 ns (2.8 %)] (Figure 3.29b, Table 3.12). The observed increase in the lifetime in the host-guest mixture further supports the Förster energy transfer. From these studies we notice that, lifetime of the major species has increased in the thin film state and with PVK it has shown further increase. In the solution state the fluorescence lifetime is reduced due to the solute-solvent interaction. But in the solid state the propeller shape of the molecule reduces intermolecular interaction, leading to an enhancement of the lifetime. Further the Förster energy transfer promotes the increase in the lifetime in the host-guest mixture.

The film formed on a glass plate in the matrix of polyvinyl carbazole (as in the device structure) exhibited morphological stability as evident from the AFM images obtained after annealing at different temperatures (Figure 3.30).

Table 3.12. Data obtained from the time resolved photoluminescence experiments.

Entry	Fraction (lifetime) (τ_1)	Fraction (lifetime) (τ_2)	Fraction (lifetime) (τ_3)
PT-T solution[a]	100 % (5.12 ns)	-	-
PT-T thin film[b]	8.12 % (4.07 ns)	91.88 % (19.02 ns)	-
PT-T + PVK thin film	18.48 % (5.36 ns)	78.67 % (19.67 ns)	2.85 % (0.89 ns)

[a]Concentration: 3 μM solution in chloroform; [b]Concentration of solution used for spin coating: 3 mM in chloroform; for solution λ_{exc} = 405 nm, monitored at λ_{max} = 484 nm and for thin film λ_{exc} = 405 nm, monitored at λ_{max} = 535 nm, at rt.

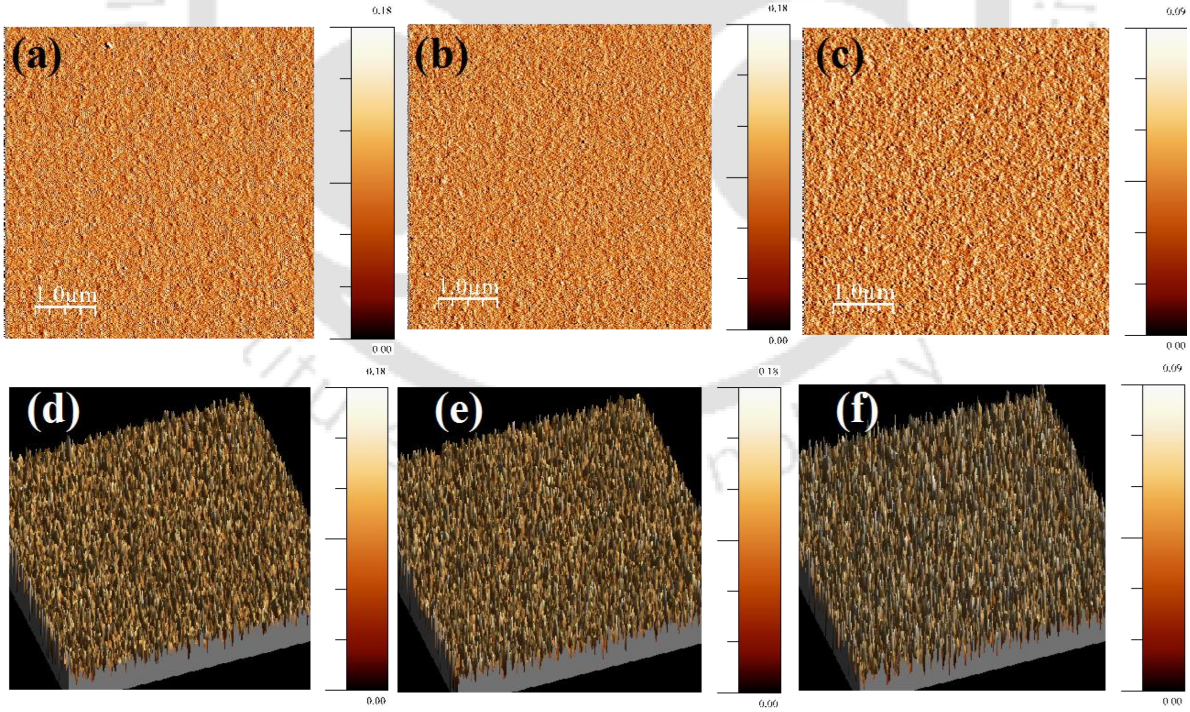

Figure 3.30. (a) AFM phase contrast images obtained for the spin coated film of PVK and 10% compound **PT-T**; (b) for the spin coated film annealed at 70 °C for 10 min; (c) for the spin coated film annealed at 140 °C for 10 min; (d-f) AFM topographic images corresponding to a-c.

3.11. Conclusion

In summary, we have synthesized a star-shaped triazine-perylene conjugate that can be utilized as an emissive layer in OLEDs. This star shaped donor-acceptor (D-A) structure was a low melting solid with a good solubility and film forming nature due to its propeller shape. From the TDDFT calculations, we have visualized the changes in the energy levels of HOMO, LUMO levels and energy separation with respect to the molecular structure. Similarly, the changes in the singlet, triplet energies and the value of ΔE_{ST} with respect to the molecular structure was calculated. This star shaped molecule did not exhibit intramolecular charge transfer and the ΔE_{ST} is quite high in comparison to standard TADF emitters. Further studies to enhance the steric hindrance between the donor groups and the central acceptor to achieve a large dihedral angle will be attempted in future. This may lead to the spatial separation of highest occupied and lowest unoccupied NTOs, which in turn lead to a small ΔE_{ST} and improved RISC. Additionally, this star-shaped molecule exhibited bright green fluorescence with a high quantum yield. When used as a sole emissive layer in OLEDs, this material exhibited a good performance, while as a guest material in a PVK matrix led to a much improved performance. This compound is promising as it shows high brightness, current efficiency, power efficiency and EQE. Thus, the introduction of star-shaped architecture with a push-pull design promotes an improved charge migration along with a better charge recombination, to enhance the device efficiency.

3.12. Experimental section

Synthesis of compound **1c** was done according to Chapter 2.

Synthesis of compound **PT-T**

To a solution of compound **1c** (0.17 mmol, 3.1 equiv.) in dry THF (7 mL) under argon atmosphere, kept in ice bath, *n*-BuLi/hexane solution (1.6 M, 0.17 mmol, 3.1 equiv.) was added drop wise. After 45 minutes of stirring, the ice bath was removed. In another round bottomed flask, a suspension of cyanuric chloride (0.05 mmol, 1 equiv.) in dry THF (3 mL) was prepared. The solution of lithiated anion of **1c** was slowly added to the slurry of cyanuric chloride under argon atmosphere and refluxed in oil bath for 5 h. After cooling the reaction mixture, few drops of water were added to quench the reaction mixture and the excess solvent was evaporated under reduced pressure. The residue was dissolved in methylene chloride and washed with water, brine and dried over anhydrous sodium sulphate. Crude product was purified with column chromatography by using DCM-Hexane mixture as an eluent to yield a bright yellow colored waxy solid.

R_f = 0.81 (20% EtOAc-hexane); bright yellow waxy solid, yield: 55%; IR (KBr pellet) ν_{max} in cm^{-1}: 2957, 2924, 2854, 1721, 1568, 1455, 1413, 1262, 1185, 1154, 803; ^1H NMR (600 MHz, $CDCl_3$, 298 K): δ 9.66 (s, 6H, H_{Ar}), 8.81 (d, J = 6 Hz, 6H, H_{Ar}), 8.39 (d, J = 6 Hz, 6H, H_{Ar}), 4.38 (bs, 12H, -OCH_2), 4.25 (bs, 6H, -OCH_2), 4.10 (bs, 6H, -OCH_2), 1.81 (bs, 12H, -OCH_2-$\underline{CH_2}$), 1.43-0.29 (m, 216H, 108 × -CH_2); ^{13}C NMR (150 MHz, $CDCl_3$, 298 K): δ 168.58, 168.16, 166.07, 139.51, 133.22, 131.93, 131.29, 130.83, 130.23, 126.25, 125.02, 123.40, 122.83, 114.28, 66.14, 66.03, 34.05, 32.15, 32.12, 31.97, 31.84, 29.92, 29.89, 29.85, 29.81, 29.73, 29.64, 29.59, 29.56, 29.44, 29.38, 29.35, 29.23, 29.19, 28.87, 28.36, 26.34, 25.68, 22.92, 22.89, 22.74, 14.31; MALDI-TOF: exact mass calculated for $C_{195}H_{271}N_6O_{24}$ $[MH]^+$: 3081.01, found: 3081.8.

3.13. References

1. a) F. Cherioux, L. Guyard and P. Audebert, *Chem. Commun.*, 1998, 2225-2226; b) A. Pron, P. Gawrys, M. Zagorska, D. Djurado and R. Demadrillea, *Chem. Soc. Rev.*, 2010, **39**, 2577-2632.
2. a) J. Luo, Y. Zhou, Z.-Q. Niu, Q.-F. Zhou, Y. Ma and J. Pei, *J. Am. Chem. Soc.*, 2007, **129**, 11314-11315; b) D. Neher, *Macromol. Rapid Commun.*, 2001, **22**, 1365-1385.
3. a) W.-Y. Lai, R. Xia, Q.-Y. He, P. A. Levermore, W. Huang and D. D.C. Bradley, *Adv. Mater.*, 2009, **21**, 355-360; b) C. Chou, S. Hsu, K. Dinakaran, M. Chiu and K. Wei, *Macromolecules*, 2005, **38**, 745-751; c) C. Liu, Y. Li, Y. Zhang, C. Yang, H. Wu, J. Qin and Y. Cao, *Chem. Eur. J.*, 2012, **18**, 6928-6934; d) C. Liu, Q. Fu, Y. Zou, C. Yang and J. Qin, *Chem. Mater.*, 2014, ***26***, 3074-3083; e) L. Chen, P. Li, H. Tong, Z. Xie, L. Wang, X. Jing and F. J. Wang, *Polym. Sci. Part A Polym. Chem.*, 2012, **50**, 2854-2862; f) L. Chen, P. Li, Y. Cheng, Z. Xie, L. Wang, X. Jing and F. Wang, *Adv. Mater.*, 2011, **23**, 2986-2990.
4. B. Chen, J. Ding, L. Wang, X. Jing and F. Wang, *Chem. Commun.*, 2012, **48**, 8970-8972.
5. X. He, L. Chen, Y. Zhao, S. C. Ng, X. Wang, X. Sun and X. (Matthew) Hu, *RSC Adv.*, 2015, **5**, 15399-15406.
6. a) Z.-F. An, R. -F. Chen, J. Yin, G.-H. Xie, H. –F. Shi, T. Tsuboi and W. Huang, *Chem. Eur. J.*, 2011, **17**, 10871-10878; b) S. Y. Lee, T. Yasuda, H. Nomura and C. Adachi, *Applied Physics Letters*, 2012, **101**, 093306-4; c) H. Tanaka, K. Shizu, H. Miyazaki and C. Adachi, *Chem. Commun.*, 2012, **48**, 11392-11394; d) H. Tanaka, K. Shizu, H. Nakanotani and C. Adachi, *J. Phys. Chem. C*, 2014, **118**, 15985-15994; e) H. Uoyama, K. Goushi, K. Shizu, H. Nomura and C. Adachi, *Nature*, 2012, **492**, 234-238; f) A. Endo, K. Sato, K. Yoshimura, T. Kai, A. Kawada, H. Miyazaki and C. Adachi, *Applied Physics Letters*, 2011, **98**, 083302-1-3, g) A. Endo, M. Ogasawara, A. Takahashi, D. Yokoyama, Y. Kato and C. Adachi, *Adv. Mater.*, 2009, **21**, 4802-4806.
7. Y. Liu, F. Niu, J. Lian, P. Zeng and H. Niu, *Synthetic Metals*, 2010, 2055-2060.
8. D. Wagner, S. T. Hoffmann, U. Heinemeyer, I. Münster, A. Köhler and P. Strohrieg, *Chem.Mater.*, 2013, **25**, 3758-3765.
9. M. Kasha, H. R. Rawls and M. A. El-Bayoumi, *Pure Appl. Chem.*, 1965, **11**, 371-392.
10. a) F. Würthner, C. Thalacker, S. Diele and C. Tschierske, *Chem. Eur. J.*, 2001, **7**, 2245-2253; b) A. S. Achalkumar, U. S. Hiremath, D. S. S. Rao, S. K. Prasad and C. V. Yelamaggad, *J. Org. Chem.*, 2013, **78**, 527-544.
11. J. Tong, Y. J. Wang, Z. Wang, J. Z. Sun and B. Z. Tang, *J. Phys. Chem. C*, 2015, **119**, 21875-21881.
12. Y. Hong, J. W. Y. Lam and B. Z. Tang, *Chem. Commun.*, 2009, 4332-4353.
13. a) M. J. Frisch, G. W. Trucks, H. B. Schlegel, G. E. Scuseria, M. A. Robb, J. R. Cheeseman, G. Scalmani, V. Barone, G. A. Petersson, H. Nakatsuji, X. Li, M. Caricato, A. V. Marenich, J. Bloino, B. G. Janesko, R. Gomperts, B. Mennucci, H. P. Hratchian, J. V. Ortiz, A. F. Izmaylov, J. L. Sonnenberg, D. Williams-Young, F. Ding, F. Lipparini, F. Egidi, J. Goings, B. Peng, A. Petrone, T. Henderson, D. Ranasinghe, V. G. Zakrzewski, J. Gao, N. Rega, G. Zheng, W. Liang, M. Hada, M. Ehara, K. Toyota, R. Fukuda, J. Hasegawa, M. Ishida, T. Nakajima, Y. Honda, O. Kitao, H. Nakai, T. Vreven, K. Throssell, J. A. Montgomery, Jr., J. E. Peralta, F. Ogliaro, M. J. Bearpark, J. J. Heyd, E. N. Brothers, K. N. Kudin, V. N. Staroverov,

T. A. Keith, R. Kobayashi, J. Normand, K. Raghavachari, A. P. Rendell, J. C. Burant, S. S. Iyengar, J. Tomasi, M. Cossi, J. M. Millam, M. Klene, C. Adamo, R. Cammi, J. W. Ochterski, R. L. Martin, K. Morokuma, O. Farkas, J. B. Foresman, and D. J. Fox, *Gaussian*, Inc., Wallingford CT, 2016; b) C. Lee, W. Yang and R. G. Parr, *Phys. Rev. B*, 1988, **37**, 785-789; c) A. D. Becke, *J. Chem. Phys.*, 1993, **98**, 1372-1377.

14. G.-J. Zhao and K.-L. Han *J. Phys. Chem. A*, 2009, **16**, 4788-4794.
15. M. Cai, T. Xiao, E. Hellerich, Y. Chen, R. Shinar and J. Shinar, *Adv. Mater.*, 2011, 23, 3590-3596.
16. a) H. Ulla, M. R. Kiran, B. Garudachari, M. N. Satyanarayan, G. Umesh and A. M. Isloor, *Opt. Mater.*, 2014, **37**, 311-321; b) H. Ulla, M. R. Kiran, B. Garudachari, T.N. Ahipa, K. Tarafder, A. V. Adhikari, G. Umesh and M.N. Satyanarayan, *J Mol. Struc.*, 2017, **1143**, 344-354; c) S. Chidirala, H. Ulla, A. Valaboju, M. R. Kiran, M. E. Mohanty, M. N. Satyanarayan, G. Umesh, K. Bhanuprakash and V. J. Rao, *J. Org. Chem.*, 2015, **81**, 603-614.
17. E. Kozma, W. Mróz, F. Villafiorita-Monteleone, F. Galeotti, A. Andicsová-Eckstein, M. Catellani and C. Botta, *RSC Adv.*, 2016, **6**, 61175-61179.

Chapter 4

Columnar Self-Assembly of Electron-Deficient Dendronized Bay-Annulated Perylene Bisimides

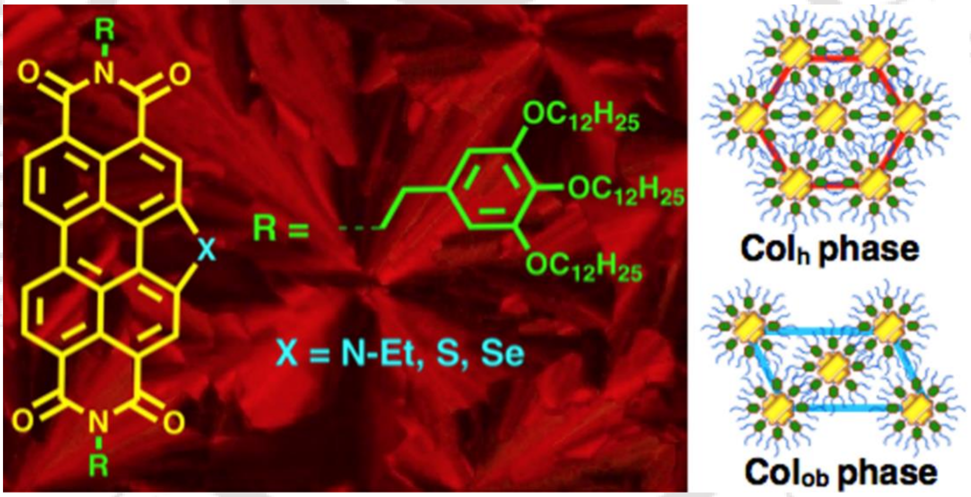

Results have been published in;

- *Chem. Eur. J.*, 2018, **24**, 3566-3575

4.1. Introduction

Perylene bisimides are receiving increasing attention from the scientific community working in the field of organic electronics and self-assembly. They have been tested for variety of applications like organic solar cells,[1] field effect transistors,[2] light emitting diodes[3] and light harvesting antennae.[4] Although there are several *p*-type organic semiconductors reported, the number of n-type semiconductors are less. The progress in organic electronics always faced with a bottleneck, *i.e.* the dearth of suitable n-type organic semiconductors with high mobility and stability. Perylene bisimides due to their electron withdrawing imide substituents serve as electron deficient n-type semiconductors. PBIs, when prepared by reacting perylene tetracarboxylic acid dianhydride (PTCDA) with alkyl/aryl amines with peripheral substitution have shown the tendency to stabilize various functional supramolecular self-assemblies like J-aggregates, light harvesting assemblies, vesicles, liquid crystals and chiral discriminators.[5,6] Further modifications in their physical and self-assembling properties, were realized by *bay*-substitution. But it has to be noted that *bay*-substitution affects the planarity of the molecule and hence the self-assembly behavior of the PBI derivatives. In previous chapters, we have realized *bay*-annulated perylene tetraesters (PTEs), which were planar and exhibited columnar self-assembly over a wide thermal range. This is interesting due to the fact that, by heteroatom *bay*-annulation, one can modify the physical properties of these molecules without sacrificing the planarity and self-assembly. Dendronized PBIs prepared by connecting the various benzylamines with peripheral substitution with flexible alkyl chains have shown to self-assemble into columnar (Col) phases.[7,9] Here, the central PBI unit is a very rigid aromatic unit exhibiting strong π-π interactions, while the peripheral trialkoxy benzyl group provides a flexible unit. Organization of these n-type semiconductors to form one-dimensional (1D) columnar structures, have advantages in comparison to the polymeric or single crystalline organic semiconductors.[9] This is because such self-assembling molecular motifs have better solubility, ease of purification, reproducibility and ease of handling in comparison to polymers and single crystals.[8] Col phases formed by the stacking of disc-shaped molecules provide the anisotropic charge carrier mobility along the columns, thus can be compared to molecular wires. PBIs could be a possible alternative to fullerenes, which are popular as electron accepting materials in organic solar cells. However, to become an efficient alternative to fullerene based acceptors, these molecules have to be synthetically modified and their properties have to be studied. There have been reports on the introduction of various heteroatoms like oxygen, nitrogen, sulphur and selenium in the *bay* region of perylene derivatives by annulation. This has led to transformed aromatic systems with fascinating properties. Incorporation of sulfur and selenium in organic semiconductors is widely explored due to the intermolecular S···S and Se···Se interactions, which also help to stabilize the molecular self-assembly and hence improve 1D conductivity.[10] Motivated by our success in stabilizing luminescent Col self-assembly in heteroatom *bay*-annulated PTEs over a wide thermal range, we envisaged the synthesis of their bisimide counterparts.

4.2. Results and discussion

4.2.1. Synthesis and molecular structural characterization

The synthetic route used for the synthesis of *bay*-annulated perylene bisimides is depicted in Scheme 4.1. Perylene-3,4,9,10-tetracarboxylic dianhydride was subjected to hydrolysis and the tetracarboxylate salt obtained was acidified with dilute HCl to make the pH ≈8-9. This on refluxing in the presence of Aliquat 336 and *n*-bromobutane yielded the corresponding tetraester (**1**) in good yield. The tetraester obtained was nitrated under mild condition to obtain the *bay*-substituted mono nitro derivative **2** in good yield. The nitro compound **2** on triethyl phosphite mediated Cadogan reaction yielded the *N*-annulated perylene tetraester (**3**). The heating of nitro compound in presence of sulphur or selenium powder in anhydrous NMP yielded the corresponding S and Se annulated PTEs (Compound **6** and **8**). The *N*-annulated perylene tetraester (**3**) was *N*-ethylated in presence of sodium hydride as a base to give compound **4**. The *bay*-annulated tetraesters **4, 6** and **8** on heating in the presence of *p*-toluene sulphonic acid (PTSA) monohydrate, yielded the respective anhydrides (**5, 7** and **9**). These *bay*-annulated perylene dianhydrides were treated with 3,4,5-Tris(dodecyloxy)benzylamine under microwave conditions, to yield the corresponding bisimides **PBI-N, PBI-S** and **PBI-Se** in excellent yields. The application of microwave assisted synthesis in presence of zinc acetate and imidazole improved the yields ranging from 80-90%, in comparison to the conventional method.[7a] The synthesis of the key intermediate 3,4,5-Tris(dodecyloxy)benzylamine (**14**) is provided in Scheme 4.2. Ethyl gallate was *O*-alkylated with 1-Bromododecane under Williamson's ether conditions to obtain compound **10**. This was reduced to corresponding benzyl alcohol (**11**) on treating with lithium aluminum hydride (LAH) under anhydrous conditions. On treatment with thionyl chloride, corresponding benzyl chloride (**12**) was prepared. Reaction of compound **12** with potassium phthalimide yielded its *N*-benzylated derivative **13**, which on hydrolysis

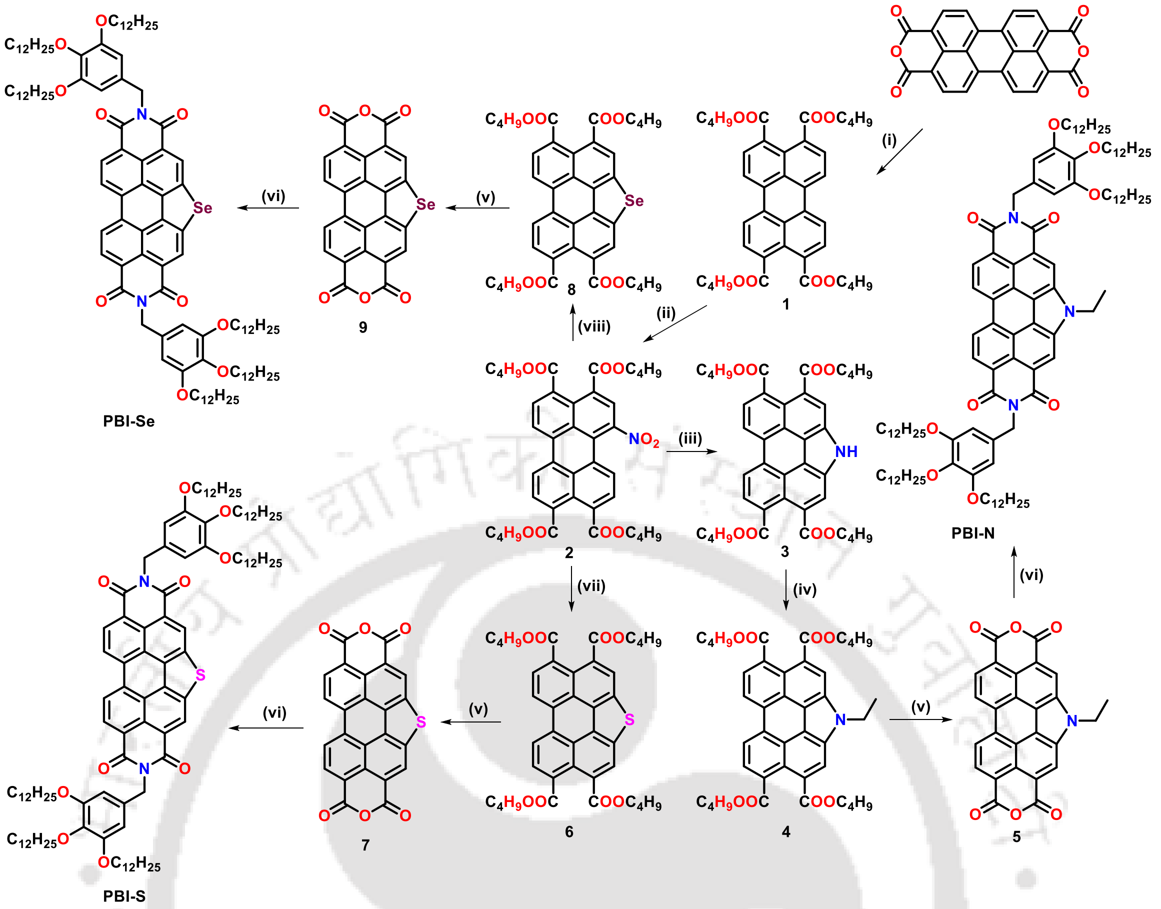

Scheme 4.1. Reagents and conditions: (i) KOH, H_2O, 70 °C, 0.5 h, 1M HCl, Aliquat 336, KI,1-bromobutane, reflux, 12 h (76%); (ii) $NaNO_2$, HNO_3, 0 °C, 1 h (90%); (iii) triethyl phosphite, 160 °C, reflux, 4 h, N_2 (60 %); (iv) NaH, 1-iodoethane, dry THF, reflux, 17 h (75%); (v) *p*-toluene sulphonic acid monohydrate, toluene, 100 °C, 30 h (90%); (vi) **14**, zinc acetate, imidazole, 165 °C, microwave, 30 min. (80-90%); (vii) sulfur powder, anhyd. NMP, N_2, 70 °C, 0.5 h, 180 °C, 17 h (55%); (viii) selenium powder, anhyd. NMP, N_2, 70 °C, 0.5 h, 180 °C, 17 h (55%).

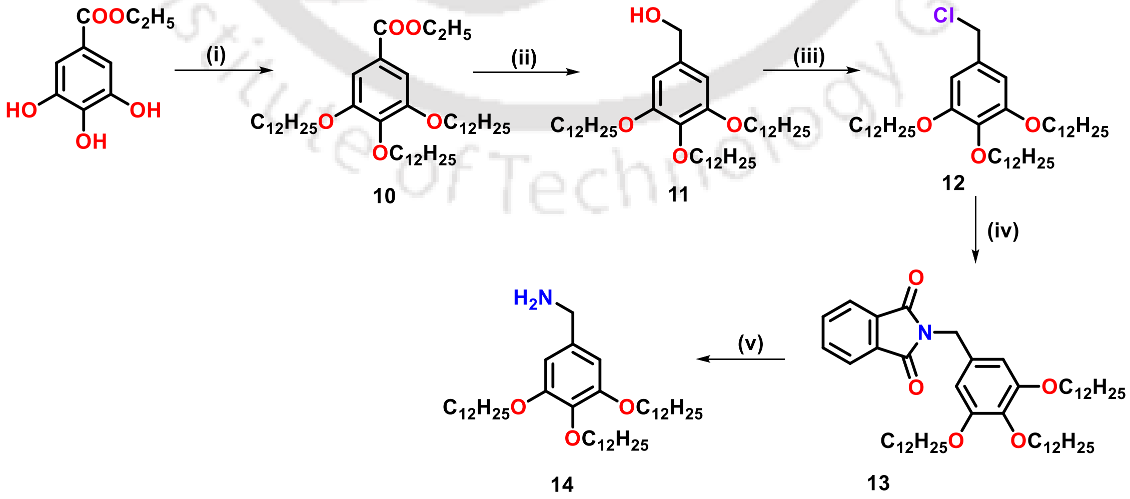

Scheme 4.2. Reagents and Conditions: (i) 1-bromododecane, anhyd. K_2CO_3, dry DMF, 24 h 90 °C, 85%; (ii) LAH, dry THF, rt, 2 h, 95%; (iii) $SOCl_2$, dry DCM, rt, 95%; (iv) potassium phthalimide, DMF, 90 °C, 18 h (95%); (v) $NH_2NH_2.H_2O$, methanol, 95 °C, 1 h (95 %)

yielded the corresponding benzylamine **14**, as reported earlier.[7c] We have prepared simple perylene bisimide from the amine **14** by reacting it with perylene bisanhydride in order to compare with the thermal and photophysical behavior of the corresponding heteroatom *bay*-annulated PBIs. All the intermediates and final compounds were characterized with ^{1}H NMR, ^{13}C NMR, IR, MALDI-TOF/ESI-HRMS techniques. The overlay of the ^{1}H NMR spectra shows the proton adjacent to the hetero atom is more deshielded, in comparison to other protons on perylene ring (Figure 4.1). Among the *bay*-annulated perylene tetraesters, where the proton H_c of selenium annulated perylene tetraester resonated down field.

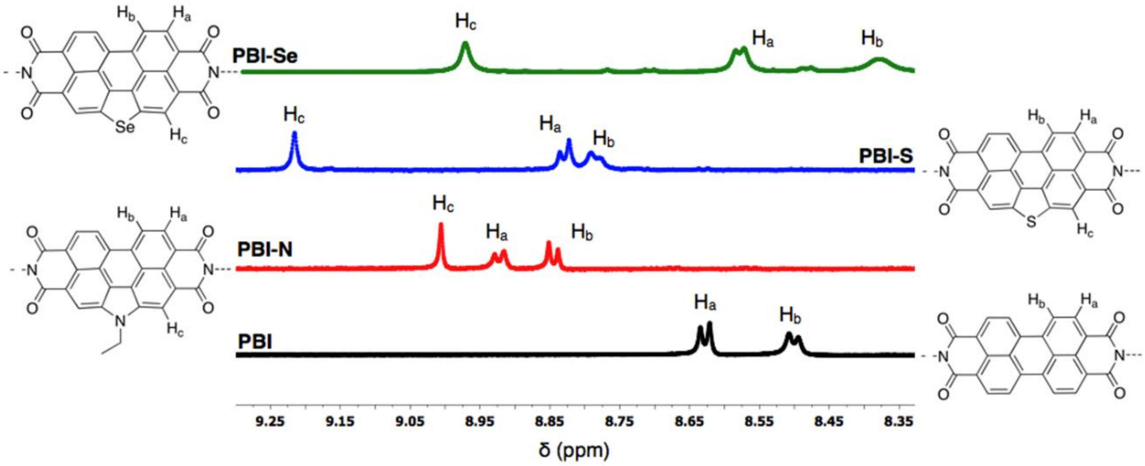

Figure 4.1. Overlay of the expanded region of the ^{1}H NMR spectra ($CDCl_3$, 600 MHz) of PBI and *bay*-annulated PBIs.

4.2.2. Thermal behavior

The thermal stability of these compounds was investigated with the help of thermogravimetric analysis (TGA). *S*-annulated compound **PBI-S** exhibited higher thermal stability in contrast to parent PBI, *N*- and *Se*-annulated PBIs (Figure 4.3d). Thermotropic mesomorphic behavior of the PBIs was investigated as follows; the samples sandwiched between a glass slide and a coverslip were tested for the shearability and birefringence on heating in a programmable hot stage associated with a polarizing optical microscope (POM). The phase transitions and associated enthalpies were obtained by differential scanning calorimetry (DSC) thermograms, while the mesophases are assigned with the help of X-ray diffraction (XRD) studies. In comparison to perylene bisimide without annulation the *bay*-annulated PBIs exhibited lower clearing temperatures (Figure 4.2). The phase transition temperatures and associated enthalpy changes are presented in Table 4.1.

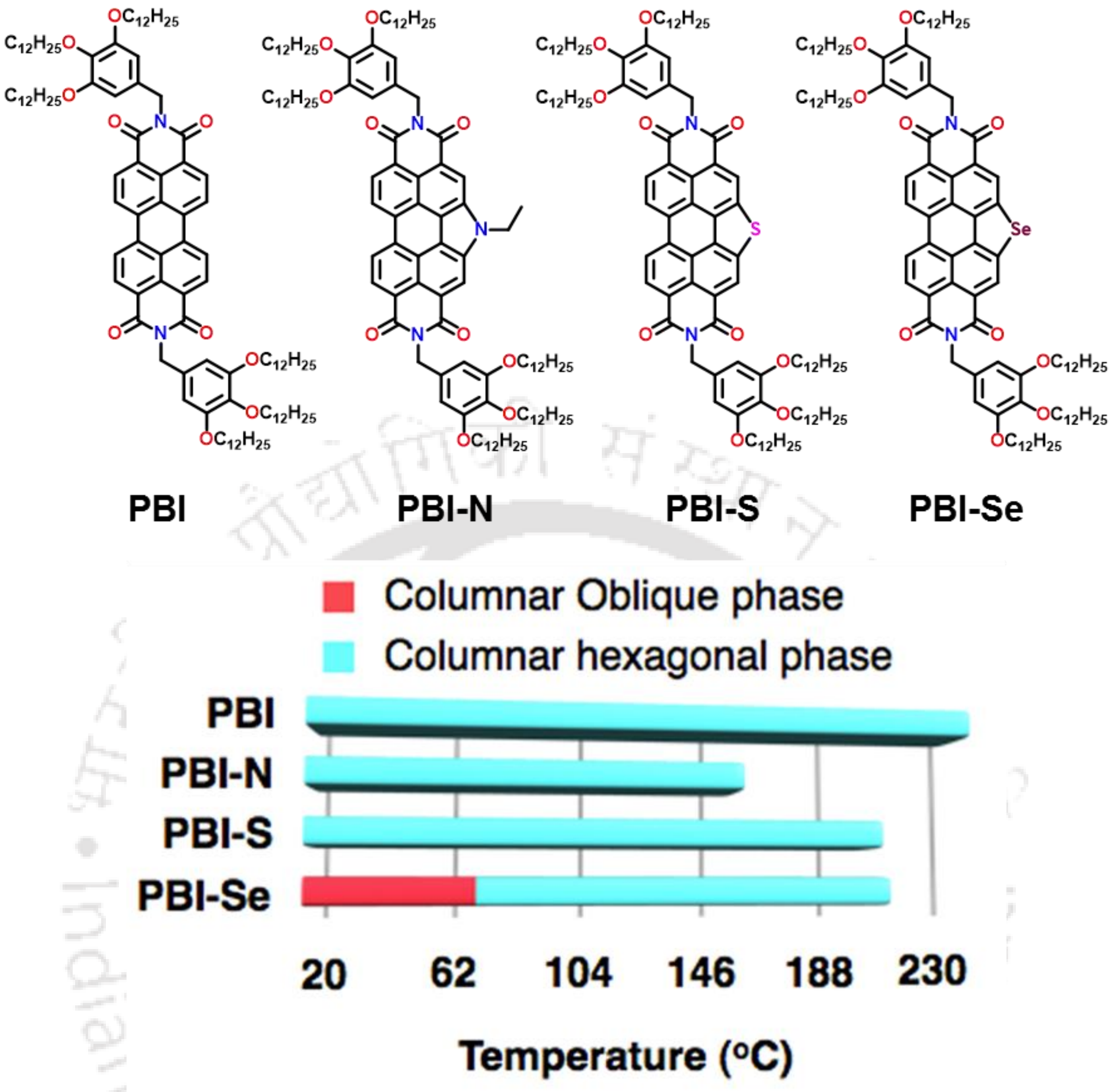

Figure 4.2. Molecular structures of PBI and *bay*-annulated PBIs and the bargraph representing their thermal behavior (based on first cooling scan).

Table 4.1. Phase transition temperatures[a] (°C) and corresponding enthalpies (kJ/mol) of DLCs.

Phase sequence		
Entry	**Second Heating**	**First Cooling**
PBI-N	Col_{h2} 77.8 (0.7) Col_{h1} 156.1 (1.4) I	I 152 (1.7) Col_{h1} 69.4 (1.5) Col_{h2}[c]
PBI-S	Col_h 200.6 (2.3)	I 196.4 (2.9) Col_h [c]
PBI-Se	Cr 78.6 (2.3) Col_{ob} 125.1 (9.4) Col_h 202.5 (2.2) I	I 198.6 (2.7) Col_h 70 Col_{ob}[b, d]

[a]Peak temperatures in the DSC thermograms obtained during the second heating and first cooling cycles at 5 °C/min; [b]the transition observed only under microscope. [c]the mesophase freezing in the glassy state; [d]Crystallization was not detected on cooling; Cr = Crystal phase; Col_h = Columnar hexagonal phase; Col_{ob} = Columnar oblique phase; I = Isotropic phase.

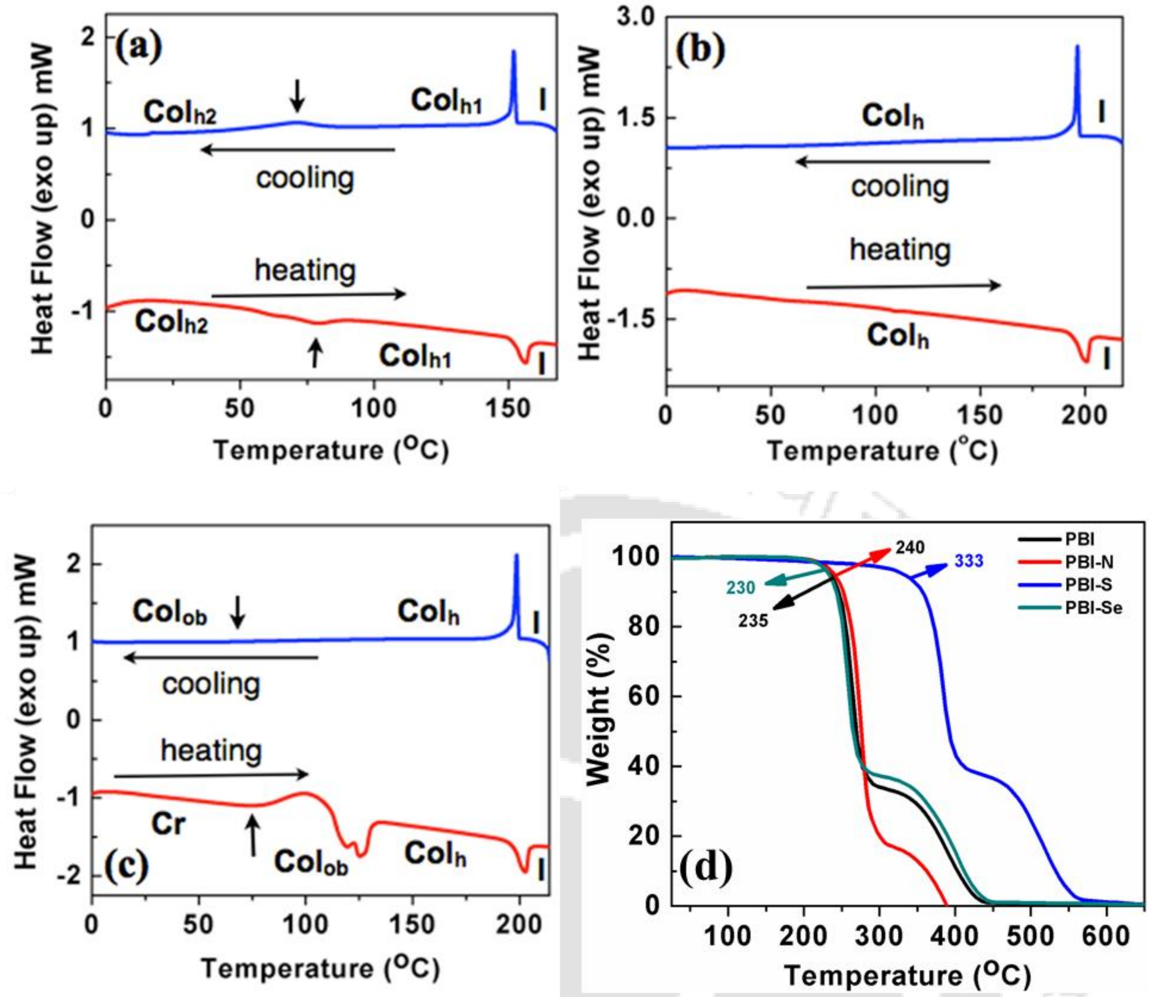

Figure 4.3. (a) DSC thermograms obtained for **PBI-N**; (b) **PBI-S** and (c) **PBI-Se** in the first cooling and second heating scans; (d) TGA curves obtained for *bay*-annulated PBIs at a rate of 10 °C/min under N_2 atmosphere.

Compound **PBI-N** on heating showed a transition around 102 °C, with an increase in the birefringence along with the fluidity, which corresponds to a crystal to mesophase transition, before reaching the clearing temperature of 156 °C (Figure 4.3a). On cooling the isotropic liquid at rate of 5 °C/min, showed the formation of highly birefringent mosaic pattern starting at 152 °C. At around 69 °C, a transition with an enthalpy change of 1.5 kJ was observed, but no change was observed in the optical texture, which remained unchanged till room temperature, without any signs of crystallization (Figure 4.3a). In the second heating a transition at 78 °C ($\Delta H = 0.7$ kJ/mol) with a slight increase in the brightness and fluidity was noted. This phase existed till 156 °C, after which the phase transformed into an isotropic liquid. These changes were corresponding to high and low temperature phases, which were difficult to distinguish, except a decrease in the birefringence in the low temperature phase (Figure 4.4a and b). Thus we decided to investigate these mesophases by XRD studies at different temperature intervals. XRD studies of the sample carried out at 145 °C After cooling from its isotropic melt showed an intense sharp peak at low angle with a Bragg spacing d = 27.97 Å in the low angle region.

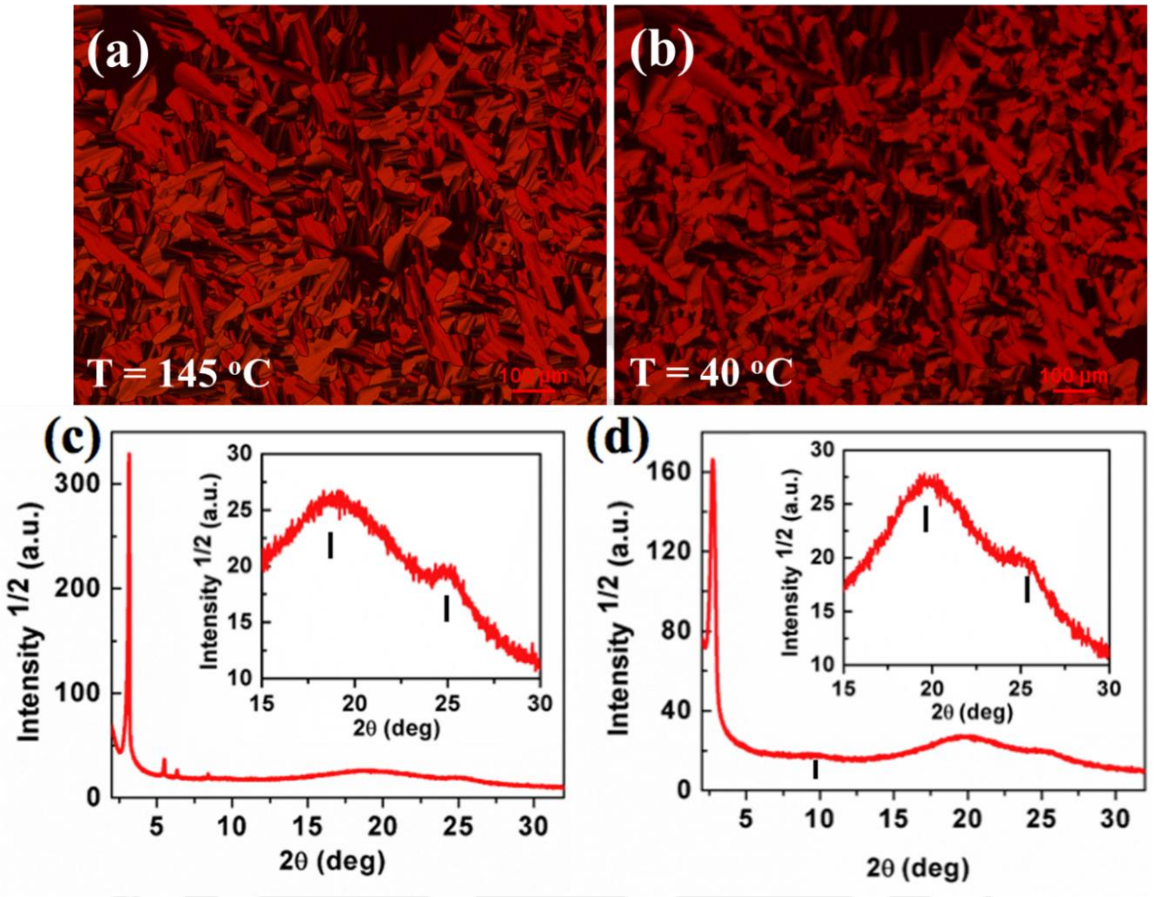

Figure 4.4. (a, b) POM images (under crossed polarizer) obtained for **PBI-N** and the XRD profiles depicting the intensity against the 2θ obtained for the $\mathrm{Col_{h1}}$ phase (c) at 145 °C and $\mathrm{Col_{h2}}$ phase (d) at 28 °C.

Further several reflections with d- spacing of 16.12, 13.94 and 10.52 Å were observed in the middle-angle region ($5^{o} < 2\theta < 10^{o}$). These reflections could be indexed into Miller indices of 100, 110, 200 and 210 with the ratio of $1:1/\sqrt{3}:1/\sqrt{4}:1/\sqrt{7}$ and therefore these values fit very well with the lattice of the $\mathrm{Col_h}$ phase (Figure 4.4c). In the wide-angle region two diffused peaks were observed at a d-spacing of 4.64 and 3.54 Å. The first of these peaks can be attributed to the packing of floppy alkyl chains and the second one is arising from the packing of aromatic cores within the column. It is interesting to note that within the Col phase these molecules are packing with an intimate overlap of aromatic cores, which is beneficial for 1D charge migration. The calculated lattice parameter 'a' was found to be 32.3 Å, which is approximately 35% lesser than the molecular diameter obtained from the molecular model in its all *trans* conformation (Figure 4.5, Table 4.2). This decrease may

Table 4.2. Results of (*hkl*) indexation of XRD profiles of **PBI-N** and **PBI-S** at a given temperature (T) of mesophases[a]

Compounds (D/Å)	Phase (T/ºC)	d_{obs} (Å)	d_{cal} (Å)	Miller indices (*hkl*)	Lattice parameters (Å), Lattice area S (Å^2), Molecular volume V (Å^3)
PBI-N (49.45)	145 (Col$_{h1}$)	27.97 16.12 13.94 10.52 4.64 (h_a) 3.54 (h_c)	27.97 16.15 13.99 10.57	100 110 200 210 001	a = 32.30 c = 3.54 S = 903.6 V = 3203 Z = 1.1
	100 (Col$_{h1}$)	27.89 16.08 13.91 10.50 4.57 (h_a) 3.51 (h_c)	27.89 16.10 13.95 10.54	100 110 200 210 001	a = 32.21 c = 3.51 S = 898.2 V = 3157.1 Z = 1.1
	40 (Col$_{h2}$)	32.11 9.08 4.47 (h_a) 3.53 (h_c)	32.11 (diffuse)	100	a = 37.08 c = 3.53 S = 1190.8 V = 4205.6 Z = 1.5
PBI-S (48.37)	194 (Col$_h$)	28.15 16.21 14.03 10.60 4.71 (h_a) 3.51 (h_c)	28.15 16.25 14.08 10.64	100 110 200 210 001	a = 32.51 c = 3.51 S = 915.2 V = 3208.4 Z = 1.1
	120 (Col$_h$)	27.69 15.94 13.81 10.42 9.18 4.62 (h_a) 3.46 (h_c)	27.69 15.99 13.84 10.47 9.23	100 110 200 210 300 001	a = 31.97 c = 3.46 S = 885.3 V = 3064.1 Z = 1.1
	80 (Col$_h$)	27.47 15.81 13.69 10.33 4.54 (h_a) 3.44 (h_c)	27.47 15.86 13.74 10.38	100 110 200 210 001	a = 31.72 c = 3.44 S = 871.5 V = 3000.6 Z = 1.1
	40 (Col$_h$)	27.93 16.13 13.86 9.58 4.48 (h_a) 3.43 (h_c)	27.93 16.13 13.97 (diffuse)	100 110 200 300 001	a = 32.25 c = 3.43 S = 900.9 V = 3092.5 Z = 1.1

[a]The diameter (D) of the disc (estimated from Chem 3D Pro 8.0 molecular model software from Cambridge Soft). d_{obs}: spacing observed; d_{cal}: spacing calculated (deduced from the lattice parameters; a for Col$_h$ phase; c is height of the unit cell). The spacings marked h_a and h_c correspond to diffuse reflections in the wide-angle region arising from correlations between the alkyl chains and core regions, respectively. Z indicates the number of molecules per columnar slice of thickness h_c estimated from the lattice area S and the volume V.

be due to the folding of the peripheral flexible chains, which decrease the effective diameter of the molecule in the Col phase or due to the interdigitation of the flexible chains of **PBI-N** of one column with that of the neighbouring column. From the lattice parameter ‘*a*’, we could calculate the number of molecules (*Z*) present in the unit hexagonal cell with the height (h_c) of 3.54 Å and found to be one. This means that each stratum of the column is formed by single molecule, which is packed with an intermolecular distance of 3.54 Å. The XRD pattern obtained at lower temperature (at 100 °C) in high temperature phase regime was almost same with a lowering of ‘*a*’ and the core-core distance (h_c) (Table 4.2).

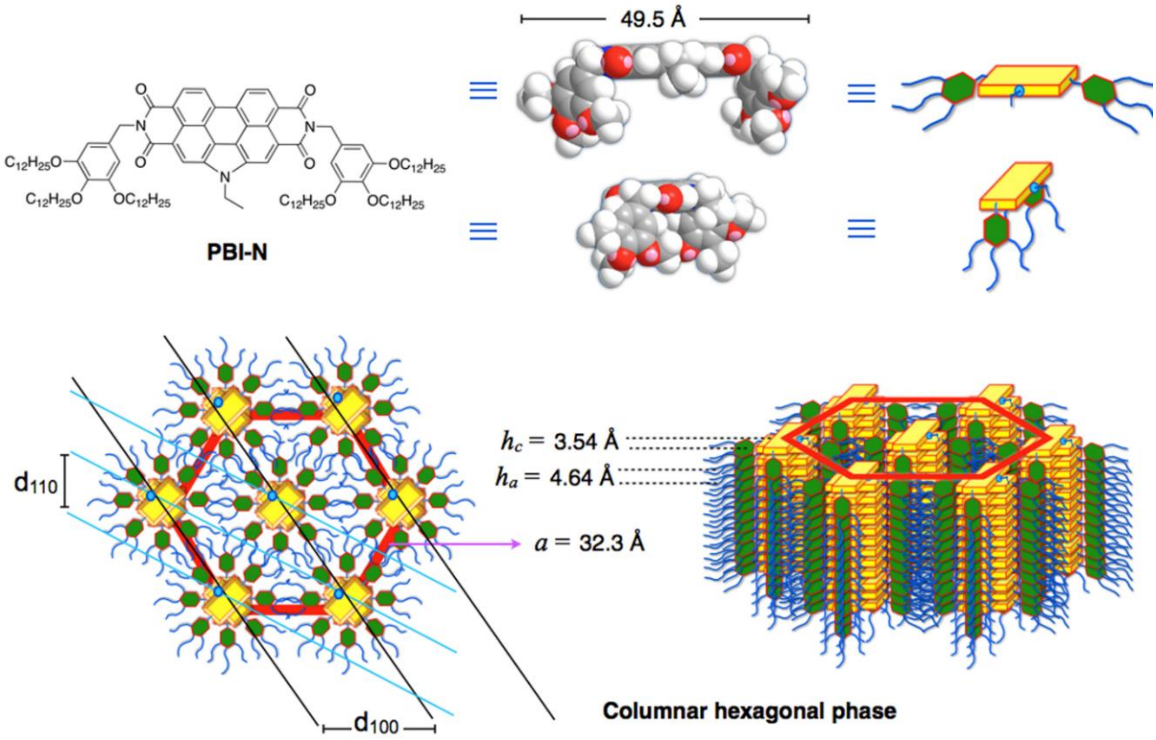

Figure 4.5. Schematic showing the energy minimized structure of **PBI-N** and its self-assembly into columnar hexagonal (Col_{h1}) phase (XRD data at 145 °C is considered for the illustration).

We were curious to know the nature of the low temperature phase, thus the XRD studies were carried out at 40 °C. The XRD pattern obtained at 40 °C, exhibited a single sharp peak at low angle, along with two diffused peak at wide angle, which confirms the phase to be a Col_h. A diffused peak with a *d*-spacing of 9.1 Å was observed and the ratio of this with the first *d*-spacing was found to be 1:1/√3, which usually corresponds to the Miller indices 220 in a hexagonal lattice (Figure 4.4d). Though it is not explicit to assign the Col_h phase from the observation of single sharp peak at low angle, the absence of other peaks has been ascribed to a minimum in the form factor.[11] The optical texture remained unaffected even at ambient temperature, and the sample was not shearable, suggesting the freezing of Col_h phase in the glassy state. For the sake of identification, we have denoted the high temperature Col_h phase as Col_{h1} and the low temperature Col_h phase as Col_{h2}. Such transitions between Col$_h$ phases are rarely observed.[12] The self-assembly of **PBI-N** in Col$_{h1}$ phase is illustrated in Figure 4.5.

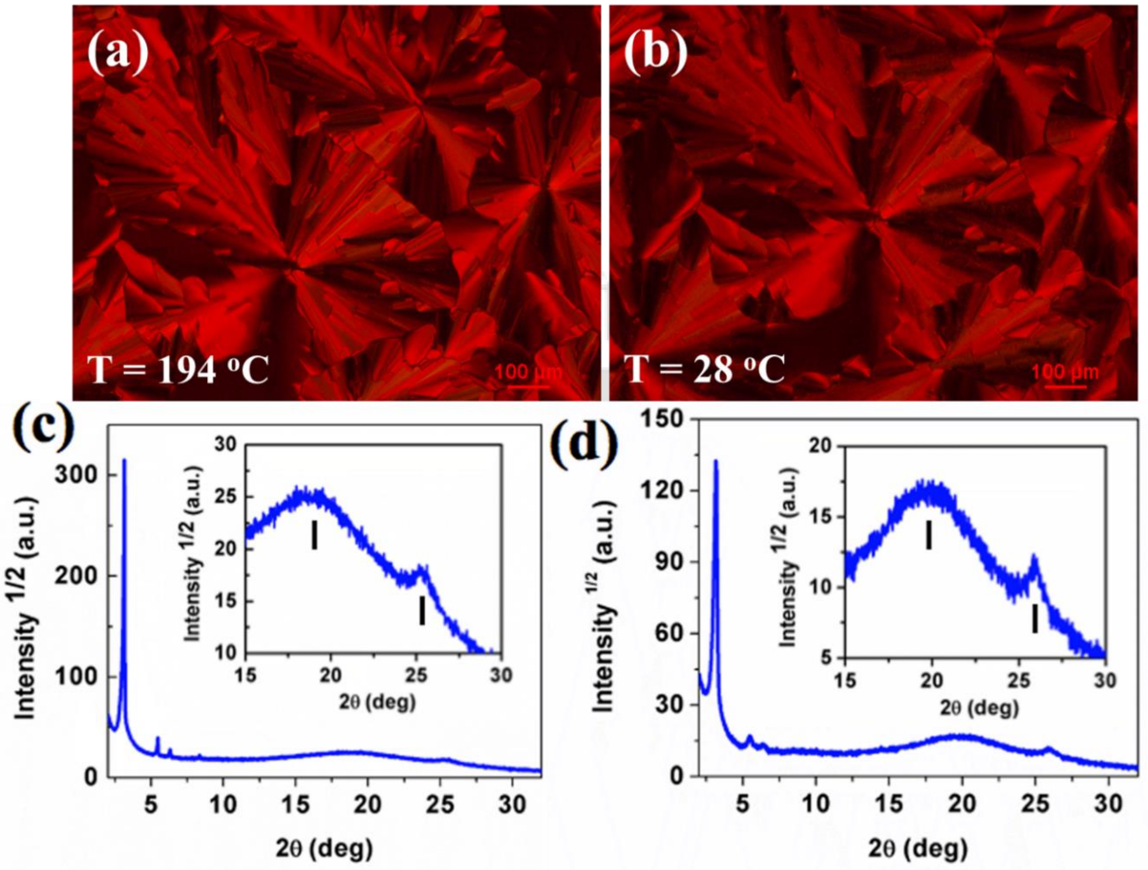

Figure 4.6. (a, b) POM images (under crossed polarizer) obtained for **PBI-S** and the XRD profiles depicting the intensity against the 2θ obtained for the Col$_h$ phases (c) at 194 °C and (d) at 40 °C.

PBI-S and **PBI-Se** exhibited enantiotropic Col$_h$ phase, but with higher melting and clearing temperatures than **PBI-N**, which may be due to the enhanced S···S and Se···Se interactions (intra or intercolumnar).[10] In addition, we should note that these compounds do not have an ethyl substitution near to the core as in the case of **PBI-N**, which might reduce the core-core interactions. The thermal range of Col phase of both these molecules was found to be almost same. Compound **PBI-S**, on heating, melted at ≈123 °C, with a large enthalphy change (ΔH = 34.2 kJ/mol) corresponding to Cr-mesophase transition as noted in DSC scans in concurrence with the POM observations. This mesophase cleared at ≈201 °C. On cooling the isotropic liquid, pseudofocal conic fan-like texture appeared which persisted till room temperature (Figure 4.6a, b). DSC cooling scan did not show any signs of crystallization even up to 0 °C (Figure 4.3b), however the material was not shearable, which confirmed the freezing of the mesophase in glassy state. XRD studies at different

Table 4.3. Results of (*hkl*) indexation of XRD profiles of **PBI-Se** at a given temperature (T) of mesophases[a]

Compounds (D/Å)	**Phase (T/°C)**	d_{obs} **(Å)**	d_{cal} **(Å)**	**Miller indices (*hkl*)**	**lattice parameters (Å), lattice area S (Å^2), molecular volume V (Å^3)**
PBI-Se (48.468)	195 (Col$_h$)	28.24	28.24	100	a = 32.60
		16.25	16.30	110	c = 3.51
		14.07	14.12	200	S = 920.6
		10.62	10.67	210	V = 3233.9
		4.69 (h_a)			Z = 1.1
		3.51 (h_c)		001	
	140 (Col$_h$)	27.86	27.47	100	a = 31.72
		16.03	15.86	110	c = 3.48
		13.88	13.74	200	S = 871.5
		10.48	10.38	210	V = 3035.6
		4.59 (h_a)			Z = 1
		3.48 (h_c)		001	
	80 (Col$_h$)	27.43	27.86	100	a = 32.17
		15.81	16.09	110	c = 3.45
		13.69	13.93	200	S = 896.5
		10.34	10.53	210	V = 3099.7
		4.43 (h_a)			Z = 1.1
		3.45 (h_c)		001	
	RT/24 (Col$_{ob}$)	45.98	45.98	01	a = 28.04
		27.24	27.24	11	b = 48.96
		26.33	26.33	10	c = 3.44
		22.96	22.99	02	γ = 69.9°
		15.21	15.33	03	S = 1289.2
		13.58	13.62	22	V = 4434.8
		11.31	11.50	04	Z = 1.5
		9.08	9.08	33	
		8.26	8.15	16	
		6.47	6.52	45	
		4.31	diffuse		
		4.26	4.26	-54	
		3.99	4.01	-55	
		3.84	3.88	-63	
		3.44	3.52	-65	

[a] The diameter (D) of the disc (estimated from Chem 3D Pro 8.0 molecular model software from Cambridge Soft). d_{obs}: spacing observed; d_{cal}: spacing calculated (deduced from the lattice parameters; a for Col$_h$ phase; a and b for Col$_{ob}$ phase; c is height of the unit cell). The spacings marked h_a and h_c correspond to diffuse reflections in the wide-angle region arising from correlations between the alkyl chains and core regions, respectively. Z indicates the number of molecules per columnar slice of thickness h_c estimated from the lattice area S and the volume V.

temperature intervals, like 194, 120, 80 and 40 °C were performed. All the XRD profiles exhibited a similar pattern corresponding to Col$_h$ phase. For example, the XRD pattern at 194 °C (Figure 4.6c), exhibited a strong reflection with a *d*-spacing of 28.2 Å at low angle region along with low intensity reflections at the middle angle region with *d*-spacings of 16.21, 14.03 and 10.6 Å. The reciprocal spacing ratio was found to be 1:√3:√4:√7. These *d*-spacings can be indexed into Miller indices of 100, 110, 200 and 210 of a hexagonal lattice (Table 4.2). At wide angle, diffused spacings corresponding to 4.71 Å and 3.51 Å were observed, which are corresponding to the alkyl chain packing and core-core stacking respectively. This confirms the Col$_h$ phase, and further the XRD profiles obtained at low temperature (Figure 4.6d) also corresponds to the same confirming the monomesomorphic behavior of **PBI-S**. *Se*-annulated PBI (**PBI-Se**) on heating melted at ≈130 °C, with a large enthalphy change ($\Delta H = 32.8$ kJ/mol) corresponding to Cr-mesophase transition. This was in accordance with the POM observation that showed increased fluidity and birefringence. The clearing point was almost same with that of the **PBI-S**, but the melting point was higher than that of **PBI-S**. As per the DSC scan in cooling cycle a transition corresponding to isotropic to mesophase was observed (Figure 4.3c). It was very hard to detect any change in the pseudo focal conic texture except the blurring of the dark homeotropic background (Figure 4.7a, b), which was seen around 70 °C. Thus we have carried out XRD at different temperature intervals. The XRD patterns obtained at 195, 140 and 80 °C were almost same corresponding to Col$_h$ phase (Figure 4.7c, Table 4.3), while the one obtained at room temperature (Figure 4.7d) showed several peaks at low and middle angle region. These *d*-spacings could be indexed to a Col phase with a parallelogram lattice of an oblique symmetry (Col$_{ob}$), with the lattice parameters $a = 28.04$ and $b = 48.96$ Å with a tilt angle $\gamma = 69.9^{o}$. The core-core stacking distance '*c*' was found to be 3.44 Å. Thus the number of discs present in a unit cell (*Z*) turns to be 1.5. Thus, **PBI-Se** exhibited a bimesomorphic behavior, with high temperature Col$_h$ phase and low temperature Col$_{ob}$ phase. This phase appears to be 3D-ordered, although the XRD peaks can be assigned to Col$_{ob}$ phase. The presence of a non-negligible diffuse maximum at wide angles does suggest enough disorder in the medium, which could be of either plastic or glassy in nature. Conclusive evidence was not found, as no peak required all non-zero *hkl* values. The observation of Col$_{ob}$ phase corresponds to the enhanced intermolecular interactions in **PBI-Se** in comparison to the other two PBIs, which is also reflected in its higher melting point in comparison to **PBI-S**. However, the second heating showed a cold crystallization at ≈79 °C (2.3 kJ/mol), which was not noticed during the first cooling cycle in DSC (Figure 4.3c). It also should be noted that the XRD at room temperature was taken in the first cooling cycle. Thus somewhere below this temperature crystallization occurs, which was not seen in the case of **PBI-N** and **PBI-S**.

During these X-ray studies we had some interesting findings, which is due to the minute structural differences arising from the *bay*-annulation. The XRD patterns obtained for **PBI-N** at low temperature *i.e.* Col$_{h2}$ phase shows that this phase is less ordered in comparison to the high temperature Col$_{h1}$ phase. This is in contradiction to what is expected

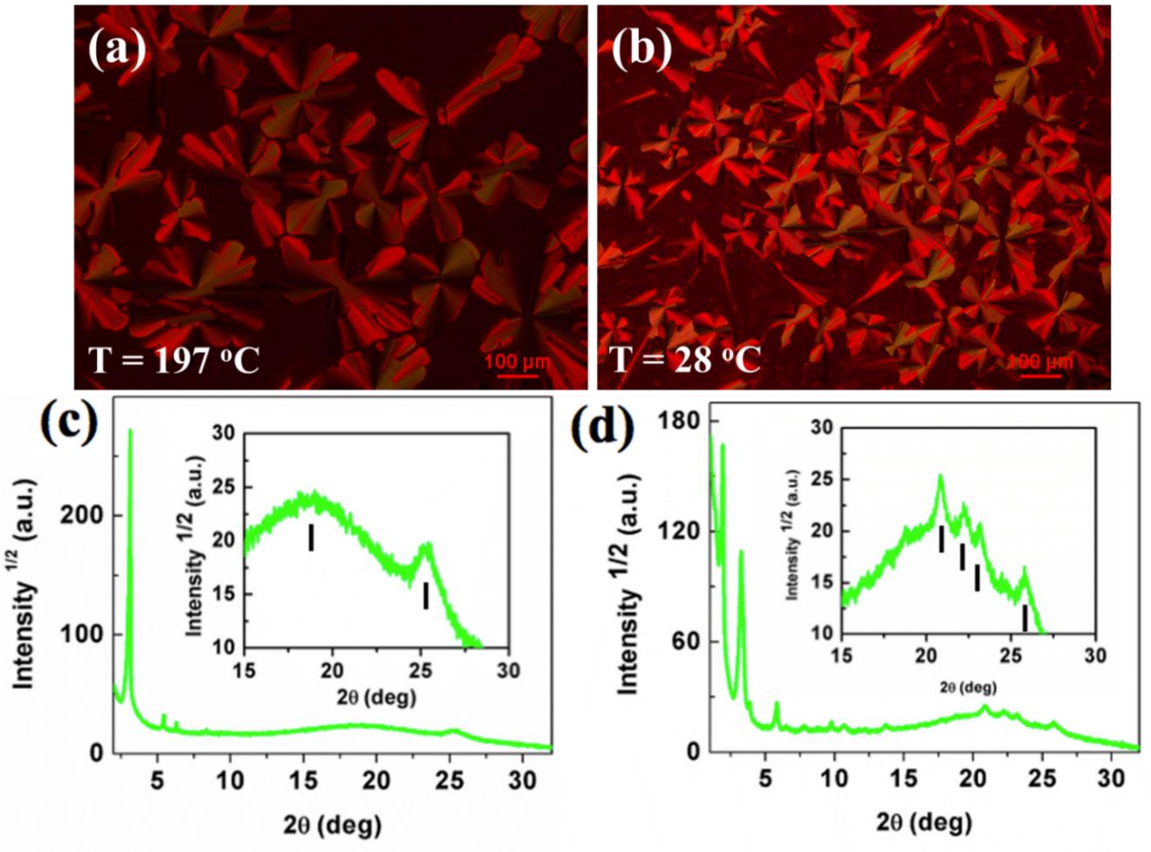

Figure 4.7. (a, b) POM images (under crossed polarizer) obtained for **PBI-Se** and the XRD profiles depicting the intensity against the 2θ obtained for the Col$_h$ phase (c) at 195 ºC and for the Col$_{ob}$ phase (d) at 24 ºC.

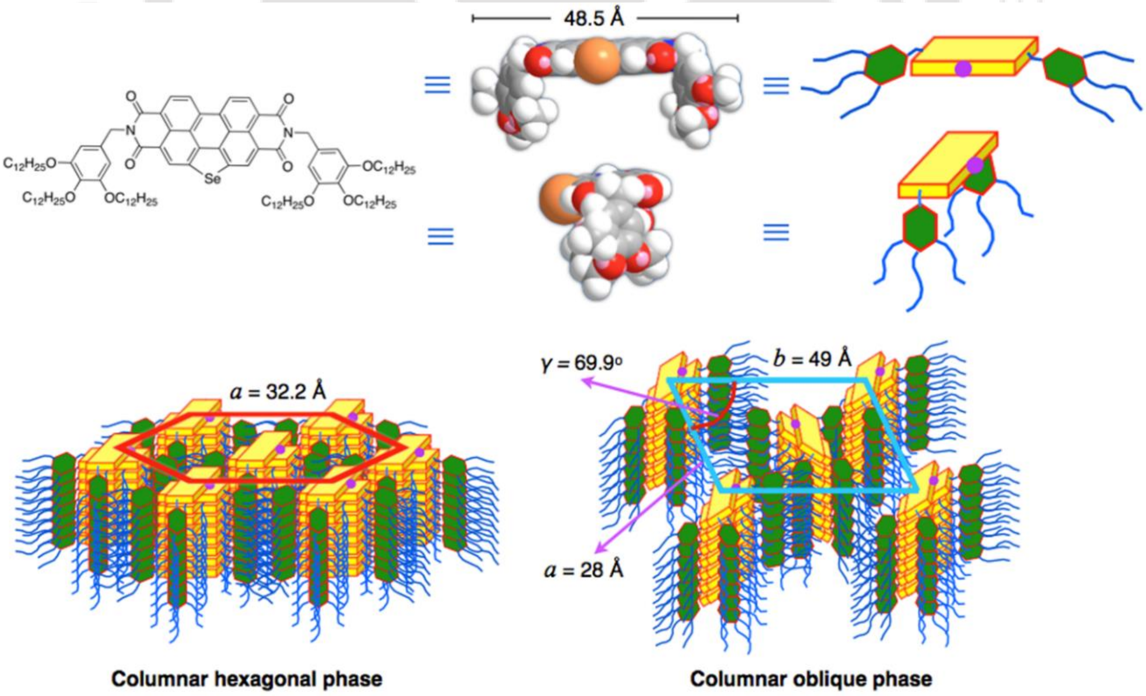

Figure 4.8. Schematic showing the energy minimized structure of **PBI-Se** and its self-assembly into Col$_h$ phase (XRD data at 80 ºC is considered for the illustration) and Col$_{ob}$ phase (XRD data at 24 ºC is considered for the illustration).

on lowering the temperature. Usually the phase becomes more ordered, due to the reduced mobility of the molecules along with a lowered core-core distance. But the observed difference, where the peaks at low angle become broad and diffuse was found to be reproducible and genuine. Similar effect was noticed in the case of **PBI-S**, but it was not that drastic. The main structural aspect that should be borne in mind is that in the case of **PBI-N** where the effect is drastic has an ethyl group substitution at the *bay*-nitrogen position. This can, in principle be considered like an extended arm of the hydrocarbon having substantial degree of freedom to move about the plane of the perylene core. At high temperatures, *i.e.* in the Col$_{h1}$ phase, when the terminal chains have a substantial folded character (molten chains), the effect due to the ethylene part is less dominant. Thus the interfaces between the lattice planes are reasonably flat, a feature that is evident from the stronger signal for the peak associated with the core-core correlation. Concomitantly the core-core distance is also lower. At much lower temperature, in the Col$_{h2}$ phase, a large increase in the diameter (*a*) of the columns is seen (increasing by ~5 Å from the value in the Col$_{h1}$ phase) signifies that the terminal chains are more spread out. Intuitively, this should have led to a flatter lattice plane and consequently better-packed molecular cores. However, the experiments show the opposite as seen by reduced number of sharp peaks at low angles, and a far weaker core-core peak. This must be due to the increasing influence of the wagging by the ethyl group in the core region. The reduced overall entropy of the system must be making the ethyl group to occupying regions above or below the plane of the core, and less biased towards being in that plane; this should increase the core-core distance as is clear from the X-ray studies. This diminishes the interaction between the neighbouring discs, a feature evident from the weakened core-core peak, making the lattice plane interfaces rough and in turn reducing the number of low-angle peaks. The presence of the sulphur atom in the **PBI-S** case also has some of these features, but the effect is much smaller, as sulphur is less bulky compared to the ethyl group. It is possible that the rarely observed transition between two hexagonal columnar phases (Col$_{h1}$-Col$_{h2}$) is caused by the presence of the ethyl group in the core-region. In the selenium case (**PBI-Se**) probably the disturbance leads towards the tilting of the columnar lattice (Col$_{ob}$ phase), although only after a three-dimensional ordering (as seen by a number of sharp peaks) sets in.

4.2.3. Density functional theory (DFT) calculation

We have used density functional theory (DFT) calculations to visualize the energy minimized structures of the PBIs and the energy levels of the frontier molecular orbitals

(HOMO-LUMO) of all the compounds (Figure 4.9).[13] The energy minimized structures for **PBI, PBI-N, PBI-S** and **PBI-Se** showed in Figure 4.9a. Images of frontier molecular orbitals (FMOs) and the differences in their energies provide knowledge about the length of conjugation and band gap level, which helps in comparing the perylene bisimide with its *bay*-annulated derivatives. In the energy minimized structures, we can notice the planar perylene and two out of plane benzyl rings. Side view presented in Figure 4.9b distinguishes the *bay*-annulated PBIs from the parent PBI. In the case of parent PBI, the benzyl wings are positioned at two different planes, while in the case of *bay*-annulated PBIs, two benzyl wings are on the same side of the central perylene ring, leading to a cup shape. Such an orientation helps the molecules to pack into more ordered columns as shown in Figure 4.5 and Figure 4.8.[7a]

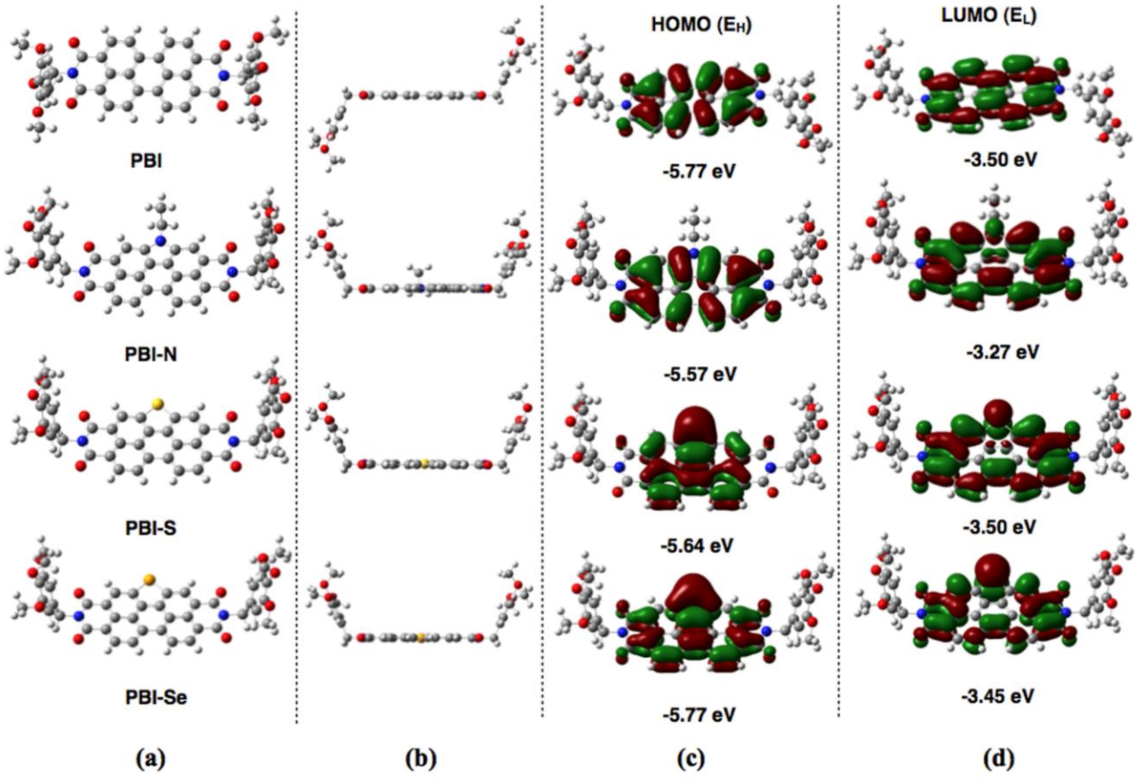

Figure 4.9. (a) Optimized geometry of compounds **PBI**, **PBI-N**, **PBI-S** and **PBI-Se**; (b) side view of the same; (c) HOMO and (d) LUMO frontier molecular orbitals of compounds **PBI**, **PBI-N**, **PBI-S** and **PBI-Se** at the B3LYP/6-31G(dp) level. E_H and E_L denote energies of the highest occupied molecular orbital (HOMO) and the lowest unoccupied molecular orbital (LUMO), respectively.

The contours of the HOMO and LUMO of PBIs are shown in Figure 4.9c and d.The HOMO-LUMO energy levels of PBIs are distributed on the entire aromatic ring. PBIs are considered as closed chromophoric (electronically decoupled) systems due to the presence of nodes of the HOMO and LUMO orbitals on imide nitrogen atoms. Thus, the substitution at imide nitrogen does not alter the optical properties significantly.[14] *Bay*-annulation increased the HOMO and LUMO levels in comparison to the simple perylene bisimide. In the case of annulated derivatives, HOMO and LUMO levels were found to be spreading over heteroatom. The theoretical band gaps for **PBI, PBI-N, PBI-S** and **PBI-Se** were found to be 2.27, 2.3, 2.14 and 2.32 eV respectively.

4.2.4. Photophysical and electrochemical studies

Photophysical properties of these compounds were explored by obtaining their absorption and emission spectra in micromolar chloroform solutions (Figure 4.10, Table 4.4). The absorption spectra of these PBIs were well-structured and showed the characteristic four vibronic bands, with the longest absorption wavelength was centered in the range of 503-532 nm. Compound **PBI-N** was slightly red-shifted in comparison to **PBI**, while **PBI-S** and **PBI-Se** exhibited slightly blue shifted absorption spectra. All the PBIs exhibited high molar extinction coefficients at their absorption maxima (ε: 14,700 to 20,300 L.mol^{-1}cm^{-1}). The optical band gap calculated from the absorption onset showed that the optical band gap of **PBI** and **PBI-N** were almost matching while that of the **PBI-S** and **PBI-Se** shown an increase. Emission spectra of these compounds showed two main bands, with the high intensity band was in the range of 517-545 nm. The Stoke's shift was found to be less in the range of 448-596 cm^{-1}.

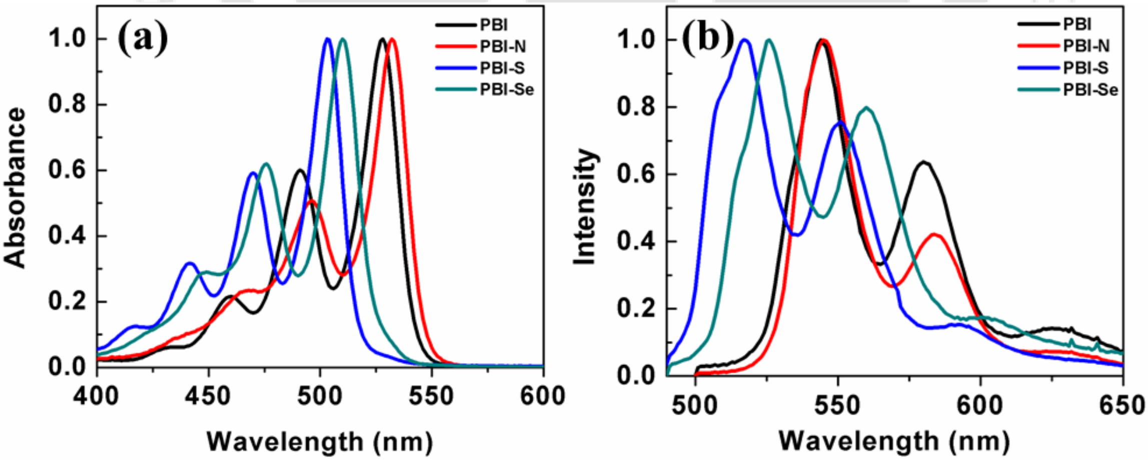

Figure 4.10. (a) Absorption and (b) emission spectra in micromolar THF solution for **PBI**, **PBI-N**, **PBI-S** and **PBI-Se**.

Cyclic voltammetry (CV) studies are carried out to understand the electronic energy levels that decide the energy and electron transfer process and reversibility of a redox process. CV studies were carried out in anhydrous dichloromethane solutions (Table 4.5).

Table 4.4. Photophysical properties[a] of PBIs in solution.

	Absorption (nm)	**ε (L.mol^{-1}cm^{-1})**	**Emission[b] (nm)**	**Stokes shift (cm^{-1})**	**$\Delta E_{g,opt}$[c] (eV)**
PBI	528, 491, 460 430	18259	544, 580	557	2.28
PBI-N	532, 496, 468, 438	14797	545, 584	448	2.27
PBI-S	503, 470, 442, 417	16600	517, 551	538	2.39
PBI-Se	510, 476, 449, 421	20310	526, 560	596	2.34

[a]micromolar solutions in $CHCl_3$; [b]the excitation wavelength λ_{ex} = 460, 468, 442 and 449 nm respectively for compound **PBI, PBI-N, PBI-S** and **PBI-Se**; [c]calculated from the red edge of the absorption band.

PBIs are known to be electron deficient n-type semiconductors and known to have high electron affinity. Among these compounds, only **PBI** and **PBI-N** exhibited two reversible reduction peaks (Figure 4.11a). It was difficult to obtain the oxidation potentials of these electron deficient compounds even with a CV measurement window up to +1 V *vs* $Ag/AgNO_3$. Thus we have calculated the HOMO levels, by subtracting the LUMO energy values from the optical band gap that was obtained from the absorption onset of the compounds in solutions. From the CV studies it is found that the *bay*-annulated PBIs showed increased LUMO levels in comparison to **PBI** (Figure 4.11b). A small increase of 0.18 eV in the HOMO level was noted in the case of **PBI-N**, while **PBI-S** and **PBI-Se** displayed a lowering of HOMO levels by 0.08 and 0.04 eV respectively (Figure 4.11b). The values obtained from CV studies followed the same general trend that was obtained from DFT calculations.

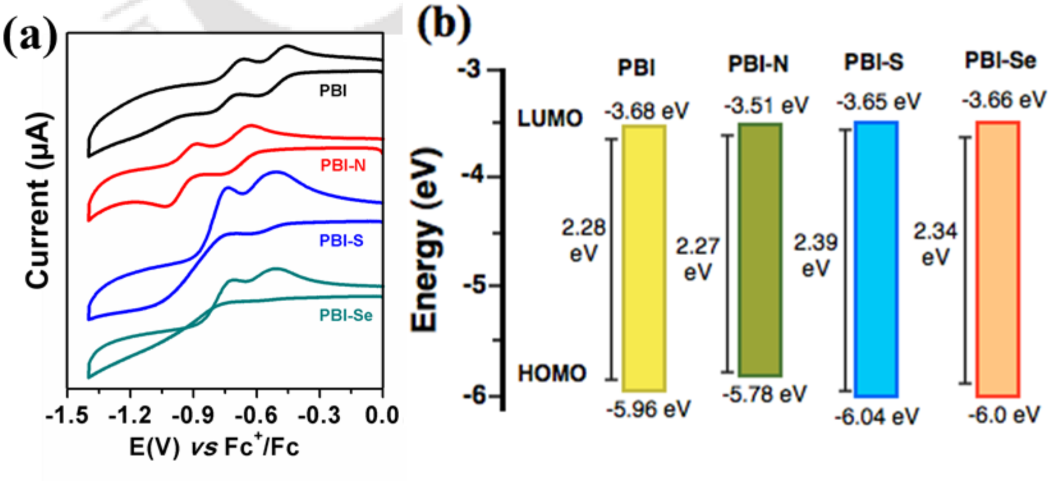

Figure 4.11. (a) Cyclic voltammograms of **PBI** and *bay*-annulated **PBI**s; (b) Energy band level diagram showing HOMO and LUMO energy levels of the same.

Table 4.5. Electrochemical properties of PBIs in solution^{a,b}

Entry	$E_{1red}{}^{c}$	$E_{LUMO}{}^{d,e}$	$E_{HOMO}{}^{d,f}$	$\Delta E_{g,opt}{}^{d,g}$
PBI	-0.57	-3.68	-5.96	2.28
PBI-N	-0.74	-3.51	-5.78	2.27
PBI-S	-0.60	-3.65	-6.04	2.39
PBI-Se	-0.59	-3.66	-6.00	2.34

^{a}in Dichloromethane solutions; ^{b}Experimental conditions: Ag/AgNO$_3$ as reference electrode, Glassy carbon working electrode, Platinum wire counter electrode, TBAP (0.1 M) as a supporting electrolyte, room temperature; ^{c}in volts (V); ^{d}in eV; ^{e}Estimated from the formula by using $E_{LUMO} = -(4.8 - E_{1/2}$, Fc/Fc^{+} + E_{red}, onset) eV; ^{f}Estimated from the formula $E_{HOMO} = E_{LUMO} - E_{g,}$ opt) eV; ^{g}calculated from the red edge of the absorption band (544, 547, 519, 530 nm respectively). $E_{1/2}$, Fc/Fc^{+} = 0.55.

4.3. Conclusion

In conclusion, we have synthesized three new electron-deficient heteroatoms *bay*-annulated perylene bisimides stabilizing ordered columnar phase over a wide temperature range. The *N*- and *S*-annulated perylene bisimides showed columnar hexagonal phase, while the *Se*-annulated perylene bisimide exhibited columnar oblique phase in addition to the columnar hexagonal phase. The Col phase on cooling freezes into glassy state, this is quite impressive to obtain the highly ordered structure in the devices, by thermal annealing. These molecules exhibit high molar extinction coefficients along with the absorption spectra covering the most of the visible spectrum, which will be important for solar cells with a scope to improve further by the structure modulation. The optical band gaps are low with minor differences observed in the HOMO and LUMO levels. Further structural modifications are needed to approach the fullerene’s HOMO and LUMO levels, however this serves as a starting point. DFT calculations revealed the cup-like conformation of these molecules in the energy-minimized structure, which may support their columnar self-assembly along with the π-π interactions and nanophase segregation. Considering the scarcity of n-type semiconductors in literature, these compounds could give rise to a variety of alternatives to synthesize highly ordered n-type columnar self-assemblies. The microwave-assisted synthesis further improved the synthetic access to such materials in good yields.

4.4. Experimental section

In this section the detailed synthesis procedure and the molecular structural characterization data have been presented for the intermediates and target compounds mentioned in the scheme.

Synthesis of tetrakis(butyl) perylene-3,4,9,10-tetracarboxylate (**1**)

Perylenetetracarboxylic dianhydride (2.5 mmol, 1 equiv.) was dissolved in 30 mL aqueous KOH (13.76 mmol, 5.4 equiv.) solution and stirred at 70 °C for 0.5 h. The solution was filtered and pH value of filterate was adjusted to 8-9 using 10% HCl. Then Aliquat 336 (0.9 mmol, 0.4 equiv.) and KI (1.4 mmol, 0.6 equiv.) were charged into the solution and then stirred vigorously for 10 min. 1-bromo-butane (15.3 mmol, 6 equiv.) was added to this reaction mixture. After the addition the reaction mixture was refluxed for 12 h until a red oil floats on the top and the rest of the solution becomes clear. Subsequently, chloroform (10 mL) was poured into the mixture and filtered through the celite bed to remove unreacted part and the celite bed was washed with chloroform. This chloroform layer was separated and washed twice with 15% sodium chloride solution, dried over sodium sulfate and concentrated in vacuo to get a viscous concentrate. Methanol was added to precipitate the compound from this concentrate. The solid was precipitated filtered and dried in vacuum.

R_f = 0.6 (20% EtOAc-hexane); orange solid, yield: 76%; IR (KBr pellet) ν_{max} in cm^{-1}: 2960, 2930, 2872, 1725, 1627, 1590, 1308, 1279, 1172, 1136, 1097; ^1H NMR (600 MHz, $CDCl_3$, 298 K): 8.04 (d, J = 6Hz, 4H, H_{Ar}), 7.90 (d, J = 12Hz, 4H, H_{Ar}), 4.35 (t, 8H, 4 × $-OCH_2$), 1.82-1.78 (m, 8H, 4 × $-OCH_2$-$\underline{CH_2}$), 1.62-1.49 (m, 8H, 4 ×CH_2), 1.01 (t, 12H, 4 × $-CH_3$); ^{13}C NMR (150 MHz, $CDCl_3$, 298 K): 168.77, 132.95, 130.48, 128.97, 128.79, 121.47, 65.53, 30.87, 19.49, 14.04; MALDI-TOF: exact mass calculated for $C_{40}H_{44}O_8$ $[M]^+$: 652.3, found: 652.5.

Synthesis of tetrakis(butyl) 1-nitroperylene-3,4,9,10-tetracarboxylate (**2**)

To a solution of **1** (0.7 mmol, 1 equiv.) in dichloromethane (15 mL), added $NaNO_2$ (0.7 mmol, 1 equiv.) at 0 °C and stirred. To this well stirred suspension, 69% HNO_3 (3.42 mmol, 5 equiv., 10% solution in dichloromethane) was added dropwise. This mixture was stirred at 0 °C for 1 h. The reaction mixture was poured into water and extracted with dichloromethane (25 mL). Finally, organic layer was dried over anhydrous Na_2SO_4 and concentrated. The crude product was purified by column chromatography on neutral alumina. Elution with 50% dichloromethane-hexane yielded the desired product.

R_f = 0.6 (20% EtOAc-hexane); red viscous liquid, yield: 90%; IR (KBr pellet) ν_{max} in cm^{-1}: 2958, 2928, 2872, 1725, 1660, 1591, 1533, 1516, 1459, 1435, 1356, 1281, 1165, 1104, 1020, 805, 749 ; ^1H NMR (600 MHz, $CDCl_3$, 298 K): 8.34-8.29 (m, 2H, H_{Ar}), 8.24 (s, 1H, H_{Ar}), 8.18 (d, 1H, H_{Ar}), 8.10 (d, 1H, H_{Ar}), 7.95-7.93 (m, 1H, H_{Ar}), 7.86-7.84 (m, 1H, H_{Ar}), 4.37-4.33 (m, 8H, 4 × $-OCH_2$), 1.81-1.77 (m, 8H, 4 × $-OCH_2$-$\underline{CH_2}$), 1.51-1.46 (m, 8H, 4 ×CH_2), 1.01-0.98 (m, 12H, 4 × $-CH_3$); ^{13}C NMR (150 MHz, $CDCl_3$, 298 K): 168.21, 168.03, 167.96, 166.82, 146.17, 133.59, 132.34, 132.08, 131.40, 131.33, 130.80, 130.36, 129.9, 129.64, 129.06, 128.51, 128.38, 127.5, 126.63, 125.66, 123.21, 122.68, 66.23, 65.89, 65.84, 65.75, 30.75, 30.71, 29.85, 19.40, 13.96; MALDI-TOF: exact mass calculated for $C_{40}H_{43}NO_{10}$ $[M]^-$: 697.3, found: 697.8.

Synthesis of tetrakis(butyl) 1H-phenanthrocarbazole-3,4,9,10-tetracarboxylate (**3**)

A mixture of compound **2** (0.6 mmol) and triethyl phosphite (7 mL) were refluxed for 4 h under argon atmosphere. Reaction mixture was cooled to room temperature and methanol was added to this solution to precipitate the compound. This precipitated product was filtered off and washed with water, dried in vacuum. Further purification was done by repeated recrystallization from dichloromethane-methanol system.

R_f = 0.6 (20% EtOAc-hexane); yellow solid, yield: 60%; IR (KBr pellet) ν_{max} in cm^{-1}: 3458, 2959, 2927, 2853, 1722, 1637, 1593, 1426, 1277, 1187, 1154; ^{1}H NMR (600 MHz, $CDCl_3$, 298 K): 9.42 (s, 1H, NH), 8.01 (d, *J* = 12 Hz, 2H, H_{Ar}), 7.94-7.92 (m, 4H, H_{Ar}), 4.54-4.5 (m, 8H, 4 × $-OCH_2$), 1.97-1.92 (m, 8H, 4 × $-OCH_2$-$\underline{CH_2}$), 1.66-1.61 (m, 8H, $-CH_2$), 1.10 (t, 12H, 4 × $-CH_3$); ^{13}C NMR (150 MHz, $CDCl_3$, 298 K): 169.87, 130.9, 130.13, 128.36, 127.41, 127.12, 122.97, 122.6, 121.51, 119.23, 117.63, 65.67, 65.57, 31.12, 31.07, 19.65, 19.63, 14.13; MALDI-TOF: exact mass calculated for $C_{40}H_{43}NO_8$ $[M]^+$: 665.3, found: 665.7.

Synthesis of tetrabutyl 1-ethyl-1H-phenanthrocarbazole-3,4,9,10-tetracarboxylate (**4**)

A mixture of compound **3** (0.12 mmol, 1 equiv.), sodium hydride (0.36 mmol, 3 equiv.) and ethyl iodide (0.18 mmol, 1.53 equiv.) in a dry THF was refluxed for overnight under argon atmosphere. After cooling to room temperature, water (2 mL) was added to the mixture and stirred for 10 min at 0 °C. The resulting mixture was extracted with dichloromethane, the extract was washed with water and brine. Finally, organic layer was dried over anhyd. Na_2SO_4 and concentrated. The crude residue obtained was purified by column chromatography on neutral alumina. Elution with hexane, 50% dichloromethane-hexane solution followed by dichloromethane to yield the desired product.

R_f = 0.6 (15% EtOAc-hexane); Yellowish solid, yield: 75%; IR (KBr pellet) ν_{max} in cm^{-1}: 2959, 2929, 2873, 1720, 1586, 1258, 1213, 1186, 1149; ^{1}H NMR (600 MHz, $CDCl_3$, 298 K): 8.49 (d, *J* = 6 Hz, 2H, H_{Ar}), 8.22 (s, 2H, H_{Ar}), 8.18 (d, *J* = 6Hz, 2H, H_{Ar}), 4.74-4.7 (m, 2H, -*N*-CH_2), 4.45-4.42 (m, 8H, 4 × $-OCH_2$), 1.87-1.82 (m, 8H, 4 × $-OCH_2$-$\underline{CH_2}$), 1.56-1.5 (m, 8H, 4 × $-CH_2$), 1.25 (bs, 3H, -*N*-CH_2-CH_3), 1.04-1.01 (m, 12H, 4 × $-CH_3$); ^{13}C NMR (150 MHz, $CDCl_3$, 298 K): 169.73, 169.32, 131.94, 131.44, 129.23, 128.18, 127.8, 124.37, 123.33, 121.93, 118.12, 117.88, 65.67, 65.56, 40.8, 30.99, 30.97, 29.91, 19.55, 16.73, 14.10, 14.09; MALDI-TOF: exact mass calculated for $C_{42}H_{47}NO_8$ $[M]^+$: 693.3, found: 693.7.

Synthesis of *N*-annulated perylenetetracarboxylic dianhydride (**5**)

A mixture of compound **4** (0.43 mmol, 1 equiv.) and p-toluene sulphonic acid monohydrate (2.16 mmol, 5 equiv.) in toluene (7 mL) was heated at 100 °C for 30 h. After cooling at room temperature, the mixture was filtered it, washed with methanol and dried under vacuum. The crude product was sufficiently pure and used for next step reaction without any purification. The yield of the crude product was found to 90%.

Synthesis of tetrakis(butyl) perylenothiophene-3,4,9,10-tetracarboxylate (**6**)

A mixture of compound **2** (0.26 mmol, 1 equiv.) and Sulfur powder (2.602 mmol, 10 equiv.) was heated to dissolve in *N*-methylpyrrolidone (10 mL) at 70 °C for 30 min. and then refluxed at 180 °C under Ar atmosphere for overnight until the starting material could not be detected by TLC. After cooling to room temperature, 2 M HCl was added, then the precipitate was filtered, washed with water and dried. The crude product was purified by column chromatography on neutral alumina. Elution with 20-30% DCM-hexane system followed by 50% DCM-hexane system yields the desired product in good yield. Further purification was done by addition of concentrate solution of compound in cold methanol gives the waxy product.

R_f = 0.6 (20% EtOAc-hexane); orange solid, yield: 55%; IR (KBr pellet) ν_{max} in cm^{-1}: 2955, 2927, 2869, 1720, 1583, 1467, 1414, 1384, 1366, 1259, 1187, 1170, 1155, 1120, 1041, 749 ; ^{1}H NMR (600 MHz, $CDCl_3$, 298 K): 8.59-8.57 (m, 4H, H_{Ar}), 8.27 (d, J = 6Hz, 2H, H_{Ar}), 4.44-4.41 (m, 8H, 4 × -OCH_2), 1.87-1.81 (m, 8H, 4 × OCH_2-$\underline{CH_2}$), 1.56-1.51 (m, 8H, 4 × CH_2), 1.04-1.01 (m, 12H, 4 × -CH_3); ^{13}C NMR (150 MHz, $CDCl_3$, 298 K): 168.86, 168.73, 135.16, 132.08, 130.61, 129.99, 129.4, 126.26, 125.61, 125.43, 121.92, 65.79, 65.68, 30.95, 30.92, 19.56, 19.53, 14.06; MALDI-TOF: exact mass calculated for $C_{40}H_{42}O_8S$ $[M]^+$: 682.2, found: 682.4.

Synthesis of *S*-annulated perylenetetracarboxylic dianhydride (**7**)

A mixture of compound **6** (0.85 mmol, 1 equiv.) and *p*-toluene sulphonic acid monohydrate (4.25 mmol, 5 equiv.) in toluene (10 mL) was heated at 100 °C for 30 h. After cooling at room temperature, the mixture was filtered it, washed with methanol and dried under vacuum. The crude product was sufficiently pure and used for next step reaction without any purification. The yield of the crude product was found to 90%.

Synthesis of tetrakis(butyl) perylenoselenophene-3,4,9,10-tetracarboxylate (**8**)

A mixture of compound **2** (0.26 mmol, 1 equiv.) and Selenium powder (2.602 mmol, 10 equiv.) was heated to dissolve in *N*-methylpyrrolidone (10 mL) at 70 °C for 30 min. and then refluxed at 180 °C under Ar atmosphere for overnight until the starting material could not be detected by TLC. After cooling to room temperature, 2 M HCl was added, then the precipitate was filtered, washed with water and dried. The crude product was purified by column chromatography on neutral alumina. Elution with 20-30% DCM-hexane system followed by 50% DCM-hexane system yields the desired product in good yield. Further purification was done by addition of concentrate solution of compound in cold methanol gives the waxy product.

R_f = 0.6 (20% EtOAc-hexane); orange solid, yield: 55%; IR (KBr pellet) ν_{max} in cm^{-1}: 2955, 2927, 2869, 1719, 1582, 1467, 1406, 1384, 1259, 1189, 1155, 1107, 1041, 800, 748 ; ^{1}H NMR (400 MHz, $CDCl_3$, 298 K): 8.57-8.53 (m, 4H, H_{Ar}), 8.24-8.23 (m, 2H, H_{Ar}), 4.41 (bs, 8H, 4 × -OCH_2), 1.86-1.82 (m, 8H, 4 × OCH_2-$\underline{CH_2}$), 1.55-1.51 (m, 8H, 4 × -CH_2), 1.04-1.01 (m, 12H, 4 × -CH_3); ^{13}C NMR (100 MHz, $CDCl_3$, 298 K): 168.91, 168.7, 137.59, 133.33, 132.23, 129.95, 129.3, 128.73, 128.69, 126.99, 125.75, 121.61, 65.76, 65.65, 30.93, 30.91, 19.55, 19.53, 14.09, 14.08; MALDI-TOF: exact mass calculated for $C_{40}H_{42}O_8Se$ $[M]^+$: 730.2, found: 730.8.

Synthesis of *Se*-annulated perylenetetracarboxylic dianhydride (**9**)

A mixture of compound **8** (0.75 mmol, 1 equiv.) and *p*-toluene sulphonic acid monohydrate (3.74 mmol, 5 equiv.) in toluene (10 mL) was heated at 100 °C for 30 h. After cooling at room temperature, the mixture was filtered it, washed with methanol and dried under vacuum. The crude product was sufficiently pure and used for next step reaction without any purification. The yield of the crude product was found to 90%.

Synthesis of ethyl 3,4,5-tri(dodecyloxy) benzoate (**10**)

A mixture of ethyl gallate (25.2 mmol, 1equiv.), anhyd. K_2CO_3 (166.5 mmol, 6.6 equiv.), *n*-bromododecane (83.3 mmol, 3.3 equiv.) were taken in dry DMF (20 mL) and heated at 90 ^{o}C for 17 h under nitrogen atmosphere. Then the reaction mixture was poured into ice-water and extracted with CH_2Cl_2. The combined extract was washed with water and brine and later dried over anhyd. Na_2SO_4 and concentrated. The crude product was purified by silica gel column chromatography. Elution with hexane followed by 5-10% ethylacetate-hexane yielded the desired product.

R_f = 0.61 (10% EtOAc-hexane); Low melting white solid; yield: 85%; IR (KBr pellet) ν_{max} in cm^{-1}: 2924, 2853, 1716, 1590, 1504, 1465, 1432, 1333, 1222, 1119; ^{1}H NMR ($CDCl_3$, 600 MHz, 298 K): δ 7.25 (s, 2H, Ar), 4.35 (q, 2H, *J* = 6 Hz, $COOCH_2$), 4.01 (m, 6H, 3 × OCH_2), 1.23-1.83 (m, 60H, 30 × CH_2), 0.87-0.89 (m, 12H, 4 × CH_3); ^{13}C NMR ($CDCl_3$, 150 MHz, 298 K): 166.66, 153.01, 142.57, 125.26, 108.24, 73.68, 69.40, 61.14, 32.14, 30.54, 29.95, 29.92, 29.85, 29.79, 29.61, 29.54, 26.30, 22.90, 14.30; HRMS (ESI+) exact mass calculated for $C_{45}H_{83}O_5$ $[MH]^+$: 703.6235, Found: 703.6199.

Synthesis of 3,4,5- tridodecyloxybenzyl alcohols (**11**):

To a stirred suspension of lithium aluminium hydride (LAH) (21.3 mmol, 1.5 equiv.) in dry THF (20 mL) under nitrogen atmosphere, added the solution of ethyl 3,4,5-tri(dodecyloxy) benzoate **10** (14.2 mmol, 1 equiv.) in dry THF drop wise at 0 ^{o}C. Then the reaction mixture was allowed to reach room temperature and stirred for 2 h. Excess LAH present was quenched by the addition of Rochelle's salt solution. Reaction mixture was extracted with EtOAc (6 × 30 ml). The combined extracts were washed with water, dried over anhyd Na_2SO_4 and concentrated in vacuo. Purification was done by column chromatography over silica gel with 10% EtOAc-hexane as eluent.

R_f = 0.15 (10% EtOAc-hexane), white solid, yield: 95%; IR (KBr pellet) ν_{max} in cm^{-1}: 3417.27, 2922.36, 2852.51, 1590.29, 1467.09, 1438.45, 1334.39, 1231.90, 1124.64, 806.80, 722.27, 466.28; ^{1}H NMR ($CDCl_3$, 600 MHz, 298 K): δ 6.55 (s, 2H, Ar), 4.59-4.60 (d, 2H, $PhCH_2$), 3.92-3.98 (m, 6H, 3 × OCH_2), 1.26-1.81 (m, 60H, 30 × CH_2), 0.88 (t, 9H, 3 × CH_3); ^{13}C NMR ($CDCl_3$, 100 MHz, 298 K): 153.46, 137.75, 136.27, 105.52, 73.65, 69.29, 65.86, 32.16, 32.14, 30.53, 29.97, 29.95, 29.92, 29.87, 29.84, 29.63, 29.58, 26.35, 26.32, 22.91, 14.33; HRMS (ESI+) exact mass calculated for $C_{43}H_{80}O_4$ $[MH]^+$: 661.6129, Found: 661.6128.

Synthesis of 3,4,5- tridodecyloxybenzyl chloride (**12**):

3,4,5-tridodecyloxybenzyl alcohol **11** (4.5 mmol, 1equiv.) was dissolved in Dry DCM (20 mL) with stirring and cooled to 0 ^{o}C under Ar atmosphere. $SOCl_2$ (3.18 equiv.) was added to the above reaction mixture and stirred at the room temperature for 2 h. The reaction mixture was slowly quenched with saturated $NaHCO_3$. Reaction mixture was extracted with methylene chloride and the organic layer was washed with saturated brine solution, and dried over Na_2SO_4. A light yellowish solid was obtained on removal of solvent which was used without further purification for next step reaction.

R_f = 0.5 (5% EtOAc-hexane), light yellowish solid, yield: 95 %; IR (KBr pellet) ν_{max} in cm^{-1}: 2954, 2921, 2849, 1594, 1506, 1466, 1441, 1393, 1334, 1246, 1125, 830; ^1H NMR ($CDCl_3$, 600 MHz, 298 K): δ 6.56 (s, 2H, Ar), 4.51 (s, 2H, $PhCH_2$), 3.92-3.98 (m, 6H, 3 × OCH_2), 1.26-1.80 (m, 60H, 30 × CH_2), 0.88 (t, 9H, 3 × CH_3); ^{13}C NMR ($CDCl_3$, 150 MHz, 298 K): 153.21, 138.28, 132.32, 107.06, 73.47, 69.14, 47.01, 31.95, 30.34, 30.3, 29.77, 29.72, 29.66, 29.39, 26.11, 22.72, 14.14; LRMS (ESI+) molecular mass calculated for $C_{43}H_{80}ClO_3$ $[MH]^+$: 680.55, Found: 680.77.

Synthesis of 2-(3,4,5-tris(dodecyloxy)benzyl)isoindoline-1,3-dione (**13**)

Potassium phthalimide (12.9 mmol, 1.1 equiv.) was added to the solution of 3,4,5-tridodecyloxy benzyl chloride (12.1 mmol, 1 equiv.) in DMF. The reaction mixture was stirred at 90 °C for 18 h. cooled the reaction mixture to room temperature, poured the mixture in water and extracted with methylene chloride several times. The combined organic layer was washed with 0.2 N KOH, water, saturated NH_4Cl, dried over anhy. Na_2SO_4 and concentrated under reduced pressure after filtration. The resulting crude compound was purified by column chromatography using methylene chloride as eluent to give white solid.

R_f = 0.4 (10% EtOAc-hexane); white solid, yield: 95%; IR (KBr pellet) ν_{max} in cm^{-1}: 2921, 2851, 1773, 1714, 1593, 1503, 1467, 1435, 1391, 1343, 1326, 1247, 1234, 1119, 1095, 735; ^1H NMR (600 MHz, $CDCl_3$, 298 K): 7.84-7.83 (m, 2H, H_{Ar}), 7.70-7.69 (m, 2H, H_{Ar}), 6.65 (s, 2H, H_{Ar}), 4.72 (s, 2H, $PhCH_2$), 3.95 (t, 4H, $-OCH_2$), 3.89 (t, 2H, $-OCH_2$), 1.78-1.25 (m, 66H, 33 × $-CH_2$), 0.89-0.86 (m, 9H, 3 × $-CH_3$); ^{13}C NMR (150 MHz, $CDCl_3$, 298 K): 168.27, 153.33, 137.98, 134.14, 132.36, 131.58, 123.53, 107.61, 73.59, 69.27, 42.15, 32.14, 29.96, 29.92, 29.88, 29.86, 29.65, 29.6, 29.59, 26.31, 22.91, 14.33; HRMS (ESI mode) exact mass calculated for $C_{51}H_{84}NO_5$ $[MH]^+$: 790.63, found: 790.67.

Synthesis of (3,4,5-tris(dodecyloxy)phenyl)benzylamine (**14**)

A mixture of compound **13** (43 mmol, 1 equiv.) and hydrazine hydrate (3 equiv.) in methanol were stirred at 95 °C for 1 h. After the disappearance of starting imide, methanol was removed under reduced pressure and residue was diluted with dichloromethane and washed with 10% KOH. The combined aqueous layer was extracted with dichloromethane. The combined organic layer was washed with brine and dried over Na_2SO_4. After removal of solvent the product obtained as viscous liquid in 95% yield, which on keeping in low temperature becomes waxy solid, which was used for next step without further purification.

R_f = 0.3 (20% EtOAc-hexane); low melting waxy solid, yield: 95%; IR (KBr pellet) ν_{max} in cm^{-1}: 3433, 2922, 2852, 1589, 1505, 1467, 1438, 1379, 1334, 1230, 1120, 721; ^1H NMR (600 MHz, $CDCl_3$, 298 K): 6.51 (d, 2H, J = 6 Hz H_{Ar}), 4.32 (s, 1H, H-NH), 3.98-3.9 (m, 6H, $-OCH_2$), 3.77 (s, 1H, -H-NH), 2.09-1.26 (m, 66H, 33 × $-CH_2$), 0.88 (t, 9H, 3 × $-CH_3$); ^{13}C NMR (150 MHz, $CDCl_3$, 298 K): 153.42, 138.56, 137.21, 105.66, 73.63, 69.32, 69.26, 46.94, 32.16, 32.14, 29.97, 29.95, 29.92, 29.87, 29.86, 29.67, 29.64, 29.58, 26.32, 22.91, 14.33; MALDI-TOF exact mass calculated for $C_{43}H_{79}O_3$ $[M-NH_2]^+$: 643.6, found: 644.01.

Synthesis of **PBI**

A mixture of PTCDA (0.14 mmol, 1 equiv.), tris-dodecyloxybenzylamine (0.28 mmol, 2.05 equiv.), zinc acetate (0.14 mmol, 1 equiv) and imidazole (1 g) were taken in microwave vessel, flushed with nitrogen and put in microwave reactor. The mixture was heated to 165 ^{o}C for 30 minutes at 35 W. After cooling, reaction mixture was poured in 2N HCl (10 mL) and extracted with chloroform. Organic mixture was washed with water and saturated sodium chloride solution. The crude compound was purified by neutral alumina column chromatography using 50% chloroform-hexane system further purification done by recrystallization from chloroform-methanol system.

R_f = 0.4 (20% EtOAc-hexane); Red waxy solid, yield: 92%; IR (KBr pellet) ν_{max} in cm^{-1}: 2952, 2924, 2854, 1697, 1665, 1595, 1580, 1502, 1467, 1439, 1404, 1371, 1332, 1240, 1171, 1114, 858, 809, 753, 719; ^{1}H NMR (600 MHz, $CDCl_3$, 298 K): 8.63 (d, J = 6 Hz, 4H, H_{Ar}), 8.50 (d, J = 12 Hz, 4H, H_{Ar}), 6.84 (s, 4H, H_{Ar}), 5.29 (s, 4H, $PhCH_2$), 3.99 (t, 8H, 4 × $-OCH_2$), 3.89 (t, 4H, 2 × $-OCH_2$), 1.80-1.24 (m, 116H, 58 × $-CH_2$), 0.86 (t, 18H, 6 × $-CH_3$); ^{13}C NMR (150 MHz, $CDCl_3$, 298 K): δ 163.39, 153.22, 138.06, 134.60, 132.27, 131.64, 129.29, 126.32, 123.37, 123.14, 108.48, 73.63, 69.39, 44.12, 32.15, 30.55, 29.94, 29.90, 29.83, 29.71, 29.68, 29.60, 26.37, 26.34, 22.91, 14.34, 14.32; MALDI-TOF exact mass calculated for $C_{110}H_{166}N_2NaO_{10}$ $[MNa]^+$: 1698.24, found: 1698.80.

Synthesis of **PBI-N**

A mixture of compound **5** (0.14 mmol, 1 equiv.), tris-dodecyloxybenzylamine (0.28 mmol, 2.05 equiv.), zinc acetate (0.14 mmol, 1 equiv) and imidazole (1 g) were taken in microwave vessel, flushed with nitrogen and put in microwave reactor. The mixture was heated to 165 ^{o}C for 30 minutes at 35 W. After cooling, reaction mixture was poured in 2N HCl (10 mL) and extracted with chloroform. Organic mixture was washed with water and saturated sodium chloride solution. The crude compound was purified by neutral alumina column chromatography using 50% chloroform-hexane system further purification done by recrystallization from chloroform-methanol system.

R_f = 0.4 (20% EtOAc-hexane); Red solid, yield: 80%; IR (KBr pellet) ν_{max} in cm^{-1}: 2955, 2921, 2852, 1692, 1655, 1601, 1560, 1505, 1467, 1440, 1380, 1365, 1331, 1303, 1236, 805; ^{1}H NMR (600 MHz, $CDCl_3$, 298 K): 9.0 (s, 2H, H_{Ar}), 8.92 (d, J = 12 Hz, 2H, H_{Ar}), 8.86 (d, 2H, H_{Ar}), 6.89 (s, 4H, H_{Ar}), 5.42 (s, 4H, $PhCH_2$), 4.93 (d, J = 6 Hz, 2H, $N-CH_2$), 4.0 (t, 8H, 4 × $-OCH_2$), 3.89 (t, 4H, 2 × $-OCH_2$), 1.81-1.22 (m, 116H, 58 × $-CH_2$), 0.86 (t, 18H, 6 × $-CH_3$); ^{13}C NMR (150 MHz, $CDCl_3$, 298 K): δ 165.12, 163.91, 153.24, 137.96, 134.30, 132.80, 132.64, 127.87, 124.37, 123.82, 122.26, 121.68, 121.60, 119.47, 118.82, 108.35, 73.61, 69.37, 44.43, 41.77, 32.13, 30.54, 29.95, 29.93, 29.92, 29.88, 29.87, 29.83, 29.70, 29.58, 29.57, 26.38, 26.34, 22.89, 16.96, 14.32, 14.31; MALDI-TOF exact mass calculated for $C_{112}H_{169}N_3NaO_{10}$ $[MNa]^+$: 1739.27, found: 1739.80

Procedure for synthesis of **PBI-S**

A mixture of compound **7** (0.14 mmol, 1 equiv), tris-dodecyloxybenzylamine (0.28 mmol, 2.05 equiv), zinc acetate (0.14 mmol, 1 equiv) and imidazole (1 g) were taken in microwave vessel, flushed with nitrogen and put in microwave reactor. The mixture was heated to 165 ^{o}C for 30 minutes at 35 W. After cooling, reaction mixture was poured in 2N HCl (10 mL) and extracted with chloroform. Organic mixture was washed with water and saturated sodium chloride solution. The crude compound was purified by neutral alumina column chromatography using 50% chloroform-hexane system further purification done by recrystallization from chloroform-methanol system.

R_f = 0.4 (20% EtOAc-hexane); Orange solid, yield: 85%; IR (KBr pellet) ν_{max} in cm^{-1}: 2956, 2920, 2552, 1694, 1658, 1596, 1561, 1468, 1430, 1335, 1313, 1238, 1170, 1120, 1011, 809, 748, 720; ^1H NMR (600 MHz, $CDCl_3$, 298 K): 9.22 (s, 2H, H_{Ar}), 8.83 (d, J = 12 Hz, 2H, H_{Ar}), 8.79 (d, J = 6 Hz, 2H, H_{Ar}), 6.89 (s, 4H, H_{Ar}), 5.39 (s, 4H, $PhCH_2$), 4.01 (t, 8H, 4 × -OCH_2), 3.89 (t, 4H, 2 × -OCH_2), 1.80-1.22 (m, 118H, 59 × -CH_2), 0.85 (t, 18H, 6 × -CH_3); ^{13}C NMR (150 MHz, $CDCl_3$, 298 K): δ 163.74, 163.31, 153.27, 138.08, 132.81, 132.38, 130.95, 129.64, 127.42, 125.65, 123.43, 122.66, 122.56, 122.25, 108.50, 73.63, 69.39, 44.38, 32.14, 30.55, 29.93, 29.90, 29.88, 29.83, 29.72, 29.58, 26.39, 26.34, 22.90, 22.89, 14.33, 14.31; MALDI-TOF exact mass calculated for $C_{110}H_{164}N_2O_{10}S$ $[M]^-$: 1705.2, found: 1705.7.

Procedure for synthesis of **PBI-Se**

A mixture of compound **9** (0.14 mmol, 1 equiv), tris-dodecyloxybenzylamine (0.28 mmol, 2.05 equiv), zinc acetate (0.14 mmol, 1 equiv) and imidazole (1 g) were taken in microwave vessel, flushed with nitrogen and put in microwave reactor. The mixture was heated to 165 °C for 30 minutes at 35 W. After cooling, reaction mixture was poured in 2N HCl (10 mL) and extracted with chloroform. Organic mixture was washed with water and saturated sodium chloride solution. The crude compound was purified by neutral alumina column chromatography using 50% chloroform-hexane system further purification done by recrystallization from chloroform-methanol system.

R_f = 0.4 (20% EtOAc-hexane); Orange solid, yield: 84%; IR (KBr pellet) ν_{max} in cm^{-1}: 2955, 2920, 2852, 1693, 1655, 1593, 1558, 1506, 1468, 1427, 1371, 1334, 1312, 1237, 1172, 1120, 1009, 809, 749; ^1H NMR (600 MHz, $CDCl_3$, 298 K): 8.98 (s, 2H, H_{Ar}), 8.58 (d, J = 6 Hz, 2H, H_{Ar}), 8.37 (bs, 2H, H_{Ar}), 6.91 (s, 4H, H_{Ar}), 5.36 (s, 4H, $PhCH_2$), 4.04 (t, 8H, 4 × -OCH_2), 3.9 (t, 4H, 2 × -OCH_2), 1.81-1.21 (m, 118H, 59 × -CH_2), 0.85 (t, 18H, 6 × -CH_3); ^{13}C NMR (150 MHz, $CDCl_3$, 298 K): δ 163.69, 163.36, 153.28, 140.65, 138.09, 133.88, 133.04, 132.37, 129.89, 129.58, 125.96, 123.93, 122.96, 122.32, 121.86, 108.51, 73.63, 69.40, 44.34, 32.14, 30.56, 29.94, 29.89, 29.84, 29.72, 29.59, 26.40, 26.35, 22.90, 14.33, 14.31; MALDI-TOF exact mass calculated for $C_{110}H_{64}N_2O_{10}Se$ $[M]^-$: 1753.1, found: 1753.7.

4.5. References

1. a) L. Schmidt-Mende, A. Fechtenkötter, K. Müllen, E. Moons, R. H. Friend and J. D. MacKenzie, *Science*, 2001, **293**, 1119-1122; b) B. A. Gregg and R. A. Cormier, *J. Am. Chem. Soc.*, 2001, **123**, 7959-7960; c) A. J. Breeze, A. Salomon, D. S. Ginley, B. A. Gregg, H. Tillmann and H. H. Horhold, *Appl. Phys. Lett.*, 2002, **81**, 3085-3087; d) B. A. Gregg, *J. Phys. Chem.*, 1996, **100**, 852-859; d) A. D. Hendsbee, J.-P. Sun, W. K. Law, H. Yan, I. G. Hill, D. M. Spasyuk, and G. C. Welch, *Chem. Mater.*, 2016, **28**, 7098-7109.
2. a) H. E. Katz, Z. Bao and S. L. Gilat, *Acc. Chem. Res.*, 2001, **34**, 359-369; b) F. Würthner, *Angew. Chem., Int. Ed.*, 2001, **40**, 1037-1039; c) P. Jonkheijm, N. Stutzmann, Z. Chen, D. M. de Leeuw, E. W. Meijer, A. P. H. J. Schenning and F. Würthner, *J. Am. Chem. Soc.*, 2006, **128**, 9535–9540.
3. a) M. A. Angadi, D. Gosztola and M. R. Wasielewski, *Mater. Sci. Eng. B*, 1999, **63**, 191-194; b) A. Kraft, A. C. Grimsdale and A. B. Holmes, *Angew. Chem., Int. Ed.*, 1998, **37**, 402-428; c) P. Ranke, I. Bleyl, J. Simmerer, D. Haarer, A. Bacher and H. W. Schmidt, *Appl. Phys. Lett.*, 1997, **71**, 1332-1334; d) A. Kraft, A. C. Grimsdale and A. B. Holmes, *Angew. Chem., Int. Ed.*, 1998, **37**, 402-428; e) S. Alibert-Fouet, S. Dardel, H. Bock, M. Oukachmih, S. Archambeau, I. Seguy, P. Jolinat and P. Destruel, *ChemPhysChem*, 2003, **4**, 983-985; f) S.-C. Lo and P. L. Burn, *Chem. Rev.*, 2007, **107**, 1097-1116; g) E. Kozma, W. Mro´z, F. V.-Monteleone, F. Galeotti, A. A´-Eckstein, M. Catellani and C. Botta, *RSC Adv.*, 2016, **6**, 61175-61179; h) J. Vollbrecht, S. Blazy, P. Dierks, S. Peurifoy, H. Bock, and H. Kitzerow, *ChemPhysChem*, 2017, **18**, 2024-2032.
4. a) T. E. Wood and A. Thompson, *Chem. Rev.*, 2007, **107**, 1831-1861; b) R. S. Loewe, K. Tomizaki, W. J. Youngblood, Z. Bo and J. S. Lindsey, *J. Mater. Chem.*, 2002, **12**, 3438-3451; c) K. Tomizaki, R. S. Loewe, C. Kirmaier, J. K. Schwartz, J. L. Retsek, D. F. Bocian, D. Holten and J. S. Lindsey, *J. Org. Chem.*, 2002, **67**, 6519-6534.
5. F. Würthner, C. R. Saha-Möller, B. Fimmel, S. Ogi, P. Leowanawat and D. Schmidt, *Chem. Rev.*, 2016, **116**, 962-1052.
6. F. Würthner, *Chem. Commun.*, 2004, 1564-1579.
7. a) V. Percec, M. Peterca, T. Tadjiev, X. Zeng, G. Ungar, P. Leowanawat, E. Aqad, M. R. Imam, B. M. Rosen, U. Akbey, R. Graf, S. Sekharan, D. Sebastiani, H. W. Spiess, P. A. Heiney, and S. D. Hudson, *J. Am. Chem. Soc.*, 2011, **133**, 12197-12219; b)V. Percec, S. D. Hudson, M. Peterca, P. Leowanawat, E. Aqad, R. Graf, H. W. Spiess, X. Zeng, G. Ungar, and P. A. Heiney, *J. Am. Chem. Soc.*, 2011, **133**, 18479-18494; c) V. Percec, H.-J. Sun, P. Leowanawat, M. Peterca, R. Graf, H. W. Spiess, X. Zeng, G. Ungar, and P. A. Heiney, *J. Am. Chem. Soc.*, 2013, **135**, 4129-4148; d) B. E. Partridge, P. Leowanawat, E. Aqad, M. R. Imam, H.-J. Sun, M. Peterca, P. A. Heiney, R. Graf, H. W. Spiess, X. Zeng, G. Ungar, and V. Percec, *J. Am. Chem. Soc.*, 2015, **137**, 5210-5224; e) D. Sahoo, M. Peterca, E. Aqad, B. E. Partridge, P. A. Heiney, R. Graf, H. W. Spiess, X. Zeng, and V. Percec, *J. Am. Chem. Soc.*, 2016, **138**, 14798-14807; f) C. Roche, H.-J. Sun, P. Leowanawat, F. Araoka, B. E. Partridge, M. Peterca, D. A. Wilson, M. E. Prendergast, P. A. Heiney, R. Graf, H. W. Spiess, X. Zeng, G. Ungar and V. Percec, *Nature Chemistry*, 2016, **8**, 80-89; g) D. Sahoo, M. Peterca, E. Aqad, B. E. Partridge, P. A. Heiney, R. Graf, H. W. Spiess, X. Zeng, and V. Percec, *ACS Nano*, 2017, **11**, 983-991; h) M.-S. Ho, B. E. Partridge, H.-J. Sun, D. Sahoo, P. Leowanawat, M. Peterca, R. Graf, H. W.

Spiess, X. Zeng, G. Ungar, P. A. Heiney, C.-S. Hsu and V. Percec, *ACS Comb. Sci.*, 2016, **18**, 723-739.

8. a) R. J. Bushby and O. R. Lozman, *Curr. Opin. Colloid Interface Sci.*, 2002, **7**, 343-354; b) S. Laschat, A. Baro, N. Steinke, F. Giesselmann, C. Hägele, G. Scalia, R. Judele, E. Kapatsina, S. Sauer, A. Schreivogel and M. Tosoni, *Angew. Chem., Int. Ed.*, 2007, **46**, 4832-4887; c) S. Kumar, *Isr. J. Chem.*, 2012, **52**, 820-829; d) T. Wöhrle, I. Wurzbach, J. Kirres, A. Kostidou, N. Kapernaum, J. Litterscheidt, J. C. Haenle, P. Staffeld, A. Baro, F. Giesselmann and S. Laschat, *Chem. Rev.*, 2016, **116**, 1139-1241.

9. B. M. Rosen, C. J. Wilson, D. A. Wilson, M. Peterca, M. R. Imam, and V. Percec, *Chem. Rev.* 2009, **109**, 6275-6540.

10. a) J. Dhar, N. Venkatramaiah, A. Anitha and S. Patil, *J. Mater. Chem. C*, 2014, **2**, 3457-3466; b) Y. Sun, L. Tan, S. Jiang, H. Qian, Z. Wang, D. Yan, C. Di, Y. Wang, W. Wu, G. Yu, S. Yan, C. Wang, W. Hu, Y. Liu, and D. Zhu, *J. Am. Chem. Soc*.**,** 2007, **129**, 1882-1883; c) L. Tan, W. Jiang, L. Jiang, S. Jiang, Z. Wang, S. Yan, and W. Hu, *Applied Physics Letters*, 2009, **94**, 153306 (1-3); d) Y. Zagranyarski, L. Chen, D. Jänsch, T. Gessner, C. Li and K. Müllen, *Org. Lett.*, 2014, **16**, 2814-2817; e) W. Jiang, Y. Zhou, H. Geng, S. Jiang, S. Yan, W. Hu, Z. Wang, Z. Shuai, and J.Pei, *J. Am. Chem. Soc.*, 2011, **133**, 1-3; f) D. Adam, P. Schuhmacher, J. Simmerer, L. Hayssling, K. Siemensmeyer, K. H. Etzbach, H. Ringsdorf and D. Haarer, *Nature*, 1994, **371**, 141-143; g) H. Iino, T. Usui and J. Hanna, *Nat. Commun.*, 2015, **6**, 6828; h) B. Kohne, K. Praefke, T. Derz, W. Frischmuth and C. Gansau, *Chem. Zeit.*, 1984, **108**, 408-410; i) A. Patra, Y. H. Wijsboom, S. S. Zade, M. Li, Y. Sheynin, G. Leitus and M. Bendikov, *J. Am. Chem. Soc.*, 2008, **130**, 6734; j) D. J. Schipper, L. C. H. Moh, P. Müller and T. M. Swager, *Angew. Chem., Int. Ed.*, 2014, 53, 5847; k) A. Bedi, S. Debnath and S. S. Zade, *Chem. Comm.*, 2014, **50**, 13454-13456.

11. a) A. S. Achalkumar, U. S. Hiremath, D. S. Shankar Rao, S. Krishna Prasad and C. V. Yelamaggad, *J. Org. Chem.*, 2013, **78**, 527-544; b) C. F. Van Nostrum, A. W. Bosman, G. H. Gelinck, P. G. Schouten, J. M. Warman, A. P. M. Kentgens, M. A. C. Devillers, A. Meijerink, S. J. Picken, U. Sohling, A.-J. Schouten and R. J. M. Nolte, *Chem. Eur. J.*, 1995, **1**, 171-182; c) J. Barbera, R. Gimenez and J. L. Serrano, *Chem. Mater.*, 2000, **12**, 481-489; d) J. L. Serrano and T. Sierra, *Chem. Eur. J.*, 2000, **6**, 759-766; e) S. Ito, M. Ando, A. Nomura, N. Morita, C. Kabuto, H. Mukai, K. Ohta, J. Kawakami, A. Yoshizawa and A. Tajiri, *J. Org. Chem.*, 2005, **70**, 3939-3949; f) A. Hayer, V. de Halleux, A. Kohler, A. El-Garoughy, E. W. Meijer, J. Barbera, J. Tant, J. Levin, M. Lehmann, J. Gierschner, J. Cornil and Y. H. Geerts, *J. Phys. Chem. B*, 2006, **110**, 7653-7659.

12. S. Ito, M. Ando, A. Nomura, N. Morita, C. Kabuto, H. Mukai, K. Ohta, J. Kawakami, A. Yoshizawa and A. Tajiri, *J. Org. Chem.*, 2005, **70**, 3939-3949.

13. a) M. J. Frisch, G. W. Trucks, H. B. Schlegel, G. E. Scuseria, M. A. Robb, J. R. Cheeseman, G. Scalmani, V. Barone, G. A. Petersson, H. Nakatsuji, X. Li, M. Caricato, A. V. Marenich, J. Bloino, B. G. Janesko, R. Gomperts, B. Mennucci, H. P. Hratchian, J. V. Ortiz, A. F. Izmaylov, J. L. Sonnenberg, D. Williams-Young, F. Ding, F. Lipparini, F. Egidi, J. Goings, B. Peng, A. Petrone, T. Henderson, D. Ranasinghe, V. G. Zakrzewski, J. Gao, N. Rega, G. Zheng, W. Liang, M. Hada, M. Ehara, K. Toyota, R. Fukuda, J. Hasegawa, M. Ishida, T. Nakajima, Y. Honda, O. Kitao, H. Nakai, T. Vreven, K. Throssell, J. A. Montgomery, Jr., J. E. Peralta, F. Ogliaro, M. J. Bearpark, J. J. Heyd, E. N. Brothers, K. N. Kudin, V. N. Staroverov, T. A. Keith, R. Kobayashi, J. Normand, K. Raghavachari, A. P. Rendell, J. C.

Burant, S. S. Iyengar, J. Tomasi, M. Cossi, J. M. Millam, M. Klene, C. Adamo, R. Cammi, J. W. Ochterski, R. L. Martin, K. Morokuma, O. Farkas, J. B. Foresman, and D. J. Fox, *Gaussian*, Inc., Wallingford CT, 2016; b) C. Lee, W. Yang and R. G. Parr, *Phys. Rev. B*, 1988, **37**, 785-789; c) A. D. Becke, *J. Chem. Phys.*, 1993, **98**, 1372-1377.

14. H. Langhals, S. Demmig and H. Huber, *Spectrochim. Acta A*, 1988, **44A**, 1189-1193.

Chapter 5a

Microwave Assisted-Method for the Synthesis of Perylene Ester Imides as a Gateway Toward Unsymmetrical Perylene Bisimides

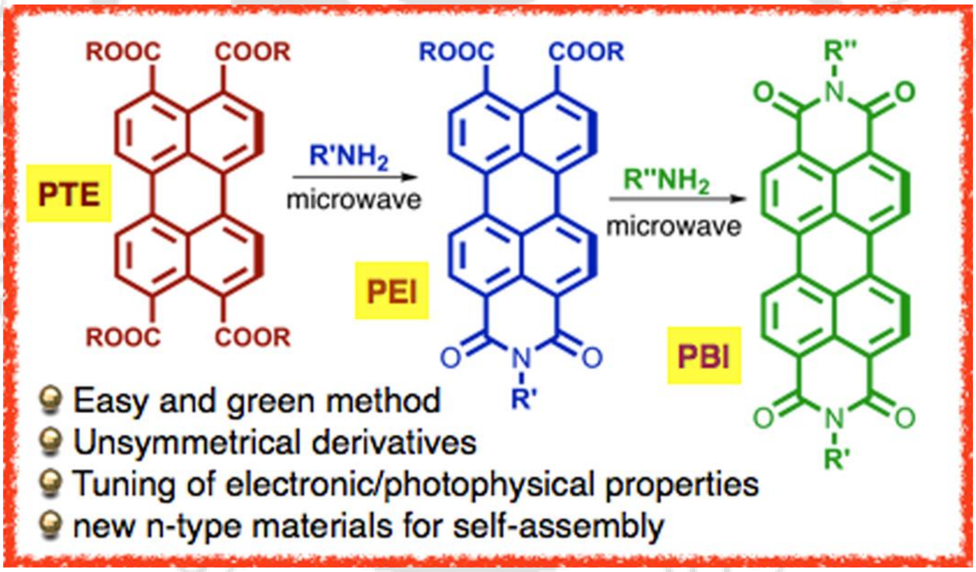

Results have been published in;

- *J. Org. Chem.*, 2018, **83**, 6290-6300

5.1. Introduction

Perylene bisimide (PBI) based molecules are known to exhibit interesting properties and found applications as photo stable dyes, highly luminescent materials, as a component of photoreceptors of photocopiers and laser printers. They are also utilized as electron acceptors in organic solar cells (OSCs) or as active components in organic field effect transistors (OFETs), or as building block materials for liquid crystalline and organogel self-assembly.[1] More recently, suitably functionalized PBIs have been utilized for the functionalization of gold nanorods that exhibit unique self-assembly and photophysical behavior.[1f-i] Further, with the availability of several positions that can be substituted, the photophysical and electronic properties can be modified. The *bay*-substitution of the PBIs had shown to shift the emission toward the red region, with an increase in the Stokes shift and fluorescence lifetime.[2a] The increased stability of such *bay*-substituted PBIs make them potential materials for lasing applications.[2b] Tetraesters of perylene tetracarboxylic acids (PTEs), which are structurally related to PBIs were also utilized as materials in the area of liquid crystals,[3] fluorescent dyes,[4] electron acceptors in light harvesting antennae,[5] and organic light emitting diodes (OLEDs).[6] Similar to PBIs, PTEs have a significant electron-accepting ability due to the four carboxylate groups. They are also capable of forming aggregates with strong π-π overlap in both solutions[7] and the solid state.[8] Recently, perylene tetracarboxylic diester monoimides (PEIs), are attracting an increasing interest due to their intermediate electron deficient nature between PTEs and PBIs as well as a higher solubility.[9] As the name suggests, here an imide and two ester groups are connected to the same perylene core. Nonetheless, in comparison to PBIs, the applications of PTEs and PEIs are relatively limited. Most of the reported PTEs are the symmetrically substituted ones, whereas PEIs that are explored are only limited to simple alkyl derivatives. In comparison, the applications of PBIs have seen a steady rise due to their tunability to alter the properties by unsymmetric substitution with various amines. However, the balancing of the electronic levels of organic semiconductors with respect to electrodes is vital for their application in organic electronic devices. The synthesis of PEIs, which are inherently unsymmetric is a bit challenging. An overview of the research done over the past years is presented in Scheme 5.1. A common approach to obtain alkyl-substituted PEI starts with diimidification of perylene tetracarboxylic acid bisanhydride (PTCBA) with an alkylamine, which is followed by its monohydrolysis under mild conditions.[10,11] Recently, a few reports on obtaining PEIs are described. Yang *et al.* recently reported perylene imido-diesters with

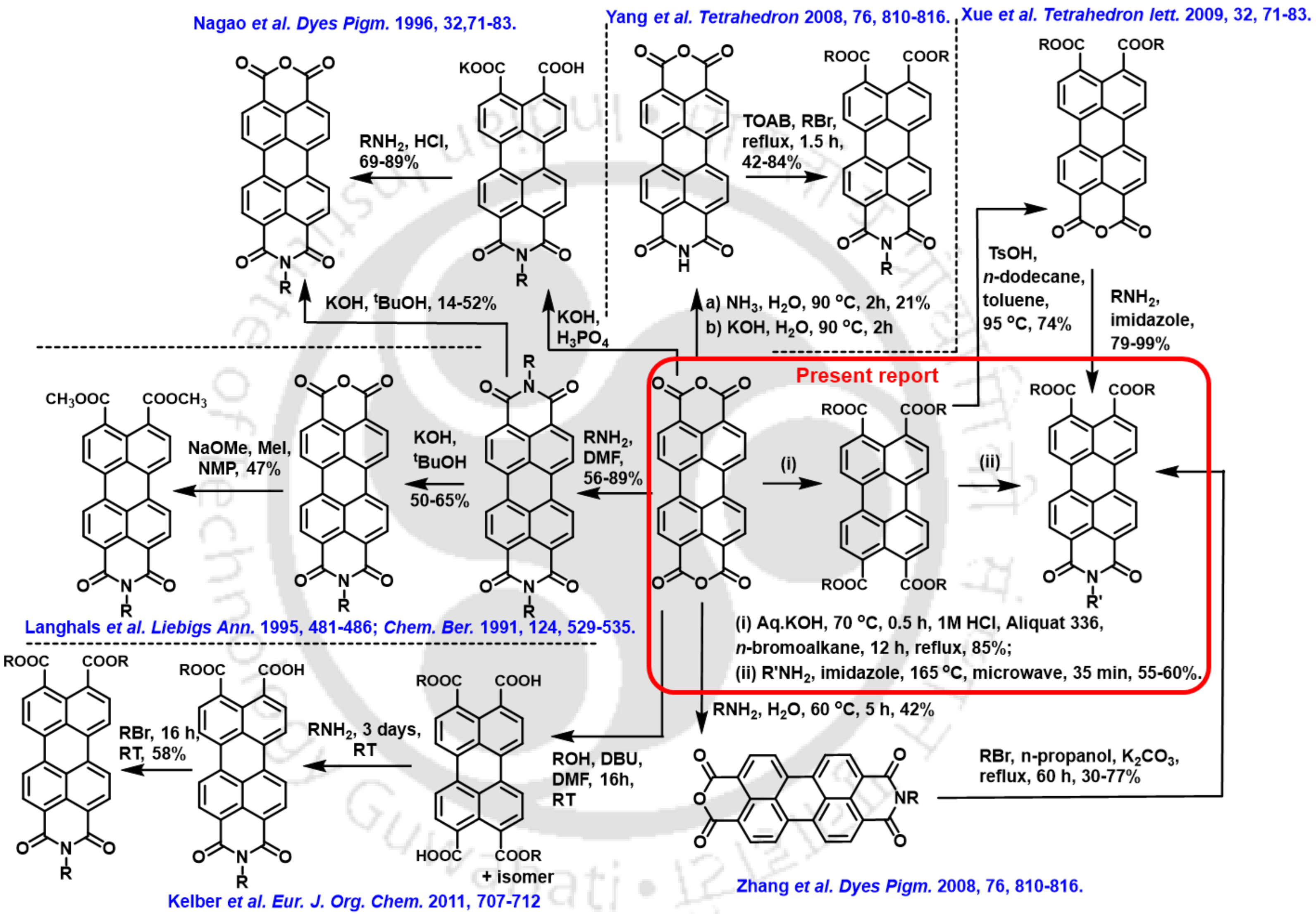

Scheme 5.1. Various routes to prepare PEIs/the key intermediates to prepare them over the years.

three *n*-alkyl substituents of the same length.[9a] Their synthetic approach provided unsubstituted perylene tetracarboxylic monoimido-monoanydride in low yield, which after isolation was subjected to phase-transfer trialkylation of its dipotassium salt. This required an excess amount of the alkyl bromide. In spite of providing access to PEIs, its drawback is the inability to obtain unsymmetrically substituted PEIs. Zhang *et al* reported the preparation of PEIs by the reaction of alkyl bromides with perylene tetracarboxylic monoanhydride monoimide.[9b] Here, the perylene tetracarboxylic bisanhydride (PTCBA) was treated with *n*-alkylamine, which results in the formation of two products, *i.e.*, the perylene tetracarboxylic monoanhydride monoimide and the other one is corresponding PBI. After the isolation of monoanhydride monoimide, it is treated with the required alkyl bromide to obtain the PEI.[9b] The yield was varying from 30-77%. Xue *et al.* prepared perylene tetracarboxylic monoanhydride diester from corresponding PTE. This, on treatment with *n*-alkyl amine yielded the PEI.[9c] Although the yields are good, it involves three steps. Earlier, PEIs were also obtained by the controlled hydrolysis of PTCBA with a base to obtain monoanhydride, and its treatment with alkylamine to get alkyl imidoanhydride which can be further converted to the PEI.[10,11] Such alkylimidoanhydrides can then be esterified to get PEI, or may be condensed with another amine to obtain PBI.[12,13] These procedures require the isolation of monoimido monoanhydride (PEA). However, when the monoimido monoanhydride is formed, it possesses an increased solubility in comparison to that of PTCBA. Due to this, its reactivity is increased and often it gives the symmetric PBI. Kelber *et al*. recently approached this problem in a different way.[14] They obtained perylene teracarboxylic diester from PTCBA, after which they added alkyl amine to obtain imido-ester-acid, which on treatment with bromoalkane yielded imido-diester. However, this reaction depends on the initial solubility of the initial starting material in excess alcohol and alkyl bromides, thus it can be used only for small chain alcohols. In addition, corresponding alkyl bromides are also required in addition to long reaction duration. All of these previous work made us investigate the problem of obtaining PEI in a simple, high yielding method. In this chapter, we have presented a high yielding method for the preparation of PEI in two steps, starting from PTCBA. PTCBA is converted to its PTE and later this is treated with the required amine under microwave conditions to yield the requisite PEI (Scheme 5.2). The PEI obtained can be converted to an unsymmetric PBI if required, thus providing an easy access to unsymmetrical PBIs.

5.2. Result and discussion

Initially, we thought of treating PTCBA directly with the requisite amine to get the corresponding imide anhydride, but this suffers from the insolubility of the starting material in most of the solvents and the increased reactivity of the imide anhydride formed due to its higher solubility than PTCBA, which eventually ends up in the formation of symmetrical PBI. Microwave-assisted synthesis has attracted the material and synthetic chemists, as it provides a green alternative to obtain useful products in higher yields under milder reaction conditions along with higher product purities. Microwaves greatly accelerate the rate of the reactions in comparison to conventional heating.[15] There are few reports on the application of microwave-assisted synthesis to obtain symmetrical perylene bisimides.[16] However, utilization of microwave-assisted synthesis to obtain unsymmetrical derivatives is not reported to the best of our knowledge. The time for the reaction was optimized as 35 min to obtain the maximum yield. Compared to earlier methods, which had several low yielding steps with a difficulty in isolation, this method is straightforward and provides a good yield of 50-55%. The remaining amount of PTE is converted to PBI, which is highly insoluble and remains trapped with the neutral alumina used for the column chromatography. Further, we studied the substrate scope of this procedure. PTE **1** was treated with different aliphatic and aromatic amines (Scheme 5.4, Table 5.1) to obtain corresponding PEIs. Further, we wanted to test the scope of this reaction in the preparation of perylene tetracarboxylic diester monoimides from *bay*-annulated perylene tetraesters (**4-6**). *Bay*-annulated perylene tetraesters with heteroatoms like nitrogen, sulfur and selenium have shown an ordered columnar hexagonal (Col$_h$) phase over a wide thermal range along with a good luminescence. The *bay*-substitution and *bay*-extension of perylene derivatives provided an access to modify the photophysical and electrochemical properties of perylene derivatives.[17-19] In previous Chapter 3a, we have seen that the host-guest OLEDs based on *bay*-annulated perylene tetraesters exhibiting room temperature Col$_h$ phase. Thus considering the importance of *bay*-annulated perylene derivatives, we thought of synthesizing the *bay*-annulated PEIs (BAPEIs) by utilizing the corresponding perylene tetraesters (BAPTEs) with four *n*-butyloxy chains. These tetraesters were prepared similarly to the previous Chapter. These BAPTEs were treated with 1-aminooctadecane (**8**) under microwave conditions, which yielded the corresponding BAPEIs in good yields (Scheme 5.2, Table 5.1).

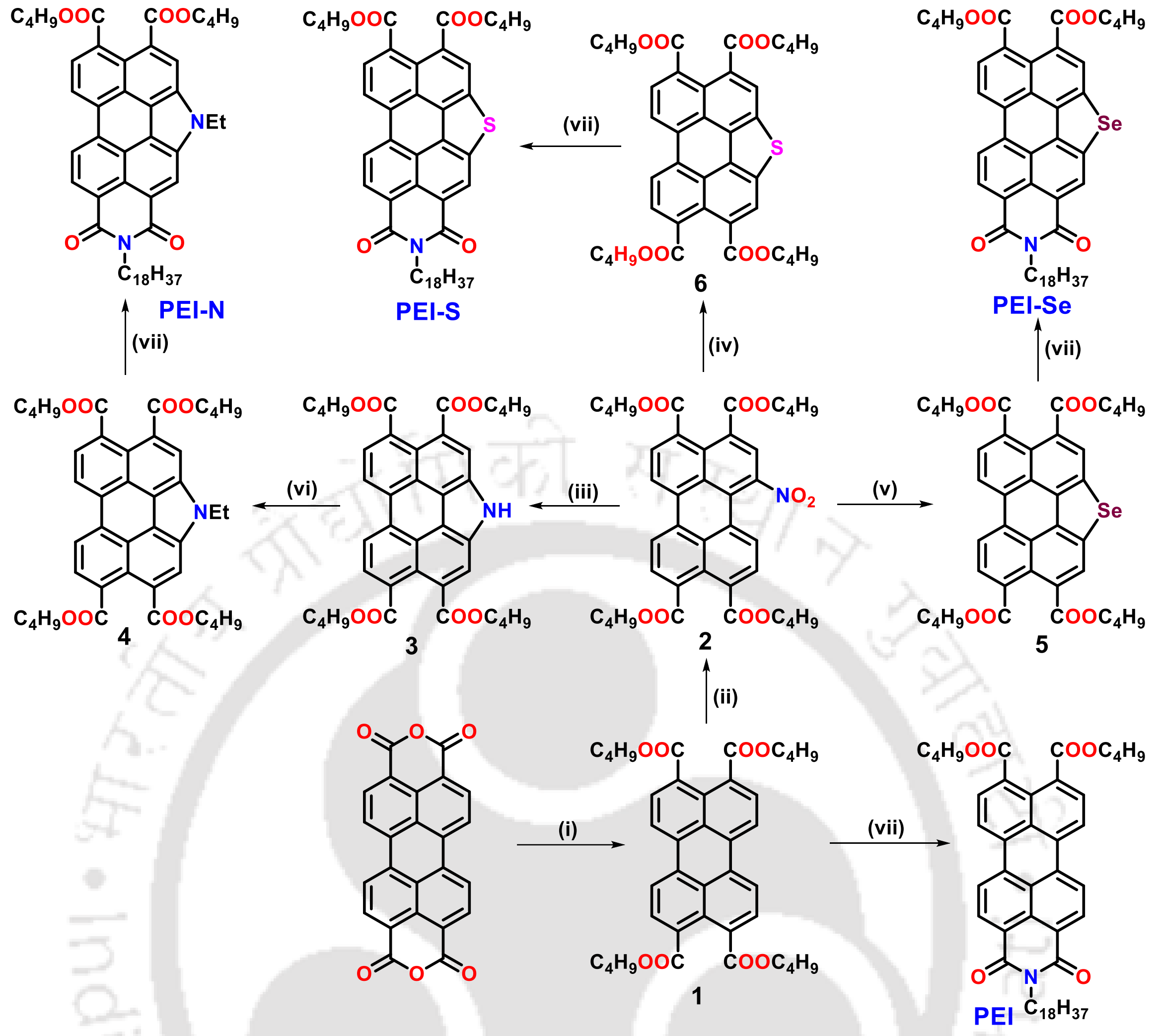

Scheme 5.2. Synthesis of **PEI** and *bay*-annulated **PEIs**; Reagents and conditions: (i) KOH, H_2O, 70 °C, 0.5 h, 1 M HCl, Aliquat 336, KI, 1-bromo-butane, reflux, 12 h (76%); (ii) $NaNO_2$, HNO_3, 0 °C, 1h (90%); (iii) triethyl phosphite, 160 °C, reflux, 4 h, N_2 (60%); (iv) sulfur powder, anhyd. NMP, N_2, 70 °C, 0.5 h, 180 °C, 17 h (55%); (v) selenium powder, anhyd. NMP, N_2, 70 °C, 0.5 h, 180 °C, 17 h (55%); (vi) NaH, 1-iodoethane, dry THF, reflux, 17 h (75%); (vii) 1-aminooctadecane, imidazole, 165 °C, microwave, 35 min. (50-55%).

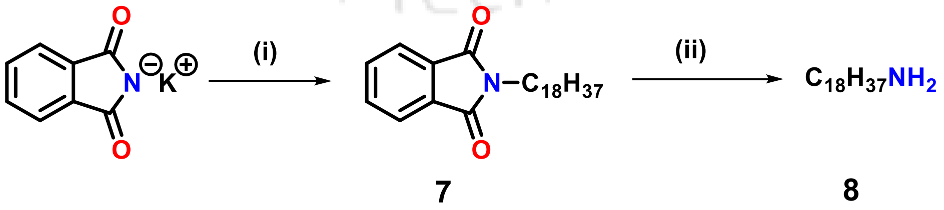

Scheme 5.3. Synthesis of 1-amino-octadecane (**8**); Reagents and Conditions: (i) 1-bromooctadecane, DMF, 90 °C, 18 h (95%); (ii) $NH_2NH_2.H_2O$, methanol, 95 °C, 1 h (95%)

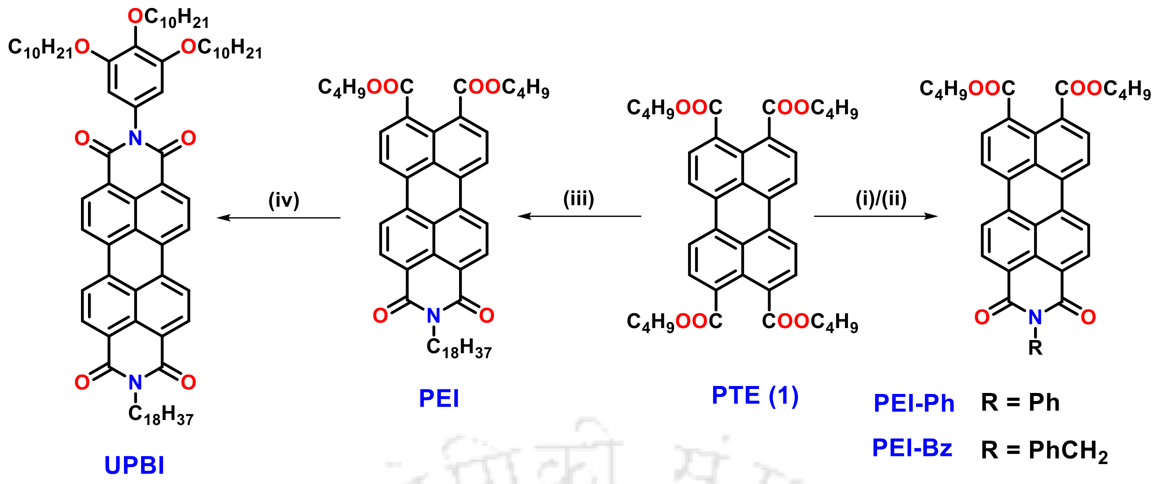

Scheme 5.4. Synthesis of different perylene ester imides **(PEIs)** and an unsymmetrical perylene bisimide (**UPBI**); Reagents and Conditions: (i) aniline, imidazole, 165 ºC, 35 min. (55%); (ii) benzylamine, imidazole, 165 ºC, 35 min. (58%); (iii) 1-aminooctadecane, imidazole, 165 ºC, 35 min. (55%); (iv) 3,4,5-tri-*n*-decyloxy aniline, imidazole, zinc acetate, 165 ºC, 35 min. (75%).

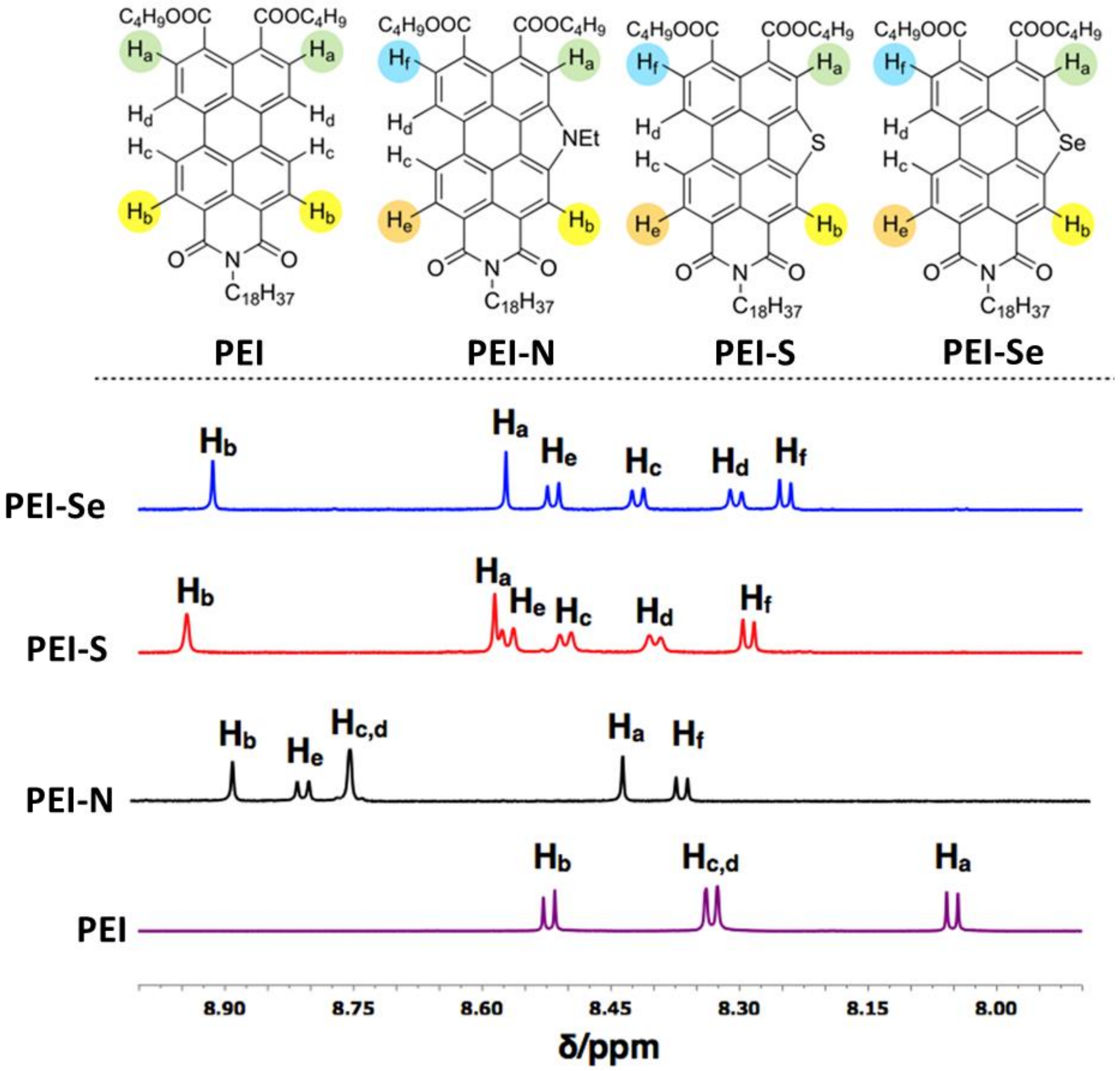

Figure 5.1. Overlay of the expanded region of the ^{1}H NMR spectra of compounds PEI and BAPEIs.

The compound **8** was prepared by Gabriel's phthalimide synthesis (Scheme 5.3).[20] An unsymmetrical PBI (**UPBI**) was also prepared in good yield using the PEI as starting material to show the utility of this method (Scheme 5.4, Table 5.1). The synthesized compounds were completely characterized with the help of ^{1}H, ^{13}C NMR, IR spectroscopy and Elemental analysis/ HRMS/ MALDI-TOF mass spectrometry. The ^{1}H NMR spectra of the BAPEIs were interesting and the effect of the inclusion of the heteroatom in the molecular structure was evident with the change of the chemical shifts of the aromatic protons. The protons near to the imide group appear in the downfield region, while the protons near the esters resonate in the upfield region in the case of PEI. The *bay* protons (H_c and H_d) appear in between the two sets of protons. The presence of the heteroatoms gives rise to a complex pattern by breaking the symmetry. In the case of compound **PEI-N**, H_c and H_d resonate at the same position, while protons in *ortho* -positions split to form doublets. In the case of *S*- and *Se*-annulated BAPEIs, H_c and H_d also appear as doublets in addition to the doublets of H_e and H_f. The aromatic signals obtained for compound **PEI-Se** are similar to that of compound **PEI-S** but they appear upfield (Figure 5.1).

Table 5.1. Substrate scope of the present reaction for the synthesis of various **PEIs** and **UPBI.**

Starting material	**Reactant**	**Yield** (%)
PTE (1)[a]	*n*-Octyldecylamine	**PEI** (55)
PTE (1)[a]	Aniline	**PEI-Ph** (55)
PTE (1)[a]	Benzylamine	**PEI-Bz** (58)
BAPTE (4)[a]	*n*-Octyldecylamine	**PEI-N** (55)
BAPTE (6)[a]	*n*-Octyldecylamine	**PEI-S** (55)
BAPTE (5)[a]	*n*-Octyldecylamine	**PEI-Se** (55)
PEI[b]	3,4,5-tri-*n*-decyloxyaniline	**UPBI** (75)
[a]imidazole, 165 °C, microwave, 35 min.; [b]imidazole, zinc acetate, 165 °C, microwave, 35 min.		

Photophysical properties of these compounds were explored by obtaining their absorption and emission spectra in micromolar chloroform solutions (Table 5.2, Figure 5.2a, b). The absorption spectra of these **PEI** and **BAPEI**s were well-structured and showed the characteristic vibronic bands. There was not much change observed in the case of **PEI** and *N*-annulated derivative **PEI-N** as both of them exhibited an absorption maximum centered at 506 nm. However, the absorption spectra of *S*- and *Se*-annulated derivatives were blue shifted with the absorption maxima centered at 480 and 486 nm respectively. All PEIs exhibited high molar extinction coefficients at their absorption maxima (ε: 11,500-15,500 L.mol^{-1}cm^{-1}). The optical band gap calculated from the absorption onset showed that the optical band gaps of **PEI** and *N*-annulated derivative were almost similar (2.28-2.33 eV), while that of the *S*- and *Se*-annulated derivatives shown an increase (2.42-2.44 eV). Emission spectra of these compounds showed two main bands, with the high intensity band was in the range of 499-543 nm. The Stokes shift was found to be more for PEI (1347 cm^{-1}) and for other PEIs the value was in the range of 774-793 cm^{-1}. Introduction of heteroatoms led to a blue-shifted emission spectra for the *bay*-annulated derivatives. Relative fluorescence quantum yields measured with respect to fluorescein (0.1 M NaOH solution, Q_f = 0.79), showed a higher quantum yield for **PEI**, **PEI-N** and **PEI-S**, but a lower quantum yield for compound **PEI-Se** (Table 5.2). Both the solution and thin films showed visually perceivable emission under the UV light of long wavelength. A weak emission was noticed for *Se*-derivative **PEI-Se**, due to the 'heavy atom effect'. The absorption and emission spectra obtained in thin film state were found to be broad and blue shifted, while the emission spectra have shown a red-shift (Figure 5.2c and d), which confirmed the formation of H-type aggregates,[21a] though it may not be a classic H-aggregate with an exact overlap of the molecules one above the other. In the case of perylene based molecules without any *bay*-substitution, it is quite common to see that such molecules aggregate one above the other, with their major absorption band getting blue shifted indicating the predominant H-type excitonic coupling.[21b] Here, as a consequence of a rotational displacement of neighboring molecules, the optical transition into the lower energy exciton state becomes allowed,[22] as evidenced by the second absorption band at a longer wavelength (Figure 5.2a and c, Table 5.2). The particular arrangement and the concomitant photophysical properties of the aggregates are strongly dependent on the substituents at the *peri*-position.

In literature, for PBIs bearing electronically active rather innocent trialkyl-phenyl substituents, a relatively long-lived excited state with an appreciably high fluorescence quantum yield of 47% has been reported,[21b] which was attributed to the relaxation of the exciton into an excimer.[21c] As these PEIs are unsymmetrically substituted, they are slightly rotated from the exact overlap, to accommodate the steric bulk of ester functional groups. Because of this slight rotation there will not be a perfect overlap as observed in the case of the classical H-aggregates leading to the complete luminescence quenching. This is clearly visible in the overlay of the emission spectra of thin films with that of the solutions. A huge reduction in the emission intensity was observed because of the aggregation caused quenching.

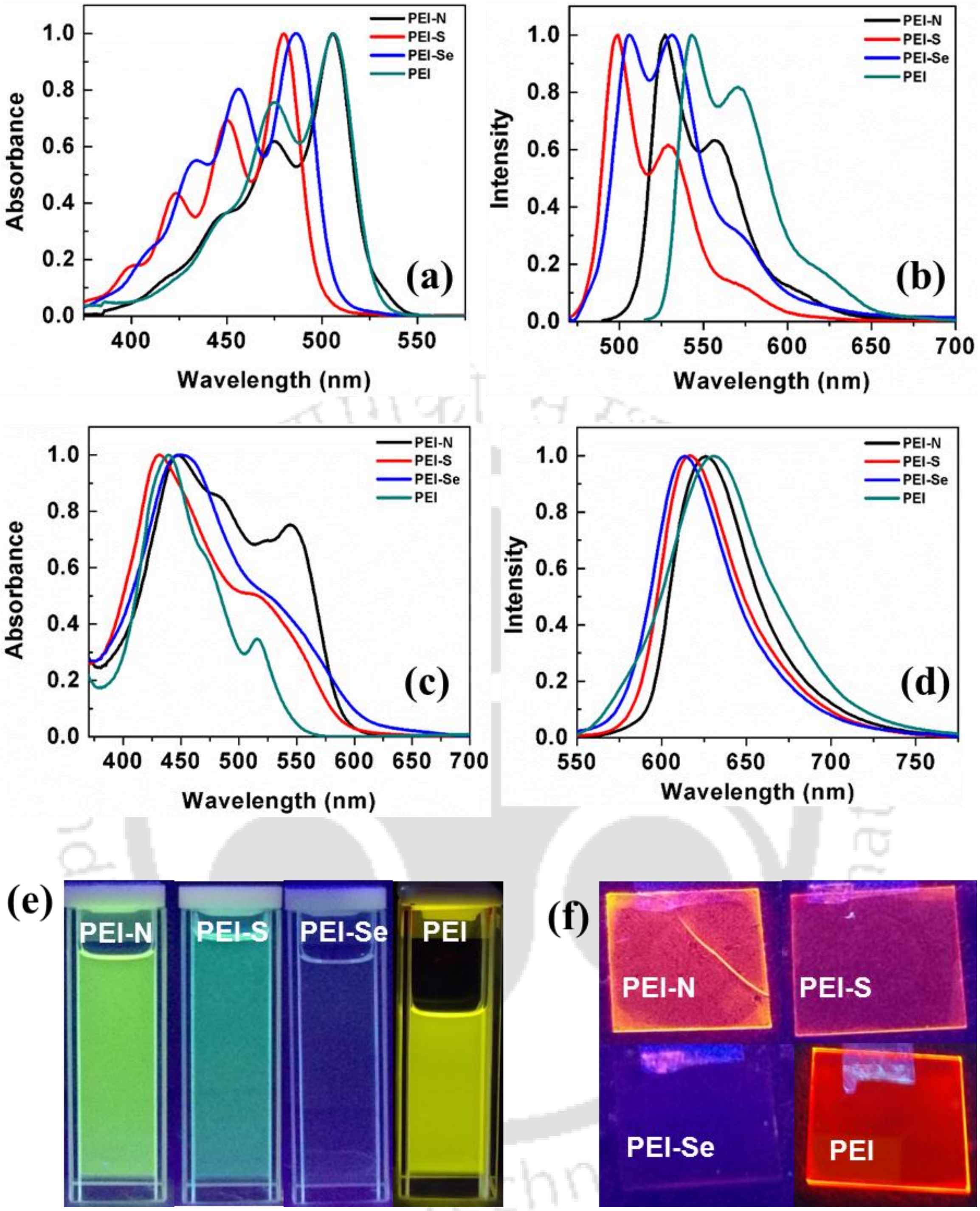

Figure 5.2. (a) Absorption and (b) emission spectra in micromolar chloroform solution of *bay*-annulated **PEIs** and **PEI**; (c) absorption and (d) emission spectra of the spin coated films of *bay*-annulated **PEIs** and **PEI**; (e) Images of the same solutions under the UV light of long wavelength (f) Images of the same thin films under the UV light of long wavelength (λ = 365 nm).

Cyclic voltammetry (CV) studies are carried out to understand the electronic energy levels that decide the energy and electron transfer process and reversibility of a redox process. CV studies were carried out in anhydrous dichloromethane solutions (Table 5.2). PBIs are known to be electron deficient n-type semiconductors and are known to have a high electron affinity.[1] We expected the PEIs to be less electron deficient in comparison to PBIs. All of the PEIs exhibited two quasi-reversible reduction peaks, which are due to the reduction of the neutral molecule to a radical anion in the first step and to a dianion in the second step (Figure 5.3a). The addition of the first electron in the first reduction increases the electron density on the carbonyl of imide. The addition of the second electron in the second reduction is supported by the ability of the core to delocalize this extra electron density to reduce the Coulombic repulsion of similar charges.[23] It was difficult to obtain the oxidation potentials of these electron deficient compounds even with a CV measurement

Table 5.2. Photophysical and electrochemical properties of **PEI** and **BAPEI**s.

Solution[a]						**Thin film**[d]		**Cyclic Voltammetry**[e,f]		
Entry	**Absorption (nm)**	**Emission**[b] **(nm)**	**$\Delta E_{g,opt}$**[c] **(eV)**	**Stokes shift (cm^{-1})**	**ϕ**[g]	**Absorption (nm)**	**Emission**[b] **(nm)**	**E_{1red} (V)**	**E_{HOMO}**[g] **(eV)**	**E_{LUMO}**[h] **(eV)**
PEI	506, 475, 446	543, 571, 622	2.33	1347	0.93	439, 516	631	-0.81	-5.86	-3.53
PEI-N	506, 475, 448, 417	527, 557, 615	2.28	788	0.89	447, 544	626	-0.96	-5.66	-3.38
PEI-S	480, 450, 423, 399	499, 529, 579	2.42	793	0.70	434, 514	616	-0.92	-5.84	-3.42
PEI-Se	486, 456, 434, 408	505, 531, 577	2.44	774	0.06	451, 533	615	-0.92	-5.86	-3.42

[a]micromolar solution in chloroform, [b]excited at 506 for **PEI** and **PEI-N**, 480, 486 nm for **PEI-S** and **PEI-Se** respectively, [c]calculated from the red edge of the longest wavelength in the absorption spectrum [d]prepared from the millimolar solution in chlorobenzene, [e]micromolar solution in dichloromethane, [f]Experimental conditions: Ag/$AgNO_3$ as reference electrode, Glassy carbon working electrode, Platinum wire counter electrode, TBAP (0.1 M) as a supporting electrolyte, room temperature, [g]Estimated from the formula $E_{HOMO} = E_{LUMO} - \Delta E_{g(UV)}$eV ; [h]Estimated from the formula by using $E_{LUMO} = -(4.8 - E_{1/2,\ Fc/Fc^+} + E_{red,\ onset})$ eV; $E_{1/2,\ Fc/Fc^+} = 0.462$ eV, [g]relative quantum yields are calculated with respect to Fluorescein in 0.1M NaOH solution as the standard, $Q_f = 0.79$.

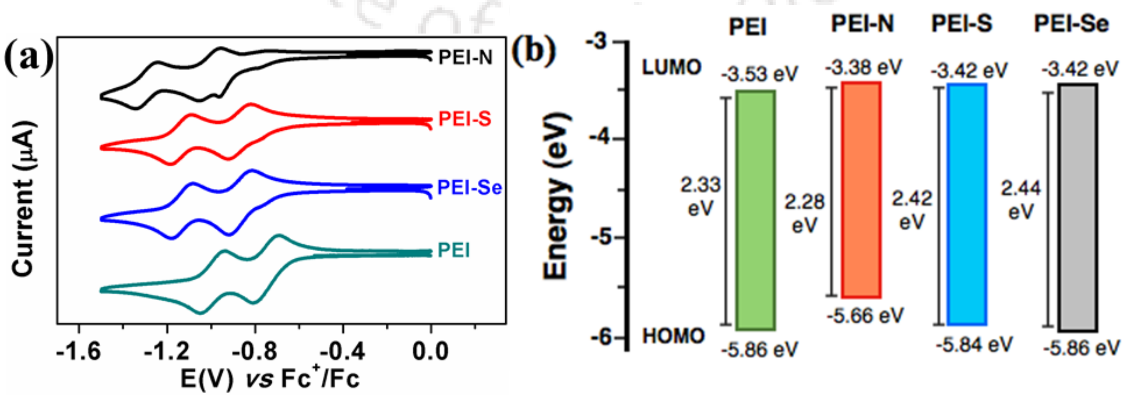

Figure 5.3. (a) Cyclic voltammograms of **PEI** and *bay*-annulated **PEI**s; (b) Energy band level diagram showing HOMO- and LUMO- energy levels of **PEI** and **BAPEI**s.

window up to +1 V *vs* Ag/AgNO$_3$. Thus we have estimated the HOMO levels, by subtracting the LUMO energy values from the optical band gap that was obtained from the absorption onset of the respective compounds in solutions. From the CV studies it was found that the *bay*-annulated PEIs showed increased LUMO levels in comparison to **PEI** (Figure 5.3b). A small increase of 0.15 eV in the LUMO level was noted in the case of **PEI-N**, while **PEI-S** and **PEI-Se** displayed a lowering of LUMO levels by 0.11 eV respectively, with respect to the LUMO of **PEI** (Figure 5.3b). Thus in the case of compound **PEI-N**, an increase in the HOMO level was observed, while that of compound **PEI-S** and **PEI-Se** remained fairly unaltered.

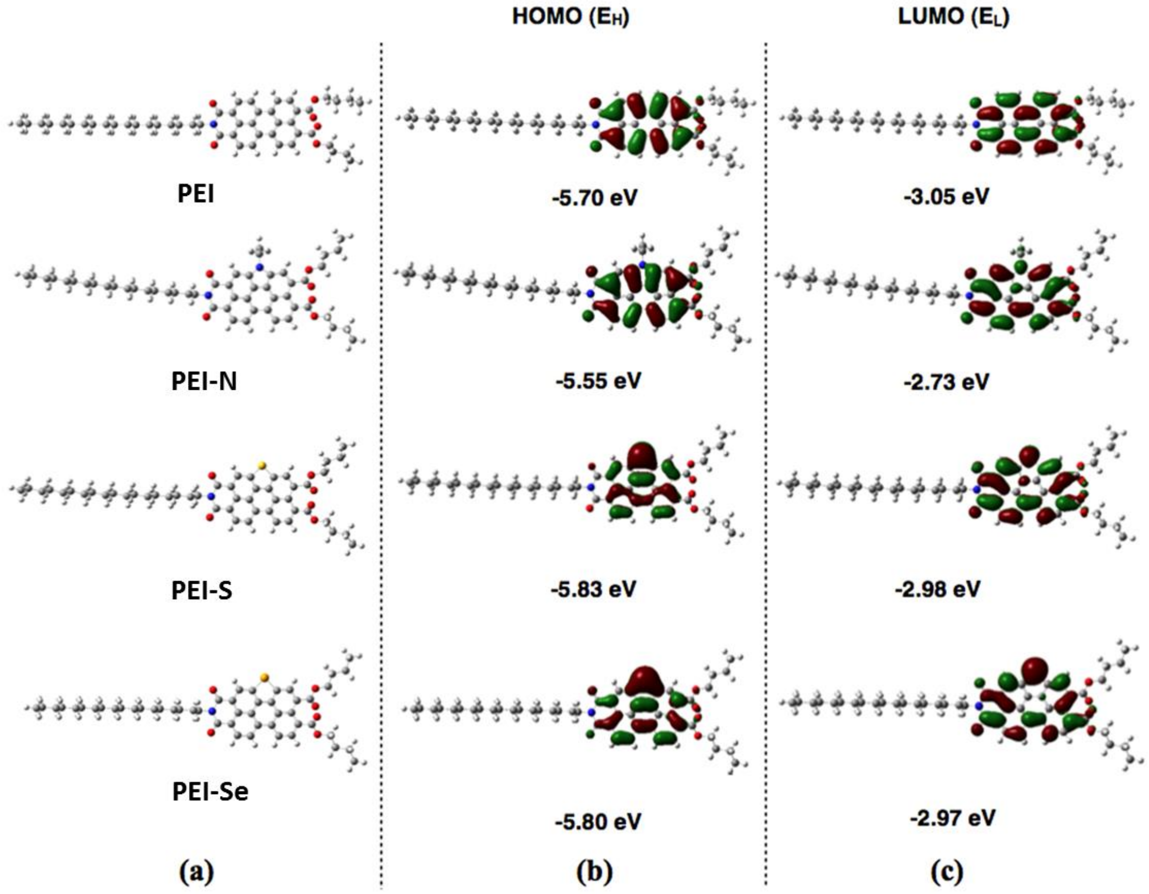

Figure 5.4. (a) Optimized geometry of compounds **PEI** and **BAPEI**s; (b) HOMO and (c) LUMO frontier molecular orbitals of compounds of the same at the B3LYP/6-31G(dp) level. E_H and E_L denote energies of the highest occupied molecular orbital (HOMO) and the lowest unoccupied molecular orbital (LUMO), respectively.

We further probed the energy levels and their separations with the help of DFT calculations.[24] The energy-minimized structures for **PEI, PEI-N, PEI-S** and **PEI-Se** are shown in Figure 5.4a. Images of frontier molecular orbitals (FMOs) and the differences in their energies offer information about the length of conjugation and the separation of energy levels, which helps in comparing the **PEI** with its *bay*-annulated derivatives. In the energy-minimized structures, we can notice that the planarity of the perylene ring remains unchanged after *bay*-annulation. The contours of the HOMO and LUMO of PBIs are shown in Figure 5.4b and c. The HOMO-LUMO energy levels of PEIs are distributed on the entire aromatic ring. Imide groups are known to be closed chromophoric (electronically decoupled) systems. This is due to the presence of nodes of the HOMO and LUMO orbitals on imide nitrogen atoms, while some electron density is found to be distributed on the ester group or oxygen atoms. Thus, the substitution at imide nitrogen does not alter the optical properties significantly, but the *bay*-annulation is supposed to affect the HOMO-LUMO levels. In the case of *bay*-annulated derivatives, HOMO and LUMOs were found to be spreading over heteroatoms (for compounds **PEI-S** and **PEI-Se)**. In the case of compound **PEI-N,** only the LUMO was distributed on the *N* atom, which serves as a node for HOMO. In fact, the HOMO and LUMO levels of *bay*-annulated PEIs have increased in comparison to the simple PEI. The HOMO-LUMO separations for **PEI, PEI-N, PEI-S** and **PEI-Se** were found to be 2.65, 2.82, 2.85 and 2.83 eV respectively.

5.3. Conclusion

In this chapter, we have presented an easy microwave assisted method for the synthesis of unsymmetric PEIs by treating PTEs with requisite amines, in a good yield. This microwave-assisted synthetic method has a wide substrate scope including various PTEs, *bay*-annulated PTEs, aliphatic amines, aromatic amines and benzylamines. Particularly, the application of this method to *bay*-annulated tetraesters, provides *bay*-annulated PEIs, which provide new avenues in organic semiconductors. Photophysical and electrochemical properties of the *bay*-annulated PEIs were studied in comparison with the simple PEI along with the DFT calculations to visualize the electronic energy levels. Moreover, this synthetic method provides an easy access to synthesize unsymmetrical perylene bisimides, which are very important materials from the viewpoint of organic electronics as well as supramolecular self-assembly. Some of the PEIs (PEI-N, PEI-S and PEI-Se) have been utilized for the fabrication of OLEDs, are briefly described in chapter 5b.

5.4. Experimental section

In this section the detailed synthesis procedure and the molecular structural characterization data have been presented for the intermediates and target compounds mentioned in the scheme.

Synthesis of tetrakis(butyl) perylene-3,4,9,10-tetracarboxylate (**1**)

Perylenetetracarboxylic dianhydride (5 mmol, 1 equiv.) was dissolved in 30 mL aqueous KOH (27 mmol, 5.4 equiv.) solution and stirred at 70 °C for 0.5 h. The solution was filtered and pH value of filterate was adjusted to 8-9 using 10% HCl. Then Aliquat 336 (1.8 mmol, 0.4 equiv.) and KI (1 mmol, 0.2 equiv.) were charged into the solution and then stirred vigorously for 10 min. 1-Bromobutane (31 mmol, 6 equiv.) was added to this reaction mixture. After the addition the reaction mixture was refluxed for 12 h until a red oil floats on the top and the rest of the solution becomes clear. Subsequently, chloroform (10 mL) was poured into the mixture and filtered through the celite bed to remove unreacted part and the celite bed was washed with chloroform. This chloroform layer was separated and washed twice with 15% sodium chloride solution, dried over sodium sulfate and concentrated in vacuo to get a viscous concentrate. Methanol was added to precipitate the compound from this concentrate. The solid was precipitated, filtered and dried in vacuum.

R_f = 0.6 (20% EtOAc-hexane); orange solid, yield: 76%; IR (KBr pellet) ν_{max} in cm^{-1}: 2960, 2930, 2872, 1725, 1627, 1590; ^1H NMR (600 MHz, $CDCl_{3,}$ 298 K): 8.04 (d, J = 7.8Hz, 4H, H_{Ar}), 7.90 (d, J = 7.8Hz, 4H, H_{Ar}), 4.36-4.34 (m, 8H, 4 × $-OCH_2$), 1.82-1.78 (m, 8H, 4 × $-OCH_2$-$\underline{CH_2}$), 1.62-1.49 (m, 8H, 4 ×CH_2), 1.02-1.0 (m, 12H, 4 × $-CH_3$) ; ^{13}C NMR (150 MHz, $CDCl_3$, 298 K): 168.8, 132.9, 130.5, 129, 128.8, 121.5, 65.5, 30.9, 19.5, 14; MALDI-TOF: exact mass calculated for $C_{40}H_{44}O_8$ $[M]^+$: 652.3, found: 652.5; HRMS (APCI mode) exact mass calculated for $C_{40}H_{44}O_8$ $[M]^-$: 652.3042, found: 652.3297.

Synthesis of tetrakis(butyl)-1-nitroperylene-3,4,9,10-tetracarboxylate (**2**)

To a solution of **1** (1.4 mmol, 1 equiv.) in dichloromethane (15 mL), added $NaNO_2$ (0.7 mmol, 1 equiv.) at 0 °C and stirred. To this well stirred suspension, 69% HNO_3 (3.42 mmol, 5 equiv., 10% solution in dichloromethane) was added dropwise. This mixture was stirred at 0 °C for 1 h. The reaction mixture was poured into water and extracted with dichloromethane (25 mL). Finally, organic layer was dried over anhyd Na_2SO_4 and concentrated. The crude product was purified by column chromatography on neutral alumina. Elution with 50% dichloromethane-hexane yielded the desired product.

R_f = 0.6 (20% EtOAc-hexane); red viscous liquid, yield: 90%; IR (KBr pellet) ν_{max} in cm^{-1}: 2958, 2928, 2872, 1725, 1660, 1591, 1533, 1356; ^1H NMR (600 MHz, $CDCl_{3,}$ 298 K): 8.34-8.29 (m, 2H, H_{Ar}), 8.24 (s, 1H, H_{Ar}), 8.18 (d, J = 6Hz, 1H, H_{Ar}), 8.10 (d, J = 6Hz, 1H, H_{Ar}), 7.95-7.93 (m, 1H, H_{Ar}), 7.86-7.84 (m, 1H, H_{Ar}), 4.37-4.33 (m, 8H, 4 × $-OCH_2$), 1.81-1.77 (m, 8H, 4 × $-OCH_2$-$\underline{CH_2}$), 1.51-1.46 (m, 8H, 4 ×CH_2), 1.01-0.98 (m, 12H, 4 × $-CH_3$); ^{13}C NMR (150 MHz, $CDCl_3$, 298 K): 168.2, 168, 167.9, 166.8, 146.2, 133.6, 132.3, 132.1, 131.4, 131.3, 130.8, 130.4, 129.9, 129.6, 129.1, 128.5, 128.4, 127.5, 126.6, 125.7, 123.2, 122.7, 66.2, 65.9, 65.8, 65.7, 30.7, 30.7, 29.8, 19.4, 14; MALDI-TOF: exact mass calculated for $C_{40}H_{43}NO_{10}$ $[M]^-$: 697.3, found: 697.8; Elemental analysis calcd. (%) for $C_{40}H_{43}NO_{10}$: C 68.85, H 6.21, N 2.01; found: C 69.19, H 6.26, N 2.11.

Synthesis of tetrakis(butyl) 1H-phenanthrocarbazole-3,4,9,10-tetracarboxylate (**3**)

A mixture of compound **2** (0.6 mmol) and triethyl phosphite (7 mL) were refluxed for 4 h under argon atmosphere. Reaction mixture was cooled to room temperature and methanol was added to this solution to precipitate the compound. This precipitated product was filtered off and washed with water, dried in vacuum. Further purification was done by repeated recrystallization from dichloromethane-methanol system.

R_f = 0.6 (20% EtOAc-hexane); yellow solid, yield: 60%; IR (KBr pellet) ν_{max} in cm^{-1}: 3458, 2959, 2927, 2853, 1722, 1637, 1593; ^1H NMR (600 MHz, $CDCl_3$, 298 K): 9.42 (s, 1H, NH), 8.01 (d, J = 7.8 Hz, 2H, H_{Ar}), 7.94-7.92 (m, 4H, H_{Ar}), 4.54-4.5 (m, 8H, 4 × $-OCH_2$), 1.97-1.92 (m, 8H, 4 × $-OCH_2$-$\underline{CH_2}$), 1.66-1.61 (m, 8H, $-CH_2$), 1.10 (t, J = 7.2Hz, 12H, 4 × $-CH_3$); ^{13}C NMR (150 MHz, $CDCl_3$, 298 K): 169.9, 130.9, 130.1, 128.4, 127.4, 127.1, 122.6, 121.5, 119.2, 117.6, 65.7, 65.6, 31.1, 31.1, 19.6, 19.6, 14.1; MALDI-TOF: exact mass calculated for $C_{40}H_{43}NO_8$ $[M]^+$: 665.3, found:665.7; Elemental analysis calcd. (%) for $C_{40}H_{43}NO_8$: C 72.16, H 6.51, N 2.1; found: C 72.06, H 6.45, N 2.08.

Synthesis of tetrabutyl 1-ethyl-1H-phenanthro carbazole-3,4,9,10-tetracarboxylate (**4**)

A mixture of compound **3** (0.24 mmol, 1 equiv.), sodium hydride (60% in wax, 0.36 mmol, 3 equiv.) and ethyl iodide (0.18 mmol, 1.53 equiv.) in a dry THF was refluxed for overnight under argon atmosphere. After cooling to room temperature, water (2 mL) was added to the mixture and stirred for 10 min at 0 °C. The resulting mixture was extracted with dichloromethane and the extract was washed with water and brine. Finally, organic layer was dried over anhyd. Na_2SO_4 and concentrated. The crude residue obtained was purified by column chromatography on neutral alumina. Elution with hexane, 50% DCM-hexane solution followed by dichloromethane yielded the desired product.

R_f = 0.6 (15% EtOAc-hexane); Yellowish solid, yield: 75%; IR (KBr pellet) ν_{max} in cm^{-1}: 2959, 2929, 2873, 1720, 1586; ^1H NMR (600 MHz, $CDCl_3$, 298 K): 8.49 (d, J = 7.8Hz, 2H, H_{Ar}), 8.22 (s, 2H, H_{Ar}), 8.18 (d, J = 7.8Hz, 2H, H_{Ar}), 4.74-4.7 (m, 2H, -*N*-CH_2), 4.45-4.42 (m, 8H, 4 × $-OCH_2$), 1.87-1.82 (m, 8H, 4 × $-OCH_2$-$\underline{CH_2}$), 1.56-1.5 (m, 8H, 4 × $-CH_2$), 1.25 (bs, 3H, -*N*-CH_2-$\underline{CH_3}$), 1.04-1.01 (m, 12H, 4 × $-CH_3$); ^{13}C NMR (150 MHz, $CDCl_3$, 298 K): 169.7, 169.3, 131.9, 131.4, 129.2, 128.2, 127.8, 124.4, 123.3, 121.9, 118.1, 117.9, 65.7, 65.6, 40.8, 31, 30.9, 29.9, 19.5, 16.7, 14.1, 14.09; MALDI-TOF: exact mass calculated for $C_{42}H_{47}NO_8$ $[M]^+$: 693.3, found: 693.7; HRMS (APCI mode) exact mass calculated for $C_{42}H_{48}NO_8$ $[MH]^+$: 694.3374, found: 694.3371.

Synthesis of **PEI-N**

A mixture of compound **4** (0.25 mmol, 1 equiv.), 1-aminooctadecane (0.27 mmol, 1.1 equiv.) and imidazole (1 g) were taken in microwave vessel, flushed with nitrogen and put in microwave reactor. The mixture was heated to 165 °C for 35 minutes at 35 W. After cooling, reaction mixture was poured in 2N HCl and extracted with chloroform. Organic mixture was washed with water and saturated sodium chloride solution. The crude compound was purified by neutral alumina column chromatography using 50% chloroform-hexane system yields the desired product.

R_f = 0.4 (20% EtOAc-hexane); Red waxy solid, yield: 55%; IR (KBr pellet) ν_{max} in cm^{-1}: 2958, 2924, 2854, 1712, 1695, 1679, 1597; ^1H NMR (600 MHz, $CDCl_3$, 298 K): 8.88 (s, 1H, H_{Ar}), 8.81 (d, *J* = 7.8 Hz, 1H, H_{Ar}), 8.75 (s, 2H, H_{Ar}), 8.44 (s, 1H, H_{Ar}),8.37 (d, *J* = 7.8 Hz, 1H, H_{Ar}), 4.85-4.81 (m, 2H, -*N*CH_2), 4.47-4.44 (m, 4H, 2 × -OCH_2), 4.33 (m, 2H, N-CH_2), 1.86-1.83 (m, 6H, CH_2), 1.74 (t, 3H, -*N*CH_2-CH_3), 1.55-1.24 (m, 34H, 17 × -CH_2), 1.03-1.00 (m, 6H, 2 × -CH_3), 0.88-0.86 (m, 3H, -CH_3); ^{13}C NMR (150 MHz, $CDCl_3$, 298 K): 169.3, 168.8, 165, 163.8, 132.7, 132.3, 131.6, 130.5, 130.4, 130.4, 127.8, 126.8, 124, 123.5, 123, 122.8, 121.4, 120, 119.9, 119.7, 118.8, 117.8, 117.3, 116.8, 66, 65.9, 41.1, 40.9, 32.1, 31, 30.9, 29.9, 29.9, 29.9, 29.9, 29.6, 22.9, 19.6, 19.6, 16.7, 14.3, 14.1; MALDI-TOF exact mass calculated for $C_{52}H_{66}N_2O_6$ $[M]^-$: 814.5, found: 814.9; HRMS (APCI mode) exact mass calculated for $C_{52}H_{67}N_2O_6$ $[MH]^+$: 815.4994, found: 815.4993.

Synthesis of tetrakis(butyl) perylenothiophene-3,4,9,10-tetracarboxylate (**6**)

A mixture of compound **2** (0.26 mmol, 1 equiv.) and Sulfur powder (2.602 mmol, 10 equiv.) was heated to dissolve in *N*-methylpyrrolidone (10 mL) at 70 °C for 30 min. and then refluxed at 180 °C under Argon atmosphere for overnight by TLC monitoring. After cooling to room temperature, 2 M HCl was added, the precipitate was filtered, washed with water and dried. The crude product was purified by column chromatography on neutral alumina. Elution with 20-30% DCM-hexane system followed by 50% DCM-hexane system yields the desired product. Further purification was done by the addition of concentrated solution of compound in cold methanol.

R_f = 0.6 (20% EtOAc-hexane); orange solid, yield: 55%; IR (KBr pellet) ν_{max} in cm^{-1}: 2955, 2927, 2869, 1720, 1583; ^{1}H NMR (600 MHz, $CDCl_3$, 298 K): 8.59-8.57 (m, 4H, H_{Ar}), 8.27 (d, *J* = 7.8Hz, 2H, H_{Ar}), 4.44-4.41 (m, 8H, 4 × -OCH_2), 1.87-1.81 (m, 8H, 4 × OCH_2-CH_2), 1.56-1.51 (m, 8H, 4 × CH_2), 1.04-1.01 (m, 12H, 4 × -CH_3); ^{13}C NMR (150 MHz, $CDCl_3$, 298 K): 168.9, 168.7, 135.2, 132.1, 130.6, 130, 129.4, 126.3, 125.6, 125.4, 121.9, 65.8, 65.7, 30.9, 30.92, 19.6, 19.5, 14.1; MALDI-TOF: exact mass calculated for $C_{40}H_{42}O_8S$ $[M]^+$: 682.3, found: 682.4; HRMS (APCI mode) exact mass calculated for $C_{40}H_{42}O_8S$ $[M]^+$: 682.2595, found: 682.2578.

Synthesis of **PEI-S**

A mixture of compound **6** (0.22 mmol, 1 equiv.), 1-amino-octadecane (0.24 mmol, 1.1 equiv.) and imidazole (1 g) were taken in microwave vessel, flushed with nitrogen and put in microwave reactor. The mixture was heated to 165 °C for 35 minutes at 35 W. After cooling, reaction mixture was poured in 2N HCl and extracted with chloroform. Organic mixture was washed with water and saturated sodium chloride solution. The crude compound was purified by neutral alumina column chromatography using 50% chloroform-hexane to get the desired product.

R_f = 0.4 (20% EtOAc-hexane); Orange red waxy solid, yield: 55%; IR (KBr pellet) ν_{max} in cm^{-1}: 2959, 2924, 2853, 1727, 1697, 1655, 1629, 1590; ^{1}H NMR (600 MHz, $CDCl_3$, 298 K): 8.94 (s, 1H, H_{Ar}), 8.58 (s, 1H, H_{Ar}), 8.57 (d, *J* = 8.4 Hz, 1H, H_{Ar}), 8.51 (d, *J* = 7.8 Hz, 1H, H_{Ar}), 8.4 (d, *J* = 7.8 Hz, 1H, H_{Ar}), 8.29 (d, *J* = 7.8 Hz, 1H, H_{Ar}), 4.48-4.44 (m, 4H, 2 × -OCH_2), 4.28-4.25 (m, 2H, N-CH_2), 1.9-1.82 (m, 6H, CH_2), 1.59-1.24 (m, 34H, 17 × -CH_2), 1.07-1.03 (m, 6H, 2 × -CH_3), 0.87 (t, *J* = 7.2 Hz 3H, -CH_3); ^{13}C NMR (150 MHz, $CDCl_3$, 298 K): 168.3, 168.2, 163.4, 163.1, 137.1, 135, 132.4, 131.1, 130.8, 130.5, 130.3, 129.2, 128.7, 128.5, 126, 125.7, 125.4, 124.8, 124.4, 122.4, 121.1, 120.9, 120.7, 120.5, 66.1, 65.9, 41.1, 32.1, 29.9, 29.9, 29.9, 29.9, 29.6, 22.9, 19.6, 19.6, 14.3, 14.1, 14.12; MALDI-TOF exact mass calculated for $C_{50}H_{61}NO_6S$ $[M]^-$: 803.4, found: 803.6; HRMS (APCI mode) exact mass calculated for $C_{50}H_{62}NO_6S$ $[M]^+$: 804.4292, found: 804.4295.

Synthesis of tetrakis(butyl) perylenoselenophene-3,4,9,10-tetracarboxylate (**5**)

A mixture of compound **2** (0.26 mmol, 1 equiv.) and Selenium powder (2.602 mmol, 10 equiv.) was heated to dissolve in *N*-methylpyrrolidone (10 mL) at 70 °C for 30 min. and then refluxed at 180 °C under Ar atmosphere for overnight until the starting material could not be detected by TLC. After cooling to room temperature, 2 M HCl was added, then the precipitate was filtered, washed with water and dried. The crude product was purified by column chromatography on neutral alumina. Elution with 20-30% DCM-hexane system followed by 50% DCM-hexane system yields the desired product. Further purification was done by addition of concentrate solution of compound in cold methanol gives the product.

R_f = 0.6 (20% EtOAc-hexane); orange solid, yield: 55%; IR (KBr pellet) ν_{max} in cm^{-1}: 2955, 2927, 2869, 1719, 1582; ^{1}H NMR (400 MHz, CDCl$_3$, 298 K): 8.57-8.53 (m, 4H, H$_{Ar}$), 8.24-8.23 (m, 2H, H$_{Ar}$), 4.41 (bs, 8H, 4 × -OCH$_2$), 1.86-1.82 (m, 8H, 4 × $OCH_2\text{-}\underline{CH_2}$), 1.55-1.51 (m, 8H, 4 × -CH$_2$), 1.04-1.01 (m, 12H, 4 × -CH$_3$); ^{13}C NMR (100 MHz, CDCl$_3$, 298 K): 168.9, 168.7, 137.6, 133.3, 132.2, 129.9, 129.3, 128.7, 128.7, 127, 125.7, 121.6, 65.8, 65.6, 30.9, 30.9, 19.5, 19.5, 14.1, 14.08; MALDI-TOF: exact mass calculated for $C_{40}H_{42}O_8Se$ [M]$^+$: 730.2, found: 730.8; Elemental analysis calcd. (%) for $C_{40}H_{42}O_8Se$: C 65.84, H 5.80; found: C 65.74, H 5.80.

Synthesis of **PEI-Se**

A mixture of compound **5** (0.21 mmol, 1 equiv.), 1-amino-octadecane (0.23 mmol, 1.1 equiv.) and imidazole (1g) were taken in microwave vessel, flushed with nitrogen and placed in microwave reactor. The mixture was heated to 165 °C for 35 minutes at 35 W. After cooling, reaction mixture was poured into 2N HCl and extracted with chloroform. Organic mixture was washed with water and saturated sodium chloride solution. The crude compound was purified by neutral alumina column chromatography using 50% chloroform-hexane system to yield the desired product.

R_f = 0.4 (20% EtOAc-hexane); Dark red waxy solid, yield: 55%; IR (KBr pellet) ν_{max} in cm^{-1}: 2959, 2924, 2853, 1724, 1701, 1651, 1597; ^{1}H NMR (600 MHz, CDCl$_3$, 298 K): 8.91 (s, 1H, H$_{Ar}$), 8.57 (s, 1H, H$_{Ar}$), 8.52 (d, J = 7.8 Hz, 1H, H$_{Ar}$), 8.42 (d, J = 7.8 Hz, 1H, H$_{Ar}$), 8.31 (d, J = 8.4 Hz, 1H, H$_{Ar}$), 8.25 (d, J = 7.8 Hz, 1H, H$_{Ar}$), 4.47-4.44 (m, 4H, 2 × -OCH$_2$), 4.26-4.23 (m, 2H, N-CH$_2$), 1.9-1.81 (m, 6H, CH$_2$), 1.57-1.24 (m, 34H, 17 × -CH$_2$), 1.07-1.03 (q, 6H, 2 × -CH$_3$), 0.87 (t, J = 7.2 Hz, 3H, -CH$_3$); ^{13}C NMR (150 MHz, CDCl$_3$, 298 K): 168.4, 168.2, 163.3, 163.1, 139.8, 137.4, 133.3, 132.6, 131.4, 131.1, 130.5, 130, 129.1, 128.4, 128.2, 126.1, 125.7, 124.6, 122.3, 122, 120.8, 120.5, 119.9, 66, 65.9, 41, 32.1, 30.9, 29.9, 29.7, 29.6, 27.6, 22.9, 19.6, 14.3, 14.1; MALDI-TOF exact mass calculated for $C_{50}H_{61}NO_6Se$ [M]$^-$: 851.4, found: 851.6; Elemental analysis calcd. (%) for $C_{50}H_{61}NO_6Se$: C 70.57, H 7.23, N 1.65; found: C 70.29, H 7.44, N 1.57.

Synthesis of 2-octadecylisoindoline-1,3-dione (**7**)

Potassium phthalimide (12.9 mmol, 1.1 equiv.) was added to the solution of 1-bromo-octadecane (12.1 mmol, 1 equiv.) in DMF. The reaction mixture was stirred at 90 °C for 18 h, cooled the reaction mixture to room temperature, poured the mixture in water and extracted with methylene chloride several times. The combined organic layer was washed with 0.2 N KOH, water, saturated NH_4Cl, dried over anhyd Na_2SO_4 and concentrated under reduced pressure after filtration. The resulting crude compound was purified by column chromatography using methylene chloride as eluent to give white solid.

R_f = 0.4 (10% EtOAc-hexane); white solid, yield: 95%; IR (KBr pellet) ν_{max} in cm^{-1}: 2965, 2917, 2849, 1775, 1701; ^{1}H NMR (600 MHz, $CDCl_3$, 298 K): 7.83-7.82 (m, 2H, H_{Ar}), 7.70-7.69 (m, 2H, H_{Ar}), 3.67-3.65 (m, 2H, $-NCH_2$), 1.68-1.64 (m, 2H, $-NCH_2-CH_2$), 1.31-1.23 (m, 30H, 15 × $-CH_2$), 0.88-0.85 (m, 3H, $-CH_3$); ^{13}C NMR (150 MHz, $CDCl_3$, 298 K): 168.7, 134, 132.4, 123.3, 38.3, 32.1, 29.9, 29.8, 29.7, 29.6, 29.4, 27.1, 22.9, 14.3; HRMS (ESI mode) exact mass calculated for $C_{26}H_{42}NO_2$ [MH]$^+$: 400.3210, found: 400.3217.

Synthesis of 1-amino-octadecane (**8**)

A mixture of compound **7** (10 mmol, 1 equiv.) and 80% hydrazine hydrate (30.2 mmol, 3 equiv.) in methanol were stirred at 95 °C for 1 h. after the disappearance of starting imide, methanol was removed under reduced pressure and residue was diluted with dichloromethane and washed with 10% KOH. The combined aqueous layer was extracted with dichloromethane. The combined organic layer was washed with brine and dried over anhyd Na_2SO_4. After removal of solvent the product was obtained as a white solid.

R_f = 0.3 (20% EtOAc-hexane); white solid, yield: 95%; IR (KBr pellet) ν_{max} in cm^{-1}: 3334, 2956, 2918, 2851; ^{1}H NMR (600 MHz, $CDCl_3$, 298 K): 2.67-2.64 (m, 2H, $-NCH_2$), 1.41-1.40 (m, 2H, $-NCH_2-CH_2$), 1.34 (s, 2H, NH_2), 1.24-1.23 (m, 30H, 15 × $-CH_2$), 0.87-0.84 (m, 3H, $-CH_3$); ^{13}C NMR (150 MHz, $CDCl_3$, 298 K): 42.5, 34.1, 32.1, 29.9, 29.7, 29.6, 27.1, 22.9, 14.3; HRMS (ESI mode) exact mass calculated for $C_{18}H_{40}N$ [MH]$^+$: 270.3155, found: 270.3152.

Synthesis of **PEI**

A mixture of compound **1** (0.46 mmol, 1 equiv.), 1-amino-octadecane (51 mmol, 1.1 equiv.) and imidazole (1.1g) were taken in microwave vessel, flushed with nitrogen and put in microwave reactor. The mixture was heated to 165 °C for 35 minutes at 35 W. After cooling, the reaction mixture was poured in 2N HCl and extracted with chloroform. Organic mixture was washed with water and brine solution. The crude compound was purified by neutral alumina column chromatography using 50% chloroform-hexane system yields the desired product. This was further purified by recrystallization from DCM-methanol system.

R_f = 0.4 (20% EtOAc-hexane); Bright orange solid, yield: 55%; IR (KBr pellet) ν_{max} in cm^{-1}: 2958, 2923, 2852, 1714, 1693, 1649, 1618, 1597; ^{1}H NMR (600 MHz, $CDCl_3$, 298 K): δ 8.53 (d, J = 8.4 Hz, 2H, H_{Ar}), 8.34 (d, J = 7.8 Hz, 4H, H_{Ar}), 8.05 (d, J = 7.8 Hz, 2H, H_{Ar}), 4.37-4.34 (m, 4H, 2 × $-OCH_2$), 4.19-4.17 (m, 2H, $N-CH_2$), 1.83-1.73 (m, 6H, CH_2), 1.54-1.24 (m, 34H, 17 × $-CH_2$), 1.01 (t, J = 7.2 Hz, 6H, 2 × $-CH_3$), 0.88-0.86 (m, 3H, $-CH_3$); ^{13}C NMR (150 MHz, $CDCl_3$, 298 K): δ 168.5, 163.7, 135.6, 132.3, 132.1, 131.5, 130.5, 129.4, 129.3, 129.2, 126.1, 122.7, 122.3, 122, 65.8, 40.8, 32.1, 30.8, 29.9, 29.9, 29.86, 29.8, 29.6, 29.58, 28.4, 27.4, 22.9, 19.5, 14.3, 14; MALDI-TOF exact mass calculated for $C_{50}H_{64}NO_6$ [MH]$^+$: 774.5, found: 774.6; HRMS (APCI mode) exact mass calculated for $C_{50}H_{64}NO_6$ MH]$^+$: 774.4728, found: 774.4730.

Synthesis of **PEI-Ph**

A mixture of compound **1** (0.15 mmol, 1 equiv.), aniline (0.17 mmol, 1.1 equiv.) and imidazole (0.7 g) were taken in microwave vessel, flushed with nitrogen and put in microwave reactor. The mixture was heated to 165 °C for 35 minutes at 35 W. After cooling, reaction mixture was poured into 2N HCl and extracted with chloroform. Organic mixture was washed with water and saturated sodium chloride solution. The crude compound was purified by neutral alumina column chromatography using 50% DCM-hexane system followed by DCM yields the desired product. This was further purified by recrystallization from DCM-methanol system.

R_f = 0.4 (20% EtOAc-hexane); Bright red solid, yield: 55%; IR (KBr pellet) ν_{max} in cm^{-1}: 2959, 2931, 2872, 1707, 1660, 1593; ^{1}H NMR (600 MHz, CDCl$_3$, 298 K): δ 8.63 (d, J = 7.8 Hz, 2H, H$_{Ar}$), 8.44-8.40 (m, 4H, H$_{Ar}$), 8.10 (d, J = 8.4 Hz, 2H, H$_{Ar}$), 7.60-7.57 (m, 2H, H$_{Ar\text{-}phenyl}$), 7.52-7.49 (m, 1H, H$_{Ar\text{-}phenyl}$), 7.38-7.37 (m, 2H, H$_{Ar\text{-}phenyl}$), 4.38-4.35 (m, 4H, 2 × -OCH$_2$), 1.83-1.78 (m, 4H, CH$_2$), 1.54-1.48 (m, 4H, CH$_2$CH$_3$), 1.01 (t, J = 7.2 Hz, 6H, 2 × -CH$_3$); ^{13}C NMR (150 MHz, CDCl$_3$, 298 K): δ 168.4, 164, 136.1, 135.5, 132.3, 132.28, 132, 130.6, 129.8, 129.7, 129.4, 129.3, 129, 128.8, 126.4, 123, 122.4, 122.1, 65.8, 30.8, 19.5, 14; MALDI-TOF exact mass calculated for $C_{38}H_{32}NO_6$ [MH]$^+$: 598.2, found: 598.3; HRMS (APCI mode) exact mass calculated for $C_{38}H_{32}NO_6$ [MH]$^+$: 598.2224, found: 598.2224.

Synthesis of **PEI-Bz**

A mixture of compound **1** (0.15 mmol, 1 equiv.), benzyl amine (0.17 mmol, 1.1 equiv.) and imidazole (0.7 g) were taken in microwave vessel, flushed with nitrogen and put in microwave reactor. The mixture was heated to 165 °C for 35 minutes at 35 W. After cooling, reaction mixture was poured in 2N HCl and extracted with chloroform. Organic mixture was washed with water and saturated sodium chloride solution. The crude compound was purified by neutral alumina column chromatography using 50% DCM-hexane system followed by DCM yields the desired product. This was further purified by recrystallization from DCM-methanol system.

R_f = 0.4 (20% EtOAc-hexane); Bright orange solid, yield: 58%; IR (KBr pellet) ν_{max} in cm^{-1}: 2960, 2933, 2873, 1720, 1697, 1657, 1594; ^{1}H NMR (600 MHz, CDCl$_3$, 298 K): δ 8.41 (d, J = 7.8 Hz, 2H, H$_{Ar}$), 8.22 (d, J = 7.8 Hz, 2H, H$_{Ar}$), 8.17 (d, J = 6 Hz, 2H, H$_{Ar}$), 8.01 (d, J = 7.8 Hz, 2H, H$_{Ar}$), 7.61 (d, J = 7.8 Hz, 2H, H$_{Ar\text{-}phenyl}$), 7.37-7.35 (m, 2H, H$_{Ar\text{-}phenyl}$), 7.29-7.27 (m, 1H, H$_{Ar\text{-}phenyl}$), 5.38 (s, 2H, PhCH$_2$), 4.36 (t, J = 6.6 Hz, 4H, 2 × -OCH$_2$), 1.83-1.79 (m, 4H, CH$_2$), 1.54-1.48 (m, 4H, CH$_2$CH$_3$), 1.03-1.00 (m, 6H, 2 × -CH$_3$); ^{13}C NMR (150 MHz, CDCl$_3$, 298 K): δ 168.4, 163.7, 137.5, 135.6, 132.1, 132.1, 131.6, 130.5, 129.4, 129.3, 129.2, 129.1, 128.7, 127.8, 125.9, 122.8, 122.1, 121.8, 65.8, 43.8, 30.8, 19.5, 14; MALDI-TOF exact mass calculated for $C_{39}H_{34}NO_6$ [MH]$^+$: 612.2, found: 612.4; HRMS (APCI mode) exact mass calculated for $C_{39}H_{34}NO_6$ [MH]$^+$: 612.2381, found: 612.2385.

Synthesis of **UPBI**

A mixture of compound **PEI** (0.05 mmol, 1 equiv.), 3,4,5-tris(decyloxy)aniline (0.06 mmol, 1.1 equiv.), zinc acetate (0.05 mmol, 1 equiv.) and imidazole (0.5 g) were taken in microwave vessel, flushed with nitrogen and put in microwave reactor. The mixture was heated to 165 ^{o}C for 35 minutes at 35 W. After cooling, reaction mixture was poured in 2N HCl and extracted with chloroform. Organic mixture was washed with water and saturated sodium chloride solution. The crude compound was purified by neutral alumina column chromatography using 50% DCM-hexane system, followed by DCM to obtain the desired product.

R_f = 0.4 (20% EtOAc-hexane); Dark red waxy solid, yield: 75%; IR (KBr pellet) ν_{max} in cm^{-1}: 2958, 2924, 2854, 1699, 1662, 1594; ^{1}H NMR (600 MHz, $CDCl_3$, 298 K): δ 8.52-8.50 (m, 2H, H_{Ar}), 8.37-8.35 (m, 2H, H_{Ar}), 8.20-8.19 (m, 2H, H_{Ar}), 8.13-8.12 (m, 2H, H_{Ar}), 4.17-4.15 (m, 2H, N-CH_2), 4.06-4.04 (m, 2H, -OCH_2), 3.98-3.96 (m, 4H, 2 × -OCH_2), 1.83-1.73 (m, 8H, CH_2), 1.54-1.24 (m, 74H, 37 × -CH_2), 0.91-0.89 (m, 3H, -CH_3), 0.88-0.85 (m, 9H, -CH_3); ^{13}C NMR (150 MHz, $CDCl_3$, 298 K): δ 163.4, 163, 153.9, 138.4, 134.2, 133.8, 131.3, 130.8, 130.1, 129.3, 128.7, 125.9, 125.8, 123.4, 123.3, 123.1, 122.9, 107, 73.7, 69.3, 41.1, 32.2, 32.1, 30.7, 30.1, 30, 29.9, 29.92, 29.8, 29.86, 29.72, 29.7, 29.68, 29.65, 29.6, 29.58, 28.3, 27.5, 26.4, 26.4, 23, 22.9, 14.4, 14.3, 14.3; MALDI-TOF exact mass calculated for $C_{78}H_{111}N_2O_7$ $[MH]^+$: 1187.8386, found: 1187.823; Elemental analysis calcd. (%) for $C_{78}H_{110}N_2O_7$: C 78.88, H 9.34, N 2.36; found: C 78.82, H 9.39, N 2.46.

5.5. References

1. a) F. Würthner, *Chem. Commun.*, 2004, 1564-1579; b) C. Huang, S. Barlow, and S. R. Marder, *J. Org. Chem.*, 2011, **76**, 2386-2407; c) S. Chen, P. Slattum, C. Wang, and Ling Zang, *Chem. Rev.*, 2015, **115**, 11967-11998; d) F. Würthner, C. R. Saha-Möller, B. Fimmel, S. Ogi, P. Leowanawat and D. Schmidt, *Chem Rev.*, 2016, **116**, 962-1052; e) K. Y. Law, *Chem. Rev.*, 1993, **93**, 449-486; f) C. Xue, O. Birel, M. Gao, S. Zhang, L. Dai, A. Urbas and Q. Li, *J. Phys. Chem. C*, 2012, **116**, 10396-10404; g) C. Xue, Y. Xue, L Dai, A. Urbas and Q. Li, *Adv. Optical Mater.*, 2013, **1**, 581-587; h) C. Xue, K. Gutierrez-Cuevas, M. Gao, A. Urbas and Q. Li, *J. Phys. Chem. C*, 2013, **117**, 21603-21608; i) C. Xue, O. Birel, Y. Xue, L. Dai, A. Urbas and Q. Li, *J. Phys. Chem. C*, 2013, **117**, 6752-6758.
2. a) V. Sivamurugan, K. Kazlauskas, S. Jursenas, A. Gruodis, J. Simokaitiene, J. Grazulevicius and S. Valiyaveettil, *J. Phys. Chem. B*, 2010, **114**, 1782-1789; b) A. Miasojedovas, K. Kazlauskas, G. Armonaite, V. Sivamurugan, S. Valiyaveettil, J. Grazulevicius, S. Jursenas, *Dyes and Pigments*, 2012, **92**, 1285-1291.
3. S. Benning, H. S. Kitzerow, H. Bock and M. F. Achard, *Liq. Cryst.*, 2000, **27**, 901-906.
4. H. Langhals, J. Karolin and L. B. Å. Johansson, *J. Chem. Soc., Faraday Trans.*, 1998, **94**, 2919-2922
5. a) M. J. Yang, S. L. Lu and Y. Li, J. *Mater. Sci. Lett.*, 2003, **22**, 813-815; b) T. Hassheider, S. A. Benning, M. W. Lauhof, H. S. Kitzerow, H. Bock, M. D. Watson and K. Müllen, *Mol. Cryst. Liq. Cryst.*, 2004, **413**, 461-472.
6. T. Hassheider, S. A. Benning, H.-S. Kitzerow, M.-F. Achard and H. Bock, *Angew. Chem. Int. Ed.*, 2001, **40**, 2060-2063.
7. A. Arnaud, J. Belleney, F. Boue, L. Bouteiller, G. Carrot and V. Wintgens, *Angew. Chem. Int. Ed.*, 2004, **43**, 1718-1721.
8. I. Seguy, P. Jolinat, P. Destruel, R. Mamy, H. Allouchi, C. Courseille, M. Cotrait and H. Bock, *ChemPhysChem*, 2001, **2**, 448-452.
9. a) L. Yang, M. Shi, M. Wang and H. Chen, *Tetrahedron*, 2008, **64**, 5404-5409; b) X. B. Zhang, Y. F. Wu, J. Z. Li, F. Li and M. Li, *Dyes Pigments*, 2008, **76**, 810-816; c) C. Xue, R. Sun, R. Annab, D. Abadi and S. Jin, *Tetrahedron Letters*, 2009, **50**, 853-856.
10. H. Langhals, S. Sprenger and M.-T. Brandherm, *Liebigs Ann.*, 1995, 481-486.
11. a) H. Kaiser, J. Lindner and H. Langhals, *Chem. Ber.*, 1991, **124**, 529-535; b) Y. Nagao, T. Naito, Y. Abe and T. Misono, *Dyes and Pigments*, 1996, **32**, 71-83.
12. a) R. Gomez, J. L. Segura and N. Martín, *Org. Lett.*, 2005, **7**, 717-720; b) S. M. Lindner and M. Thelakkat, *Macromolecules*, 2004, **37**, 8832-8835; c) H. Langhals, M. Rauscher, J. Strübe and D. Kuck, *J. Org. Chem.*, 2008, **73**, 1113-1116.
13. a) L. D. Wescott and D. L. Mattern, *J. Org. Chem.*, 2003, **68**, 10058-10066; b) R. Kota, R. Samudrala, and D. L. Mattern, *J. Org. Chem.*, 2012, **77**, 9641-9651.
14. J. Kelber, H. Bock, O. Thiebaut, E. Grelet, and H. Langhals, *Eur. J. Org. Chem.*, 2011, 707-712.
15. a) C. O. Kappe, *Angew. Chem. Int. Ed.*, 2004, **43**, 6250-6284; b) A. de la Hoz, A. Diaz-Ortiz and A. Moreno, *Chem. Soc. Rev.*, 2005, **34**, 164-178.
16. F. Rigodanza, E. Tenori, A. Bonasera, Z. Syrgiannis and M. Prato, *Eur. J. Org. Chem.*, 2015, 5060-5063.

17. M. Schulze, M. Philipp, W. Waigel, D. Schmidt and F. Würthner, *J. Org. Chem.*, 2016, **81**, 8394-8405.
18. S. Sengupta, R. K. Dubey, R. W. Hoek, S. P. van Eeden, D. D. Gunbaş, F. C. Grozema, E. J. Sudhölter and W. F. Jager, *J. Org. Chem.*, 2014, **79**, 6655-6662.
19. T. Yang, J. Pu, J. Zhang and W. Wang, *J. Org. Chem.*, 2013, **78**, 4857-4866.
20. X. Kong, Z. He, Y. Zhang, L. Mu, C. Liang, B. Chen, X. Jing and A. N. Cammidge, *Org. Lett.*, 2011, **13**(4), 764-767.
21. a) F. Würthner, T. E. Kaiser and C. R. Saha-Möller, *Angew. Chem. Int. Ed.*, 2011, **50**, 3376-3410; b) Z. Chen, V. Stepanenko, V. Dehm, P. Prins, L. D. Siebbeles, J. Seibt, P. Marquetand, V. Engel and F. Würthner, *Chem. Eur. J.*, 2007, **13**, 436-449; c) R. F. Fink, J. Seibt, V. Engel, M. Renz, M. Kaupp, S. Lochbrunner, H.-M. Zhao, J. Pfister, F. Würthner and B. Engels, *J. Am. Chem. Soc.*, 2008, **130**, 12858-12859.
22. a) E. G. McRae and M. Kasha, *J. Chem. Phys*, 1958, **28**, 721-722; b) M. Kasha, H. Rawls and M. A. El-Bayoumi, *Pure Appl. Chem.*, 1965, **11**, 371-392.
23. a) S. K. Lee, Y. Zu, A. Herrmann, Y. Geerts, K. Müllen and A. J. Bard, *J. Am. Chem. Soc.*, 1999, **121**, 3513-3520; b) A. Pron, R. R. Reghu, R. Rybakiewicz, H. Cybulski, D. Djurado, J. V. Grazulevicius, M. Zagorska, I. Kulszewicz-Bajer and J.-M. Verilhac, *J. Phys. Chem. C*, 2011, **115**, 15008-15017.
24. a) M. J. Frisch, G. W. Trucks, H. B. Schlegel, G. E. Scuseria, M. A. Robb, J. R. Cheeseman, G. Scalmani, V. Barone, G. A. Petersson, H. Nakatsuji, X. Li, M. Caricato, A. V. Marenich, J. Bloino, B. G. Janesko, R. Gomperts, B. Mennucci, H. P. Hratchian, J. V. Ortiz, A. F. Izmaylov, J. L. Sonnenberg, D. Williams-Young, F. Ding, F. Lipparini, F. Egidi, J. Goings, B. Peng, A. Petrone, T. Henderson, D. Ranasinghe, V. G. Zakrzewski, J. Gao, N. Rega, G. Zheng, W. Liang, M. Hada, M. Ehara, K. Toyota, R. Fukuda, J. Hasegawa, M. Ishida, T. Nakajima, Y. Honda, O. Kitao, H. Nakai, T. Vreven, K. Throssell, J. A. Montgomery, Jr., J. E. Peralta, F. Ogliaro, M. J. Bearpark, J. J. Heyd, E. N. Brothers, K. N. Kudin, V. N. Staroverov, T. A. Keith, R. Kobayashi, J. Normand, K. Raghavachari, A. P. Rendell, J. C. Burant, S. S. Iyengar, J. Tomasi, M. Cossi, J. M. Millam, M. Klene, C. Adamo, R. Cammi, J. W. Ochterski, R. L. Martin, K. Morokuma, O. Farkas, J. B. Foresman, and D. J. Fox, *Gaussian*, Inc., Wallingford CT, 2016; b) C. Lee, W. Yang and R. G. Parr, *Phys. Rev. B*, 1988, **37**, 785-789; c) A. D. Becke, *J. Chem. Phys.*, 1993, **98**, 1372-1377.

Chapter 5b

First example of White Organic Electroluminescence Utilizing Perylene Ester Imides

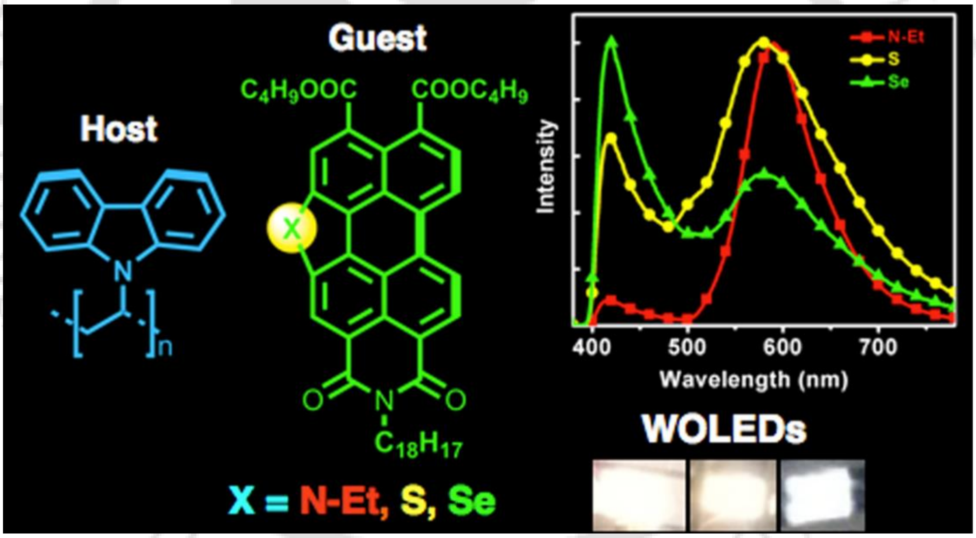

Results have been published in;

- *ChemistrySelect*, 2018, **3**, 5123-5129

5.6. Introduction

First pioneered by Tang *et al.*,[1] the research on organic light-emitting diodes (OLEDs) has grown exponentially with widespread scientific and industrial applications due to their excellent features. Presently, the OLEDs commercialized in market have been manufactured based on thermal evaporation technique under high vacuum. The low molecular weight luminescent organic semiconductors are often processed by this method. However, the spin-casting or ink-jet printing of solution processable electroluminescent main-chain conjugated polymers hold the advantage of simplicity and cheaper cost.[2] OLEDs, in comparison to other contenders in display technology, have several advantages like their ability to be fabricated into thin and light-weight display systems over a large area, faster response time, wide-viewing angle, high color contrast and lower power requirements. The advent of first white OLED (WOLED) by Kido *et al.*,[3] that was created by a single emissive layer composed of three fluorescent dyes (blue, green and orange color), enhanced the interest in WOLEDs, due to their potential applications in flat-panel displays and solid-state lighting. The importance of WOLEDs besides their application as a light source, arises from the fact that they can be utilized in the creation of full color OLED display panels by combining with color filters. They can serve as a backlight for liquid crystal displays too. White light emission is realized by having two or three complementary color emitters or by using three primary color emitters. This requires the doping or combination of several components.[4] In literature, the problem of obtaining an efficient WOLEDs has been approached with different classes of materials like small organic molecules,[5] specifically tailored polymers,[6] blends of different luminescent polymers,[7-9] and layered polymer structures,[10] integration of the above materials with phosphorescent iridium complexes,[11] or blending of emissive semiconducting polymers with organometallic emitters.[12]

Perylene bisimides are known to be reasonably inexpensive, stable chromophores, which can be synthetically tailored as per the requirement through the incorporation of different functionalities. They possess a large band gap, high absorption coefficient and high luminescence quantum yield. In addition, they are known for their high chemical/thermal stability along with a resistance to photochemical degradation.[13] These properties make them archetype materials for their application in organic electronic devices like organic solar cells (OSCs), organic light-emitting diodes (OLEDs) and organic field-effect transistors (OFETs).[14] Perylene based molecules are extensively used in building the self-assembled supramolecular systems because of their inclination to aggregate under different conditions.[13] However, among the organic materials, the development of n-type organic semiconductor materials has typically lagged their p-type counterparts due to their sensitivity to oxygen and moisture. Hence, several attempts are being made continuously to synthesize new n-type materials and explore previously unknown properties related to these compounds. Working in this direction, we focused on the development and utilization of tetraesters of perylene tetracarboxylic acids (PTEs), which are structurally related to perylene bisimides (PBIs) and have significant electron-accepting ability. However, due to the synthetic difficulty in obtaining the unsymmetric molecular structure, perylene tetracarboxylic diester monoimides (PEIs) have received very less attention.[15]

5.7. Results and discussion

We have shown an easy method for the synthesis of unsymmetric PEIs, by treating the perylene tetraesters (PTEs) with the requisite amine under microwave condition in previous Chapter. This method was utilized to obtain corresponding perylene ester imides from hetero-atom *bay*-annulated perylene tetraesters in good yields (Scheme 5.5). It is important to mention that these results have revealed that the newly developed unsymmetrical perylenetetracarboxylic diester monoimides (PEIs) are more soluble as compared to symmetrical PBIs. In addition, the unsymmetrical substitution provides an opportunity to tune the photophysical properties and the energy levels of frontier molecular orbital with respect to the work function of the electrodes. These compounds exhibited good emission in solution and thin films along with good thermal stability at least up to 200 °C (Figure 5.5). Relative fluorescence quantum yields measured with respect to fluorescein

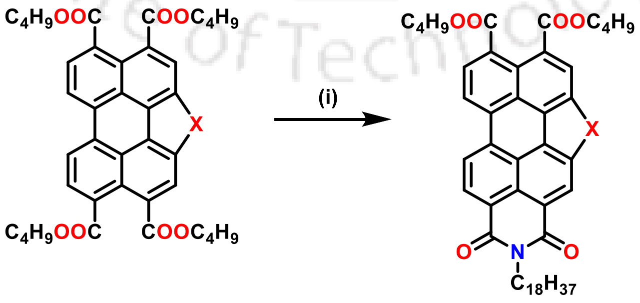

4: X = N-Et
5: X = S
6: X = Se

PEI-N: X = N-Et
PEI-S: X = S
PEI-Se: X = Se

Scheme 5.5. Synthesis of *bay*-annulated perylene ester imides; Reagents and conditions: (i) 1-amino-octadecane, imidazole, 165 °C, microwave, 35 min. (50-55%).

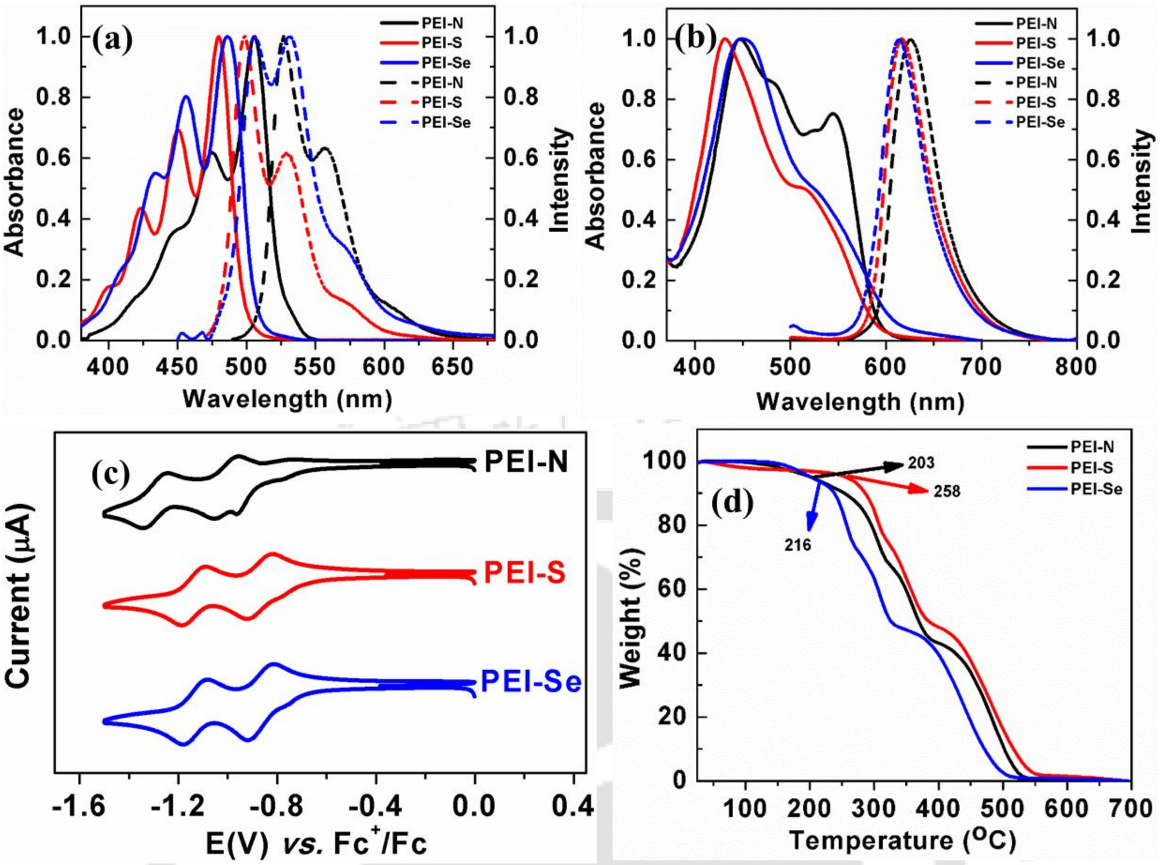

Figure 5.5. (a) Absorption (continuous line) and emission spectra (broken line) in micromolar chloroform solution and (b) in thin films of compounds **PEI-N**, **PEI-S** and **PEI-Se**; (c) Cyclic voltammograms of *bay*-annulated PEIs; (d) TGA curves obtained for *bay*-annulated PEIs at a rate of 10 ºC/min under N_2 atmosphere.

(0.1 M NaOH solution, Q_f = 0.79), showed a higher quantum yield for **PEI-N** and **PEI-S** (0.89 and 0.7), but a lower quantum yield for compound **PEI-Se** (0.06). The CV studies revealed the reversible redox process and the electron deficient nature of the PEIs (Figure 5.5c). Herein, we are describing important multiple properties of the newly synthesized PEI molecules and their photophysical behavior, processing advantages via higher solubility, energy level tuning via easy functional group modification, morphology and device parameters, that are all very unique and not observed previously with any imide derivatives. Utilizing these newly synthesized molecules, we have demonstrated that instead of having a material with an emission covering entire visible spectrum, which is very difficult to synthesize and realize, it is possible to achieve the white light emission with a suitable combination of host matrix, emissive material and electron transport layer. To the best of our knowledge this is the first report on the application of this new class of materials in organic electronic devices and OLEDs in particular.

To study the electroluminescent properties of the synthesized luminescent materials, solution processed OLEDs were fabricated utilizing the PEIs as emissive layer, owing to their excellent solubility in common organic solvents. All the devices have been fabricated using the method described in Chapter 3a. In our previous Chapter 3a, we have observed that, host-guest OLEDs with PTEs exhibited superior performance in comparison to the devices based on PTEs alone. In addition, PVK is known to have exceptional film forming property and good miscibility with widely varied emissive materials.[16,17] PVK has a LUMO energy level of -2.2 eV and a HOMO energy level of -5.8 eV. PEDOT:PSS was therefore coated on ITO (indium tin oxide, which serves as a transparent anode) as a hole injection layer to facilitate more hole injection from the anode side. PEDOT:PSS is widely used as HIL (hole injection layer) material which also has the advantages of smoothening the ITO surface, decreasing the turn-on voltage and reducing the probability of electrical shorts. Eventually this extends the device lifetime. A bilayer cathode consisting of LiF (lithium fluoride) and Al (aluminum) was considered, where LiF functions as EIL (electron-injecting layer). Also, to improve recombination in the emissive layer, it is important to confine the electrons and holes to the emissive layer. Since PVK has a higher hole mobility as compared to its electron mobility, without any hole blocking or electron transporting layer, there is a strong probability that the excitons are generated in the vicinity of the cathode and get quenched by the electrode. Two different electron transport layers Bathophenonthroline (Bphen) or 2,2′,2"-(1,3,5-Benzinetriyl)-tris(1-phenyl-1-*H*-benzimidazole) (TPBi) with deeper HOMO level than that of PVK were therefore used as ETL (electron-transporting/hole-blocking layer) materials. Incorporation of BPhen or TPBi as ETL reduces the injection barrier for the electrons from the cathode to the emissive layer of the device and facilitates more electron injection and provides a barrier for the holes from the emissive layer.[18] At the same time it also shifts the recombination zone away from the cathode thereby reducing the probability of quenching. This combination leads to the following two device structures, where the ETL materials are interchanged, *i.e.* Device configuration **1**: ITO/ PEDOT:PSS/ (PVK:**PEIs**)/BPhen/LiF/Al and Device configuration **2**: ITO/PEDOT:PSS/ (PVK:**PEIs**)/TPBi/LiF/Al (Figure 5.6a). The doping ratio of PVK and dopant were in the weight percentage ratio of 15:1. Energy level diagram of the materials used in these devices with respect to the electrodes is given in Figure 5.6b.

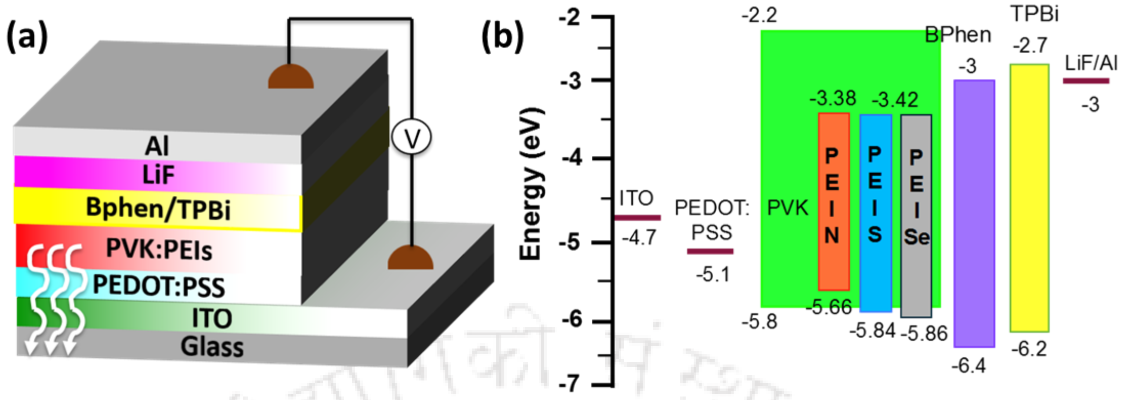

Figure 5.6. (a) Schematic of the device configuration (**1** or **2**); (b) Energy-level diagram of the materials used in the OLEDs.

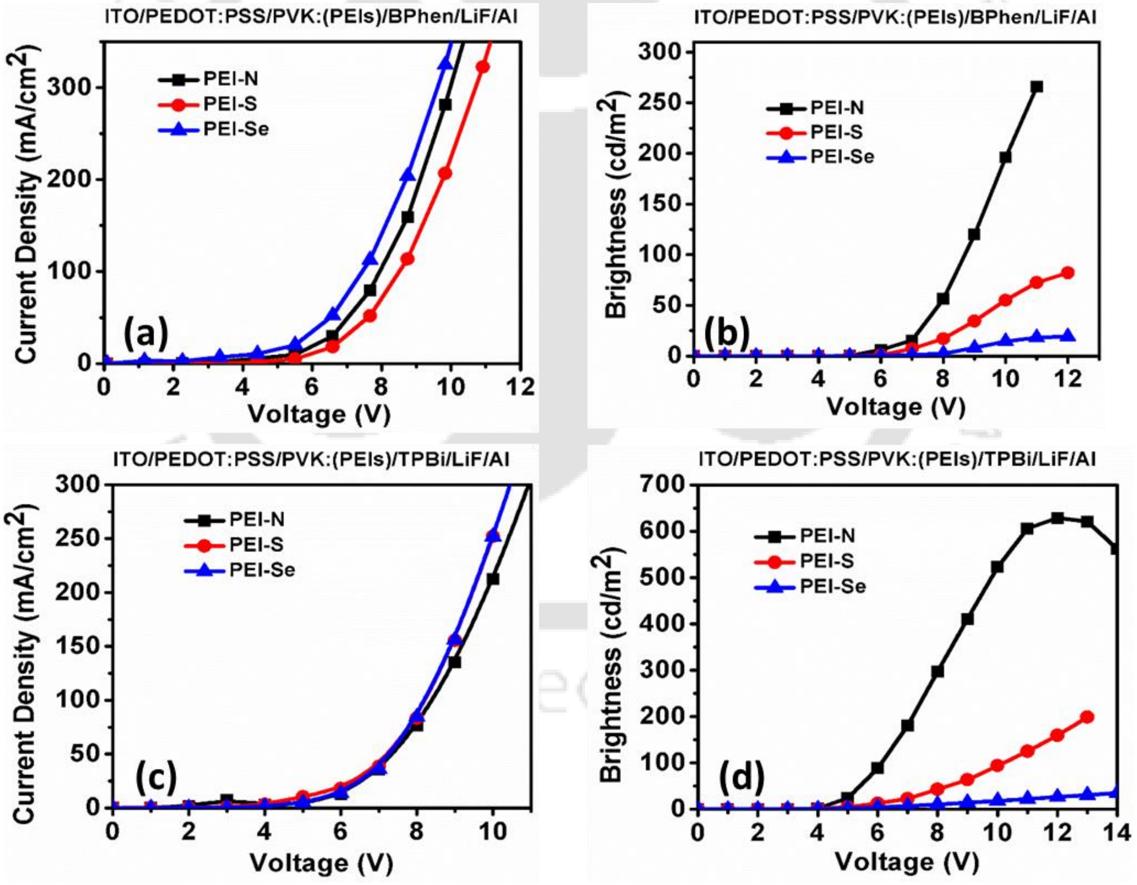

Figure 5.7. (a) Current density *vs.* voltage curves (J–V curves) in a linear scale for device configuration **1** and (c) for device configuration **2**; (b) Brightness *vs.* voltage curves (B–V) in a linear scale of the device configuration **1** and (d) for device configuration **2**.

Figure 5.7a and c shows the current density *vs.* voltage curves (J–V curves) and Figure 5.7b and d show the brightness *vs.* voltage curves (B–V) of the devices with BPhen and TPBi as ETL materials. The key device properties PEI molecules in the device configuration **PEI-N** and **PEI-S** are summarized in Table 5.3 and Table 5.4 respectively. The devices with BPhen as ETL were found to exhibit a brightness value of 265.8 cd/m^2, 82.1 cd/m^2 and 19.3 cd/m^2 for compounds **PEI-N**, **PEI-S** and **PEI-Se** respectively, whereas the devices with TPBi as ETL were found to exhibit a brightness values of 628.5 cd/m^2, 145.1 cd/m^2 and 35.3 cd/m^2 for the same compounds. From these results, it has been observed that the devices with TPBi as ETL exhibited improved brightness and lowered turn on voltage as compared to the devices with BPhen as ETL. This is due to the lower electron injection barrier of TPBi-PVK interface that facilitates more electron injection into the emissive layer resulting in an increased recombination at a comparatively lower voltage.[19]

Table 5.3. Properties of OLEDs fabricated with BPhen (Device configuration **1**)

PEIs	Turn on voltage (V)*	Maximum brightness (cd/m^2)	Peak wavelength (nm)	CIE coordinates (x,y)	Color correlated Temperature (CCT) (K)
PEI-N	5.30	265.82	416, 583	(0.48, 0.42)^a, (0.49,0.46)^b	2571^a, 2647^b
PEI-S	6.08	82.08	415, 585	(0.50, 0.43)^a, (0.48,0.44)^b	2415^a, 2688^b
PEI-Se	6.97	19.31	416, 588	(0.47, 0.40)^a, (0.48,0.42)^b	2471^a, 2453^b
*Turn-on voltage is defined as the voltage needed for the device to reach a brightness level of 1 cd/m^2; ^{a}6V, ^{b}12V					

Table 5.4. Properties of OLEDs fabricated with TPBi (Device configuration **2**)

PEIs	Turn on voltage (V)*	Maximum brightness (cd/m^2)	Peak wavelength (nm)	CIE coordinate (x,y)	Color correlated Temperature (CCT) (K)
PEI-N	3.68	628.45	416, 590	(0.56, 0.42)^a, (0.50,0.44)^b	2388^b
PEI-S	3.94	145.10	419, 577	(0.36, 0.33)^a, (0.39,0.38)^b	4173^a, 3724^b
PEI-Se	4.29	35.34	419, 581	(0.37, 0.31)^a, (0.32,0.28)^b	3496^a, 6194^b
*Turn-on voltage is defined as the voltage needed for the device to reach a brightness level of 1 cd/m^2; ^{a}6V, ^{b}14V					

The EL spectra of the devices with BPhen and TPBI as ETL materials are shown in Figure 5.8a and 5.8b along with the corresponding CIE coordinates (Figure 5.8c and 5.8d). From the EL spectra, it has been observed that all the devices exhibit two peaks, one due to the PVK host and the other due to the dopant luminescent materials suggesting partial energy transfer from PVK host to the LC dopants. The less intense blue emission peak in the EL spectra of compound **PEI-N** based devices suggest higher energy transfer from host PVK to compound **PEI-N** as compared to that in case of compound **PEI-S** and **PEI-Se**. Another important observation from the EL spectra was that the intensity of the blue emission is more in case of TPBi based devices as compared to those of BPhen based devices. This may be due to the fact that the lower electron injection barrier at the PVK-TPBi interface, results in more number of electron injections at the LUMO level of the PVK resulting in more blue emission from PVK. From the EL spectra, near white emission was observed from the devices with PVK doped with compound **PEI-S** and **PEI-Se** as emissive layer and TPBi as the ETL (Figure 5.8d and 5.8e). To confirm this, we

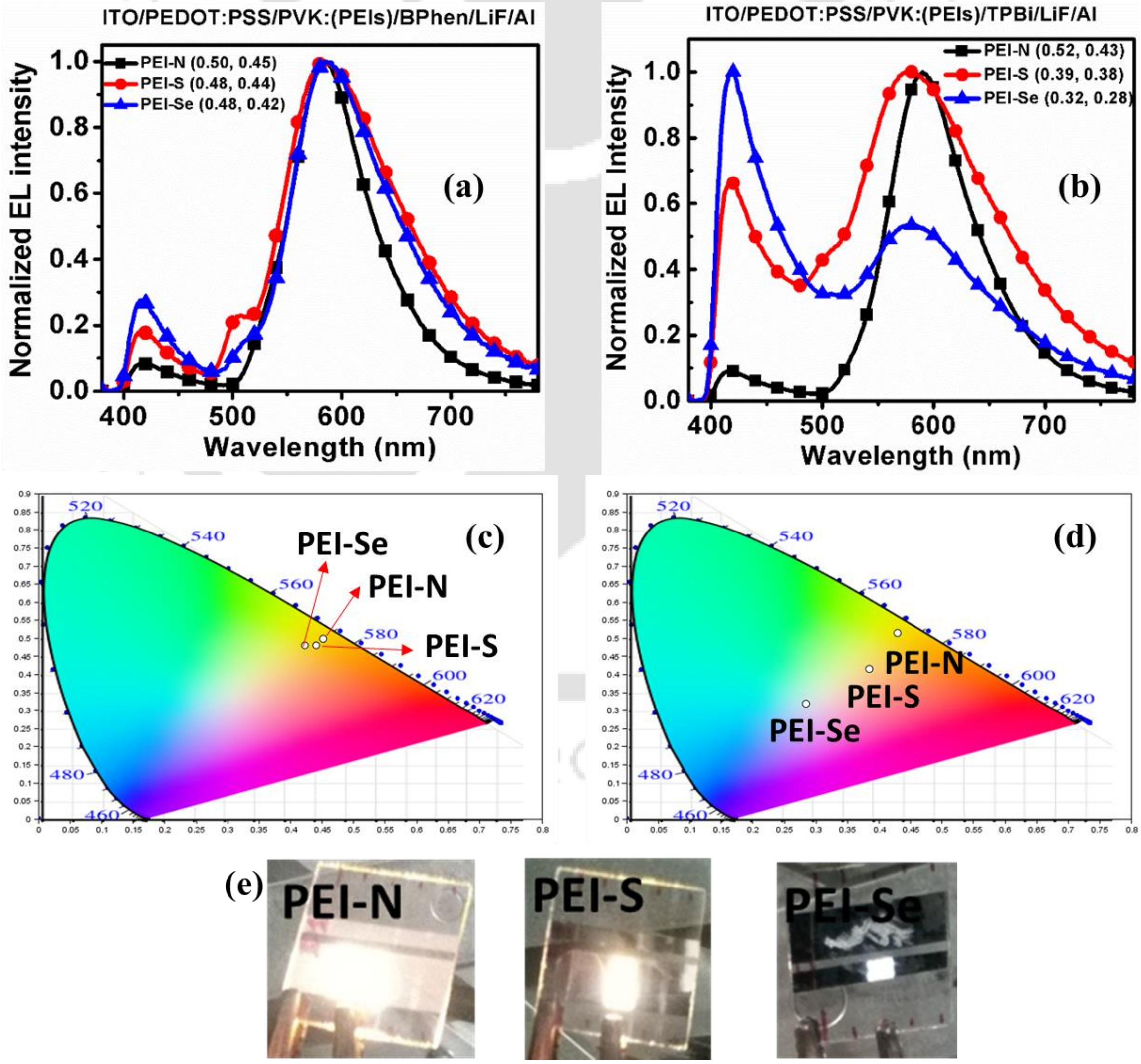

Figure 5.8. (a) Electroluminescence spectra obtained from device **1** with BPhen as ETL and (b) device **2** with TPBi as ETL; (c) Chromaticity diagram of the device **1** with BPhen as ETL and (d) device **2** with TPBi as ETL; (e) Images of the devices with TPBi as an electron transport layer.

have also studied the voltage dependent EL spectra of all the fabricated devices. The voltage dependent EL spectra of all the devices are shown in Figure 5.9. From Figure 5.9, it has been observed that the relative increase in intensity of the blue emission from PVK is more in comparison to the emission of luminescent material with the applied voltage. The CIE coordinate and the color correlated temperature of the devices varied from (0.48, 0.42) and 2571 K at 6V to (0.49, 0.46) and 2647 K at 12V for compound **PEI-N**, from (0.50, 0.43) and 2415 K at 6V to (0.48,0.44) and 2688 K at 12V for compound **PEI-S** and from (0.47, 0.40) and 2471 K at 6V to (0.48,0.42) and 2453 K at 12V for compound **PEI-Se** in case of device configuration **1** with BPhen as ETL. Similarly, CIE coordinate and the color correlated temperature of the devices varied from (0.56, 0.42) at 6V to (0.50, 0.44) and 2388 K at 14V for compound **PEI-N**, from (0.36, 0.33) and 4173 K at 6V to (0.39, 0.38) and 3724 K at 14V for compound **PEI-S** and from (0.37, 0.31) and 3496 K at 6V to (0.32, 0.28) and 6194 K at 14V for compound **PEI-Se** in case of device configuration **2** with TPBi as ETL. We assume that this may be due to the charge trapping behavior of the luminescent materials. At lower voltage, the emission from the PEIs is found to be dominant which may be due to the exciton formation in the PEI molecule as a result of its charge trapping ability. However, at high bias, excitons are formed on both PVK and PEIs due to large injection of electrons and holes and as a result an increase in the emission intensity from PVK was observed.[20] The fact that the intensity of the blue

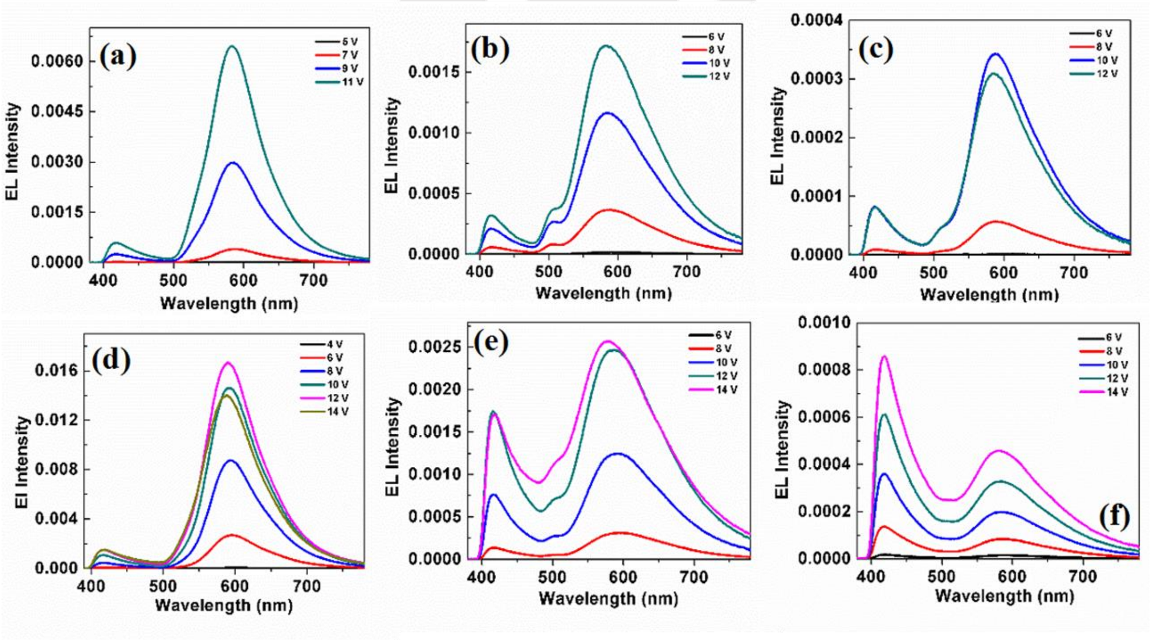

Figure 5.9. (a) Voltage *versus* electroluminescence intensity of the devices **PEI-N**, (b) **PEI-S** and (c) **PEI-Se** with BPhen; and (d) for devices **PEI-N**, (e) **PEI-S** and (f) **PEI-Se** with TPBi as ETL.

emission is more in case of TPBi based devices due to more electron injection that results from its lower injection barrier as compared to that of BPhen based devices supports our aforesaid assumption.

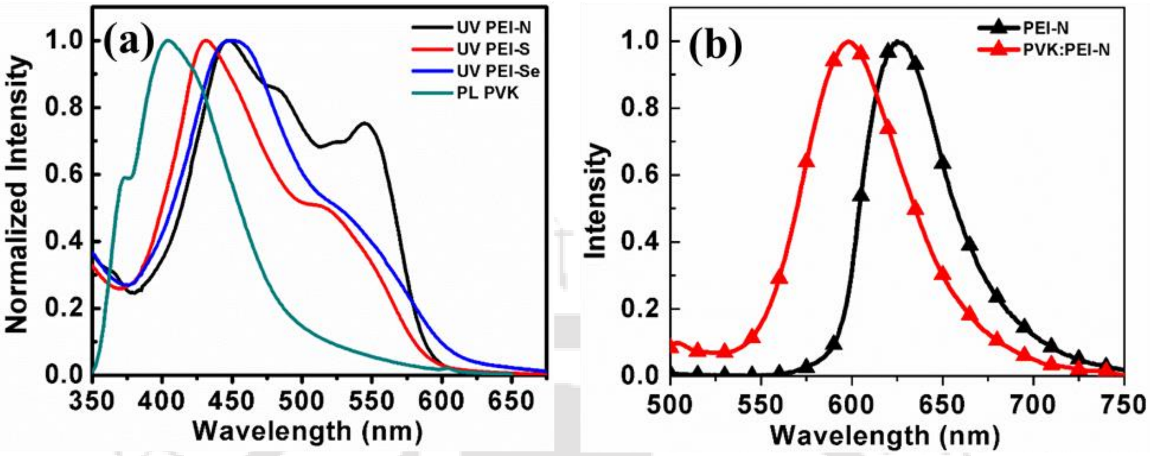

Figure 5.10. (a) Overlay UV spectra of compounds **PEI-N**, **PEI-S** and **PEI-Se** over the fluorescence spectrum of PVK in the thin film state; (b) Fluorescence spectra overlay of compound **PEI-N** and PVK:**PEI-N** mixture.

To understand the role of PVK in energy transfer to the PEI derivatives we have overlaid the fluorescence spectra of PVK thin film on the absorption spectra of PEIs in thin film state. The spectral overlap of PVK with different PEIs was varied to different extents (Figure 5.10a). Among the PEIs, the Selenium derivative **PEI-Se** is having lesser overlap, which is evident from the prominent emission band corresponding to PVK along with the emission band from **PEI-Se** (Figure 5.9f), which may support the white emission together. However, this contribution is less in comparison to the charge recombination in PVK, which is supported more in device with the TPBi as an ETL material than in the case of device with BPhen as an ETL. In order to confirm the energy transfer from the PVK host to the dopant and its effect on the EL spectra, we have studied the time resolved photoluminescence (TRPL) spectra of the compounds **PEI-N** and **PEI-S** and the mixture of these compounds with PVK in the thin film state which were prepared by spin coating. We could not obtain the TRPL spectra of mixture PVK:**PEI-Se** because of its low fluorescence intensity. However, the observations can be extended to the case of compound **PEI-Se**, which showed the partial overlap of its absorption spectrum with the emission spectrum of PVK (Figure 5.10a). For example, fluorescence lifetime measurements carried out for the thin film of compound **PEI-N** and for the thin film of PVK:**PEI-N** showed huge difference suggesting Förster resonance energy transfer (FRET) from PVK to the **PEI-N**

(Figure 5.10b, 5.11b).[21,22] Fluorescence lifetimes of the excited species formed in the thin film of compound **PEI-N** and for the thin film of PVK:**PEI-N** were measured by monitoring their emission maxima (627 nm for the thin film of **PEI-N** and 598 nm for the thin film of PVK:**PEI-N**). The thin film of compound **PEI-N** showed a biexponential decay with two excited species [τ_1 = 3.2 ns (30 %), τ_2 = 14.1 ns (70 %)] (Figure 5.11b, Table 5.5). For the thin film of PVK:10 wt% **PEI-N**, again a biexponential decay was observed with two excited species [τ_1 = 5.8 ns (40 %), τ_2 = 23.3 ns (60 %)]. Similar behavior was observed with compound **PEI-S** and its mixture with PVK, which confirmed the FRET between host and guest (Figure 5.11). Compound **PEI-Se** exhibited a biexponential decay with two excited species, but its mixture with PVK was weakly emissive, which hindered the investigation further.

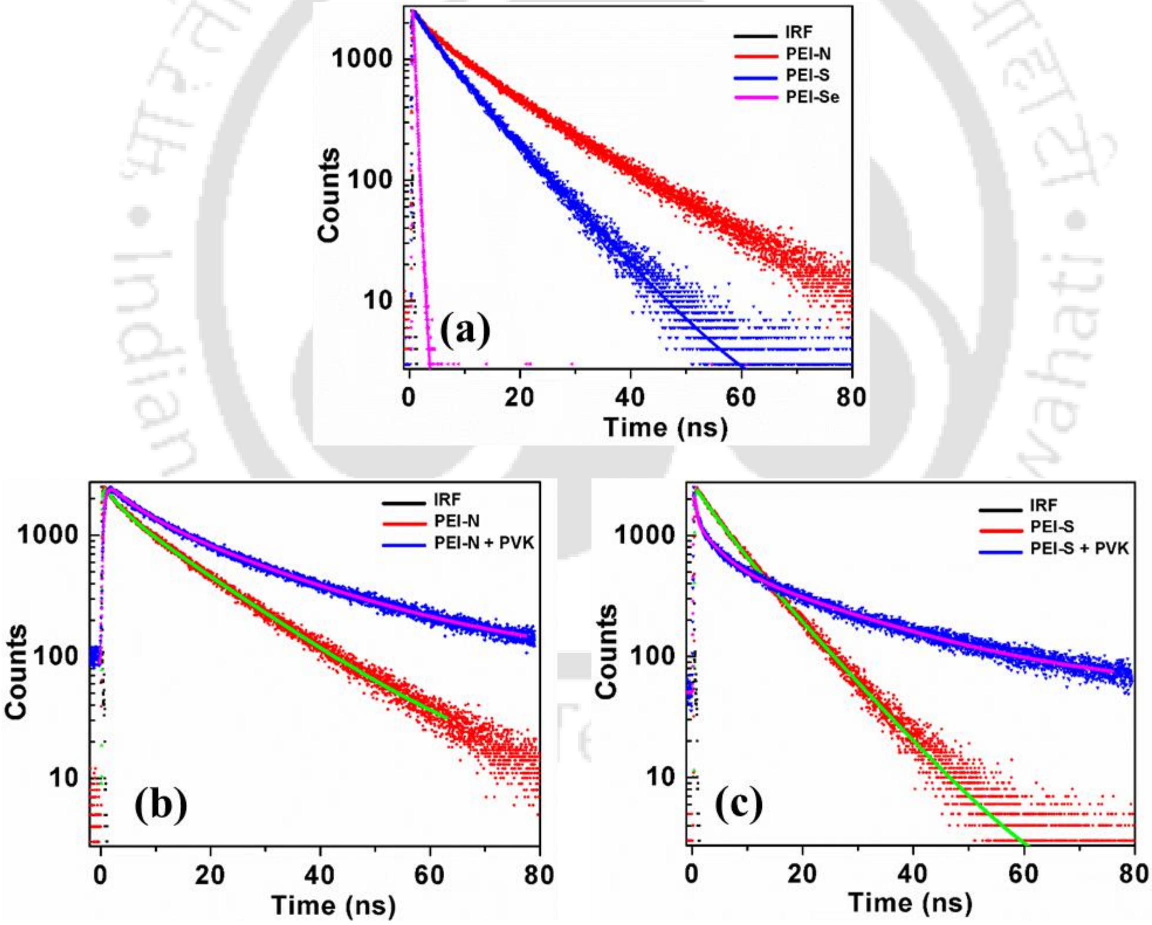

Figure 5.11. (a) The fluorescence decay of compounds **PEI-N**, **PEI-S**, **PEI-Se** (λ_{exc} = 405 nm, monitored at λ_{max} = 627 nm for **PEI-N**, 617 nm for **PEI-S** and 615 nm for **PEI-Se**) in the thin film state; (b) The fluorescence decay of compound **PEI-N** and its mixture with PVK (15:1 ratio, λ_{exc} = 340 nm, monitored at λ_{max} = 598 nm); (c) The fluorescence decay of compound **PEI-S** and its mixture with PVK (15:1 ratio, λ_{exc} = 405 nm, monitored at λ_{max} = 594 nm).

Table 5.5. Data obtained from time resolved fluorescence decay of compounds **PEI-N**, **PEI-S** and **PEI-Se**.

	Thin film of compounds[a]		**Thin film of compounds + PVK (1:15)**	
Entry	**Life time (τ_1)**	**Life time (τ_2)**	**Life time (τ_1)**	**Life time (τ_2)**
PEI-N	3.2 ns (30 %)	14.07 ns (70 %)	5.77 ns (40 %)	23.31 ns (60 %)
PEI-S	4.28 ns (36 %)	8.88 ns (64 %)	3.86 ns (56 %)	23.85 ns (44 %)
PEI-Se	3.45 ns (29 %)	8.33 ns (71 %)	-	-

[a] Concentration of solution used for spin coating: 3 mM in chloroform.

5.8. Conclusion

In conclusion, we have fabricated host-guest organic light emitting diodes by doping a series of *bay*-annulated perylene ester imides in polyvinylcarbzole (PVK) matrix. OLEDs with two different device structures were fabricated by using two different electron transport layers. The devices were found to exhibit emission from both PVK and PEIs as a result of partial Förster resonance energy transfer from PVK to the emissive dopant, although the contribution from the former one is less in case of BPhen based devices. In terms of device performance, a remarkable improvement in the emission brightness along with a reduction in the turn on voltage was noticed, when TPBi was used as an electron-transporting layer instead of BPhen. Incorporation of TPBi results in a lower electron injection barrier of TPBi-PVK interface, which facilitates more electron injection into the emissive layer thus resulting in an increased recombination at a comparatively lower voltage. Interestingly, the intensity of blue light emission was enhanced in the case of TPBi based devices that led to an overall white light emission from the OLED, which is of greater technological importance. Although the brightness of the as fabricated WOLED is less, it provides a way to achieve white light emission, with the electron-transporting layer playing a significant role in defining the emission characteristics. We have shown that instead of having a material with an emission covering whole visible spectrum, which is very difficult to synthesize, one can achieve the white emission with a suitable combination of host matrix, emissive material and electron transport layer. Further modification in the emissive materials and different sets of ETL/HIL combinations in the device fabrication are underway to enhance the higher device efficiency.

5.9. References

1. C. W. Tang and S. A. Van Slyke, *Appl. Phys. Lett.*, 1987, **51**, 913-915.
2. M. O'Neill and S. M. Kelly, *Adv. Mater*., 2011, **23**, 566-584.
3. J. Kido, M. Kimura and K. Nagai, *Science*, 1995, **267**, 1332-4.
4. a) W. Xie, Z. Wu, S. Liu and S. T. Lee, *J. Phys. D: Appl. Phys.*, 2003, **36**, 2331-2334; b) W. Xie, Z. Wu and S. Liu, *Opt. Quantum Electron.*, 2004, **36**, 635-640; c) H. Bi, K. Ye, Y. Zhao, Y. Yang, Y. Liu and Y. Wang, *Org. Electron.*, 2010, **11**, 1180-1184; d) X. Gong, S. Wang, D. Moses, G. C. Bazan and A. J. Heeger, *Adv. Mater.*, 2005, **17**, 2053-2058.
5. C. W. Ko and T. Tao, *Appl. Phys. Lett*., 2001, **79**, 4234-4236.
6. M.-L. Tsai, C.-Y. Liu, Y.-Y. Wang, J.-Y. Chen, T.-C. Chou, H.-M. Lin, S.-H. Tsai and T. J. Chow, *Chem. Mater*., 2004, **16**, 3373-3380.
7. M. Granstrom and O. Inganas, *Appl. Phys. Lett*., 1996, **68**, 147-149.
8. B. Hu and F. Karasz, *J. Appl. Phys*., 2003, **93**, 1995-2001.
9. J. I. Lee, H. Y. Chu, S. H. Kim, L. M. Do, T. Zyung and D. H. Hwang, *Opt. Mater*., 2002, **21**, 205-210.
10. J. H. Park, T.-W. Lee, Y. C. Kim, O. O. Park and J. K. Kim, *Chem. Phys. Lett*., 2005, **403**, 293-297.
11. I. Tanaka, M. Suzuki and S. Tokoto, *Jpn. J. Appl. Phys*., 2003, **42**, 2737-2740.
12. X. Gong, S. H. Lim, J. C. Ostrowski, D. Moses, C. J. Bardeen and G. C. Bazan, *J. Appl. Phys*., 2004, **95**, 948-953.
13. a) F. Würthner, *Chem. Commun*., 2004, 1564–1579; b) C. Huang, S. Barlow and S. R. Marder, *J. Org. Chem*., 2011, **76**, 2386–2407; c) S. Chen, P. Slattum, C. Wang and L. Zang, *Chem. Rev*., 2015, **115**, 11967−11998; d) F. Würthner, C. R. Saha-Möller, B. Fimmel, S. Ogi, P. Leowanawat and D. Schmidt, *Chem. Rev*., 2016, **116**, 962-1052.
14. a) Y. Lin, J. Wang, S. Dai, Y. Li, D. Zhu and X. Zhan, *Adv. Energy Mater*., 2014, **4**, 1400420 (1-5); b) G. Li, Y. Zhao, J. Li, J. Cao, J. Zhu, X. W. Sun and Q. Zhang, *J. Org. Chem*., 2015, **80**, 196-203; c) E. Kozma, W. Mro´z,a F. V.- Monteleone, F. Galeotti, A. A. -Eckstein, M. Catellania and C. Botta , *RSC Adv*., 2016, **6**, 61175–61179; d) J. E. Anthony, A. Facchetti, M. Heeney, S. R. Marder and X. W. Zhan, *Adv. Mater*., 2010, **22**, 3876-3892.
15. J. Kelber, H. Bock, O. Thiebaut, E. Grelet and H. Langhals, *Eur. J. Org. Chem*., 2011, 707-712.
16. M. Cai, T. Xiao, E. Hellerich, Y. Chen, R. Shinar and J. Shinar, *Adv. Mater*., 2011, **23**, 3590-3596.
17. J. Zou, H. Wu, C. Lam, C. Wang, J. Zhu, C. Zhong, S. Hu, C. Ho, G. Zhou, H. Wu, W. C. H. Choy, J. Peng, Y. Cao, and W. Wong, *Adv. Mater*., 2011, **23**, 2976-2980.
18. a) T. Xu, M. Yang, J. Liu, X. Wu, I. Murtaza, G. He and H. Meng, *Organic Electronics*, 2016, **37**, 93-99; b) T. Xu, Y. Zhang, B. Wang, C. Huang, I. Murtaza, H. Meng and L. Liao, *ACS Appl. Mater. Interfaces*, 2017, **9**, 2701−2710; c) T. Xu, J. Zhou, C. Huang, L. Zhang, M. Fung, I. Murtaza, H. Meng and L. Liao, *ACS Appl. Mater. Interfaces*, 2017, **9**, 10955-10962.
19. D. Das, P. Gopikrishna, R. Narasimhan, A. Singh, A. Dey and P. K. Iyer, *Phys. Chem. Chem. Phys.*, 2016, **18**, 33077-33084.
20. D. Das, P. Gopikrishna, A. Singh, A. Dey and P. K. Iyer, *Chemistry Select*, 2017, **2**, 3184-3190.
21. S.-H. Hu, T. -Q. Zhou, M.Yang, M.-H. Quan, Q.-B. Mei, B.-C. Zhai, Z.-H. Jia, W. Y. Lai and W. Huang, *Phys. Chem. Chem. Phys*., 2015, **17**, 8860-8869.

22. K. Kotwica, A. S. Kostyuchenko, P. Data, T. Marszalek, L. Skorka, T. Jaroch, S. Kacka, M. Zagorska, R. Nowakowski, A. P. Monkman, A. S. Fisyuk, W. Pisula and A. Pron, *Chem. Eur. J.* 2016, **22**, 11795-11806.